TUDelft

Delft University of Technology

Spins in diamond and silicon carbide for quantum networks

Important note
To cite this publication, please use the final published version (if applicable).
Please check the document version above.

SPINS IN DIAMOND AND SILICON CARBIDE FOR QUANTUM NETWORKS

Dissertation

for the purpose of obtaining the degree of doctor
at Delft University of Technology,
by the authority of the Rector Magnificus, Prof. dr. ir. T.H.J.J. van der Hagen,
Chair of the Board for Doctorates,
to be defended publicly on
July 12th at 12:30 o'clock

by

Sjoerd Johannes Hendrikus LOENEN

Master of Science in Applied Physics
Eindhoven University of Technology, The Netherlands,
born in Groeningen, The Netherlands.

This dissertation has been approved by the promotor:
Prof. dr. ir. R. Hanson

Composition of the doctoral committee:

Rector Magnificus	Chairperson
Prof. dr. ir. R. Hanson	Delft University of Technology, promotor
Dr. ir. T. H. Taminiau	Delft University of Technology, copromotor

Independent members:

Prof. dr. ir. C.H. van der Wal	Groningen University, The Netherlands
Prof. dr. J. Wrachtrup	Stuttgart University, Germany
Prof. dr. G.A. Steele	Delft University of Technology, The Netherlands
Dr. ir. T. van der Sar	Delft University of Technology, The Netherlands

Reserve member:

Prof. dr. Y.M. Blanter	Delft University of Technology, The Netherlands

CONTENTS

SUMMARY

A promising architecture for quantum networks consist of individual quantum processors linked together via entanglement links. These networks allow to process and transfer quantum information, and could serve as the foundation for a potential new quantum-information age, in which the advantages of quantum computation and quantum communication are used to impact society. Quantum computing promises to solve various currently intractable problems and quantum communication offers a tool for inherently safe encryption methods. To date, prototypes of these applications are being built and continuously improved.

In this thesis, we investigate electron-spin qubits associated to solid-state defects as building blocks for quantum networks. These spins have access to a register of surrounding spin qubits, such as nuclear spins, that can be used to store and process information. The spin-dependent optical transitions between the ground and excited state of the electron-spin qubit enable photon-mediated entanglement distribution over different nodes of the network. Seminal experiments using nitrogen-vacancy (NV) centers in diamond have demonstrated a 10-qubit register, a three-node network and quantum teleportation. Further scaling benefits from qubit registers with better control fidelities, which are robust against network operation. Besides, large-scale networks based on NV centers are challenging due to a sub-optimal optical interface. This has motivated efforts to investigate Group-IV defects in diamond and defect centers in silicon carbide (SiC) as future quantum network nodes. These arguments form the basis for the results achieved in this thesis.

In chapter 3, we investigate P1 centers, which are substitutional nitrogen defects in diamond with an associated electron spin. These spins could serve as an additional qubit layer on top of the regularly used nuclear-spin qubits affiliated with carbon-13 isotopes. We implement projective measurements to prepare the multiple P1-center degrees of freedom, such as the charge state, Jahn-Teller axis, nuclear spin and electron spin. In addition, we exploit these measurements to realize control and single-shot readout of the nuclear and electron spin. Finally, we investigate P1 centers as potential qubits by generating an entangled state of two P1-center electron spin qubits.

Chapter 4 aims to improve the nuclear-spin quantum memory robustness under network operation. Stochastic electron-spin dynamics during entanglement generation imparts correlated noise on nuclear-spin qubits. Measurements on a subset of these nuclear-spin qubits (spectator qubits) in combination with real-time feed-forward show promise to extend the ability to protect an arbitrary quantum state stored in a nuclear-spin qubit.

In chapter 5, we develop tools to investigate the optical coherence of single-photon emitters, and apply this to the V2 defect embedded in a nanopillar etched directly from commercially available bulk SiC. Through laser excitation and subsequent photon detection, we prepare the system in a specific spectral configuration that allows us to investigate diffusion and ionisation dynamics that happens under arbitrary laser illumination. Subsequently, we present a photoluminescence experiment that imposes minimal disturbance to the system under study and measure near Fourier-linewidth limited optical transitions. Through Landau-Zener-Stückelberg interference, we confirm the high degree of optical coherence of single defects in commercially available bulk SiC.

Finally, in chapter 6, the focus is twofold. First, we focus on a proposal to generate a multi-qubit register based on magnetically coupled electron-spin defects in SiC. We provide simulations on the defect-creation strategy based on He^+-ion irradiation and devise an architecture to simultaneously allow individual electron-spin control and intra-electron dipolar couplings above 10 kHz. Secondly, we simulate and fabricate photonic crystal cavities geared to boost the optical properties of silicon-vacancy defects for quantum network applications.

In summary, the results in this thesis advance the understanding of electron spin interactions, noise-mitigation and spin-photon interfaces for solid-state defect based quantum networks.

SAMENVATTING

Een veelbelovende strategie om kwantumnetwerken te realiseren is om individuele kwantumcomputers aan elkaar te linken door middel van verstrengeling. Zulke kwantumnetwerken zijn in staat om informatie op een kwantummechanische manier te verwerken en te verzenden, en kunnen daarmee het fundament vormen van een nieuw technologisch tijdperk. Een tijdperk waarin kwantumberekeningen en kwantumcommunicatie gebruikt worden om impact te leveren op de maatschappij. De manier waarop een kwantumcomputer werkt, geeft de mogelijkheid om een set van problemen op te lossen die momenteel niet op te lossen zijn. Anderzijds kan kwantumcommunicatie dienen als middel om inherent veilige encryptymethodes te realiseren. Vandaag de dag worden prototypes van dit soort kwantumsystemen gebouwd, en wordt er continue gewerkt om deze prototypes te verbeteren en op te schalen naar een grootte waarmee ze impact kunnen leveren op de maatschappij.

In deze thesis bestuderen we een bepaalde implementatie om zulke kwantumnetwerken te bouwen, namelijk netwerken gebaseerd op elektronenspins behorende bij roosterdefecten in vaste stoffen. Zulke spins kunnen fungeren als kwantummechanische rekenunits, genaamd quantum bits, ofwel qubits. Via deze elektronenspins kunnen ander spin-gebaseerde qubits, zoals kenspin-qubits, gecontroleerd worden om zodanig kwantuminformatie op te slaan en te verwerken. De spin-afhankelijke optische transities tussen de grond- en geexciteerde toestand van de elektronspin qubit stelt ons in staat om via fotonen verstrengeling te genereren tussen verschillende nodes van een netwerk. Baanbrekende experimenten met behulp van het stikstof-gat center (nitrogen vacancy, NV, center), een roosterdefect in diamant, hebben laten zien dat het mogelijk is om een 10-qubit register en een 3-node netwerk te maken evenals kwantumteleportatie te realiseren. Om verder op te schalen is het belangrijk om de qubits beter te kunnen controleren en om ze robuust te maken tijdens netwerk activiteiten. Daarnaast maakt het suboptimale optisch interface van het NV-center het uitdagend om een grootschalig netwerk te bouwen met dit defect. Dit heeft onderzoek in alternatieve defecten, zoals group-IV defecten in diamant of defecten in silicium carbide (SiC), gestimuleerd. De argumenten hierboven vormen de basis van het onderzoek naar diamant en SiC voor quantum netwerken in deze thesis, waarvan de resultaten als volgt gepresenteerd zullen worden.

In hoofdstuk 3 onderzoeken we P1 centers. Een P1 center is een stikstofatoom in het diamantrooster met een bijbehorende elektronspin. Zulke spins zouden een extra laag qubits kunnen vormen bovenop de meer gebruikelijke qubits gevormd door kernspins behorende bij koolstof-13 isotopen. We implenteren projectieve metingen om meerdere P1-center vrijheidsgraden, zoals de ladingstoestand, de Jahn-Teller as, de kernspin en de elektronspin te initialiseren. Tevens gebruiken we deze metingen om controle

over de kernspins en het elektronspin te realiseren en om hun toestanden uit te lezen in een enkele repetitie van het experiment. Uiteindelijk belichten we de potentie van individuele P1 centers als mogelijke qubits door een verstrengelde toestand te realiseren tussen twee elektronenspins die horen bij twee individuele P1 centers.

Hoofdstuk 4 heeft als doel om de robuustheid van een kernspin qubit, die fungeert als kwantumgeheugen, te verbeteren terwijl er actief processen gedraaid worden op het kwantumnetwerk, waarbij die processen het doel hebben het netwerk op te schalen naar meerdere nodes. De elektronspin qubit ondergaat tijdens zulk process een stochastische evolutie, wat gecorreleerde ruis op meerdere kernspin qubits veroorzaakt. Metingen op een subset van deze kernspin qubits (spectator qubits genoemd) in combinatie met "real-time feedforward" laten veelbelovende resultaten zien die kunnen helpen om een arbitrare kwantumtoestand langer te beschermen dan wanneer er geen spectator qubits gebruikt zouden worden.

In hoofdstuk 5 onderzoeken we de optische coherentie van enkele foton emitters via een 'check-probe' methode. We passen deze methode toe op een enkel V2 center in een nanopilaar gemaakt uit commercieel verkrijgbaar bulk SiC. Door middel van laser excitatie en daaropvolgende fotonemissie prepareren we het systeem in een bepaalde toestand die ons in staat stelt de diffusie- en ionisatiedynamica vast te stellen die zich afspeeld onder excitatie van verschillende lasers. Vervolgens presenteren we een fotoluminescentie methode die het systeem wat we onderzoeken minimaal verstoort, en meten we optische lijnbreedtes dicht tegen de Fourierlimiet aan. Via Landau-Zener-Stückelberg interferentie bevestigen we hoge optische coherentie van enekele defecten in commercieel verkrijgbare bulk SiC.

Uiteindelijk, in hoofdstuk 6, is de focus tweeledig. Eerst focussen we op een voorstel wat betreft de creatie van een multi-qubit register gebaseerd op magnetisch gekoppelde elektron-spin roosterdefecten in SiC. We tonen simulaties gericht op de strategie om roosterdefecten te creëren met He^+-ion bestraling en bedenken een methode om controle over individuele elektron-spin qubits te realiseren onder de conditie dat er intra-elektronspin koppelingen van sterker dan 10 kHz zijn. Ten tweede simuleren en fabriceren we fotonische kristal trilholtes die gemaakt zijn om de optische eigenschappen, in de context van kwantumnetwerken, van het V2 defect in SiC te verbeteren.

1

INTRODUCTION

1.1. A BRIEF HISTORY OF QUANTUM INFORMATION

The late 30's and 40's of the 20th century mark a critical period in relation to the communication and computational technologies that are nowadays abundantly available and heavily used. In 1937, Alan Turing published pioneering work on the concept of a theoretical computing device, which was soon named a Turing Machine[1]. Turing was also heavily involved in the realisation of the Bombe computer, famously known for the decryption of the German Enigma cipher system in 1940. In 1945, thanks to the (war-motivated!) investments of the US government, the first programmable electronic general-purpose digital computer named ENIAC was realized[2]. In 1948, Claud Shannon provided a mathematical theory of digital communication that provided a way to quantify information and marked the start of information theory[3]. This work sparked the word *bit*, an abbreviation of binary informational unit. A year later, Shannon published seminal work on cryptography systems[4].

The computation units of the first computers, including ENIAC, were based on vacuum tubes. Vacuum tubes however were bulky, unreliable and generated a large amount of heat. Soon after, computers became transistor-based. Transistors are much smaller in size and more energy-efficient in operation, and revolutioneized the computer industry. In 1969, the ARPANET was realized. Here four computers were remotely connected for the first time in a packet-switched network, which marked the start of the internet[5]. Both transistor-based computers, and the communication between individual nodes in a network, were not able to be operated without errors. To overcome this, error-correction protocols were established, pioneered by Hamming in 1950[6]. The central idea is that the information to be analyzed, or sent, is encoded in a redundant way. This allows to both detect, and correct, errors. Error-correction is key for reliable operation of the internet, and is of significant importance of the world-wide data storage and computing infrastructure.[7–10]

Clearly the transistor was a key enabler for the efficient operation and impact of the computer and our ability to communicate digitally. The development of the transistor, along with other ubiquitous technologies like lasers, was only made possible through a thorough understanding of quantum mechanics. However, all these technologies

1

were not reliant on the manipulation of individual quantum states[11,12]. Around 1980, physicists and mathematicians realized that the exponentially-growing state space of quantum mechanical systems could fundamentally not be simulated or calculated on a regular, classical, computer[13–15]. In 1982, Feynman proposed to harness quantum physics itself to simulate quantum mechanical systems[13] and in 1985 David Deutsch extended upon this idea and proposed a general-purpose programmable quantum computer[16]. The computational units of these computers were coined quantum bits[17], or qubits, and could leverage the purely quantum mechanical properties of superposition and entanglement. Close to 10 years later, Shor proposed one of the first quantum algorithms that provided an advantage over its classical counterparts[18]. His algorithm allowed to factor large numbers into their prime factors in polynomial time, while classical algorithms require an exponential runtime. This provided a treat to information security as many communication protocols are based on RSA encryption, which relies on the computational hardness of factoring prime numbers[19]. Shor's algorithm therefore at the same time fueled a growing interest both in quantum research and secure communication in the advent of quantum computation.

For the execution of useful large-scale quantum algorithms, such as Shor's algorithm, very low error rates (below $\sim 10^{-10}$) per operation are required[20,21]. Such low error rates, and hence the realisation of a useful quantum computer, were thought to be infeasible because of the uncontrolled interaction of quantum systems with their environment, known as decoherence[22]. However, inspired by classical error-correction protocols, Shor proposed a form of quantum error correction[23]. This allowed quantum computers to be resilient to both decoherence and faulty quantum gate operations, which implicated that a fault-tolerant quantum computer was feasible[24]. In addition, Bennett and Brassard boosted the field of quantum cryptography by proposing a way to realize inherently secure communication[25].

These developments generated a large influx of financial and human resources to the field of quantum technology, which, amongst others, led to the first experimental realization of Shor's algorithm[26]. Initially, efforts to accurately manipulate and control individual quantum states were mostly limited to University labs and research institutions. Recently however, quantum technology matured also outside of research institutions in a commercial setting. The global interest in quantum technology, and its corresponding industry, is reflected by yearly investments of over a billion dollar[27]. In the domain of secure communication, nowadays there are multiple companies that offer quantum key distribution as a commercial service[28,29]. In the quantum computing domain, landmark experiments have now demonstrated algorithms that are intractable for the most advanced supercomputers[30–32] and quantum computers with a hundred to a thousand qubits are realized[21,33]. An interesting challenge still remains. Even with the introduction of quantum error correction protocols, quantum computers require very low error rates, as well as millions of qubits to solve practically useful problems[20].

1.2. SOLID-STATE QUANTUM NETWORKS

Large-scale entanglement-based quantum networks show promise to enable both large-scale quantum computations as well as quantum communications on the same platform[34]. An interesting approach is to construct the network out of many (near-) identical nodes that can store and process quantum information and can distribute information via quantum channels[35]. Each node contains a register of high-fidelity memory and processing qubits. By establishing inter-node entanglement, e.g. via photon-based links, these nodes can be interfaced. This simultaneously scales up the available quantum register and allows to communicate quantum information. An interesting approach to build a quantum network is to use photonic links to establish inter-node entanglement[35]. These types of networks are the focus of this thesis.

Pioneering work on smaller-scale prototypes of such networks have been performed using different quantum hardware platforms. Optically-mediated remote entanglement between individually controllable qubits can be achieved via multiple strategies[36] and has been demonstrated in trapped ions and atoms[37–40], quantum dots[41,42] and defects in diamond[43–46]. Building on these results, key quantum network protocols such as entanglement distillation[47], non-local quantum gates[48], entanglement swapping[45] and quantum teleportation[49] have been realized.

A suitable quantum network node based on optically mediated inter-node entanglement is identified by three requirements[34,50]. 1) Each node provides a qubit-photon interface to allow a high-rate of entanglement distribution over the network. 2) Quantum information must be faithfully stored in a node, even under network operation. 3) High-fidelity operations allow to execute (distributed) multi-qubit protocols over the network, such as error-correction. Defects in the solid-state are an interesting platform for quantum networks as they combine (most of) these requirements, and were key to the realisation of some of the aforementioned quantum network demonstrations. Also, their solid-state nature avoids the need for ultra-high vacuum and complex laser cooling systems and provides an avenue for on-chip integration[51], as well as nanofabrication to enhance the qubit-photon interface[52]. Additionally, several defects allow operation at relatively high temperatures (1-20K)[53].

Figure 1.1 shows a schematic overview of a solid-state quantum network. Each node contains a register of processing qubits (yellow) in conjunction with an optically addressable communication qubit (purple) that enables multi-node entanglement via photonic links. I will now briefly elaborate on the three quantum network node requirements and outline the current challenges. Thereafter, I will outline the chapters of this thesis, which are motivated by the these requirements and challenges.

1. Qubit-photon interface for entanglement generation
   For solid state defects, the communication qubit is an electron spin associated to the defect. A simplified level structure of such electron spin is depicted in figure 1.1b, where spin-dependent optical transitions between the ground and excited
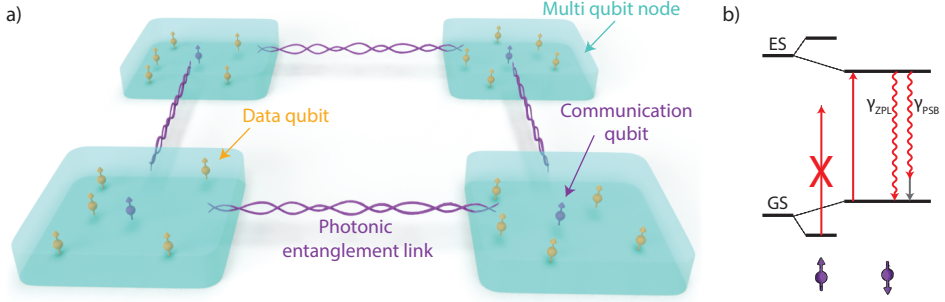
Figure 1.1: **Schematic overview of a modular solid state quantum network. a)** Each node contains an electron spin with an optical interface that serves as a communication qubit (purple) capable of generating entanglement between remote nodes via photonic links. Additionally, data qubits (yellow), either being nuclear or electronic spins, surround the communication qubit and can process and store quantum information. **b)** Simplified level structure of the electronic spin that serves as the communication qubit. Spin-dependent transitions can be driven. Two radiative decay mechanisms are shown. One only involves the emission of a photon (curved red arrow) and a phonon (grey arrow) and is characterized by the phonon-sideband decay rate γ_{PSB}. The other transitions is absent of phonon emission and characterized by the zero-phonon line decay rate γ_{ZPL}.

state are present. This is crucial for emission- and reflection-based entanglement schemes[36]. In addition, there are two other requirements. Firstly, the transitions should be coherent, meaning they are (close to) Fourier-linewidth limited. Secondly, the photon emission from the excited state should not involve the emission of a phonon, which is only satisfied for the so-called zero-phonon line (ZPL), characterized by the decay rate γ_{ZPL}[36,46,54]. However, for solid-state emitters, there are also phonon-assisted optical transitions, called phonon-sideband (PSB), characterized by γ_{PSB}. Additionally, there are non-radiative decay channels that hinder efficient entanglement generation. Finally, entanglement generation requires the ZPL photons of different emitters to be indistinguishable, which can either be realized by having spectrally identical emitters[45], or by using frequency conversion[55]. In conclusion, a key challenge to realize high entanglement generation rates is to realize defects where γ_{ZPL} simultaneously is high, narrow-linewidth and dominant over other decay mechanisms, and where the ZPL photons from distinct emitters can be made indistinguishable.

2. Quantum memory under network operation
   Large-scale quantum networks benefit from access to qubits that are robust (remain coherent) under continuous operation of the network. This pertains to faithful storage of quantum states while new entangled links are repeatedly distributed over the network[56–59]. This capability is captured by the active 'link efficiency', $\eta_{\text{link}}^* = r_{\text{ent}}/r_{\text{dec}}$, where r_{ent} is the inter-node entanglement generation rate (see point 1) and r_{dec} is the decoherence rate of data qubits while generating new entangled links, or more generally under network operation[60]. Advanced network protocols require $\eta_{\text{link}}^* \gg 1$[56–58,61], but current quantum networks all operate in

the regime where $\eta^*_{\text{link}} < 1$ [60]. To overcome this, improvements can either be made in r_{ent}, which maps to the challenge outlined in point 1, or in r_{dec}. Work that I co-authored [60], but is not included in this thesis, focused on using weakly coupled nuclear-spin qubits coupled to a single nitrogen-vacancy (NV) center in isotopically purified diamond samples to achieve a projected two-order of magnitude improvement of η^*_{link} compared to state of the art.

3. A qubit register with high-fidelity quantum gates
   A register of qubits coupled to the communication qubit (electron spin) allows to swap entanglement from the communication qubit to one these qubits, and subsequently generate new entangled links. Additionally, these qubits can provide the ability to execute complex protocols if high-fidelity quantum operations are available. Nuclear-spin qubits surrounding the electron spin are an interesting resource for that purpose and have been used to demonstrate a 10-qubit register [62]. Following this work, primitives of fault-tolerant quantum computation using nuclear spin qubits coupled to a single NV center were demonstrated, work that I co-authored [63]. In addition to these nuclear spins, electron spins coupled to the communication qubit potentially provide an additional layer of qubits on top of the nuclear-spin qubits. However, when left uncontrolled, these spins manifest as a source of noise. Therefore, an understanding of the dynamics of the spin environment will both boost the ability to suppress noise and scale up the available qubit register.

1.3. THESIS OVERVIEW

This thesis presents experimental progress towards the the challenges for quantumnetworks based on defects in diamond and silicon carbide, which are outlined in the previous section. The thesis is organized as follows:

- **Chapter 2** introduces the three electronic spin defects investigated in this thesis. These include the NV center in diamond, the P1 center in diamond and the V2 defect in silicon carbide. This chapter also explains the experimental apparatus used in this thesis. I will elaborate on the control of carbon nuclear spins surrounding the NV center, which also serves as a starting point for the control of the heterogeneous nuclear spin environment of silicon carbide. I continue outlining the charge-resonance check, an experimental sequence routinely used throughout this thesis to prepare the electron-spin defects in a desired configuration, and present an overview of the experimental timescales and parameters used throughout this thesis. I conclude by discussing photonic structures used for enhanced light collection efficiency and to enhance the ZPL transition rate (see requirement 1 above) via Purcell enhancement.

- **Chapter 3** presents the detection, control and entanglement of individual P1 centers (substitutional nitrogen defects) coupled to a single NV center in diamond. P1 centers are one of the most abundant electron spin defects in diamond and

1

are sometimes coined as dark defects because fluorescence of (individual) P1 centers has not been detected. A thorough understanding of the dynamics of complex electronic spin defects, such as P1 centers, aids to address the challenge of requirement 3. In chapter 3, we use projective measurements to initialise and read out the many degrees of freedom of the P1 center, such as the charge state, Jahn-Teller axis, nuclear spin and electron spin. We demonstrate individual control of multiple P1 centers in the spin bath. We capitalize on these tools by realizing an entangled state between two P1 centers, which demonstrates the potential of these, and other, dark electron-spin defects as a qubit platform.

• **Chapter 4** investigates the use of spectator qubits for real-time noise mitigation in the context of realizing robust quantum-network memories. We protect the state stored in a nuclear-spin memory qubit, which is coupled to a single NV center, under the process of entanglement generation. We do this by measurements on other nuclear-spin qubits (spectator qubits) in combination with real-time feedforward based on these measurements. This protection is enabled since the noise experienced by the spectator qubits is correlated to the noise experienced by the memory qubit. We present different strategies on how spectator qubits can be used, and identify the disturbance due to the spectator-qubit measurement as a factor that suppresses the potential of spectator qubits. We then realize a gate-based spectator qubit implementation that bypasses the need to perform spectator-qubit measurements, and verify that it outperforms the measurement-based spectator qubit approach. Finally, we present a study at what anticipated entanglement generation success probabilities the spectator qubit approach provides an advantage. The work in this chapter fosters the progress towards the challenge outlined in requirement 2.

• Realising NV centers that simultaneously have a narrow-linewidth ZPL transition as well as a high γ_{ZPL} (see challenge 1) has hindered scaling up quantum networks based on NV centers[53,64,65]. This motivated research into alternative defects such as Group-IV defects in diamond and defects in silicon carbide (SiC). SiC experiences many of the advantageous properties of diamond. In addition, the commercial availability, heterogeneous integration and photonic properties make silicon carbide attractive for on-chip integration of solid-state defects.
In **chapter 5**, we investigate the laser-induced spectral diffusion dynamics of a single silicon vacancy embedded in nanopillars fabricated in commercially available bulk silicon carbide. By thresholding on a minimum obtained luminescence rate, we initialize the system in a specific spectral configuration. This allows to apply external perturbations and subsequently check the how they influence the spectral dynamics, enabling to isolate diffusion and ionisation. Additionally, by running photoluminescence experiments that induce minimal disturbance to the system under study, we measure close to Fourier-limited optical transitions within an inhomogeneously broadened spectrum of about 50 times this Fourier limit. Finally, Landau-Zener-Stückelberg interference confirms the (near-)Fourier

limited linewidths in commercially available bulk silicon carbide. This highlights the potential of the V2 center, and silicon carbide as a host, for quantum network applications.

- **Chapter 6** is compartmentalized in two distinct parts. In part one, we propose how to generate electron-spin clusters using He^+-ion irradiation in SiC nanopillars. We require individual optical and magnetic control of these electron spins and present an architecture along with simulations on how to realize this. In addition, we show preliminary results on the fabrication of such a spin cluster. The investigation of electronic spin clusters contributes to the challenge in requirement 3.
  Part two focuses on the fabrication of nanophotonic crystal cavities to boost the optical interface of silicon vacancies in SiC (challenge requirement 1). We show simulations to achieve cavities with a high quality factor and low mode volume, beneficial for Purcell enhancement. Specifically, we investigate cavities geared to the optical dipole of the silicon vacancy defect. We conclude this chapter by presenting our first demonstrations of cavity fabrication using a silicon-carbide-on-insulator platform.

- **Chapter 7** summarises and concludes the findings of this thesis. I will also discuss opportunities for future experiments build upon the work shown here.

1

REFERENCES

[1] A. M. Turing, *On Computable Numbers, with an Application to the Entscheidungsproblem,* Proceedings of the London Mathematical Society **s2-42**, 230 (1937).

[2] Wikipedia, *ENIAC,* Wikipedia (2023), accessed: 2024-01-18. Page Version ID: 1191929101.

[3] C. E. Shannon, *A mathematical theory of communication,* The Bell System Technical Journal **27**, 379 (1948).

[4] C. E. Shannon, *Communication theory of secrecy systems,* The Bell System Technical Journal **28**, 656 (1949).

[5] J. Abbate, *From ARPANET to Internet: A History of ARPA-sponsored Computer Networks, 1966-1988* (University of Pennsylvania, 1994).

[6] R. W. Hamming, *Error Detecting and Error Correcting Codes,* Bell System Technical Journal **29**, 147 (1950).

[7] S. Kumari, D. L. Gahalod and D. S. Changlani, *Study of Different Types of Error Detection and Correction Code in Wireless Communication,* International Journal of Scientific Research in Science, Engineering and Technology **9**, 448 (2022).

[8] R. Goodman and M. Sayano, *The reliability of semiconductor RAM memories with on-chip error-correction coding,* IEEE Transactions on Information Theory **37**, 884 (1991).

[9] D. Rossi, N. Timoncini, M. Spica and C. Metra, *Error correcting code analysis for cache memory high reliability and performance,* in *2011 Design, Automation & Test in Europe* (2011) pp. 1–6.

[10] M. Saadoon *et al., Fault tolerance in big data storage and processing systems: A review on challenges and solutions,* Ain Shams Engineering Journal **13**, 101538 (2022).

[11] J. P. Dowling and G. J. Milburn, *Quantum technology: the second quantum revolution,* Philosophical Transactions of the Royal Society of London. Series A: Mathematical, Physical and Engineering Sciences **361**, 1655 (2003).

[12] A. Acín *et al., The quantum technologies roadmap: a European community view,* New Journal of Physics **20**, 080201 (2018).

[13] R. P. Feynman, *Simulating physics with computers,* International Journal of Theoretical Physics **21**, 467 (1982).

[14] Y. Manin, *Computable and Uncomputable*, Vol. 128 (Sovetskoye Radio, Moscow, 1980).

[15] J. Preskill, *Quantum computing 40 years later,* (2023), arXiv:2106.10522 [quant-ph].

[16] D. Deutsch, *Quantum theory, the Church–Turing principle and the universal quantum computer,* Proceedings of the Royal Society of London. Series A, Mathematical, Physical and Engineering Sciences **400**, 97 (1985).

[17] B. Schumacher, *Quantum coding,* Physical Review A **51**, 2738 (1995).

[18] P. Shor, *Algorithms for quantum computation: discrete logarithms and factoring,* in *Proceedings 35th Annual Symposium on Foundations of Computer Science* (1994) pp. 124–134.

[19] R. L. Rivest, A. Shamir and L. M. Adleman, *Cryptographic communications system and method,* (1983).

[20] M. E. Beverland *et al.*, *Assessing requirements to scale to practical quantum advantage,* (2022), arXiv:2211.07629 [quant-ph].

[21] D. Bluvstein *et al.*, *Logical quantum processor based on reconfigurable atom arrays,* Nature **626**, 58 (2024).

[22] S. Haroche and J.-M. Raimond, *Quantum Computing: Dream or Nightmare?* Physics Today **49**, 51 (1996).

[23] P. W. Shor, *Scheme for reducing decoherence in quantum computer memory,* Physical Review A **52**, R2493 (1995).

[24] P. Shor, *Fault-tolerant quantum computation,* in *Proceedings of 37th Conference on Foundations of Computer Science* (1996) pp. 56–65.

[25] C. H. Bennett and G. Brassard, *Quantum cryptography: Public key distribution and coin tossing,* Theoretical Computer Science Theoretical Aspects of Quantum Cryptography – celebrating 30 years of BB84, **560**, 7 (2014).

[26] L. M. Vandersypen *et al.*, *Experimental realization of Shor's quantum factoring algorithm using nuclear magnetic resonance,* Nature **414**, 883 (2001).

[27] McKinsey, *Quantum Technology Monitor,* (2023).

[28] E. Diamanti, H.-K. Lo, B. Qi and Z. Yuan, *Practical challenges in quantum key distribution,* npj Quantum Information **2**, 1 (2016).

[29] F. Xu, X. Ma, Q. Zhang, H.-K. Lo and J.-W. Pan, *Secure quantum key distribution with realistic devices,* Reviews of Modern Physics **92**, 025002 (2020).

[30] F. Arute *et al.*, *Quantum supremacy using a programmable superconducting processor,* Nature **574**, 505 (2019).

[31] H.-S. Zhong *et al.*, *Quantum computational advantage using photons,* Science **370**, 1460 (2020).

[32] Y. Wu *et al.*, *Strong Quantum Computational Advantage Using a Superconducting Quantum Processor,* Physical Review Letters **127**, 180501 (2021).

1

1

[33] D. Castelvecchi, *IBM releases first-ever 1,000-qubit quantum chip,* Nature **624**, 238 (2023).

[34] S. Wehner, D. Elkouss and R. Hanson, *Quantum internet: A vision for the road ahead,* Science **362**, eaam9288 (2018).

[35] H. J. Kimble, *The quantum internet,* Nature **453**, 1023 (2008).

[36] H. K. C. Beukers *et al.*, *Tutorial: Remote entanglement protocols for stationary qubits with photonic interfaces,* (2023), arXiv:2310.19878 [quant-ph].

[37] D. L. Moehring *et al.*, *Entanglement of single-atom quantum bits at a distance,* Nature **449**, 68 (2007).

[38] S. Ritter *et al.*, *An elementary quantum network of single atoms in optical cavities,* Nature **484**, 195 (2012).

[39] J. Hofmann *et al.*, *Heralded Entanglement Between Widely Separated Atoms,* Science **337**, 72 (2012).

[40] L. Stephenson *et al.*, *High-Rate, High-Fidelity Entanglement of Qubits Across an Elementary Quantum Network,* Physical Review Letters **124**, 110501 (2020).

[41] A. Delteil *et al.*, *Generation of heralded entanglement between distant hole spins,* Nature Physics **12**, 218 (2016).

[42] R. Stockill *et al.*, *Phase-Tuned Entangled State Generation between Distant Spin Qubits,* Physical Review Letters **119**, 010503 (2017).

[43] H. Bernien *et al.*, *Heralded entanglement between solid-state qubits separated by three metres,* Nature **497**, 86 (2013).

[44] P. C. Humphreys *et al.*, *Deterministic delivery of remote entanglement on a quantum network,* Nature **558**, 268 (2018).

[45] M. Pompili *et al.*, *Realization of a multinode quantum network of remote solid-state qubits,* Science **372**, 259 (2021).

[46] C. M. Knaut *et al.*, *Entanglement of Nanophotonic Quantum Memory Nodes in a Telecommunication Network,* (2023), arXiv:2310.01316 [quant-ph].

[47] N. Kalb *et al.*, *Entanglement distillation between solid-state quantum network nodes,* Science **356**, 928 (2017).

[48] S. Daiss *et al.*, *A quantum-logic gate between distant quantum-network modules,* Science **371**, 614 (2021).

[49] S. L. N. Hermans *et al.*, *Qubit teleportation between non-neighbouring nodes in a quantum network,* Nature **605**, 663 (2022).

[50] M. Ruf, N. H. Wan, H. Choi, D. Englund and R. Hanson, *Quantum networks based on color centers in diamond,* Journal of Applied Physics **130**, 070901 (2021).

[51] J.-H. Kim, S. Aghaeimeibodi, J. Carolan, D. Englund and E. Waks, *Hybrid integration methods for on-chip quantum photonics,* Optica **7**, 291 (2020).

[52] A. Sipahigil *et al.*, *An integrated diamond nanophotonics platform for quantum-optical networks,* Science **354**, 847 (2016).

[53] D. D. Awschalom, R. Hanson, J. Wrachtrup and B. B. Zhou, *Quantum technologies with optically interfaced solid-state spins,* Nature Photonics **12**, 516 (2018).

[54] S. L. N. Hermans *et al.*, *Entangling remote qubits using the single-photon protocol: an in-depth theoretical and experimental study,* New Journal of Physics **25**, 013011 (2023).

[55] A. Stolk *et al.*, *Telecom-Band Quantum Interference of Frequency-Converted Photons from Remote Detuned NV Centers,* PRX Quantum **3**, 020359 (2022).

[56] L. Jiang, J. M. Taylor, A. S. Sørensen and M. D. Lukin, *Distributed quantum computation based on small quantum registers,* Physical Review A **76**, 062323 (2007).

[57] N. H. Nickerson, Y. Li and S. C. Benjamin, *Topological quantum computing with a very noisy network and local error rates approaching one percent,* Nature Communications **4**, 1756 (2013).

[58] N. H. Nickerson, J. F. Fitzsimons and S. C. Benjamin, *Freely Scalable Quantum Technologies Using Cells of 5-to-50 Qubits with Very Lossy and Noisy Photonic Links,* Physical Review X **4**, 041041 (2014).

[59] C. Monroe *et al.*, *Large-scale modular quantum-computer architecture with atomic memory and photonic interconnects,* Physical Review A **89**, 022317 (2014).

[60] C. E. Bradley *et al.*, *Robust quantum-network memory based on spin qubits in isotopically engineered diamond,* npj Quantum Information **8**, 1 (2022).

[61] S. De Bone, R. Ouyang, K. Goodenough and D. Elkouss, *Protocols for Creating and Distilling Multipartite GHZ States With Bell Pairs,* IEEE Transactions on Quantum Engineering **1**, 1 (2020).

[62] C. Bradley *et al.*, *A Ten-Qubit Solid-State Spin Register with Quantum Memory up to One Minute,* Physical Review X **9**, 031045 (2019).

[63] M. H. Abobeih *et al.*, *Fault-tolerant operation of a logical qubit in a diamond quantum processor,* Nature **606**, 884 (2022).

[64] A. Faraon, C. Santori, Z. Huang, V. M. Acosta and R. G. Beausoleil, *Coupling of Nitrogen-Vacancy Centers to Photonic Crystal Cavities in Monocrystalline Diamond,* Physical Review Letters **109**, 033604 (2012).

[65] C. Bradac, W. Gao, J. Forneris, M. E. Trusheim and I. Aharonovich, *Quantum nanophotonics with group IV defects in diamond,* Nature Communications **10**, 5625 (2019).

1

2

THE NV CENTER IN DIAMOND AND THE V2 CENTER IN SILICON CARBIDE: QUANTUM CONTROL, ENVIRONMENTAL SPINS AND PHOTONIC INTEGRATION

S.J.H. Loenen

The nitrogen vacancy center in diamond and the silicon vacancy center in silicon carbide are promising defects for quantum networks. Their electron spins exhibit long coherence times and a coherent spin-photon interface, which can be exploited to generate entanglement between different defects. The local environment of these defects provides opportunities to establish a local spin-based qubit register. Candidates for this register are electron spin defects, as well as the nuclear spins associated with specific isotopes of the atoms that constitute the diamond or silicon carbide lattice. Additionally, the host material allows for nanofabrication of photonic structures to boost the spin-optical interface. In this section, I will first describe how the electronic structure of the NV center provides a spin-1 ground and excited state, between which optical transitions can be driven. Then, I continue describing how we can use these transitions for quantum state initialisation and readout, and follow up by describing how we can use the NV center to control its local nuclear spin environment. Secondly, I will explain the structure of the P1-center, an electronic spin defect in diamond, and the sequence used to detect these centers via the NV. Thirdly, I will elaborate on the physics of the silicon vacancy center in silicon carbide, as well as the experimental apparatus used to study this defect. Fourthly, I will explain the protocol used to prepare our defects in the desired state prior to an experiment. Fifthly, I provide details about the experimental timescales and parameters used in this thesis. Finally, I will provide an overview of the photonic structures used in this thesis.

2.1. THE NV CENTER QUANTUM REGISTER

In this section I discuss the negatively charged nitrogen-vacancy center in diamond, from now on referred to as NV center, in the context of quantum technologies, and how we can exploit the electron spin associated to the NV center as a qubit. I will briefly highlight why diamond is an interesting host material and recap the history of NV center research. In the remainder of this section, I will firstly discuss the electronic level structure of the NV center. I will then discuss how the optical transitions that follow from the level structure are used for qubit initialisation and readout. Finally, I discuss how to decouple from, and simultaneously control, nuclear spins in the environment of the NV center.

Solid-state defects, such as the NV center, are analogous to an artificial atom trapped in a host material[1]. Diamond is an interesting host material for multiple reasons. The large electronic bandgap allows to host electronic states of the NV center distant from the valence and conduction band. This both isolates the NV center from delocalised charges, and allows to drive electronic transitions of the NV center without exchanging electrons with the diamond[2]. Its large Debye temperature suppresses phononic decoherence processes[3,4]. Diamond's high thermal conductivity allows rapid dissipation of thermal loads deposited by e.g. qubit control signals, which is relevant for experiments that require cryogenic temperatures. Also, the availability of carbon isotopes that carry a nuclear spin provides an interesting additional qubit register accessible to the NV center as I will discuss in section 2.1.3.

The NV center enjoys a rich history of research. During the late 1950s[5] and 1970s[6], hallmark electron-spin resonance studies of diamond showed signs of electron spins related to nitrogen impurities in diamond. During the 70s and 80s, optical responses at 637 nm were measured, investigated and associated to the nitrogen vacancy (NV) center[7,8]. During the 90s the electronic level structure was theoretically[9] and experimentally[10] studied, spin echo and Rabi oscillations were demonstrated for the first time[11] and magnetic resonance measurements on individually addressable NV centers were established[12]. During the 2000s the NV center gained significant interest for quantum technologies[13] and in the previous decade pioneering experiments in the context of quantum sensing[14,15], quantum computing[16,17] and quantum networks[18,19] were performed.

2.1.1. THE ELECTRONIC WAVE-FUNCTION

The derivation in this section provides background information about the origin of the NV center energy levels. Two ground state spin levels are used to define a qubit, and the spin-optical interface between the ground and excited state can be used to initialize and read out the qubit. The derivation in this section is not crucial to understand the results in the rest of this thesis. This section can be read stand-alone.

This section is based on the work of Doherty et al.[20] and Hensen[21]. In addition,

Wang also provides a detailed review on the topic of this section[22] and Maze et al. have demonstrated very analogous work[23]. Doherty et al. and Hensen provide a detailed study to solve the NV Hamiltonian (see equation (2.1)), which involves NV symmetry and group theoretical considerations. The goal here is to summarize their derivations in four steps and make the reader conceptually understand the important symmetry considerations that lead to the NV center energy level scheme. This should also clarify the meaning and importance of the labels A_1, A_2 and E often encountered when the NV energy level scheme is presented.

The NV center is a lattice defect in diamond where a nitrogen atom replaces a carbon atom adjacent to a vacancy. This provides five unbound electrons, three stemming from the carbon atoms most proximal to the vacancy and two from the nitrogen atom. In addition, an electron from the environment can be trapped which leads to the negative charge state of the NV center.

In this paragraph I recap the key ideas behind each of the four steps. 1) the NV center in the diamond lattice obeys a geometrical symmetry. This symmetry should be reflected in the electronic wave-function. In the first step, I will explain the NV symmetry. This gives rise to the labels A_1, A_2 and E, which are frequently used to label the NV energy levels. 2) I will construct the possible orbital wave-functions of a single electron, which should satisfy the NV symmetry. A natural set of basis orbitals to start from are the three unpaired sp^3 orbitals from the three carbon atoms and the sp^3 orbital from the nitrogen atom adjacent to the vacancy. 3) The orbital ground, metastable and excited state are formed by considering all six electrons and distributing them over the possible single electron orbital wave-functions while adhering to the NV symmetry. 4) The inclusion of the spin degree of freedom concludes the formation of the NV energy levels.

Before diving into the four steps, I will present the six-electron Hamiltonain of the NV center. This Hamiltonian is described as the sum of 6 single electron Hamiltonians H_i, plus the intra-electron interactions H_{ij}, and is given by

$$
\begin{aligned}
H_{NV} &= \sum_i H_i + \sum_{i>j} H_{ij} \\
&= \sum_i \left[\hat{T}_i + \hat{V}_{Ne}(\vec{x}_i, \vec{R}_0) + \hat{V}_{so}(\vec{x}_i, \vec{R}_0) \right] + \sum_{i>j} \left[\hat{V}_{ee}(\vec{x}_i, \vec{x}_j) + \hat{V}_{ss}(\vec{x}_i, \vec{x}_j) \right] \\
&= \sum_i \left[\hat{h}_i + \hat{V}_{so}(\vec{x}_i, \vec{R}_0) \right] + \sum_{i>j} \left[\hat{V}_{ee}(\vec{x}_i, \vec{x}_j) + \hat{V}_{ss}(\vec{x}_i, \vec{x}_j) \right].
\end{aligned}
\tag{2.1}
$$

Here $\hat{h}_i = \hat{T}_i + \hat{V}_{Ne}$ with $\hat{T}_i$ the kinetic energy operator for the i'th electron and $\hat{V}_{Ne}$ is the effective Coulomb potential of the interaction of the diamond nuclei and lattice electrons with the NV electron. $\hat{V}_{so}$ is the electronic spin-orbit interaction potential. The collective spatial and spin coordinates of the i'th electron are denoted by $\vec{x}_i = (\vec{r}_i, \vec{s}_i)$ and $\vec{R}_0$ denotes the coordinates of the crystal nuclei. The intra-electron interactions contain the Coulomb repulsion potential of the NV electrons $\hat{V}_{ee}$ and the dipole spin-spin

interaction $\hat{V}_{ss}$. In the following, I will explain the four steps in more detail.

1. **Geometrical symmetry**

   Since the construction of the NV center's electronic wave-function derives from the geometrical symmetry of the NV center, it is important to first understand this symmetry. The NV center in the diamond lattice is shown in figure 2.1, and obeys a C_{3v} symmetry. This means there are 3 distinct symmetry operations applicable to the NV center: 1) the identity operation, 2) rotations of $\pm\frac{2}{3}\pi$ around the axis defined by the vacancy and the nitrogen atom and 3) reflections in the three planes intersecting the nitrogen atom, the vacancy and one of the 3 carbons atoms adjacent to the vacancy, see Figure 2.1.

   The C_{3v} symmetry can be divided in three irreducible representations, which define how a certain property (here I will use a wave-function) is transformed under one of the three symmetry operations. The three irreducible representations are labelled A_1, A_2 and E and the properties are summarized table 2.1.

   The label A_1 describes that a wave-function maps to itself under all three symmetry operations and hence this wave-function has one basis function called a_1. In the group labelled A_2, a wave-function is mapped to itself for the identity and the rotation operations, but obtains "-" sign under reflection in one of the symmetry planes. Correspondingly A_2 is also described by one basis function a_2. The E symmetry is not as straightforward and consists of two basis functions e_x and e_y. A symmetry operation in the E group generally leads to a linear combination of e_x and e_y. Most importantly, the labels A_1, A_2 and E describe how a wave-function transforms under the NV symmetry operations and are respectively one, one and two dimensional.
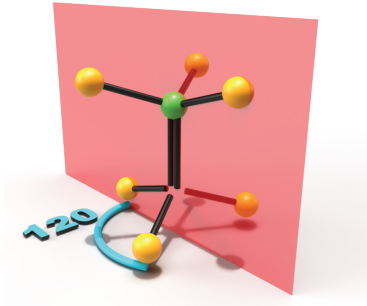
Figure 2.1: NV configuration in the diamond lattice. A nitrogen atom (green) replaces a carbon atom (yellow) adjacent to a vacancy. The vacancy gives rise to five unbound electrons, three from the three carbons and two from the nitrogen atom. In the negative charge state, a sixth electron is trapped from the environment. The blue arc shows the two rotation symmetry operations of ±120 degrees. One of the three reflection symmetry planes $3\sigma_v$ is shown in red.

Label	Basis functions	Transformation	E	$2C_3$	$3\sigma_v$
A_1	a_1	$a_1^* = d_1 a_1$	$d_1=1$	$d_1=1$	$d_1=1$
A_2	a_2	$a_1^* = d_2 a_2$	$d_2=1$	$d_2=1$	$d_2=-1$
E	e_x e_y	$e_x^* = d_{11}e_x + d_{12}e_y$ $e_y^* = d_{21}e_x + d_{22}e_y$ $\sum_j d_{ij}=1$	$\sum_i d_{ii}=2$	$\sum_i d_{ii}=-1$	$\sum_i d_{ii}=0$

Table 2.1: Table with the symmetry operations of the NV center's C_{3v} symmetry. The C_{3v} group has three symmetry operations: the identity (E), a rotation around ±120 degrees ($2C_3$), and a reflection in one of the three symmetry planes ($3\sigma_v$), see figure 2.1. The C_{3v} symmetry has three groups/irreducible representations (A_1, A_2 and E) that respond in a distinct way to the symmetry operations and cannot be reduced to smaller groups. Both the A_1 and A_2 group have one basis function and either respond symmetric or anti-symmetric to the symmetry operations. The E group is two dimensional and applying a symmetry operation to one of the basis functions generally leads to a linear combination of the two basisfunctions.

2. **Single-electron orbitals that transform according to the NV symmetry**

The form of the single electron sub-Hamiltonian $\hat{h}_i = \hat{T}_i + \hat{V}_{Ne}$ is completely imposed by the NV symmetry. Therefore, the solutions to this Hamiltonian will transform according to the NV symmetry, and thus the next paragraphs are dedicated to finding orbital wave-functions that transform according to the NV symmetry.

A natural starting point is the intrinsic sp^3 orbital of the missing nitrogen and the three sp^3 orbitals provided by the three missing carbon bonds. Individually, these orbitals do not satisfy the NV symmetry and therefore cannot form a basis for a single electron orbital wave-functions.

A NV symmetry obeying set of basis functions, called molecular orbitals, can however be constructed via a linear combinations of these atomic orbitals (LCAO). The four molecular orbitals are labelled a_1(N), a_1(C), e_x and e_y, corresponding to how they transform under the NV symmetry operations. (N) or (C) reflects whether the orbital function is predominantly localized on the nitrogen atom or the carbon atoms. The LCAO is a highly approximate method, but is useful to predict the number and symmetries of the molecular orbitals. Ab initio studies reveal the energy ordering of the molecular orbitals as shown in figure 2.2a, where a_1(N) and a_1(C) have mixed to form a_1', a_1.

To recap step 1 and 2: Using the intrinsically available sp^3 orbitals and the constraints set by the NV symmetry, I have now defined orbital basis functions. These are referred to as molecular orbitals and are single electron solutions of $\hat{h}_i = \hat{T}_i + \hat{V}_{Ne}$.

The next step concerns how to distribute the six electrons associated with the NV-center over these orbitals, and thus solving for $\sum_i \hat{h}_i$, while remaining compatible with the NV center symmetry. I will do this for the orbital part of the wave-function in step 3 and include the Coulomb interaction ($\hat{V}_{ee}$) between the electrons. This leads to distinct triplet and singlet energy states, which are known as the ground and metastable state of the NV center. I also unravel the excited state. In step four, I include the spin degree of freedom, required for the spin-spin ($\hat{V}_{ss}$) and spin-orbit ($\hat{V}_{so}$) interactions of equation (2.1). Thereby, step four completes the construction of the NV center electronic wave-function.

3. **Multi-electron orbitals: the ground, metastable and excited state.**

In step 2, I found the four single-electron molecular orbitals. As each molecular orbital can hold one spin up and one spin down electron, eight electrons can be hosted. In figure 2.2a I show the distribution of the electrons in the ground state. a_1' and a_1 are both filled with an electron pair and the remaining two electrons are hosted by e_x and/or e_y. Instead of looking in the electron picture, it is equivalent to look in the hole picture, meaning there are two holes distributed over e_x and/or e_y. Therefore the orbital state of the two holes can be described by a linear combination of the four possible $e_\nu e_{\nu'}$ products, with $\nu, \nu' = \{x,y\}$.

According to group theory, the four possible products of two such E-symmetry basis functions span three bases, each with their respective basis functions. The four products provide one basis function that transforms according to the A_1 symmetry, one that transforms according to the A_2 symmetry and two that trans-

form according to the E symmetry. It is this set of basis functions that describes the orbital wave-function of the different two-hole ground state configurations, which correspondingly fulfills the NV-symmetry.

By including the spin degree of freedom, along with the requirement that the total wavefunction is anti-symmetric, I find the six solutions to $\sum_i \hat{h}_i$. Only the A_2 orbital wave-function is anti-symmetric under particle exchange, and the others are symmetric[9]. The solutions thus are three orbital A_2 spin triplets, one orbital A_1 spin singlet and two orbtial E spin singlets. Note that the number six can also be easily obtained by inspection: within the manifold of e_x and e_y there are four possible distinct states, as both can host a spin up and spin down electron/hole. Considering the Pauli exclusion principle this means there are $\binom{4}{2} = 6$ different ways to distribute the holes.

Having solved for $\sum_i \hat{h}_i$, I continue by including the Coulomb interaction $\hat{V}_{ee}$, which is the only remaining spin-independent interaction in equation (2.1). The Coulomb interaction splits the ground state into distinct singlet and triplet states. The triplet states are the lowest in energy, consistent with Hund's rules. The A_1 singlet state is shown to be higher in energy than the two E singlet states. This energy ordering is schematically reflected in figure 2.2b.

I can follow the same procedure to detail the structure of the first excited state. Compared to the ground state, one electron is excited from the a_1 molecular orbital to e_x or e_y. In the hole picture, I thus have a hole in a_1 and e_x or e_y. Therefore the orbital state of the two holes can be described by a linear combination of the four possible $a_1 e_x$, $a_1 e_y$, $e_x a_1$ and $e_y a_1$ bases.

These combinations give two sets of two dimensional orbital basis functions that transform according to the E-symmetry. One of these sets is anti-symmetric under particle exchange and hence provides two spin triplets. The other set is symmetric and thus provides two spin singlets. Again the Coulomb interaction splits these orbital sets in accordance with Hund's rules, see figure 2.2b. likewise to the ground state, the eight excited states can be obtained by inspection: for the a_1 manifold there are two possible distinct states for one hole, and for the $e_{(x/y)}$ manifold there are four states for one electron. Hence there are $\binom{2}{1} \cdot \binom{4}{1} = 8$ different ways to distribute the holes in the excited state.

4. **Including the spin degree of freedom in the wave-function**

To completely solve the Hamiltonian of equation (2.1), I need to also consider the spin-spin ($\hat{V}_{ss}$) and spin-orbit ($\hat{V}_{so}$) interactions. These interactions are responsible for the fine structure of the energy level scheme in figure 2.2b. Via the spin-orbit coupling, I now also require that the spin-part of the wave-function transforms according to the NV symmetry.

Until now, I have focused on making the orbital wave-functions adhere to the NV symmetry, while the total wave-function is of course the product of the orbital part and the spin part. I finished part 3 by stating whether an orbital state had a corresponding spin singlet or spin triplet configuration. Without going into detail, these singlets and triplet configurations were expressed in the conventional basis: $\frac{1}{2}(|\uparrow\downarrow\rangle - |\downarrow\uparrow\rangle), |\uparrow\uparrow\rangle, |\downarrow\downarrow\rangle, \frac{1}{2}(|\uparrow\downarrow\rangle + |\downarrow\uparrow\rangle)$.

For the spin triplets, these basis states however do not transform according to the NV symmetry. To solve this, I take linear combinations of the spin-orbital wave-functions obtained from step 3. This provides the final wave-function symmetries corresponding to the triplet energy levels in figure 2.2b. For the excited state triplets, this results in one state of A_2 symmetry, one state of A_1 symmetry and two states (E_1, E_2) of E symmetry with a spin ± 1 character. Additionally, there are two E-symmetry states (E_x, E_y) with spin 0 character.
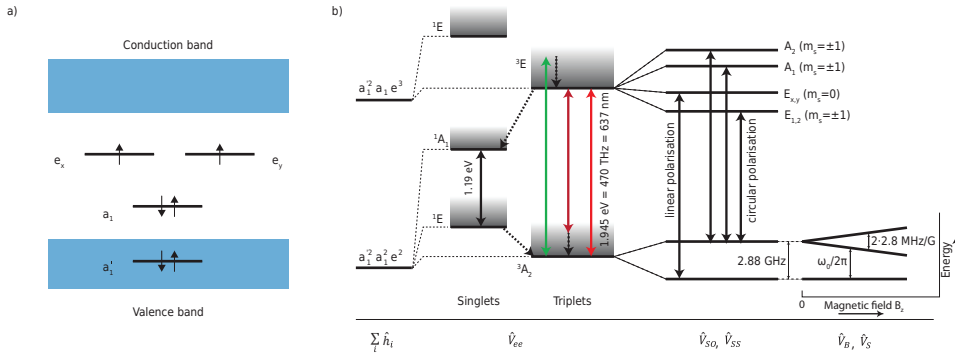

Figure 2.2: **Molecular orbital electron configuration and NV energy level diagram. a)** Position of molecular orbitals with respect to the valence and conduction band. In the ground state both the $a_1^{'}$ and a_1 molecular orbitals are filled with two electrons. The remaining two electrons are distributed over e_x and/or e_y. Here the example case of a spin up electron in both orbitals is drawn. **b)** Energy level diagram where from left to right the influence of different terms in the Hamiltonian of equation (2.1) on the energy level landscape is shown. The ground and excited state are distinguished by the different population of the molecular orbitals (left) and are split into distinct triplet and singlet states by the Coulomb interaction. The spin-orbit and spin-spin interaction provide the fine structure of the triplet states. External magnetic and strain fields can be used to further manipulate the energy levels. The symbols $^{2S+1}$K represent the spin multiplicity (S) of a state and how its wave-function transforms (K) under the NV symmetry operations (table 2.2b). Figure adapted from Hensen[24].

To recap, I first considered the spatial symmetry of the NV center in diamond and discovered there are three different symmetry operations that can be applied to the NV center symmetry. For these symmetry operations, there are three different irreducible groups that uniquely define how a certain property transforms according to these symmetry operations. These groups were labelled A_1, A_2 and E. Secondly, I solved the single electron kinetic energy and lattice potential Hamiltonian. This led to the potential molecular orbital wave-functions that a single electron can occupy. These molecular orbitals are labelled $a_1^{'}$, a_1, e_x and e_y, where the letters denote to which symmetry group these molecular orbitals belong.

Thirdly, I distributed 6 electrons, or equivalently 2 holes, over the available molecular orbitals while making sure the multi-hole orbitals still adhered to the NV symmetry. I investigated whether these multi-hole orbitals were symmetric or anti-symmetric under particle exchange which provided whether these orbitals had a corresponding spin-singlet or spin-triplet configuration. The Coulomb interaction split the singlets

and triplet states to distinct energies.

Fourthly, the spin-orbit interaction motivated the endeavor to modify the previously found multi-hole wave-functions such that now also the spin-part of the wave-function transforms according to the NV symmetry. This provided the final symmetries of fine structure states in figure 2.2b, where the fine structure is also determined by the spin-spin interaction.

The fine structure of the energy levels can further be influenced by (external) strain, electric and magnetic fields. In this thesis, I do not apply any external electric or strain field to tune the energy levels. There is strain inherent to the sample, which e.g. splits the E_x and E_y excited state energies.

I do apply external magnetic fields and use this to define two qubit states in the ground state triplet of the NV center. This ground state triplet can be described by[25]

$$H_{NV_{GS}} = \Delta_{ZFS}S_z^2 + \gamma_e(\vec{B} \cdot \vec{S}). \tag{2.2}$$

Here, $\Delta_{ZFS} \approx 2.88$ MHz is the zero-field splitting provided by the spin-spin interactions and $\vec{B} = (B_x, B_y, B_z)$ is the magnetic field vector. $\vec{S} = (S_x, S_y, S_z)$ with S_α the spin-1 operators, and the electron gyromagnetic ratio $\gamma_e = 2.802$ MHz/G. I have neglected second-order spin-orbit coupling and effects from electric (or strain) fields, as well as hyperfine interactions with nuclear spins (see section 2.1.3). In this work, I refer to the spin 0 ($m_s = 0$) ground state as $|0\rangle$ and to the level that decreases in energy with magnetic field ($m_s = -1$) as $|1\rangle$.

For the magnetic fields considered in this thesis, the energy separation between the two qubit states is in the GHz regime. Therefore, I can apply radio-frequency driving to manipulate the qubits state. I will refer to pulses used to drive between the NV qubit states as microwave (MW) pulses. I will use the term radio-frequency (RF) pulses to drive between transitions in the sub-GHz regime, see section 2.1.3. To drive between the ground and excited state of the NV center, I will use optical frequencies. Section 2.1.2 will explain the spin selective optical transitions, which enable single shot readout and ground state spin initialisation.

2.1.2. OPTICAL INTERFACE

Optical excitation enables transitions between the triplet ground and excited states. At room temperature, two-phonon Raman processes mix the excited state levels, leading to broad homogeneous linewidths of ~15 GHz[26,27]. These phonon processes are suppressed at cryogenic temperatures. All experiments on NV centers in this thesis operate at 4K, at which spin-selective excitation is possible since individual transitions are resolved with around gigahertz separations compared to their lifetime limited linewidths of 13 MHz[26,28]. Optical selection rules give rise to the transitions shown in figure 2.2b. Lateral strain lifts the degeneracy of E_x and E_y[20,23]. Different NV centers experience different strain fields, originating from their local environment. In addition,

external strain, electric and magnetic fields can be applied for controllable spectral tuning[20,23]. To preserve spin as a good quantum number, regimes where ground state level anti-crossings ($B_z \sim 1000$ G) and excited state level anti-crossings (strain and magnetic field dependent) occur are avoided.

State initialisation and readout, crucial for quantum protocols, are enabled through these optical transitions. The spin-orbit interaction couples the $m_s = \pm 1$ spin-like A_1, E_1 and E_2 excited states to the metastable singlet $^1A_1$ state. Consequently there is a significant (>40% at 4K[29]) probability to experience a non spin-conserving inter system crossing (ISC) from these excited states to the short lived A1 singlet followed by a decay into the ^{1}E singlet state[30,31]. The decay to the ground state preferentially populates the spin $m_s = 0$ state. Spin initialisation fidelities of 99.93% in 4 µs have been achieved by resonantly driving a subset of the {A_1,E_1,E_2} transitions[29].
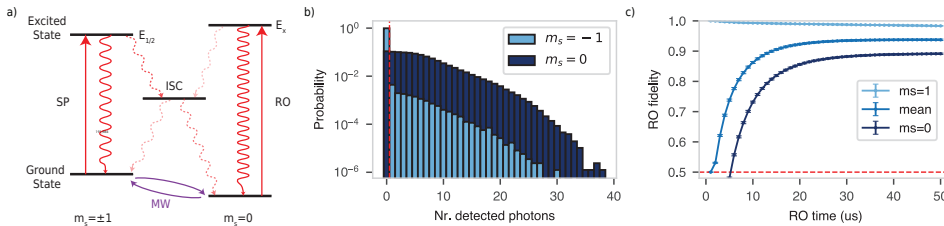

Figure 2.3: **Single-shot readout a)** NV ground and excited state level structure involving states used in optical cycling. De metastable singlet states are depicted as one effective inter system crossing (ISC) mechanism that preferentially decays to the $m_s = 0$ ground state. The readout (RO) laser is resonant with the cycling $m_s = 0$ ground to excited state transition (E_x). The SP laser is resonant with transition corresponding to the $m_s = \pm 1$ ground state and the E_1/E_2 excited state. From the E_1/E_2 states, there is a significant ISC decay rate. Driving between ground states is achieved using microwave (MW) fields. **b)**. Photon detection histogram under application of a laser on the RO transition (see a) for the state initialized in $m_s = 0$ (blue) or $m_s = \pm 1$ (orange). The red dashed line indicates the state discrimination threshold used, which, for NV SSRO used in this thesis, is one photon. **c)**. The fidelity to detect (not detect) at least one photon for the state initialized in $m_s = 0$ ($m_s = \pm 1$) as a function of applied RO laser time is shown in blue (orange). The average readout fidelity is shown in green.

Contrarily, the ISC rates from the A_2 ($m_s = \pm 1$) and the E_x and E_y ($m_s = 0$) excited states are much reduced[30,31] and consequently many spin-conserving optical cycles are possible before a non-spin conserving process occurs. Quantum state readout (RO) is achieved by resonantly exciting one highly cyclic spin transition, referred to as readout transition, see figure 2.3a. Subsequent photon detection above/below a threshold determines the spin state. The main considerations when selecting optical transitions are cyclicity, to yield a high number of emitted photons, and spectral isolation, in order to limit off-resonant excitation. The cyclicity depends on the magnetic field and lateral strain, but often the E_x transition is preferred[21,32]. For the NV center used in chapter 3 however, the intrinsic strain brings the E_x and A_1 transition in close spectral proximity and hence we use the E_y transition in that chapter.

The ability to discriminate two quantum states is captured by the single-shot readout

(SSRO) fidelity

$$F_{SSRO} = \frac{1}{2}\left(F_{0|0} + F_{1|1}\right) \tag{2.3}$$

where $F_{0|0}$ ($F_{1|1}$) is the probability to (not) obtain a photon conditioned on the state being $|0\rangle$ ($|1\rangle$). Figure 2.3b shows the histograms of the photon collection during a 50 µs readout pulse resonant with the E_x transition, conditioned on the state initialised in $|0\rangle$ (blue) and in $|1\rangle$ (orange). The data shown is for the NV center in chapter 4, and here a readout fidelity of (93.8±0.2)% is obtained by thresholding on 1 photon, see figure 2.3.

For mid-circuit measurements (see chapter 4), quantum non-demolition (QND) readouts of the NV state are important[17,33]. A stochastic change of the state of the NV center during the readout process induces dephasing on qubits coupled to the NV center[34]. In chapter 4, we use a QND-type measurement by resonant optical excitation and dynamically stopping the excitation process (within 1 µs) upon photon collection[17,35]. This prevents a subsequent non-spin-conserving optical cylce. For the NV center used in chapter 4, the probability that the electron spin is in the $|0\rangle$ state after correctly assigning the $|0\rangle$ state after the readout is 99.2%[17,35].

2.1.3. NV ELECTRON SPIN COHERENCE AND THE NUCLEAR-SPIN BATH

In the previous sections I explored the electron spin optical control for state initialisation and readout, and I discussed qubit control via microwaves. A key challenge in quantum technology is to isolate qubits from undesired interactions with their environment, while simultaneously scaling up the amount of controllable and connected qubits. In figure 2.4a, I depict a schematic overview of the NV center spin environment. Here, electronic spin defects, such as the P1-center (section 2.2) and proximal NV centers, as well as nuclear spins surround the NV center. These spin systems interact with the central NV center electron spin via the dipole-dipole or hyperfine interaction. These spin systems are a source of decoherence if they remain uncontrolled, but simultaneously provide an opportunity to scale up the available qubit register. In this section, I provide a high-level discussion of the interaction of the NV centers with its surrounding nuclear spins. I treat how this leads to decoherence of the NV center electron spin, how to decouple from this decoherence and how to control nuclear spins. For a more detailed analysis, the reader is referred to Bradley[36].

Intrinsically, the NV center hosts a nuclear spin-1 for nitrogen-14 (^{14}N) isotopes (99.63% naturally abundant) or a spin-$\frac{1}{2}$ for nitrogen-15 (^{15}N) isotopes (0.37% naturally abundant). In addition, the diamond lattice consists of carbon atoms, where the ^{13}C isotope carries a nuclear spin-$\frac{1}{2}$. Naturally, these isotopes are 1.1% abundant, but isotope engineering allows the tuning of the concentration in synthetically grown diamonds[37]. The Hamiltonian of the combined electron, ^{14}N and ^{13}C nuclear spin system is given by[36]:

$$H_{eN} = H_{NV_{GS}} + \gamma_N(\vec{B}\cdot\vec{I}_N) - QI_{z,N}^2 + \vec{S}\cdot\mathbf{A}_N\cdot\vec{I}_N + \sum_i \gamma_c\vec{B}\cdot\vec{I}_C^{(i)} + \sum_i \vec{S}\cdot\mathbf{A}_C^{(i)}\cdot\vec{I}_C^{(i)}, \tag{2.4}$$
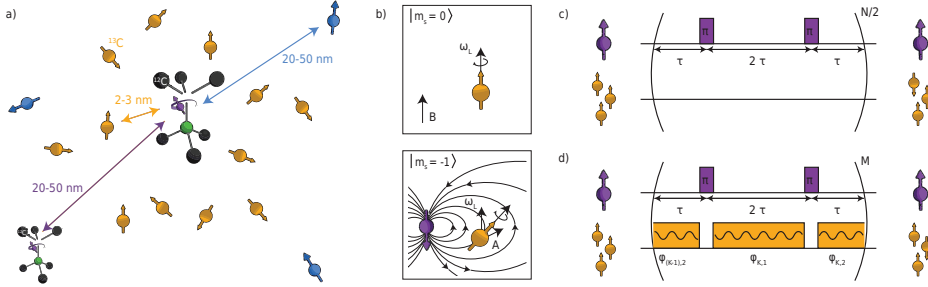
Figure 2.4: **NV spin environment and nuclear-spin evolutions conditioned on the electron-spin state. a)** Schematic representation of the NV center spin environment. Intrinsically, the NV center contains a nitrogen atom that provides a nuclear spin-1 (^{14}N isotope: 99.63% naturally abundant) or spin-$\frac{1}{2}$ (^{15}N isotope: 0.37% naturally abundant). The NV center is surrounded by nuclear spin-$\frac{1}{2}$ carbon-13 isotopes (^{13}C). Isotope engineering relative to the 1.1% ^{13}C natural abundance is possible[37]. Electronic spin defects are also naturally present. Examples are P1 centers or other proximal NV centers. All spins are coupled via magnetic interactions, such as the dipole interaction for two electron spins and the hyperfine interaction between an electron and a nuclear spin. **b)** The carbon nuclear spin precession axis and frequency are electron-spin dependent. This enables selective, universal control of these spins[38,39]. **c)** Dynamical Decoupling (DD). Pi-pulses on the NV electron spin with an interpulse delay 2τ decouple the electron spin from the surrounding environment and extend the electron spin coherence time. ^{13}C spins alternatingly experience the different rotation axes as depicted in (b). Timing τ in resonance with the hyperfine coupling of a specific ^{13}C spin enables single-qubit and electron-controlled gates on this ^{13}C spin[38]. **d)** Phase-controlled radio-frequency (RF) driving of ^{13}C spins interleaved with dynamical decoupling (DD) of the electron spin, referred to as DDRF control. The RF pulses are resonant with the ^{13}C spin conditioned on the electron being in the $m_s = -1$ state. The phase of the RF pulses is adapted to create the desired nuclear spin evolution[39].

where intra-nuclear interactions[40] are disregarded as their strength is weak compared to the interactions in equation 2.4. The nitrogen-spin gyromagnetic ratio $\gamma_N = 0.3077$ kHz/G and the quadrupolar splitting $Q = 4.95$ MHz. $\vec{I}_N = (I_{x,N}, I_{y,N}, I_{z,N})$ are the ^{14}N spin-1 operators and $\mathbf{A}_N$ is the hyperfine tensor for the electron-nitrogen interaction with components $A_{N_{\alpha\beta}}$ for $\alpha, \beta \in \{x, y, z\}$. The electron-nuclear tensor components range from 0 to ~2 MHz. The ^{13}C-spin gyromagnetic ratio $\gamma_C = 1.071$ kHz/G. $\mathbf{A}_C^{(i)}$ is the hyperfine tensor for the interaction between the electron spin and the ith ^{13}C-spin, where the components are given by the spatial position of ^{13}C-spin i and are between 0 and 50 kHz for ^{13}C-spins used in this thesis, and specifically chapter 4[41]. $\vec{I}_N = (I_{x,C}, I_{y,C}, I_{z,C})$ are the spin-$\frac{1}{2}$ operators of the ith ^{13}C spin. An important consequence of this Hamiltonian is that the nuclear spin precession axis and frequency depend on the state of the electron spin, as depicted in figure 2.4b.

The random shot-to-shot configuration of the ^{13}C spins is an important source of the natural dephasing time T_2^* for the NV electron spin. The NV center in chapter 4, hosted by a diamond with a 1.1% ^{13}C concentration, has a T_2^* of ~ 5 µs. The diamond used in chapter 3 is isotopically purified to a concentration of 0.01% ^{13}C. The significant P1 (section 2.2) concentration in that sample also contributes to the T_2^* of 94 µs. Both NV centers do not have ^{13}C spins coupled significantly stronger than the electron spin dephasing time $T_{2,e}^*$. In both chapter 3 and chapter 4, the magnetic field is predomi-

2

nantly along the z-axis with $\gamma_c B_z \gg A_{N_{\alpha\beta}}, A^i_{C_{\alpha\beta}}$. This allows to only consider $A^i_{C_{z\beta}}$ terms, known as the secular approximation. We can then decompose the electron-carbon hyperfine interaction in a component parallel ($A^{(i)}_{\parallel} S_z I_z$) and perpendicular ($A^{(i)}_{\perp} S_z I_x$) with the NV axis, where we define the coordinate frame of ^{13}C spin i such that the perpendicular hyperfine interaction acts along its x-axis.

The coherence time of the NV electron spin can be extended by the periodic application of decoupling pi-pulses on the electron spin, see figure 2.4c. This technique is referred to as dynamical decoupling (DD), and a coherence time of 1 second has been demonstrated[42]. In parallel with extending the electron spin coherence, DD enables the control of single nuclear-spin qubits by carefully choosing the interpulse delay τ in resonance with $A_{\parallel}$ of a specific ^{13}C spin[38,43,44]. The driving relies on the perpendicular hyperfine component $A_{\perp}$, which ensures the precession axes of the ^{13}C are not parallel for the different electron spin states.

To overcome the limitation to only drive ^{13}C spins with considerable $A_{\perp}$, dynamical decoupling radio-frequency (DDRF) has been developed[39]. Here dynamical decoupling pulses on the electron spin are interleaved with RF pulses. These RF pulses are resonant with a specific ^{13}C spin, conditioned on the electron spin in the $m_s = -1$ state. The phase of these RF pulses is adapted to create the desired nuclear spin evolution, see figure 2.4d. Effectively, these RF pulses fulfil the same function as $A_{\perp}$ in DD driving, and determine the Rabi frequency of the nuclear spin driving.

The power of these control techniques is demonstrated by the realization of a 10-qubit spin register, with close to a minute-long coherence time, associated with a single NV center[39]. In addition, these techniques enabled time-crystal quantum simulations[45] and quantum-error-correction protocols[35]. Also, ^{13}C spins have been used for enhanced sensing schemes[46], entanglement distillation[47] and quantum memories in quantum network protocols[48]. Extensive background on DD and DDRF control techniques, and how they are leveraged to initialise and read out ^{13}C spins, is provided by Bradley[36].

2.2. P1 CENTER

P1 centers are one of the most common electronic defects in natural type Ib and certain CVD grown or type IIa diamonds, and are formed by a substitutional nitrogen atom in the diamond lattice[5,49–51]. The P1 center is known to occur in three charge states: negative, positive and neutral[52–54]. In chapter 3, we investigate the neutral charge state of a single P1 center in detail and establish protocols to detect and control these centers. In this section, I provide background on this neutral charge state, its level structure and the Double-Electron-Electron-Resonance (DEER) technique exploited in chapter 3 to control individual P1 centers.

Detection of the neutral charge state was established via EPR measurements in 1959[5,55] and later also indirectly via NV center ODMR experiments[56–58]. A thermal

ionization energy of ~1.7 eV was found via temperature dependent electrical resistance measurements on a nitrogen rich (~200 ppb) type Ib diamond[59]. This suggests a P1 center donor level of ~1.7 eV below the conduction band, which is corroborated by several density functional theory (DFT) calculations[53,60,61]. Multiple studies on the photo-physics of P1 centers are executed that indicate an optical ionization energy between 1.9-2.2 eV[59,62–64] and witnessed a sharp feature at 4.059 eV (305 nm) and a broader feature at 4.6 eV (270 nm)[62,65,66]. Although the origin of the 4.6 eV absorption peak is still under debate, it has been proposed that this feature is associated with the excitation from the valence band maximum to create a negatively charged P1 center and a valence band hole[52]. For a review on the P1 center's level structure in the diamond band gap, I refer to Ashfold et al.[67].
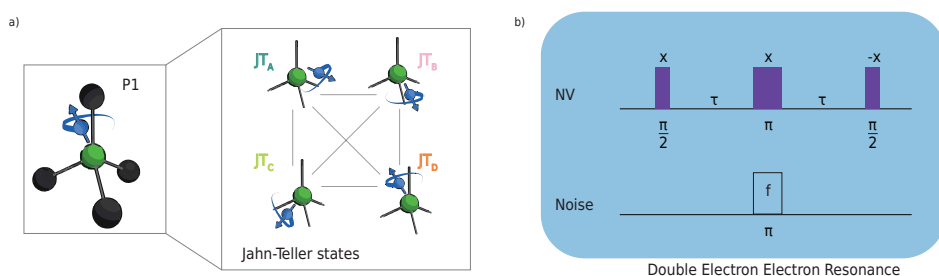
Figure 2.5: **P1 structure and level scheme. a)** The P1 center is a substitutional nitrogen atom at a carbon lattice site. In the neutral charge state, the P1 center has an associated electron spin-$\frac{1}{2}$ and a nitrogen spin-1. Additionally, it experiences a Jahn-Teller distortion that elongates one bond and preferentially populates the electron wave-function along that bond. **b)** Double electron-electron resonance sequence. A Hahn echo on the NV center's electron spin, in sync with a decoupling pulse at frequency f, will result in a drop of NV electron spin coherence if the frequency f is resonant with spins in the environment.

The aforementioned EPR and ODMR measurements have provided a detailed understanding of the spin level structure of P1 centers. The unpaired electron provided by the nitrogen atom likely resides in an antibonding orbital of s and p character[6,61]. In addition to the electron spin-1/2, a nuclear spin-1 is provided by the nitrogen (^{14}N, 99.6% natural abundance). Without distortion, the P1 center has four identical nitrogen-carbon bonds. Spontaneous symmetry breaking elongates one of these bonds by 5-36% relative to a regular carbon-carbon bond[68]. This lowers the total energy of the P1 center complex and is known as a Jahn-Teller distortion[69]. In this thesis, I refer to the elongated bond as the Jahn-Teller axis (JT axis), see figure 2.5a.

The electronic wave-function is predominantly oriented along the JT axis[5]. The energy barrier for reorientation of the P1 center's JT axis is experimentally obtained and calculated to be ~0.7 eV[68,70,71]. At cryogenic temperatures (3.3 K), the reorientation rate is below ~25 mHz and the temperature dependence of this rate has been studied by multiple groups[49,70,71]. The Hamiltonian that describes the electron spin and ^{14}N-spin is given as[5]:

$$H_{j,P1} = \gamma_e \vec{B} \cdot \vec{S}_{P1} + \gamma_n \vec{B} \cdot \vec{I}_{N,P1} + \vec{I}_{N,P1} \cdot \mathbf{P_j} \cdot \vec{I}_{N,P1} + \vec{S}_{P1} \cdot \mathbf{A_j} \cdot \vec{I}_{N,P1}, \tag{2.5}$$

where $j \in \{A, B, C, D\}$ denotes different JT axes (figure 2.5), $\vec{S}_{P1} = (S_{x,P1}, S_{y,P1}, S_{z,P1})$ the P1 electron spin-$\frac{1}{2}$ operator vector, $\vec{I}_{N,P1} = (I_{x,N,P1}, I_{y,N,P1}, I_{z,N,P1})$ the nuclear spin-1 operator vector, $\mathbf{P_j}$ the quadrupole tensor and $\vec{B}$ the applied magnetic field. The tensor $\mathbf{A_j}$ describes the hyperfine interaction between the electron and nitrogen spin, which includes both the isotropic Fermi contact term as well as the anisotropic dipole-dipole interaction. Note that for different JT axes, indicated by subscript j, only the quadrupole and hyperfine tensors differ. Building on the work of Knowles et al.[57], in chapter 3 we determine the values of these tensors to high precision.

DEER measurements, see figure 2.5c, are a tool to sense the presence of electronic spin defects that magnetically couple to the NV center[72–74]. In a DEER measurement, a Hahn-echo sequence decouples the NV center from quasi-static noise sources, which extends its coherence. However, the application of an echo pulse with a frequency f will selectively recouple the NV to environmental spins with a transition at frequency f, see figure 2.5. Hence, a loss of NV coherence detects the presence of those spins. Spectroscopy of the magnetically coupled spin bath is thus enabled by monitoring the NV coherence as a function of the frequency of the DEER echo pulse. We extensively exploit DEER in chapter 3 and show that we can initialize and read out single P1 centers using this sequence.

2.3. THE SILICON-VACANCY IN SILICON CARBIDE FOR QUANTUM NETWORKS

Thanks to the NV center's optical interface and formidable spin properties, it has been used to demonstrate numerous milestones such as multi-node quantum networks[48], multi-qubit spin registers[39] and remote quantum state teleportation[75]. However, simultaneously realising a stable narrow linewidth emission and high ZPL fraction has hindered scaling-up[76,77]. This motivated research into alternative defects that boost similar spin properties, but improved optical properties compared to the NV center. In this respect, group-IV defects in diamond have gained significant interest thanks to their first-order insensitivity to charge noise[78–81]. In parallel, defects in silicon carbide (SiC) are heavily studied[82,83].

Like diamond, SiC has a large bandgap, high Debye temperature, high thermal conductivity, and provides access over an isotopically controllable dual-type nuclear spin register. In addition, SiC possesses other advantages. Doping of SiC allows to engineer the Fermi-level, and thereby influence the preferred charge state of the quantum defect[3,84]. The second-order optical non-linearity of SiC can be used for on-chip frequency conversion[85], or potentially for on-chip optical switching via the Pockels or Kerr effect. Thanks to the use of SiC in high-power electronics, commercial SiC wafers and nanoprocessing foundries are available that potentially provide opportunities for quantum applications. Additionally, SiC can readily be integrated on insulator platforms which opens

up thin-film fabrication[85]. These features make SiC an interesting platform for quantum applications. In this section, I briefly review the history, different SiC polytypes, and defects that occur in SiC. I will then focus on the silicon-vacancy defect in the 4H-SiC polytype, which is used in chapter 5 and 6, and review its properties in the context of quantum networks.

2.3.1. Silicon carbide history and defect centers

Historically, SiC gained interest for its applications as an abrasive and later as a semiconductor[86]. It consists of double layers of silicon and carbon atoms that can be stacked in multiple ways. SiC crystals can come with over 250 different layer stacking orders, which are referred to as different SiC polytypes[87]. They generally possess similar mechanical and thermal, but varying electrical and optical, properties[88]. The three most researched polytypes, 3C-SiC, 4H-SiC and 6H-SiC are depicted in figure 2.6. While high-purity mono-crystalline silicon and germanium are produced by crystal pulling or seeding solidification from melts consisting of Si and Ge, industrially practical temperatures and pressures do not suffice to produce SiC in the same way[88]. Namely, instead of melting, SiC sublimes at these temperatures and pressures. In the late 1970s, Tairov and Tzvetkov[89,90] developed an industry-compatible sublimation growth process for 6H-SiC that was later extended to 4H-SiC, which became the most dominant type of silicon carbide because of its superior charge-carrier mobilities over 6H-SiC[87].
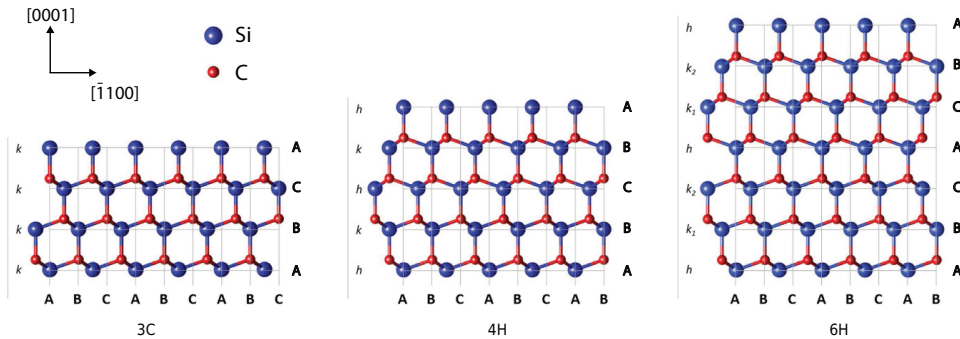
Figure 2.6: **Silicon carbide polytypes.** Three most studied silicon carbide polytypes that differ in their vertical stacking order of the silicon and carbon atom layers. Figure adapted from Ferro et al.[91].

In the photonics and optoelectronic domain, 3C-SiC initially gained a lot of attention because of the ease of hetero-epitaxial thin film CVD growth on large high purity silicon substrates, which was first reported in 1959[92]. This provided benefits such as cost-effective single crystal SiC on large silicon wafers, compatibility with CMOS infrastructure and integration with electronic structures. Still however, photonic structures typically required sophisticated processing flows which led to low yield and poor reliability. Additionally, the 20% 3C-SiC and silicon-lattice mismatch, combined with the 8% thermal expansion mismatch, unavoidably generate stacking faults and extended macroscopic defects in the growth of the 3C-SiC material[93]. This limits

the scalability of 3C-SiC. In addition, the 3C-SiC epitaxy growth results in macroscopic defects that penetrate deep down into the Si substrate[93]. These challenges motivated the use of 4H-SiC for photonic and quantum applications, which is further supported by the 4H-SiC industry maturity and the capability to host many spin-defects.

SiC hosts a multitude of optically active lattice defects. Transition metal defects such as the vanadium and molybdenum defect attracted interest for their ZPL close to the telecom band[94]. On the other hand, after their detection in EPR studies, the divacancy and silicon vacancy defects have experienced tremendous progress in terms of their coherent spin state and optical interface[83]. The divacancy is formed by adjacent vacant lattice sites, and possesses an electronic structure analogues to the NV center. The 4 non-equivalent crystallographic orientations in 4H-SiC that can form a divacancy give rise to emission wavelengths between 1078 and 1131 nm and zero field splittings between 1.22 and 1.37 GHz[95,96]. Coherence times on par with NV centers, nuclear-spin control[97] and spin-to-charge conversion single-shot readout[98] have been demonstrated. Purcell enhancement of the 8-10% ZPL emission has been demonstrated at the cost of spectral broadening[99]. Interestingly, via integration of bulk divacancies in p-i-n-junctions, Anderson et al. showed a 50-fold decrease in optical linewidth by depleting the charge environment[84].

The silicon vacancy in silicon carbide, studied in chapter 5 and 6, is a vacant lattice site at a silicon atom position and exists in 2 inequivalent lattice sites referred to as the V1 and V2 defect. The V2 defect resides at a cubic lattice site as shown in figure 2.7a, while the V1 resides in a hexagonal lattice site. The spin-$\frac{3}{2}$ ground state of both defects is described by the Hamiltonian in equation (2.6), where Δ is the ground state zero-field-splitting (ZFS), γ_e the electron gyromagnetic ratio, $\vec{B}$ the B-field vector and $\vec{S} = (S_x, S_y, S_z)$ is the vector containing the spin-$\frac{3}{2}$ operators. The V2 (V1) defect has a ground state ZFS Δ of 70 MHz (4.5 MHz) and an excited state ZFS of 1 GHz (1 GHz), and a zero-phonon-line at 916 nm (861 nm)[100–102].

$$H = \Delta S_z^2 + \gamma_e \vec{B} \cdot \vec{S} \qquad (2.6)$$

The larger ZFS of the V2 defect compared to the V1 defect enables higher Rabi frequencies without off-resonantly driving undesired transitions. Besides this advantage, a compelling other advantage of the V2 defect is that it maintains narrow optical linewidths up to 20K, rather than up to 5K as for the V1 defect[101]. This provides a closed-cycle-cryostat compatible buffer in case of sample heating due to e.g. on-chip RF driving and is one of the reasons this thesis investigates the V2 defect instead of the V1 defect.

Long spin coherence times of $T_2^* = 30$ μs and T_2 times in the order of ms, as well as control of nearby nuclear spins, have been achieved for silicon vacancy defects in isotopically purified crystals[104]. Despite these results, the V2 defect faces challenges in the optical domain. First, the fraction of ZPL emission is ~9%[103], which limits the rate at which entanglement between different defects can be established[105]. Second, see figure
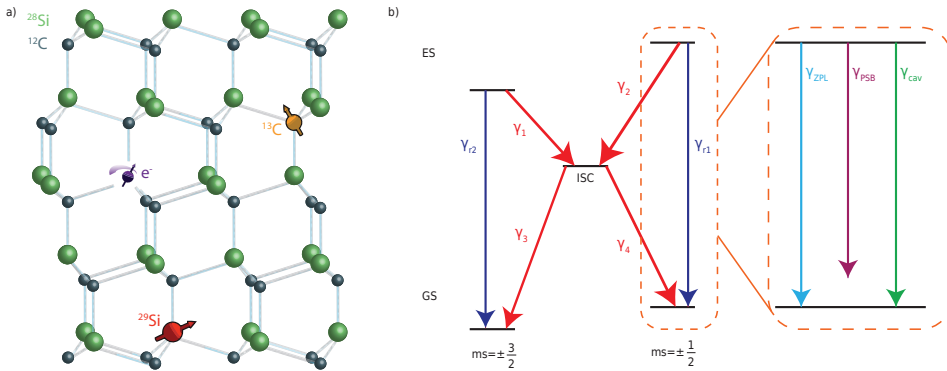
Figure 2.7: **V2 Silicon-vacancy defect in silicon carbide. a)** The V2 defect is a vacancy at the position of a silicon atom at a cubic (k) lattice site. ^{13}C and ^{29}Si isotopes carry a spin-$\frac{1}{2}$. In the negative charge state, the V2 has a spin-$\frac{3}{2}$. **b)** Electronic level structure of the negatively charged V2 defect with relevant transition decay rates. The metastable singlet states are summarized by one effective level (ISC). γ_i define the transition rates between the levels and are experimentally determined by Liu et al[103]. The transition rate from the excited state can be decomposed in a ZPL line (γ_{ZPL}) and PSB decay (γ_{PSB}) plus a potential decay channel (γ_{cav}) provided by a cavity at the ground to excited state frequency.

2.7b, the ISC transition rates γ_1 and γ_2 are relatively large compared to the radiative decay rates $\gamma_{r1/2}$, resulting in a spin flip after on average about 8 optical cycles[106]. A detailed analysis of the electronic structure and transition rates is provided by Banks et al.[106] and Liu et al.[103]. These rates severely hinder the ability to perform direct single-shot readout. Third, the dipole orientation is along the natural growth direction (c-axis) of SiC (figure 2.10b), which limits the collection efficiency via an objective parallel to this axis (see section 2.6.1).

These three challenges are simultaneously addressed by integration into a nanophotonic cavity (see section 2.6) . While initially it was believed that the V1 and V2 had very little change in their ground- and excited-state electronic wave-functions, and would therefore be robust against electrical charge noise[100], the general belief currently is that the optical dipole moment of these defects is on the same order as that of the divacancy and NV center. This also corroborates the ability to Stark tune their optical resonances over 100 GHz using ~50 V[107,108]. Irrespective of this susceptibility to electrical charges, V2 centers have been integrated in the top apexes of triangular cross-section waveguides while they maintain near lifetime-limited optical linewidths[104]. It is therefore interesting to further explore the integration of V2 defects in nanophotonic cavities and Purcell enhance spin-conserving transitions, so that direct single-shot readout and more exotic quantum protocols, such as remote entanglement between two defects, can potentially be demonstrated.

Carbon-13 (^{13}C) and silicon-29 (^{29}Si) nuclear spins surrounding the V2 defect provide a promising spin register to process and store quantum information. Control techniques derived from ^{13}C nuclear spins coupled to NV centers serve as a source of in-

spiration[38,39]. An important difference between the NV center and the V2 center is the spin-$\frac{3}{2}$ ground state of the V2 defect. However, also nuclear spin driving with central spin-$\frac{1}{2}$ electron has been demonstrated[109–111], as well as first results using a V2 center for nuclear spin driving[104].

2.3.2. EXPERIMENTAL APPARATUS

The experiments in chapter 3, chapter 4 and chapter 5 are all performed in different setups. The hardware and control logic in all these three setups is very common, and all rely on samples cryogenically cooled to ~4K in closed-cycle cryostats. In this section, I will first describe the hardware setup for the SiC research presented in chapter 5, which was designed and built during this thesis. Then, I will state the key differences between this experimental setup and the ones used for the NV center experiments in chapter 2 and chapter 3.

SiC SETUP

A schematic overview of the setup used for the SiC research is shown in figure 2.8. A PC and a microprocessor (ADwin Pro II, clock cycle 1μs) interface with all the hardware components. We use a python programming interface, along with the ADwin programming interface, to program and execute our experimental sequences. Radio-frequency (RF) and microwave (MW) signals are generated by an arbitrary waveform generator (AWG, Zurich Instruments HDAWG8), amplified (Mini-Cirucits LZY-22+), sent into the cryostat (Montana S100) and delivered to the defect via a gold stripline on the sample or via a bond-wire spanned over the sample. The RF and MW signals are used to drive ground-state electron-spin transitions, as well as nuclear spin transitions.

In addition, the setup contains optical elements. A 785 nm off-resonant laser (Cobalt 06-MLD785) is directly modulated from the ADwin and used for charge-state control. Two resonant lasers (916 nm) are modulated via acousto-optic modulators (AOM, SFO5958). The used lasers are a Toptica DLC DL pro and a Spectra-Physics Velocity TLB-6718-P. A wavemeter (HF-Angstrom WS/U-10U) and associated PID-loop stabilise the resonant laser frequencies to within 2 MHz and are used for laser frequency modulation via direct tuning of the laser cavity voltage. All lasers are combined in a single fiber using a wavelength division multiplexer (WDM, OZ Optics) before going through a $\frac{\lambda}{2}$-$\frac{\lambda}{4}$ wave-plate combination (for polarization control) and a frequency filter. Laser light is focused on the defect using a 0.9 NA microscope objective (Olympus MPLFLN 100x) at vacuum. The objective can be moved in three directions using piezo-electric stages (PI Q545.140), which are controlled by the PC and ADwin (not drawn). Light emitted from the sample can be directed to either a spectrometer (Princeton Instruments IsoPlane 81) or an avalanche photon detector (APD, Laser Components Count-50N) using an electrically controlled flip mirror. Both paths involve individual wavelength filtering. The counts on the APD are registerd by the ADwin, based on which real-time logic with a clock-cycle of 1 μs can be applied. This is used in the CR check (see section 2.4) and in chapter 4. Excitation and emission light is distinguished using a 90:10 beamsplitter. While not directly used in this thesis, the experimental setup was built with future experiments in mind. These experiments involve measurements on fiber coupled

nanophotonic devices, such that the cryostat design allows gas-tuning and hosts fiber feedthroughs.
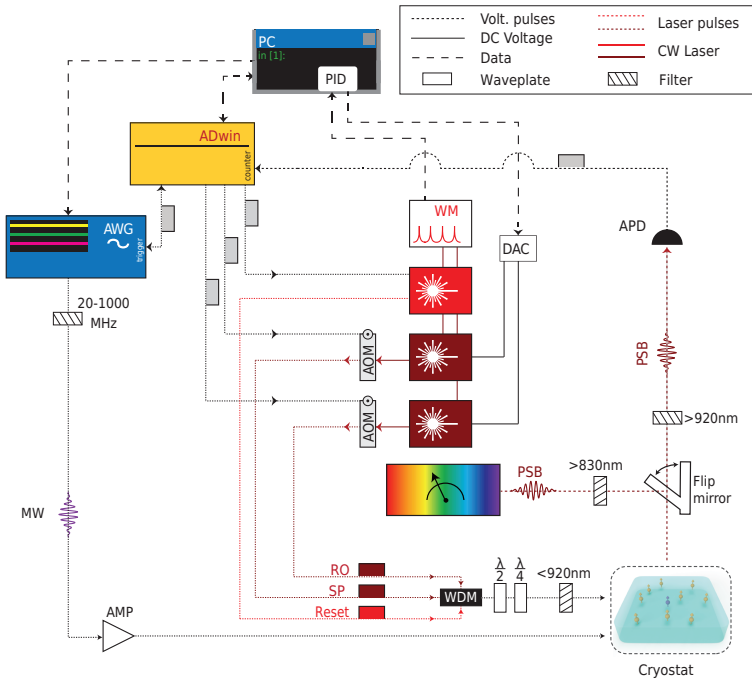
Figure 2.8: **Experimental setup.** See main text for names and model types of hardware components. Experimental sequences are programmed using a PC (python) and the microcontroller (ADwin, programming language: ADbasic). **Laser systems:** An off-resonant laser is used for charge-state control and two resonant lasers are used for spin initialisation and readout. The emission of all lasers is combined using a wavelength division multiplexer (WDM). Subsequent polarization control and spectral filtering is applied prior to entering the cryostat. Resonant lasers are stabilized to 2 MHz using a wavemeter in combination with a PID loop, which changes the laser cavity length. Laser power modulation is either done directly using the ADwin, or via acousto-optic modulators (AOMs). AOMs can be controlled by the ADwin or AWG (not drawn). **Optical elements:** Light is focused using a 0.9 NA microscope objective at vacuum. The objective can be moved in three dimensions using piezo-electric stages. An electrically controllable flip mirror directs the emitted light to either the spectrometer or the APD. Both paths involve independent frequency filtering. APD collected photons are registered by the ADwin, which enables real-time logic (1 μs clock-cycle). Excitation light and emitted light enter/exit the cryostat via the same objective. For clarity, these paths are separately depicted. **Microwave electronics:** Microwave pulses (MW) are generated directly from an arbitrary waveform generator (AWG), spectrally filtered to suppress noise, and amplified before being delivered to the sample via a gold stripline or via a bond-wire spanned over the sample. Figure adapted from Bradley[36].

NV CENTER SETUP

The experimental setups used in chapter 3 and chapter 4 are similar to the one depicted in figure 2.8. An accurate description, including hardware model numbers, is described in the thesis of Bradley[39]. Here, I will highlight the main differences. As the NV operates at different optical wavelengths, the frequency filters and laser frequencies are geared

towards the NV center's resonance wavelength (515 nm off-resonant laser and 637 nm on-resonance lasers). In addition, chapter 4 uses fast laser logic, for which the AOM associated to the resonant laser used for spin-pumping is modulated via the AWG.

For the NV setups, RF signals are directly driven from the AWG. MW signals are produced with a vector source, for which the frequency, duration, waveform and phase are determined via the AWG by IQ- and pulse-modulation. Single-sideband modulation at 250 MHz is used to spectrally isolate control pulses from low-frequency noise originating from the AWG. This low-frequency noise is filtered using a 175 MHz high-pass filter. The vector source output is amplified and sent through an AWG-controlled MW switch, additionally filtered (>175 MHz) and combined with the RF signals in a diplexer. Magnetic fields at the position of the NV center are produced using permanent neodymium magnets mounted on movable stages. No spectrometer is present in the NV-based setups, and the cryostats do not have fiber feedthroughs and gas tuning capabilities.

2.4. CHARGE-RESONANCE CHECK

Section 2.1.2 elucidated the use of the optical transitions of the NV center to facilitate electron spin initialisation and readout. In this section, I label the laser used for electron spin state initialisation as the spin-pump (SP) laser, and the laser used for electron spin state readout as the readout (RO) laser. I will explain the protocol to ensure spectral overlap between these laser frequencies and a defect's optical transitions prior to each experiment. This protocol is referred to as Charge-Resonance (CR) check. In chapter 3 and 4, we use the CR-check to check the charge state of the NV center and confirm whether the lasers are on resonance with the NV center transitions. We do this both before and after the experiment. Chapter 5 uses the CR check to investigate the spectral behavior of a single V2 center in silicon carbide.

The CR-check is designed to detect both the right charge and spectral configuration, and to probabilistically randomise both in case of an undesired detection signal. The charge state can for example change via two-photon processes [112,113] and the spectral position of the optical transition can fluctuate on various timescales due to changes in the local electric field and strain environment. Causes of this spectral diffusion and broadening could e.g. be depopulation of proximal charge traps, potentially associated with P1 centers, or surface charges in case the NV is near surfaces [20,76,114,115].

The experimental sequence of the CR-check (see figure 2.9) commences with a verification step (~150 μs) on the initial charge and resonance configuration. Here, the SP- and RO-lasers are simultaneously applied while a photon detector registers the amount of collected photons. These lasers have a linewidth of around 50 kHz and are stabilized within ~1 MHz, much narrower than the lifetime limit of the optical transitions. Also, the lasers operate well below saturation power. The absence of significant photon detection (<thr1) heralds an undesired CR state. A subsequent repump pulse randomises the state prior to a new verification step. Photon detection above thr2 confirms the targeted CR state and allows the experiment to be executed. In case the
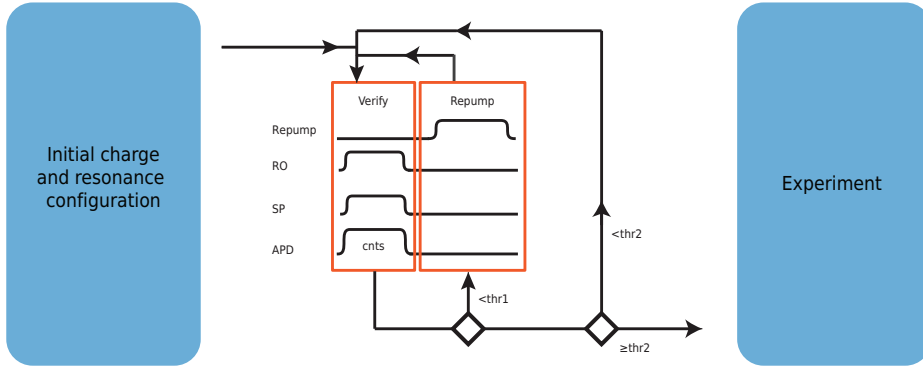
Figure 2.9: **Charge Resonance (CR) check.** Prior to starting an experiment the NV center charge and resonance state are probabilistically prepared. A verification step (150 µs) involves application of the RO and SP laser and and the detection of a number of photons exceeding a threshold (≥thr2) will herald the desired NV charge and resonance state and triggers the start of an experiment. Low (<thr1) photon detection triggers a repump pulse to reconfigure the NV charge and its electrostatic surroundings prior to another verification step.

amount of photons is equal or larger than thr1, but lower than thr2, verification step is entered again.

In the experiments used in chapter 3 and chapter 4, the repump pulse is executed off-resonantly using a strong (~10 µW) short (~50 µs) pulse. This has a strong effect on both the NV charge state and the surrounding charge configuration. Alternatively, but not used in this thesis, a much weaker pulse resonant with the neutrally charged NV state can be used. This deterministically prepares the NV center in the neutral charge state and barely disturbs the surrounding charge environment relative to the off-resonant laser pulse[116].

2.5. EXPERIMENTAL TIMESCALES AND PARAMETERS

In this section, I will recap the the relevant timescales, used powers and use cases of quantum operations, and coherence times relevant to the qubits used throughout this thesis. These values are shown in table 2.2. Note that these timescales and powers indicate the order of magnitude, the exact parameters will be different depending on the details of both the sample, the experimental setup and the specific spin investigated. The single qubit Z-gate on a ^{13}C spin is not included in table 2.2. In case we operate our experiments in a static reference frame, such Z-gate is executed by applying a waiting time on the order of the Larmor period while potentially dynamically decoupling the electron spin. During operation in the rotating frame of the ^{13}C spin, a Z-gate is compiled into other gates executed on that spin.

Process	Time	Power	Method/use case
Single qubit electron spin gate	100 ns		MW driving of electron
Electron spin initialisation	1 µs	500 nW	Initialisation in entanglement generation attempts, chapter 4
	100 µs	10 nW	Start of circuit initialisation
Electron spin readout	25 µs	1 nW	End of circuit readout
	100 µs	100 pW	Mid-circuit readout, chapter 4
CR check	Average time 300 µs	Repump power > 10 µW	
	Repump pulse 50 µs	SP power 8 nW	
	Verification period 150 µs	RO power 0.5 nW	
Electron spin T1	> 1 hour, chapter 4		
Electron spin T2*	5 µs		1.1% ^{13}C, chapter 4
	94 µs		0.01% ^{13}C & 75 ppb P1, chapter 3
Electron spin T2	1 ms		1 decoupling pulse. For both NV centers used in Ch. 3 and Ch. 4.
	1 s		20480 decoupling pulses. Measured on the NV center of Ch. 4.
Single qubit ^{13}C spin X/Y-gate	1 ms		DD driving of electron
	1 ms		RF driving of ^{13}C spins with the NV electron ms=-1
Two qubit electron-^{13}C spin gate	1 ms		
^{13}C spin initialisation & readout	2 ms		
^{13}C spin T1	> 5 min		NV electron ms=-1.
^{13}C spin T2*	10 ms		
^{13}C spin T2	50 ms		1 decoupling pulse, NV electron ms=0
	500 ms		1 decoupling pulse, NV electron ms=-1
	5 s		256 decoupling pulses, NV electron ms=-1

Table 2.2: Timescales, powers and use cases for quantum operations and coherence times for qubits discussed in this section and used throughout this thesis for experiments on NV centers. Laser powers are measured before the objective. Electron coherence times are obtained from Abobeih et al [42] and Bradley et al. [116]. ^{13}C spin coherence times are obtained from Bradley et al. [39]. The values in this table indicate the order of magnitude, exact values will likely differ samples and different spin qubits.

2.6. PHOTONIC STRUCTURES

Efficient photon collection is a key resource in exploiting the optical interface provided by solid-state defects. Both diamond ($n \approx 2.4$) and silicon carbide ($n \approx 2.6$) experience a large refractive index mismatch with air/vacuum, leading to a large fraction of photons being scattered inside the host material because of total internal reflection. While this hinders efficient free-space collection, it also provides opportunities to engineer micro- or nano-fabricated structures to guide emitted photons to e.g. collection optics [117]. In this section, I discuss several methods used and pursued in this thesis to enhance the light collection efficiency, both for free space and fiber collection. Specifically, I first focus on solid immersion lenses [118,119] and nanopillars [120,121] that modify the far-field emission pattern, but do not (significantly) affect the defect's optical decay rates. Secondly, I discuss nanophotonic cavities that, along with guiding light, can also boost the emission into desired optical modes via Purcell enhancement [77].

2.6.1. SOLID IMMERSION LENS AND NANOPILLAR

Figure 2.10 shows schematics of bulk defects in a high-refractive-index material with the optical dipole oriented parallel to the surface, and perpendicular to the surface. The dashed arrows schematically depict the radiation directions, and in these configurations I consider collection with a high NA objective from the air/vacuum side. Light rays (or k-vectors of a plane wave expansion) with angles larger than $\theta > \arcsin(1/n)$, with n the refractive index, are lost via total internal reflection. Additionally, even for angles smaller than θ, refraction at the interface distributes emission over a large range of angles that are not all collected by the numerical aperture of the objective. This can be circumvented by solid immersion lenses (SILs). SILs are half-spherical structures
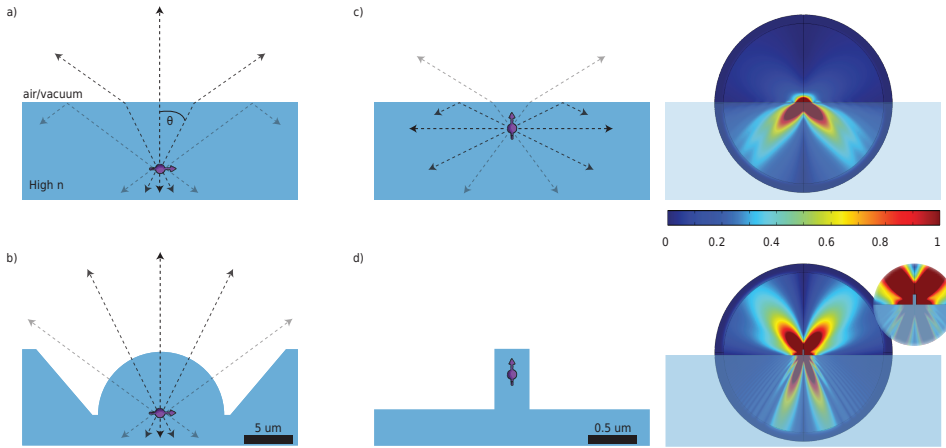
Figure 2.10: **Bulk, SIL and nanopillar radiation directions. a),b)** Schematic sketches of the radiation pattern for an optical dipole oriented parallel to the air interface in bulk (a) and in a solid immersion lens (b). Dashed arrows depict the radiation direction. Figure adapted from [122]. **c)** Schematic of radiation directions for a bulk optical dipole oriented perpendicular to the air interface (left) and simulated spatial distribution of the normalized electric field for a dipole 50 nm below the surface (right). **d)** Optical dipole in a nanopillar. Nanopillar (left) and the simulated spatial distribution of the normalized electric field for a defect placed at the center of an 1100 nm high and 300 nm diameter silicon carbide nanopillar. The inset shows a close up of the center, where the nanopillar dimensions relative to the simulation volume are visible. Simulations are reprinted from de Jong [123].

fabricated around the defect, such that light emitted towards the objective side incidents perpendicularly on the air interface. For optical dipoles as in figure 2.10a, they have demonstrated an order-of-magnitude increase in collection efficiency [118,119], which can be further improved by use of an anti-reflection coating [122].

Optical dipoles perpendicular to the surface experience a reduced collection efficiency enhancement from SILs [124]. Additionally, the footprint of an individual SIL is ~1000 μm^2, depending on the depth of the defect. Nanopillars feature much smaller footprints, are fabricated via standard resist masking and etching recipes, and perform on par or better than SILs for perpendicularly oriented dipoles [121]. One of the challenges is the positioning of the emitters inside the nanopillars, as the maximum fluorescent enhancement is observed for pillar diameters approximately half of the emission wavelength and for the dipole positioned at about half wavelength from the top [83]. The right sides of figure 2.10c,d show the far-field emission pattern for a 50 nm deep defect in bulk and in the center of a nanopillar with height 1100 nm and diameter 300 nm, leading to a 100-fold improvement in collection efficiency [123]. Simulations with a 0.9 NA objective and a defect radially central, but randomly distributed in the vertical direction of the nanopillar, demonstrate that between 10-40% of the emitted light is collected by the objective [123].

The defects investigated in this thesis relate as follows to figure 2.10. In chapter 4, we

use an NV center in a ⟨111⟩ oriented diamond where the axis that connects the nitrogen atom and the vacancy is normal to the diamond surface. Consequently, the NV optical dipole is parallel to the surface. In chapter 3 we use a ⟨100⟩ oriented diamond, where all NV center orientations have the vacancy-nitrogen axis 54.74° relative to the surface normal. In chapter 3 and 4, we use SILs fabricated via ion-beam milling. Recently, a more scalable approach based on resist reflow and etching was developed[125]. In chapter 5 and 6 we investigate a defect center in silicon carbide that has an optical dipole that is near perpendicular to the sample surface. For the experiments in chapter 5, we fabricated nanopillars to boost the light collection efficiency[121]. In chapter 6, I discuss the simulation and fabrication of photonic crystal cavities for this type of defect, see also section 2.6.2 below.

2.6.2. PHOTONIC CRYSTAL CAVITY

One of the challenges for large-scale quantum networks based on solid-state defect center is the is the realisation of a narrow-linewidth zero-phonon-line, that at the same time is the most dominant decay channel[105]. Fermi's golden rule prescribes that the transition rate between two eigenstates of an optical dipole scales with the density of photonic states. At their resonance frequencies, photonic cavities confine light and increase the photonic density of states. The increase in transition rate for an optical dipole in a cavity compared to a homogeneous medium is expressed by the Purcell factor, which scales with $\frac{Q}{V}$. Here Q is the quality factor of the cavity, which is inversely proportional to the cavity linewidth and relates to how quickly light leaks out of the cavity. V describes the occupied volume of the cavity mode. Cavities can thus be used to enhance the emission rate into the ZPL. A comprehensive derivation and description of Purcell enhancement is provided by Ruf[77].

Photonic crystals consist of periodically modulated dielectric materials. For periods on the scale of the wavelength of electromagnetic waves, this leads to frequency regions where the optical wave propagation is forbidden[117]. This gives rise to optical bandgaps, much in analogy to electronic bandgaps. Consequently, these photonic crystals can function as a mirror for light. Embedding a volume between such mirrors can create cavities with wavelength-scale mode volumes that confine light of a specific optical mode.

For quantum network and integrated photonics applications, these photonic crystal cavities (PCCs) have been fabricated in 1D[126,127] and 2D[128,129], where the dimensionality indicates along how many axes light is confined by a photonic crystal. In the remaining axes, light is confined via total internal reflection (called index guiding) and hence a large contrast in refractive index between the cavity material and the surrounding (typically air/vacuum) is desired. PCCs enable the realization of high Q-factor and low mode-volume cavities and index guiding is typically maximized by suspending the cavity. In addition, PCCs guide leaked light into a well-defined spatial mode beneficial for collection efficiency.
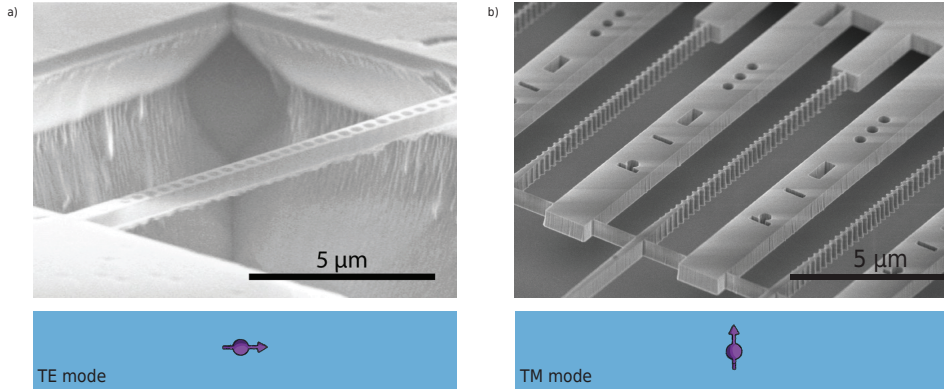
Figure 2.11: **Photonic crystal cavity designs. a)** SEM image[77] of an undercut "perforated waveguide" photonic crystal cavity designed to boost the transverse electric (TE) optical mode, suitable for optical dipoles oriented parallel to the air interface. **b)** SEM image of an undercut "alligator-type" photonic crystal cavity designed to boost the transverse magnetic (TM) optical mode, suitable for optical dipoles oriented perpendicular to the air interface.

The way in which the refractive index contrast is periodically modulated, determines the spectral width of bandgaps formed for transverse electric- (TE) and transverse magnetic-like (TM) modes. Suspended, perforated waveguide-like structures such as in figure 2.11a are tailored to generate larger TE-like bandgaps and are used to form cavities that have a large mode overlap with optical dipoles oriented parallel to the PCC direction[117]. These cavities have been much studied for defect centers in diamond[76,126] and advanced cavity mediated light-matter interaction has been demonstrated[127,130]. Recently, they have also been used for TE-like optical dipoles in silicon carbide[85,99,131].

TM-like modes are perpendicular to TE-like modes. Correspondingly photonic crystal cavities that create a large TM bandgap consist of pillars with a large refractive index surrounded by low refractive index material[117]; the inverse of perforated waveguide-like structures. The optical dipole associated with the silicon carbide defect investigated in chapter 5 and 6 is oriented to have a large overlap with TM modes. To simultaneously tailor a cavity to such an optical dipole, but circumvent the fabrication of free hanging pillars, we fabricate the alligator-type PCCs depicted in figure 2.11, see chapter 6. We have connected the pillars with a ridge of a width close to 40 nm and reshaped the pillars to optimize for cavity Q-factor. Recently, similar structures have also been theoretically and experimentally studied for diamond[132,133].

REFERENCES

[1] V. Acosta and P. Hemmer, *Nitrogen-vacancy centers: Physics and applications,* MRS Bulletin **38**, 127 (2013).

[2] J. R. Weber *et al.*, *Quantum computing with defects,* Proceedings of the National Academy of Sciences **107**, 8513 (2010).

[3] G. Wolfowicz *et al.*, *Quantum guidelines for solid-state spin defects,* Nature Reviews Materials **6**, 906 (2021).

[4] S. Maity *et al.*, *Coherent acoustic control of a single silicon vacancy spin in diamond,* Nature Communications **11**, 193 (2020).

[5] W. V. Smith, P. P. Sorokin, I. L. Gelles and G. J. Lasher, *Electron-Spin Resonance of Nitrogen Donors in Diamond,* Physical Review **115**, 1546 (1959).

[6] J. H. N. Loubser and J. A. v. Wyk, *Electron spin resonance in the study of diamond,* Reports on Progress in Physics **41**, 1201 (1978).

[7] G. Davies and M. F. Hamer, *Optical Studies of the 1.945 eV Vibronic Band in Diamond,* Proceedings of the Royal Society of London. Series A, Mathematical and Physical Sciences **348**, 285 (1976).

[8] A. T. Collins, M. F. Thomaz and M. I. B. Jorge, *Luminescence decay time of the 1.945 eV centre in type Ib diamond,* Journal of Physics C: Solid State Physics **16**, 2177 (1983).

[9] A. Lenef and S. C. Rand, *Electronic structure of the N-V center in diamond: Theory,* Physical Review B **53**, 13441 (1996).

[10] A. Lenef *et al.*, *Electronic structure of the N-V center in diamond: Experiments,* Physical Review B **53**, 13427 (1996).

[11] S. A. Holmstrom *et al.*, *Spin Echo at the Rabi Frequency in Solids,* Physical Review Letters **78**, 302 (1997).

[12] A. Gruber *et al.*, *Scanning Confocal Optical Microscopy and Magnetic Resonance on Single Defect Centers,* Science **276**, 2012 (1997).

[13] F. Jelezko and J. Wrachtrup, *Single defect centres in diamond: A review,* physica status solidi (a) **203**, 3207 (2006).

[14] S. Zaiser *et al.*, *Enhancing quantum sensing sensitivity by a quantum memory,* Nature Communications **7**, 12279 (2016).

[15] T. Rosskopf, J. Zopes, J. M. Boss and C. L. Degen, *A quantum spectrum analyzer enhanced by a nuclear spin memory,* npj Quantum Information **3**, 1 (2017).

[16] G. Waldherr *et al.*, *Quantum error correction in a solid-state hybrid spin register,* Nature **506**, 204 (2014).

[17] J. Cramer *et al.*, *Repeated quantum error correction on a continuously encoded qubit by real-time feedback,* Nature Communications **7**, 11526 (2016).

[18] H. Bernien *et al.*, *Heralded entanglement between solid-state qubits separated by three metres,* Nature **497**, 86 (2013).

[19] B. Hensen *et al.*, *Loophole-free Bell inequality violation using electron spins separated by 1.3 kilometres,* Nature **526**, 682 (2015).

[20] M. W. Doherty, N. B. Manson, P. Delaney and L. C. L. Hollenberg, *The negatively charged nitrogen-vacancy centre in diamond: the electronic solution,* New Journal of Physics **13**, 025019 (2011).

[21] B. Hensen, *Measurement-based Quantum Computation with the Nitrogen-Vacancy centre in Diamond,* Master thesis (TU Delft), TU Delft (2010).

[22] Y. Wang, *Using spins in diamond for quantum technologies,* Dissertation (TU Delft), TU Delft (2023).

[23] J. R. Maze *et al.*, *Properties of nitrogen-vacancy centers in diamond: the group theoretic approach,* New Journal of Physics **13**, 025025 (2011).

[24] B. J. Hensen, *Quantum Nonlocality with Spins in Diamond,* Ph.D. thesis, Delft University of Technology (2016).

[25] M. W. Doherty *et al.*, *Theory of the ground-state spin of the NV$^-$ center in diamond,* Physical Review B **85**, 205203 (2012).

[26] K.-M. C. Fu *et al.*, *Observation of the Dynamic Jahn-Teller Effect in the Excited States of Nitrogen-Vacancy Centers in Diamond,* Physical Review Letters **103**, 256404 (2009).

[27] R. Albrecht, A. Bommer, C. Deutsch, J. Reichel and C. Becher, *Coupling of a Single Nitrogen-Vacancy Center in Diamond to a Fiber-Based Microcavity,* Physical Review Letters **110**, 243602 (2013).

[28] P. Tamarat *et al.*, *Stark Shift Control of Single Optical Centers in Diamond,* Physical Review Letters **97**, 083002 (2006).

[29] N. Kalb, P. C. Humphreys, J. J. Slim and R. Hanson, *Dephasing mechanisms of diamond-based nuclear-spin memories for quantum networks,* Physical Review A **97**, 062330 (2018).

[30] M. Goldman *et al.*, *Phonon-Induced Population Dynamics and Intersystem Crossing in Nitrogen-Vacancy Centers,* Physical Review Letters **114**, 145502 (2015).

[31] M. L. Goldman *et al.*, *State-selective intersystem crossing in nitrogen-vacancy centers,* Physical Review B **91**, 165201 (2015).

[32] S. J. H. Loenen, *Improving single-shot readout for diamond quantum processors,* Master thesis (TU Eindhoven), TU Eindhoven (2019).

2

[33] L. Robledo *et al.*, *High-fidelity projective read-out of a solid-state spin quantum register,* Nature **477**, 574 (2011).

[34] L. Jiang *et al.*, *Coherence of an Optically Illuminated Single Nuclear Spin Qubit,* Physical Review Letters **100**, 073001 (2008).

[35] M. H. Abobeih *et al.*, *Fault-tolerant operation of a logical qubit in a diamond quantum processor,* Nature **606**, 884 (2022).

[36] C. Bradley, *Order from Disorder: Control of Multi-Qubit Spin Registers in Diamond,* Ph.D. thesis, Delft University of Technology (2021).

[37] G. Balasubramanian *et al.*, *Ultralong spin coherence time in isotopically engineered diamond,* Nature Materials **8**, 383 (2009).

[38] T. H. Taminiau *et al.*, *Detection and Control of Individual Nuclear Spins Using a Weakly Coupled Electron Spin,* Physical Review Letters **109**, 137602 (2012).

[39] C. Bradley *et al.*, *A Ten-Qubit Solid-State Spin Register with Quantum Memory up to One Minute,* Physical Review X **9**, 031045 (2019).

[40] M. H. M. A. Abobeih, *From atomic-scale imaging to quantum fault-tolerance with spins in diamond,* Ph.D. thesis, Delft University of Technology (2021).

[41] M. H. Abobeih *et al.*, *Atomic-scale imaging of a 27-nuclear-spin cluster using a quantum sensor,* Nature **576**, 411 (2019).

[42] M. H. Abobeih *et al.*, *One-second coherence for a single electron spin coupled to a multi-qubit nuclear-spin environment,* Nature Communications **9**, 2552 (2018).

[43] S. Kolkowitz, Q. P. Unterreithmeier, S. D. Bennett and M. D. Lukin, *Sensing Distant Nuclear Spins with a Single Electron Spin,* Physical Review Letters **109**, 137601 (2012).

[44] N. Zhao *et al.*, *Sensing single remote nuclear spins,* Nature Nanotechnology **7**, 657 (2012).

[45] J. Randall *et al.*, *Many-body–localized discrete time crystal with a programmable spin-based quantum simulator,* Science **374**, 1474 (2021).

[46] V. Vorobyov *et al.*, *Quantum Fourier transform for nanoscale quantum sensing,* npj Quantum Information **7**, 1 (2021).

[47] N. Kalb *et al.*, *Entanglement distillation between solid-state quantum network nodes,* Science **356**, 928 (2017).

[48] M. Pompili *et al.*, *Realization of a multinode quantum network of remote solid-state qubits,* Science **372**, 259 (2021).

[49] C. A. J. Ammerlaan and E. A. Burgemeister, *Reorientation of Nitrogen in Type-Ib Diamond by Thermal Excitation and Tunneling,* Physical Review Letters **47**, 954 (1981).

[50] T. R. Eichhorn, C. A. McLellan and A. C. Bleszynski Jayich, *Optimizing the formation of depth-confined nitrogen vacancy center spin ensembles in diamond for quantum sensing,* Physical Review Materials **3**, 113802 (2019).

[51] S. Bussandri *et al.*, *P1 center electron spin clusters are prevalent in type Ib diamond,* (2023), arXiv:2311.05396 [physics, physics:quant-ph].

[52] R. Ulbricht *et al.*, *Single substitutional nitrogen defects revealed as electron acceptor states in diamond using ultrafast spectroscopy,* Physical Review B **84**, 165202 (2011).

[53] P. Deák, B. Aradi, M. Kaviani, T. Frauenheim and A. Gali, *Formation of NV centers in diamond: A theoretical study based on calculated transitions and migration of nitrogen and vacancy related defects,* Physical Review B **89**, 075203 (2014).

[54] S. C. Lawson, D. Fisher, D. C. Hunt and M. E. Newton, *On the existence of positively charged single-substitutional nitrogen in diamond,* Journal of Physics: Condensed Matter **10**, 6171 (1998).

[55] R. J. Cook and D. H. Whiffen, *Electron Nuclear Double Resonance Study of a Nitrogen Centre in Diamond,* Proceedings of the Royal Society of London. Series A, Mathematical and Physical Sciences **295**, 99 (1966).

[56] G. de Lange *et al.*, *Controlling the quantum dynamics of a mesoscopic spin bath in diamond,* Scientific Reports **2**, 382 (2012).

[57] H. S. Knowles, D. M. Kara and M. Atatüre, *Observing bulk diamond spin coherence in high-purity nanodiamonds,* Nature Materials **13**, 21 (2014).

[58] H. S. Knowles, D. M. Kara and M. Atatüre, *Demonstration of a Coherent Electronic Spin Cluster in Diamond,* Physical Review Letters **117**, 100802 (2016).

[59] R. G. Farrer, *On the substitutional nitrogen donor in diamond,* Solid State Communications **7**, 685 (1969).

[60] R. Jones, J. P. Goss and P. R. Briddon, *Acceptor level of nitrogen in diamond and the 270-nm absorption band,* Physical Review B **80**, 033205 (2009).

[61] A. M. Ferrari, S. Salustro, F. S. Gentile, W. C. Mackrodt and R. Dovesi, *Substitutional nitrogen in diamond: A quantum mechanical investigation of the electronic and spectroscopic properties,* Carbon **134**, 354 (2018).

[62] W. J. P. v. Enckevort and E. H. Versteegen, *Temperature dependence of optical absorption by the single-substitutional nitrogen donor in diamond,* Journal of Physics: Condensed Matter **4**, 2361 (1992).

[63] J. Rosa, M. Vaněček, M. Nesládek and L. M. Stals, *Photoionization cross-section of dominant defects in CVD diamond,* Diamond and Related Materials **8**, 721 (1999).

[64] F. J. Heremans, G. D. Fuchs, C. F. Wang, R. Hanson and D. D. Awschalom, *Generation and transport of photoexcited electrons in single-crystal diamond,* Applied Physics Letters **94**, 152102 (2009).

[65] H. B. Dyer, F. A. Raal, L. Du Preez and J. H. N. Loubser, *Optical absorption features associated with paramagnetic nitrogen in diamond,* The Philosophical Magazine: A Journal of Theoretical Experimental and Applied Physics **11**, 763 (1965).

[66] F. De Weerdt and A. T. Collins, *Determination of the C defect concentration in HPHT annealed type IaA diamonds from UV–VIS absorption spectra,* Diamond and Related Materials **17**, 171 (2008).

[67] M. N. R. Ashfold *et al.*, *Nitrogen in Diamond,* Chemical Reviews **120**, 5745 (2020).

[68] S. J. Breuer and P. R. Briddon, *Energy barrier to reorientation of the substitutional nitrogen in diamond,* Physical Review B **53**, 7819 (1996).

[69] H. A. Jahn and E. Teller, *Stability of Polyatomic Molecules in Degenerate Electronic States. I. Orbital Degeneracy,* Proceedings of the Royal Society of London. Series A, Mathematical and Physical Sciences **161**, 220 (1937).

[70] L. A. Shul'man, M. I. Zaritskii and G. A. Podzyarei, *Reorientation of the jahn- teller distortion in nitrogen impurity centers in diamond,* Sov. Phys., Solid State **8** (1967).

[71] M. I. Zaritskii and et al., *Spin-lattice relaxation of a jahn-teller nitrogen center in diamond,* Sov. Phys., Solid State **18** (1967).

[72] G. Jeschke, M. Pannier and H. W. Spiess, *Double Electron-Electron Resonance,* in *Distance Measurements in Biological Systems by EPR,* Biological Magnetic Resonance, edited by L. J. Berliner, G. R. Eaton and S. S. Eaton (Springer US, Boston, MA, 2000) pp. 493–512.

[73] P. Neumann *et al.*, *Quantum register based on coupled electron spins in a room-temperature solid,* Nature Physics **6**, 249 (2010).

[74] X. Xiao and N. Zhao, *Proposal for observing dynamic Jahn–Teller effect by single solid-state defects,* New Journal of Physics **18**, 103022 (2016).

[75] S. L. N. Hermans *et al.*, *Qubit teleportation between non-neighbouring nodes in a quantum network,* Nature **605**, 663 (2022).

[76] A. Faraon, C. Santori, Z. Huang, V. M. Acosta and R. G. Beausoleil, *Coupling of Nitrogen-Vacancy Centers to Photonic Crystal Cavities in Monocrystalline Diamond,* Physical Review Letters **109**, 033604 (2012).

[77] M. Ruf, *Cavity-enhanced quantum network nodes in diamond*, Ph.D. thesis, Delft University of Technology (2021).

[78] M. E. Trusheim *et al.*, *Transform-Limited Photons From a Coherent Tin-Vacancy Spin in Diamond,* Physical Review Letters **124**, 023602 (2020).

[79] A. Sipahigil *et al.*, *Indistinguishable Photons from Separated Silicon-Vacancy Centers in Diamond,* Physical Review Letters **113**, 113602 (2014).

[80] A. E. Rugar *et al.*, *Narrow-Linewidth Tin-Vacancy Centers in a Diamond Waveguide,* ACS Photonics **7**, 2356 (2020).

[81] R. E. Evans, A. Sipahigil, D. D. Sukachev, A. S. Zibrov and M. D. Lukin, *Narrow-Linewidth Homogeneous Optical Emitters in Diamond Nanostructures via Silicon Ion Implantation,* Physical Review Applied **5**, 044010 (2016).

[82] S. Castelletto and A. Boretti, *Silicon carbide color centers for quantum applications,* Journal of Physics: Photonics **2**, 022001 (2020).

[83] S. Castelletto *et al.*, *Silicon Carbide Photonics Bridging Quantum Technology,* ACS Photonics **9**, 1434 (2022).

[84] C. P. Anderson *et al.*, *Electrical and optical control of single spins integrated in scalable semiconductor devices,* Science **366**, 1225 (2019).

[85] D. M. Lukin *et al.*, *4H-silicon-carbide-on-insulator for integrated quantum and nonlinear photonics,* Nature Photonics **14**, 330 (2020).

[86] Wikipedia, *Silicon carbide,* (2023), accessed: 2023-11-21. Page Version ID: 1186146393.

[87] T. K. Gachovska and J. L. Hudgins, *5 - SiC and GaN Power Semiconductor Devices,* in *Power Electronics Handbook (Fourth Edition),* edited by M. H. Rashid (Butterworth-Heinemann, 2018) pp. 95–155.

[88] T. Ayalew, *SiC semiconductor devices technology, modeling and simulation,* Thesis, Technische Universität Wien (2004).

[89] Y. M. Tairov and V. F. Tsvetkov, *General principles of growing large-size single crystals of various silicon carbide polytypes,* Journal of Crystal Growth **52**, 146 (1981).

[90] Y. M. Tairov and V. F. Tsvetkov, *Investigation of growth processes of ingots of silicon carbide single crystals,* Journal of Crystal Growth **43**, 209 (1978).

[91] G. Ferro and D. Chaussende, *A new model for in situ nitrogen incorporation into 4H-SiC during epitaxy,* Scientific Reports **7**, 43069 (2017).

[92] W. G. Spitzer, D. A. Kleinman and C. J. Frosch, *Infrared Properties of Cubic Silicon Carbide Films,* Physical Review **113**, 133 (1959).

[93] A. Yi *et al.*, *Silicon carbide for integrated photonics,* Applied Physics Reviews **9**, 031302 (2022).

[94] T. Bosma *et al.*, *Identification and tunable optical coherent control of transition-metal spins in silicon carbide,* npj Quantum Information **4**, 1 (2018).

[95] N. T. Son *et al.*, *Developing silicon carbide for quantum spintronics,* Applied Physics Letters **116**, 190501 (2020).

[96] W. F. Koehl, B. B. Buckley, F. J. Heremans, G. Calusine and D. D. Awschalom, *Room temperature coherent control of defect spin qubits in silicon carbide,* Nature **479**, 84 (2011).

[97] A. Bourassa *et al.*, *Entanglement and control of single nuclear spins in isotopically engineered silicon carbide,* Nature Materials **19**, 1319 (2020).

[98] C. P. Anderson *et al.*, *Five-second coherence of a single spin with single-shot readout in silicon carbide,* Science Advances **8**, eabm5912 (2022).

[99] A. L. Crook *et al.*, *Purcell Enhancement of a Single Silicon Carbide Color Center with Coherent Spin Control,* Nano Letters **20**, 3427 (2020).

[100] R. Nagy *et al.*, *High-fidelity spin and optical control of single silicon-vacancy centres in silicon carbide,* Nature Communications **10**, 1954 (2019).

[101] P. Udvarhelyi *et al.*, *Vibronic States and Their Effect on the Temperature and Strain Dependence of Silicon-Vacancy Qubits in 4H-SiC,* Physical Review Applied **13**, 054017 (2020).

[102] S. A. Tarasenko *et al.*, *Spin and Optical Properties of Silicon Vacancies in Silicon Carbide - A Review,* physica status solidi (b) **255**, 1700258 (2018).

[103] D. Liu *et al.*, *The silicon vacancy centers in SiC: determination of intrinsic spin dynamics for integrated quantum photonics,* (2023), arXiv:2307.13648 [quant-ph].

[104] C. Babin *et al.*, *Fabrication and nanophotonic waveguide integration of silicon carbide colour centres with preserved spin-optical coherence,* Nature Materials **21**, 67 (2022).

[105] H. K. C. Beukers *et al.*, *Tutorial: Remote entanglement protocols for stationary qubits with photonic interfaces,* (2023), arXiv:2310.19878 [quant-ph].

[106] H. B. Banks *et al.*, *Resonant Optical Spin Initialization and Readout of Single Silicon Vacancies in 4H-SiC,* Physical Review Applied **11**, 024013 (2019).

[107] M. Rühl, L. Bergmann, M. Krieger and H. B. Weber, *Stark Tuning of the Silicon Vacancy in Silicon Carbide,* Nano Letters **20**, 658 (2020).

[108] D. M. Lukin *et al.*, *Spectrally reconfigurable quantum emitters enabled by optimized fast modulation,* npj Quantum Information **6**, 1 (2020).

[109] C. T. Nguyen *et al.*, *An integrated nanophotonic quantum register based on silicon-vacancy spins in diamond,* Physical Review B **100**, 165428 (2019).

[110] C. Nguyen *et al.*, *Quantum Network Nodes Based on Diamond Qubits with an Efficient Nanophotonic Interface,* Physical Review Letters **123**, 183602 (2019).

[111] M. T. Uysal *et al.*, *Coherent Control of a Nuclear Spin via Interactions with a Rare-Earth Ion in the Solid State,* PRX Quantum **4**, 010323 (2023).

[112] P. Siyushev *et al.*, *Optically Controlled Switching of the Charge State of a Single Nitrogen-Vacancy Center in Diamond at Cryogenic Temperatures,* Physical Review Letters **110**, 167402 (2013).

[113] N. Aslam, G. Waldherr, P. Neumann, F. Jelezko and J. Wrachtrup, *Photo-induced ionization dynamics of the nitrogen vacancy defect in diamond investigated by single-shot charge state detection,* New Journal of Physics **15**, 013064 (2013).

[114] V. M. Acosta *et al.*, *Dynamic Stabilization of the Optical Resonances of Single Nitrogen-Vacancy Centers in Diamond,* Physical Review Letters **108**, 206401 (2012).

[115] L. Robledo, H. Bernien, I. Van Weperen and R. Hanson, *Control and Coherence of the Optical Transition of Single Nitrogen Vacancy Centers in Diamond,* Physical Review Letters **105**, 177403 (2010).

[116] C. E. Bradley *et al.*, *Robust quantum-network memory based on spin qubits in isotopically engineered diamond,* npj Quantum Information **8**, 1 (2022).

[117] J. D. Joannopoulos, ed., *Photonic crystals: molding the flow of light,* 2nd ed. (Princeton University Press, Princeton, 2008).

[118] J. P. Hadden *et al.*, *Strongly enhanced photon collection from diamond defect centers under microfabricated integrated solid immersion lenses,* Applied Physics Letters **97**, 241901 (2010).

[119] L. Marseglia *et al.*, *Nanofabricated solid immersion lenses registered to single emitters in diamond,* Applied Physics Letters **98**, 133107 (2011).

[120] C. J. Widmann *et al.*, *Fabrication and characterization of single crystalline diamond nanopillars with NV-centers,* Diamond and Related Materials Advances in Diamond Thin Films and Novel Nanocarbon Materials, **54**, 2 (2015).

[121] M. Radulaski *et al.*, *Scalable Quantum Photonics with Single Color Centers in Silicon Carbide,* Nano Letters **17**, 1782 (2017).

[122] H. Bernien, *Control, measurement and entanglement of remote quantum spin registers in diamond,* Ph.D. thesis, Delft University of Technology (2014).

[123] T. W. de Jong, *Simulated enhancement of optical properties V_{Si} defects in 4H-SiC through nanophotonic structures,* Master thesis (TU Delft), TU Delft (2022).

[124] M. Widmann *et al.*, *Coherent control of single spins in silicon carbide at room temperature,* Nature Materials **14**, 164 (2015).

[125] F. Sardi *et al.*, *Scalable production of solid-immersion lenses for quantum emitters in silicon carbide,* Applied Physics Letters **117**, 022105 (2020).

[126] S. Mouradian, N. H. Wan, T. Schröder and D. Englund, *Rectangular photonic crystal nanobeam cavities in bulk diamond,* Applied Physics Letters **111**, 021103 (2017).

[127] M. K. Bhaskar *et al.*, *Experimental demonstration of memory-enhanced quantum communication,* Nature **580**, 60 (2020).

[128] B.-S. Song *et al.*, *Ultrahigh-Q photonic crystal nanocavities based on 4H silicon carbide,* Optica **6**, 991 (2019).

[129] G. Calusine, A. Politi and D. D. Awschalom, *Cavity-Enhanced Measurements of Defect Spins in Silicon Carbide,* Physical Review Applied **6**, 014019 (2016).

[130] C. M. Knaut *et al.*, *Entanglement of Nanophotonic Quantum Memory Nodes in a Telecommunication Network,* (2023), arXiv:2310.01316 [quant-ph].

[131] D. O. Bracher, X. Zhang and E. L. Hu, *Selective Purcell enhancement of two closely linked zero-phonon transitions of a silicon carbide color center,* Proceedings of the National Academy of Sciences **114**, 4060 (2017).

[132] J. M. Bopp *et al.*, *'Sawfish' Photonic Crystal Cavity for Near-Unity Emitter-to-Fiber Interfacing in Quantum Network Applications,* (2022), arXiv:2210.04702 [physics, physics:quant-ph].

[133] T. Pregnolato *et al.*, *Fabrication of Sawfish photonic crystal cavities in bulk diamond,* (2023), arXiv:2311.03618 [physics, physics:quant-ph].

ENTANGLEMENT OF DARK ELECTRON-NUCLEAR SPIN DEFECTS IN DIAMOND

M.J. Degen[*] , **S.J.H. Loenen**[*] , **H.P. Bartling, C.E. Bradley, A.L. Meinsma, M. Markham, D.J. Twitchen, T.H. Taminiau**

A promising approach for multi-qubit quantum registers is to use optically addressable spins to control multiple dark electron-spin defects in the environment. While recent experiments have observed signatures of coherent interactions with such dark spins, it is an open challenge to realize the individual control required for quantum information processing. Here we demonstrate the heralded initialisation, control and entanglement of individual dark spins associated to multiple P1 centers, which are part of a spin bath surrounding a nitrogen-vacancy center in diamond. We realize projective measurements to prepare the multiple degrees of freedom of P1 centers - their Jahn-Teller axis, nuclear spin and charge state - and exploit these to selectively access multiple P1s in the bath. We develop control and single-shot readout of the nuclear and electron spin, and use this to demonstrate an entangled state of two P1 centers. These results provide a proof-of-principle towards using dark electron-nuclear spin defects as qubits for quantum sensing, computation and networks.

---

[*]Equally contributing authors

3.1. INTRODUCTION

Optically active defects in solids provide promising qubits for quantum sensing[2], quantum-information processing[3–5], quantum simulations[6,7] and quantum networks[8–10]. These defects, including the nitrogen-vacancy (NV) and silicon-vacancy (SiV) centers in diamond and various defects in silicon-carbide[11–13], combine long spin coherence times[5,14–19], high-quality control and readout[3–5,15,20–22], and a coherent optical interface[8–10,16,20,23].

Larger-scale systems can be realized by entangling multiple defects together through long-range optical network links[8–10] and through direct magnetic coupling, as demonstrated for a pair of ion-implanted NV centers[24,25]. The number of available spins can be further extended by controlling nuclear spins in the vicinity. Multi-qubit quantum registers[5,25–28], quantum error correction[3,4], enhanced sensing schemes[29], and entanglement distillation[30] have been realized using nuclear spins.

The ability to additionally control dark electron-spin defects that cannot be directly detected optically would open new opportunities. Examples are studying single defect dynamics[31], extended quantum registers, enhanced sensing protocols[29,32,33] and spin chains for quantum computation architectures[34–36]. Two pioneering experiments reported signals consistent with an NV center coupled to a single P1 center (a dark substitutional nitrogen defect)[37,38], but the absence of the expected P1 electron-spin resonance signal[39] and later results revealing identical signals due to NV-^{13}C couplings in combination with an excited state anti-crossing[40], make these assignments inconclusive. Recent experiments have revealed signatures of coherent interactions between NV centers and individual dark electron-spin defects, including P1 centers[41–43], N2 centers[44] and not-yet-assigned defects[32,45–49]. Those results have revealed the prospect of using dark spin defects as qubits. However, high-quality initialisation, measurement and control of multi-qubit quantum states is required to exploit such spins as a quantum resource.

Here we demonstrate the control and entanglement of individual P1 centers that are part of a bath surrounding an NV center in diamond (Fig. 3.1a). A key property of the P1 center is that, in addition to its electron spin, it exhibits three extra degrees of freedom: the Jahn-Teller axis, a nuclear spin, and the charge state[50–52]. Underlying our selective control of individual centers is the heralded preparation of specific configurations of these additional degrees of freedom for multiple P1 centers through projective measurements. In contrast, all previous experiments averaged over these additional degrees of freedom[53 42]. We use this capability to develop initialisation, single-shot readout and control of the electron and nuclear spin states of multiple P1s, and investigate their spin relaxation and coherence times. Finally, we demonstrate the potential of these dark spins as a qubit platform by realizing an entangled state between two P1 electron spins through their direct magnetic-dipole coupling.

3.2. A SPIN BATH WITH MULTIPLE DEGREES OF FREEDOM

We consider a bath of P1 centers surrounding a single NV center at 3.3 K (Fig. 3.1a). The diamond is isotopically purified with an estimated ^{13}C concentration of 0.01%. The P1 concentration is estimated to be $\sim$ 75 ppb (see section 3.9.4). Three P1 charge states are known[51,52]. The experiments in this work detect the neutral charge state and do not generate signal for the positive and negative charge states. In addition to an electron spin ($S = 1/2$), the P1 center exhibits a ^{14}N nuclear spin ($I = 1$, 99.6% natural abundance) and a Jahn-Teller (JT) distortion, which results in four possible symmetry axes due to the elongation of one of the four N-C bonds[54]. Both the ^{14}N state and the JT axis generally fluctuate over time[55–57]. The Hamiltonian for a single neutrally-charged P1 defect in one of the four JT axis $i \in \{A,B,C,D\}$ is[50]:

$$H_{\mathbf{i},\mathrm{P1}} = \gamma_e \mathbf{B} \cdot \mathbf{S} + \gamma_n \mathbf{B} \cdot \mathbf{I} + \mathbf{I} \cdot \hat{\mathbf{P}}_{\mathbf{i}} \cdot \mathbf{I} + \mathbf{S} \cdot \hat{\mathbf{A}}_{\mathbf{i}} \cdot \mathbf{I}, \tag{3.1}$$

where γ_e (γ_n) is the electron (^{14}N) gyromagnetic ratio, $\mathbf{B}$ the external magnetic field vector, $\mathbf{S}$ and $\mathbf{I}$ are the electron spin-1/2 and nuclear spin-1 operator vectors, and $\hat{\mathbf{A}}_{\mathbf{i}}$ ($\hat{\mathbf{P}}_{\mathbf{i}}$) the hyperfine (quadrupole) tensor. We label the ^{14}N ($m_I \in -1,0,+1$) and JT states as $|m_I, i\rangle$, and the electron spin states as $|\uparrow\rangle$ and $|\downarrow\rangle$. For convenience, we use the spin eigenstates as labels, while the actual eigenstates are, to some extent, mixtures of the ^{14}N and electron spin states.

We probe the bath surrounding the NV by double electron-electron resonance (DEER) spectroscopy[41,42,45,47,53]. The DEER sequence consists of a spin echo on the NV electron spin, which decouples it from the environment, plus a simultaneous π-pulse that selectively recouples resonant P1 centers. Figure 3.1b reveals a complex spectrum. The degeneracy of three of the JT axes is lifted by a purposely slightly tilted magnetic field with respect to the NV axis ($\theta \approx 4°$). In combination with the long P1 dephasing time ($T_2^* \sim$ 50 μs, see below) this enables us to resolve all 12 main P1 electron-spin transitions – for four JT axes and three ^{14}N states – and selectively address at least one transition for each JT axis.

Several additional transitions are visible due to mixing of the electron and nuclear spin in the used magnetic field regime ($\gamma_e |\mathbf{B}| \sim A_\parallel, A_\perp$). We select 11 well-isolated transitions to fit the P1 Hamiltonian parameters and obtain $\{A_\parallel, A_\perp, P_\parallel\} = \{114.0264(9), 81.312(1), -3.9770(9)\}$ MHz and $\mathbf{B} = \{2.437(2), 1.703(1), 45.5553(5)\}$ G (section 3.9.3), closely matching ensemble ESR measurements[58]. The experimental spectrum is well described by the 60 P1 transitions for these parameters. No signal is observed at the bare electron Larmor frequency ($\approx$ 128 MHz), confirming that the P1 centers form the dominant electron spin bath.

To probe the coupling strength of the P1 bath to the NV, we sweep the interaction time in the DEER sequences (Fig. 3.1c). The curves for the different $|+1, i\rangle$ states show oscillatory features, providing a first indication of an underlying microscopic structure of the P1 bath. However, like all previous experiments[41,42,53], these measurements are a complex averaging over ^{14}N, JT and charge states for all the P1 centers, which obscures

3
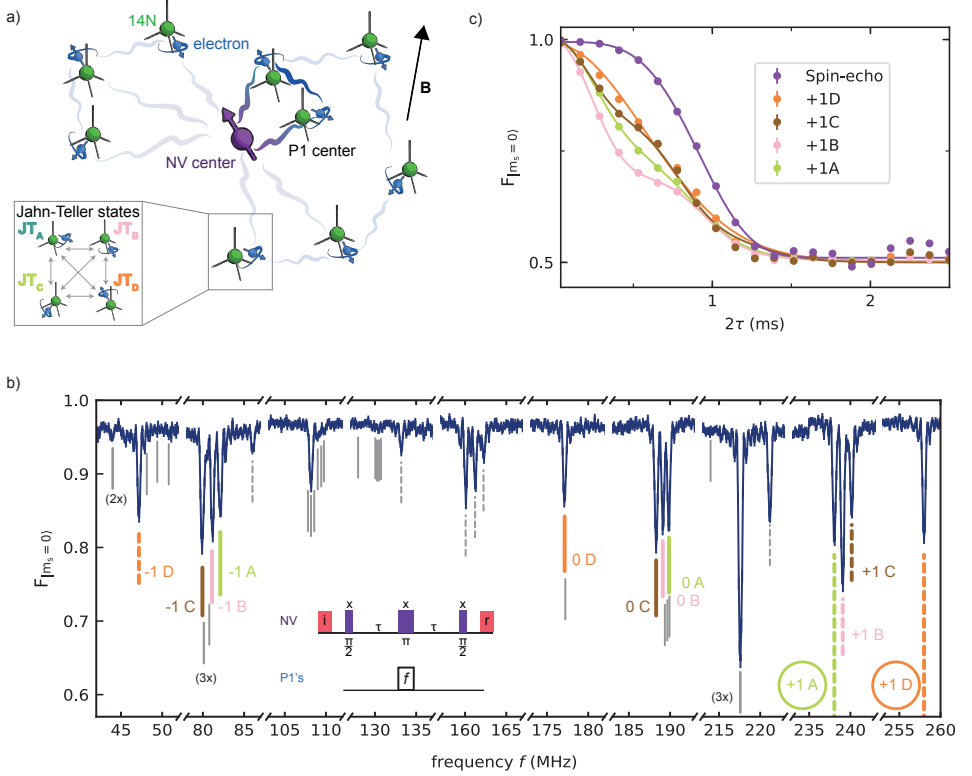
Figure 3.1: **DEER spectroscopy of a P1 spin bath. a)** We study a bath of P1 centers surrounding a single NV center. The state of each P1 center is defined by an electron spin (blue), a ^{14}N nuclear spin (green), and one of four JT axis, which can vary over time (see inset). **b)** DEER spectrum obtained by varying the frequency f (see inset). The NV is initialized in $m_s = 0$ via optical spin-pumping (i) and optically read out (r) at the end of the sequence (Methods). $F_{|m_s=0\rangle}$ is the fidelity of the final NV state with $m_s = 0$. The 12 main P1 electron-spin transitions are labelled by their nitrogen nuclear spin state and JT axis (colored lines). 11 isolated transitions (dashed lines) are used to fit the P1 Hamiltonian and all predicted transition frequencies are indicated (solid lines). In this work, we mainly use the circled transitions corresponding to $|+1,D\rangle$ and $|+1,A\rangle$. **c)** We apply a calibrated π pulse (Rabi frequency $\Omega = 250$ kHz) at a fixed frequency f, to selectively couple to P1 centers in the $|+1,i\rangle$ state ($i \in \{A,B,C,D\}$) and vary the interaction time 2τ (see inset in b). From the fits we obtain a dephasing time $T_{2,\text{DEER}}$ of 0.767(6), 0.756(7), 0.802(6) and 0.803(5) ms for the $|+1,i\rangle$ state with i corresponding to A,B,C and D respectively. A spin-echo (no pulse on P1 centers) is added for reference from which we obtain $T_{2,\text{NV}} = 0.992(4)$ ms. Error bars are one standard deviation (Methods), with a typical value 4×10^{-3}, which is smaller than the data points. See Methods for the fit functions.

the underlying structure and hinders control over individual spins.

3.3. Detecting and preparing single P1 centers.

To investigate the microscopic structure of the bath we repeatedly apply the DEER sequence and analyze the correlations in the measurement outcomes[31]. Figure 3.2a

shows a typical time trace for continuous measurement, in which groups of K=820 measurements are binned together (see Fig. 3.2b for the sequence). We observe discrete jumps in the signal that indicate individual P1 centers jumping in and out of the $|+1,D\rangle$ state. The resulting histogram (Fig. 3.2a) reveals multiple discrete peaks that indicate several P1 centers with different coupling strengths to the NV center, as schematically illustrated in Fig. 3.2c. We tentatively assign four P1 centers S1, S2, S3 and S4 to these peaks.

We verify whether these peaks originate from single P1 centers by performing cross-correlation measurements. We first apply a DEER measurement on $|+1,D\rangle$ followed by a measurement on $|+1,A\rangle$ (Fig. 3.2d). For a single P1, observing it in $|+1,D\rangle$ would make it unlikely to subsequently also find it in state $|+1,A\rangle$. We observe three regions of such anti-correlation (red rectangles in Fig. 3.2d). We define the correlation:

$$C = \frac{\mathrm{P}(N_\mathrm{A}^{\min} \leq N_{|+1,A\rangle} \leq N_\mathrm{A}^{\max} \,|\, N_\mathrm{D}^{\min} \leq N_{|+1,D\rangle} \leq N_\mathrm{D}^{\max)}}{\mathrm{P}(N_\mathrm{A}^{\min} \leq N_{|+1,A\rangle} \leq N_\mathrm{A}^{\max)}}, \tag{3.2}$$

where $N_\mathrm{A}^{\min}$, $N_\mathrm{A}^{\max}$, $N_\mathrm{D}^{\min}$ and $N_\mathrm{D}^{\max}$ define the region, and where P(X) is the probability that X is satisfied. Assuming that the states of different P1 centers are uncorrelated, a value $C < 0.5$ indicates that the signal observed in both the DEER sequences on $|+1,A\rangle$ and $|+1,D\rangle$ is associated to a single P1 center, while $C < 2/3$ indicates 1 or 2 centers (section 3.9.7).

For the three areas we find $C = 0.40(5)$, $0.22(4)$ and $0.47(5)$ for S1, S2 and S3/S4 respectively. These correlations corroborate the assignments of a single P1 to both S1 and S2 and one or two P1s for S3/S4 (the result is within one standard deviation from 0.5). Additionally, these results reveal which signals for different $|+1,i\rangle$ states belong to which P1 centers. This is non-trivial because the NV-P1 dipolar coupling varies with the JT axis, as exemplified in Fig. 3.2d (see section 3.9.2 for a theoretical treatment).

Next, we develop single-shot readout and heralded initialisation of the ^{14}N and JT state of individual P1 centers. For this, we represent the time trace data (Fig. 3.2a) as a correlation plot between subsequent measurements k and $k+1$ (Fig. 3.2e)[59–61]. We bin the outcomes using K=820 repetitions, where K is chosen as a trade-off between the ability to distinguish S1 from S2 and the disturbance of the state due to the repeated measurements (1/e value of $\sim 1.5 \times 10^4$ repetitions, see section 3.9.5). Separated regions are observed for the different P1 centers. Therefore, by setting threshold conditions, one can use the DEER measurement as a projective measurement to initialize or readout the $|m_I,i\rangle$ state of selected P1 centers, which we illustrate for S1.

First, we set an initialisation condition N(k) > N_{S1} (blue dashed line) to herald that S1 is initialized in the $|+1,D\rangle$ state and that S2, S3/S4 are not in that state. We use N(k) $\leq N_{\mathrm{notS1}}$ to prepare a mixture of all other other possibilities. The resulting conditional probability distributions of N(k + 1) are shown in Fig. 3.2f. Second, we set a threshold for state readout N_{RO} to distinguish between the two cases. We then optimize N_{S1} for the trade-off between the success rate and signal contrast, and find a combined initiali-
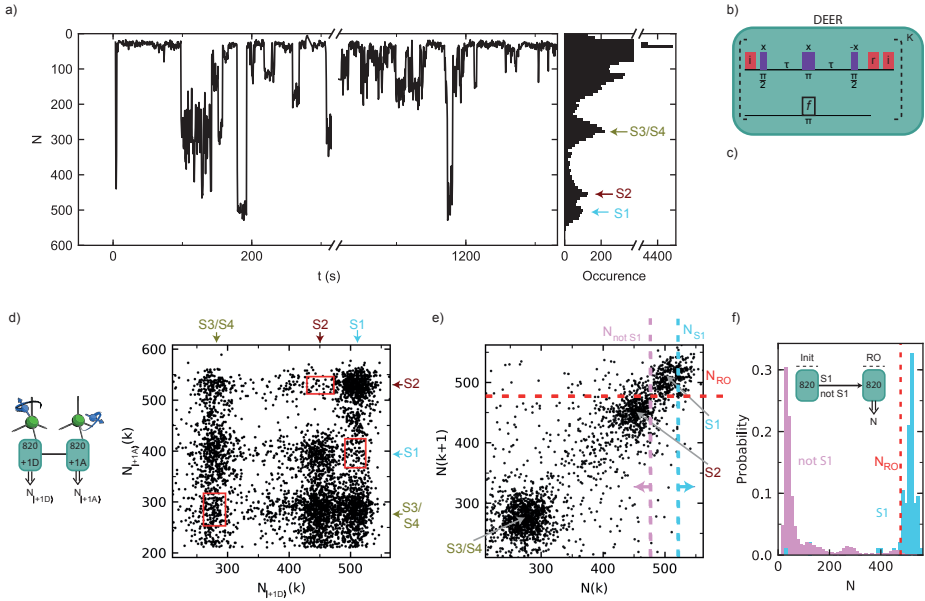
Figure 3.2: **Detection and preparation of single P1 centers. a)** Typical time trace for the DEER signal for $|+1,\mathrm{D}\rangle$. N is the total number of $m_s = 0$ NV readout outcomes in $K = 820$ repetitions of the sequence (see (b)). The discrete jumps and corresponding peaks in the histogram of the full time trace (~ 6 h, right) indicate that several individual P1s are observed (S1, S2 and S3/S4). **b)** Sequence for K repeated DEER measurements. Note that the phase of the final $\pi/2$ pulse is along -x and thus the signal is inverted as compared to Fig. 3.1b Optical initialisation (i) and readout (r) of the NV electron are indicated with red pulses. **c)** XY-plane of the NV-spin Bloch sphere before the second $\pi/2$ pulse of a DEER measurement, with the NV initialised along +z at the start. The NV spin picks up phase depending on which nearby P1 centers are in the targeted $|+1,\mathrm{D}\rangle$ state. Because the NV spin is effectively measured along the y-axis, this sequence is insensitive to the P1 electron spin state. We discuss the case of two P1 centers simultaneously in the same state, which happens with a small probability and yields a distinct signal, in section 3.9.1 **d)** Cross-correlation of two consecutive DEER measurements for $|+1,\mathrm{D}\rangle$ (K=820) and $|+1,\mathrm{A}\rangle$ (K=820). Three areas (red boxes, section 3.9.7 show an anti-correlation associated to S1, S2, and S3/S4, in agreement with the assignment of discrete P1 centers. Left: sequence for the two consecutive DEER measurements (green blocks). Double lined arrows indicate measurement outcomes. **e)** Correlation plot for consecutive measurement outcomes N(k) and N($k+1$), both for $|+1,\mathrm{D}\rangle$. Dashed lines are the thresholds used to prepare (vertical) and read out (horizontal) the JT and ^{14}N state in panel f. We use $N_{\mathrm{S1}} > 522$ to prepare S1 in $|+1,\mathrm{D}\rangle$, and S2 and S3/S4 in any other state. The condition $N_{\mathrm{notS1}} \leq 477$ prepares a mixture of all other possibilities. A threshold $N_{\mathrm{RO}} = 477$ distinguishes between those two cases in readout. **f)** Conditional probability distributions for both preparations, demonstrating initialisation and single-shot readout of the ^{14}N and JT state of S1. Inset: experimental sequence. Labelled horizontal arrows indicate conditions for passing the initialisation measurement (init).

sation and readout fidelity $F = 0.96(1)$ (see Methods). Other states can be prepared and read out by setting different conditions (section 3.9.7).
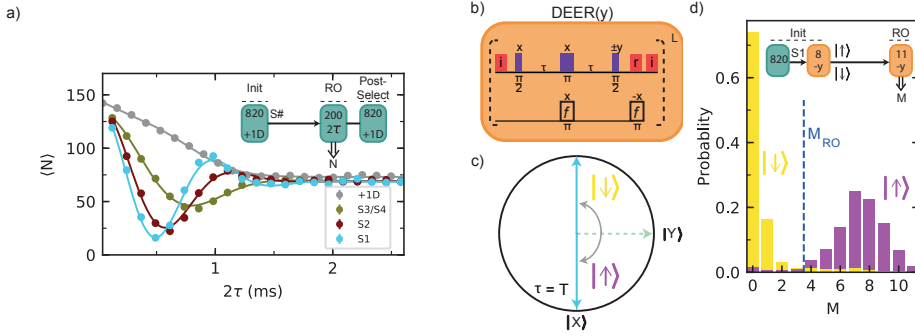
Figure 3.3: **Electron spin initialisation and readout. a)** Measuring the NV-P1 coupling strength. We initialize S1, S2, or S3/S4 in $|+1, D\rangle$ and vary the interaction time 2τ of a DEER sequence. $\langle N \rangle$ is the mean of the number of NV $m_s = 0$ outcomes for K=200 repetitions. To improve the signal, the results are post-selected on again obtaining $|+1, D\rangle$. Error bars are one standard deviation (Methods), with a typical value 1, which is smaller than the data points. Grey: without P1 initialisation (data from Fig. 3.1c). **b)** DEER(y) sequence with the readout basis rotated by $\pi/2$ compared to the DEER sequence and $\tau = \pi/2\nu$. An additional π pulse is added to revert the P1 electron spin. Optical initialisation (i) and readout (r) of the NV electron are indicated with red pulses. **c)** XY-plane of the NV Bloch sphere before the second $\pi/2$ pulse, illustrating that the DEER(y) sequence measures the P1 electron spin state (shown for positive NV-P1 coupling). **d)** Single-shot readout of the S1 electron spin. After preparation in $|+1, D\rangle$, the electron spin is initialized through a DEER(y) measurement (L=8) with thresholds $M_{|\uparrow\rangle}$ (> 6) and $M_{|\downarrow\rangle}$ ($\leq$1). Shown are the conditional probability distributions for a subsequent DEER(y) measurement with L=11 and the readout threshold M_{RO}.

3.4. CONTROL OF THE ELECTRON AND NUCLEAR SPIN

To control the electron spin of individual P1 centers, we first determine the effective dipolar NV-P1 coupling. We prepare, for instance, S1 in $|+1, D\rangle$ and perform a DEER measurement in which we sweep the interaction time (Fig. 3.3a). By doing so, we selectively couple the NV to S1, while decoupling it from S2 and S3/S4, as well as from all bath spins that are not in $|+1, D\rangle$. By applying this method we find effective dipolar coupling constants ν of $2\pi \cdot 1.910(5)$, $2\pi \cdot 1.563(6)$ and $2\pi \cdot 1.012(8)$ kHz for S1, S2 and S3/S4 respectively. Note that, if the signal for S3/S4 originates from two P1 centers, the initialisation sequence prepares either S3 or S4 in each repetition of the experiment.

We initialize and measure the electron spin state of the P1 centers through a sequence with a modified readout axis that we label DEER(y) (Fig. 3.3b). Unlike the DEER sequence, this sequence is sensitive to the P1 electron spin state. After initializing the charge, nuclear spin and JT axis, and setting the interaction time $\tau \approx \pi/(2 \cdot \nu)$, the DEER(y) sequence projectively measures the spin state of a selected P1 center (Fig. 3.3c). We first characterize the P1 electron spin relaxation under repeated application of the measurement and find a 1/e value of ~250 repetitions (section 3.9.5). We then optimize the number of repetitions and the initialisation and readout thresholds to obtain a combined initialisation and single-shot readout fidelity for the S1 electron spin of $F_{|\uparrow\rangle/|\downarrow\rangle} = 0.95(1)$ (Fig. 3.3d).
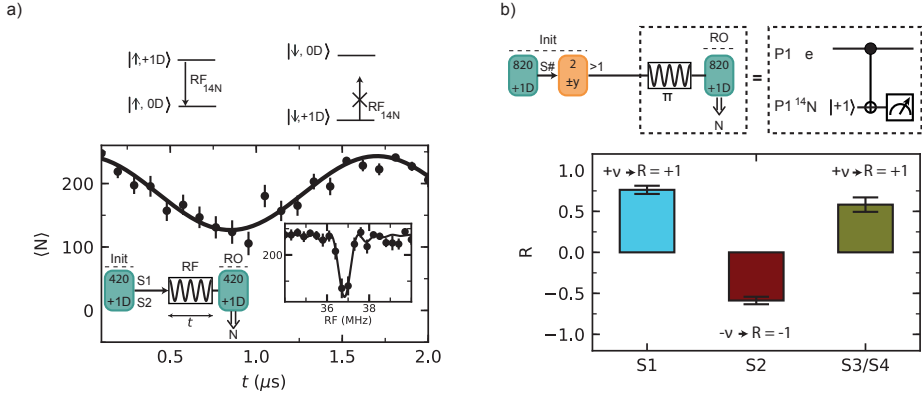
3

Figure 3.4: **Nitrogen nuclear spin control and NV-P1 coupling sign. a)** ^{14}N Rabi oscillation. Top: energy levels of the P1 electron spin in the {0D, +1D} subspace. Bottom: either S1 or S2 is prepared in $|+1, D\rangle$ and the length t of a pulse at frequency RF = RF$_{14N}$ = 36.8 MHz is varied. The nitrogen nuclear spin is driven conditionally on the electron spin state. Inset: NMR spectrum obtained by varying the frequency RF for a fixed pulse duration t. **b)** We use the ^{14}N spin to determine the sign of the NV-P1 coupling. First, we prepare a selected P1 center (K=820) and initialise its electron spin (L=2). Second, we apply a π pulse at RF$_{14N}$, which implements an electron controlled CNOT$_{e,N}$ (see level structure in (a)). The coupling sign to the NV determines the P1 electron-spin state, and, in turn, the final ^{14}N state. Finally, we measure the fidelity with the ^{14}N $|+1\rangle$ state for two opposite electron spin initialisations (+y and -y final $\pi/2$ pulse of DEER(y)). The normalized difference R of these measurements reveals the sign of the coupling (see Methods). All error bars indicate one statistical standard deviation.

We now show that we can coherently control the P1 nitrogen nuclear spin (Fig. 3.4a). To speed up the experiment, we choose a shorter initialisation sequence that prepares either S1 or S2 in the $|+1, D\rangle$ state (K=420, Methods). We then apply a radio-frequency (RF) pulse that is resonant with the $m_I = +1 \leftrightarrow 0$ transition if the electron spin is in the $|\uparrow\rangle$ state. Varying the RF pulse length reveals a coherent Rabi oscillation. Because the P1 electron spin is not polarized, the RF pulse is on resonance 50% of the time and the amplitude of the Rabi oscillation is half its maximum.

We use the combined control over the electron and nuclear spin to determine the sign of the NV-P1 couplings (Fig. 3.4b). First, we initialize the ^{14}N, JT axis and electron spin state of a P1 center. Because the DEER(y) sequence is sensitive to the sign of the coupling (Fig. 3.3c), the sign affects whether the P1 electron spin is prepared in $|\uparrow\rangle$ or $|\downarrow\rangle$. Second, we measure the P1 electron spin through the ^{14}N nuclear spin. We apply an RF pulse, which implements an electron-controlled CNOT gate on the nuclear spin (see Fig. 3.4a). Subsequently reading out the ^{14}N spin reveals the electron spin state and therefore the sign of the NV-P1 coupling. We plot the normalized difference R (Methods) for two different initialisation sequences that prepare the electron spin in opposite states. The results show that NV-P1 coupling is positive for the cases of S1 and S3/S4, but negative for S2 (Fig. 3.4b). If S3/S4 consists of two P1 centers, then they have the same coupling sign to the NV.
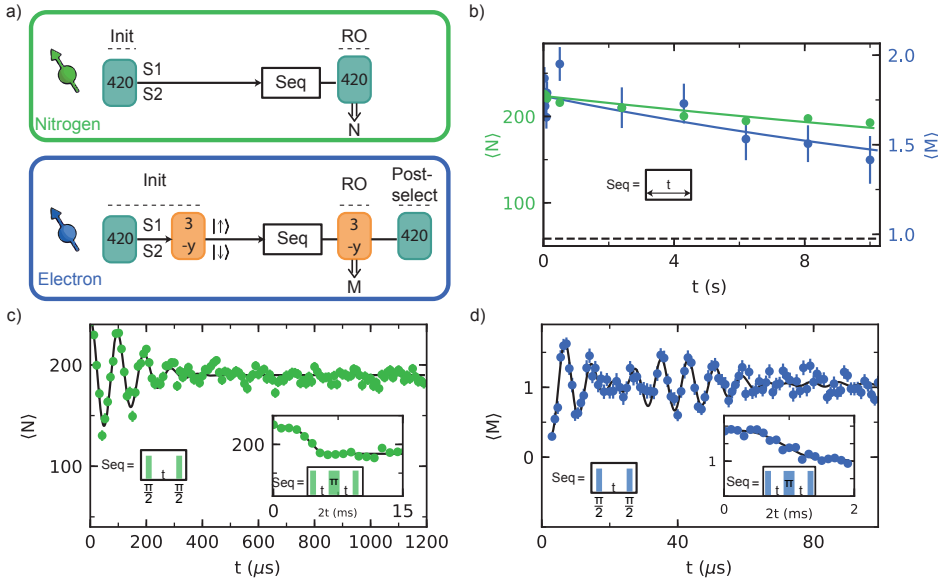
Figure 3.5: **Coherence and timescales. a)** Sequence for initialisation of either S1 or S2 in $|+1, D\rangle$ (top). Sequence for initializing all degrees of freedom of either S1 or S2, including the electron spin state (bottom). These sequences are used in b, c and d. **b)** Relaxation of a combination of: the nitrogen nuclear spin state, JT axis and charge state (green), and only the electron spin state (blue). We fit (solid lines) both curves to $o + A_0 e^{-t/T}$, where o is fixed to the uninitialized mean value (dashed line) and obtain $T = T_{|+1,D\rangle} = 40(4)$ s and $T = T_1 = 21(7)$ s. **c)** Ramsey experiment on the nitrogen nuclear spin. We fit the data (solid line) and obtain $T_{2N}^* = 0.201(9)$ ms. (inset) Nitrogen nuclear spin-echo experiment. From the fit we obtain $T_{2N} = 4.2(2)$ ms. **d)** Ramsey experiment on the electron spin. A Gaussian decay ($T_{2e}^* = 50(3)$ μs) with a single beating is observed, suggesting a dipolar coupling between S1 and S2. (inset) Electron spin-echo experiment. From the fit we obtain $T_{2e} = 1.00(4)$ ms. See Methods for complete fit functions and obtained parameters. All error bars indicate one statistical standard deviation.

3.5. SPIN COHERENCE AND RELAXATION

To assess the potential of P1 centers as qubits, we measure their coherence times. First, we investigate the relaxation times. We prepare either S1 or S2 in $|+1, D\rangle$, the NV electron spin in $m_s = 0$, and vary the waiting time t before reading out the same state (Fig. 3.5a). This sequence measures the relaxation of a combination of the nitrogen nuclear spin state, JT axis and charge state, averaged over S1 and S2. An exponential fit gives a relaxation time of $T_{|+1,D\rangle} = 40(4)$ s (Fig. 3.5b, green).

We measure the longitudinal relaxation of the electron spin by preparing either $|\uparrow\rangle$ (S1) or $|\downarrow\rangle$ (S2) (Fig. 3.5a). We post-select on the $|+1, D\rangle$ state at the end of the sequence to exclude effects due to relaxation from $|+1, D\rangle$, and find $T_{1e} = 21(7)$ s. The observed electron spin relaxation time is longer than expected from the typical P1-P1 couplings in the bath (order of 1 kHz). A potential explanation is that flip-flops are suppressed due to couplings to neighbouring P1 centers, which our heralding protocol

preferentially prepares in other $|m_I, i\rangle$ states. Below, we will show that S1 and S2 have a strong mutual coupling, which could shift them off resonance from the rest of the bath.

Second, we investigate the electron and nitrogen nuclear spin coherence via Ramsey and spin-echo experiments (Figs. 3.5c and d). We find $T_{2e}^* = 50(3)$ μs and $T_{2e} = 1.00(4)$ ms for the electron spin, and $T_{2N}^* = 0.201(9)$ ms and $T_{2N} = 4.2(2)$ ms for the nitrogen nuclear spin. The ratio of dephasing times for the electron and nitrogen nuclear spins is ~4, while the difference in bare gyromagnetic ratios is a factor ~9000. The difference is partially explained by electron-nuclear spin mixing due to the large value of $A_\perp$, which changes the effective gyromagnetic ratios of the nitrogen nuclear spin and electron spin. Based on this, a ratio of dephasing times of 12.6 is expected (see section 3.9.8). The remaining additional decoherence of the nitrogen nuclear spin is currently not understood.

The electron Ramsey experiment shows a beating frequency of 21.5(1) kHz (Fig. 3.5d). As the data is an average over S1 and S2, this suggests an interaction between these two P1 centers. Note that, whilst the signal is expected to contain 11 frequencies due to the different Jahn-Teller and nitrogen nuclear spin state combinations, the observation of a single beating frequency indicates that these are not resolved. Next, we will confirm this hypothesis and use the coupling between S1 and S2 to demonstrate an entangled state of two P1 centers.

3.6. ENTANGLEMENT OF TWO DARK ELECTRON SPINS

Thus far we have shown selective initialisation, control and single-shot readout of individual P1 centers within the bath. We now combine all these results to realize coherent interactions and entanglement between the electron spins of two P1 centers.

We first sequentially initialize both P1 centers (Fig. 3.6a). To overcome the small probability for both P1 centers to be in the desired state, we use fast logic to identify failed attempts in real-time and actively reset the states (Methods). We prepare S1 in the $|+1, D\rangle$ state and S2 in the $|+1, A\rangle$ state. By initializing the two P1 centers in these different states, we ensure that the spin transitions are strongly detuned, so that mutual flip-flops are suppressed and the interaction is effectively of the form $S_z S_z$. We then sequentially initialize both electron spins to obtain the initial state $|\uparrow\rangle_{S1} |\downarrow\rangle_{S2}$. As consecutive measurements can disturb the previously prepared degrees of freedom, the number of repetitions in each step is optimized for high total initialisation fidelity and success rate (section 3.9.11).

Next, we characterize the dipolar coupling J between S1 and S2 (Fig. 3.6b). We apply two $\pi/2$ pulses to prepare both spins in a superposition. We then apply simultaneous echo pulses on each spin. This double echo sequence decouples the spins from all P1s that are not in $|+1, D\rangle$ or $|+1, A\rangle$, as well as from the ^{13}C nuclear spin bath and other noise sources. This way, the coherence of both spins is extended from T_2^* to T_2, while
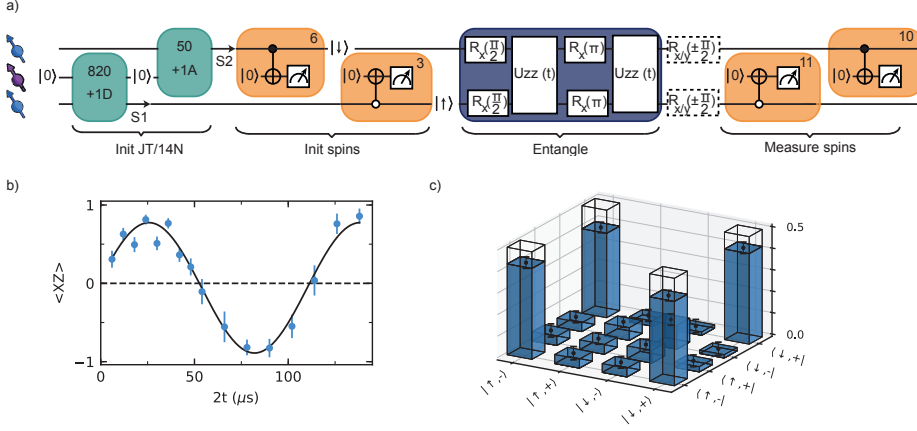
Figure 3.6: **Entanglement between two P1s. a)** Experimental sequence to measure coupling and generate entanglement between S1 and S2. DEER measurements initialize the JT axis and nitrogen state of S1 and S2 (K=820, 50 and $f = f_{+1D}, f_{+1A}$), followed by DEER(y) measurements to initialize their electron spin states (L=6, 3). Two $\pi/2$ pulses and an evolution for time $2t$ under a double echo implements the $S_z S_z$ interaction with both spins in the equatorial plane of the Bloch sphere. This is followed by single qubit gates (dashed boxes) for full 2-qubit state tomography and two final DEER(y) measurements for electron spin readout. We apply an additional initial sequence ($K = 5$, f_{+1A}) to speed up the experiment (not shown in sequence, see section 3.9.11). **b)** The coherent oscillation of the $\langle XZ \rangle$ as a function of interaction time $2t$ demonstrates a dipolar coupling $J = -2\pi \cdot 17.8(5)$ kHz between S1 and S2. **c)** Density matrix of the S1 and S2 electron spins after applying the sequence as shown in (a) for $2t = \pi/J$. The fidelity with the target state is $F = 0.81(5)$. Transparent bars indicate the density matrix for the target state $|\Psi\rangle$. All error bars indicate one statistical standard deviation.

their mutual interaction is maintained. We determine the coupling J by letting the spins evolve and measuring $\langle XZ \rangle$ as a function of the interaction time $2t$ through a consecutive measurement of both electron spins (Fig. 3.6b). From this curve we extract a dipolar coupling $J = -2\pi \cdot 17.8(5)$ kHz between S1 in $|+1, D\rangle$ and S2 in $|+1, A\rangle$.

Finally, we create an entangled state of S1 and S2 using the sequence in Fig. 3.6a. We set the interaction time $2t = \pi/J$ so that a 2-qubit CPHASE gate is performed. The final state is (see section 3.9.10):

$$|\Psi\rangle = \frac{|\uparrow\rangle_{S1} |-\rangle_{S2} + |\downarrow\rangle_{S1} |+\rangle_{S2}}{\sqrt{2}}, \tag{3.3}$$

with $|\pm\rangle = \frac{|\uparrow\rangle \pm |\downarrow\rangle}{\sqrt{2}}$. We then perform full 2-qubit state tomography and reconstruct the density matrix as shown in Fig. 3.6c. The resulting state fidelity with the ideal state is $F = (1 + \langle XZ \rangle - \langle ZX \rangle - \langle YY \rangle)/4 = 0.81(4)$. The fact that $F > 0.5$ is a witness for two-qubit entanglement [62]. The coherence time during the echo sequence (~ 700 µs, see Methods) is long compared to π/J (~ 28 µs), and thus the dephasing during the 2-qubit gate is estimated to be at most 2%. Therefore we expect the main sources of infidelity to be the final sequential single-shot readout of the two electron spin states – no readout correction is made – and the sequential initialisation of the two electron spins (section 3.9.11).

3.7. DISCUSSION

In conclusion, we have developed initialisation, control, single-shot readout, and entanglement of multiple individual P1 centers that are part of a bath surrounding an NV center. These results establish the P1 center as a promising qubit platform. Our methods to control individual dark spins can enable enhanced sensing schemes based on entanglement [29,32,33], as well as electron spin chains for quantum computation architectures [34–36,63]. Larger quantum registers might be formed by using P1 centers to control nearby ^{13}C nuclear spins with recently developed quantum gates [5]. Such nuclear spin qubits are connected to the optically active defect only indirectly through the P1 electron spin, and could provide isolated robust quantum memories for quantum networks [64]. Finally, these results create new opportunities to investigate the physics of decoherence, spin diffusion and Jahn-Teller dynamics [31] in complex spin baths with control over the microscopic single-spin dynamics.

3.8. METHODS

Sample.
We use a single nitrogen vacancy (NV) center in a homoepitaxially chemical-vapor-deposition (CVD) grown diamond with a ⟨100⟩ crystal orientation (Element Six). The diamond is isotopically purified to an approximate 0.01% abundance of ^{13}C. The nitrogen concentration is ~75 parts per billion, see section 3.9.4. To enhance the collection efficiency a solid-immersion lens was fabricated on top of the NV center [65,66] and a single-layer aluminum-oxide anti-reflection coating was deposited [67,68].

Setup.
The experiments are performed at 3.3 Kelvin (Montana Cryostation) with the magnetic field **B** applied using three permanent magnets on motorized linear translation stages (UTS100PP) outside of the cryostat housing. We realize a long relaxation time for the NV electron spin ($T_1 > 30$ s) in combination with fast NV spin operations (peak Rabi frequency ~ 26 MHz) and readout/initialisation (~ 40 μs/100 μs), by minimizing noise and background from the microwave and optical controls [14]. Amplifier (AR 20S1G4) noise is suppressed by a fast microwave switch (TriQuint TGS2355-SM). Video leakage noise generated by the switch is filtered with a high pass filter.

Error analysis.
The data presented in this work is either a probability derived from the measurements, the mean of a distribution, or a quantity derived from those. For probabilities, a binomial error analysis is used, where p is the probability and $\sigma = \sqrt{p \cdot (1-p)/Q}$, Q being the number of measured binary values. For the mean μ of a distribution, σ_μ is calculated as $\sigma/\sqrt{Q}$, where σ is the square root average of the squared deviations from the mean and Q is the number of measurements. Uncertainties on all quantities derived from a probability or a mean are calculated using error propagation.

NV spin control and readout.
We use Hermite pulse envelopes[69,70] to obtain effective microwave pulses without initialisation of the intrinsic ^{14}N nuclear spin of the NV. We initialize and read out the NV electron spin through spin selective resonant excitation ($F = 0.850(5)$)[65]. Laser pulses are generated by acoustic optical modulators (637 nm Toptica DL Pro, for spin pumping and New Focus TLB-6704-P for single-shot spin readout) or by direct current modulation (515 nm laser, Cobolt MLD - for charge state control, and scrambling the P1 center state, see section 3.9.6). We place two modulators in series (Gooch and Housego Fibre Q) for an improved on/off ratio for the 637 nm lasers.

Magnetic field stabilization.
During several of the experiments we actively stabilize the magnetic field via a feedback loop to one of the translation stages. The feedback signal is obtained from interleaved measurements of the NV $|0\rangle \leftrightarrow |-1\rangle$ transition frequency. We use the P1 bath as a three-axis magnetometer to verify the stability of the magnetic field during this protocol (see section 8.1.6), and find a magnetic field that is stable to <3 mG along $\mathbf{z}$ and <20 mG along $\mathbf{x}, \mathbf{y}$ directions.

Heralded initialization protocols.
Initialisation of the P1 ^{14}N spin, JT axis, charge and electron spin states is achieved by heralded preparation. Before starting an experimental sequence, we perform a set of measurements that, given certain outcomes, signals that the system is in the desired state.

A challenge is that the probability for the system to be in a given desired state is low, especially in experiments with multiple P1 centers (e.g. Fig. 3.6). We realize fast initialization by combining the heralded preparation with fast logic (ADwin-Pro II) to identify unsuccessful attempts in real time and then actively reset the system to a random state. This way each step is performed only if all previous steps were successful, and one avoids being trapped in an undesired state.

To reset the P1 centers to a random state, we use photoexcitation[71] of the P1s. We apply a ~5 μs 515 nm laser pulse to scramble the ^{14}N, JT and charge states of P1 centers. See section 3.9.6 for details and the optimization procedure.

The most time-consuming step is the selective initialization of the Jahn-Teller and ^{14}N spin states, as $K = 820$ repetitions are required to distinguish the signals from the P1 centers (S1, S2 and S3/S4). However, cases for which none of these P1 centers are in the desired state can be identified already after a few repetitions (section 3.9.6). So after $K = 5$ repetitions we infer the likelihood for the desired configuration and use fast logic to determine whether to apply a new optical reset pulse or continue with the full sequence ($K = 820$). This procedure significantly speeds up the experiments (section 3.9.6). For creating the entangled state (Fig. 3.6) we use a more extensive procedure, which is detailed in section 3.9.11.

In the experiments in Figs. 2.4a and 2.5, we take an alternative approach to speed up the experiments by using a shorter initialisation sequence ($K = 420$) that does not distinguish between S1 and S2. Such a sequence prepares either S1 or S2, and the resulting data is an average over the two cases. Note that this method cannot be used in experiments where a selective initialization is required (e.g. Fig 2.3, Fig 2.4b, Fig. 2.9).

The optimization of the heralded initialization fidelities are discussed in section 3.9.11.

Initialisation and single-shot readout fidelity.
We define the combined initialisation and readout fidelity for S1 in $|+1,D\rangle$ and S2, S3/S4 not in that state as

$$F_{S1} = P(N(k+1) > N_{RO}|N(k) > N_{S1}), \tag{3.4}$$

whereas for a mixture of all other possibilities we define

$$F_{notS1} = P(N(k+1) \leq N_{RO}|N(k) \leq N_{notS1}). \tag{3.5}$$

In both cases $P(X|Y)$ is the probability to obtain X given Y. We then take the average fidelity of these two cases:

$$F = \frac{F_{S1} + F_{notS1}}{2}. \tag{3.6}$$

We initialize and measure the electron spin state of P1 centers through a DEER(y) sequence following initialisation of the $|+1,D\rangle$ state. Similarly, we use the correlation of consecutive measurements $M(k)$ and $M(k+1)$ to determine the combined initialisation and readout fidelity $F_{|\uparrow\rangle/|\downarrow\rangle}$. First, we define the fidelity for $|\uparrow\rangle$ as

$$F_{|\uparrow\rangle} = P(M(k+1) > M_{RO}|M(k) > M_{|\uparrow\rangle}), \tag{3.7}$$

and the fidelity for $|\downarrow\rangle$ as

$$F_{|\downarrow\rangle} = P(M(k+1) \leq M_{RO}|M(k) \leq M_{|\downarrow\rangle}). \tag{3.8}$$

Finally, the average combined initialisation and readout fidelity is given as

$$F_{|\uparrow\rangle/|\downarrow\rangle} = \frac{F_{|\uparrow\rangle} + F_{|\downarrow\rangle}}{2}. \tag{3.9}$$

For a description of the optimization of the single-shot readout fidelities, we refer to section 3.9.11.

Data analysis.
The DEER measurements in Fig. 3.1c are fitted to:

$$a_0 + A_0 \cdot \text{Exp}[-(2\tau/T_{2,DEER})^2] \cdot (1 + B_0 \cos(\omega \cdot \tau)) \tag{3.10}$$

from which we find $T_{2,DEER}$ of 0.767(6), 0.756(7), 0.802(6) and 0.803(5) ms for $|+1,A\rangle$, $|+1,B\rangle$, $|+1,C\rangle$ and $|+1,D\rangle$, respectively. The obtained values for ω are 2π·2.12(5),

$2\pi \cdot 2.14(3)$ and $2\pi \cdot 2.78(6)$ kHz with corresponding amplitudes B_0 of 0.105(5), 0.218(7), and 0.073(4) for $|+1,A\rangle$, $|+1,B\rangle$ and $|+1,C\rangle$, respectively. For $|+1,D\rangle$ we fix $B_0 = 0$.

The DEER measurements with P1 initialisation (Fig. 3.3a) and the P1 nitrogen nuclear spin Ramsey (Fig. 3.5c) are fitted to:

$$A_1 \cdot e^{-(t/T)^2} (\cos(\nu \cdot t/2)) + a_1. \tag{3.11}$$

For the dephasing time during the DEER sequence (here $t = 2\tau$) we find $T = 0.893(5)$, 0.763(8) and 0.790(8) ms for S1, S2 and S3/S4 respectively. The obtained respective dipolar coupling constants ν are $2\pi \cdot 1.894(3)$, $2\pi \cdot 1.572(6)$ and $2\pi \cdot 1.001(6)$ kHz. For the P1 nitrogen nuclear spin Ramsey we find a dephasing time of $T = T_{2N}^* = 0.201(9)$ ms.

Spin-echo experiments (Fig. 3.1c and Fig. 3.5) are fitted to

$$A_2 \cdot e^{-(t/T)^n} + a_2. \tag{3.12}$$

For the NV spin-echo (Fig. 3.1c), $T = T_2 = 0.992(4)$ ms with $n = 3.91(7)$. For the P1 nitrogen nuclear spin and electron (insets of Figure 3.5c,d) T is $T_{2N} = 4.2(2)$ ms or $T_{2e} = 1.00(4)$ ms with the exponents $n = 3.9(8)$ and $n = 3.1(5)$, respectively.

The Ramsey signal for the P1 electron spin in Fig. 3.5d is fitted to a sum of two frequencies with a Gaussian decay according to:

$$a_3 + e^{-(t/T_{2,e}^*)^2} \cdot \sum_{j=1}^{2} (A_j \cos\left((f_{\mathrm{det}} + (-1)^j f_b/2)\, t\right) + \phi_j))/2, \tag{3.13}$$

which gives a beating frequency $f_b = 2\pi \cdot 21.5(5)$ kHz.

The value R (Fig. 3.4b) is defined as

$$R = \frac{P_{(+y)} - P_{(-y)}}{P_{(+y)} + P_{(-y)}}, \tag{3.14}$$

where $P_{(+y)}$ ($P_{(-y)}$) is the probability to read out the ^{14}N spin in the $m_I = +1$ state when using a +y (-y) readout basis in the DEER(y) sequence used to initialize the electron spin (Fig. 3.4b, see section 8.1.4).

Two-qubit gate fidelity. We estimate the dephasing during the two-qubit CPHASE gate in Fig. 2.9 by extrapolation of the measured P1 electron $T_{2e} = 1.00(4)$ ms for a single spin-echo pulse (decoupled from all spins except those in $|+1,D\rangle$). We use the scaling $T_2 \propto 1/\sqrt{\langle n_{\mathrm{spins}} \rangle}$ with $\langle n_{\mathrm{spins}} \rangle$ the average number of spins coupled to during the measurement[53]. The two-qubit gate is implemented by a double echo and the two P1s are thus not decoupled from spins in $|+1,D\rangle$ and $|+1,A\rangle$, resulting in $T_2 \sim T_{2e}/\sqrt{2} \approx 700$ μs. Assuming the same decay curve as for T_{2e} ($n = 3.1$) this implies a loss of fidelity due to dephasing of ~0.4%. For a Gaussian decay ($n = 2$) the infidelity would be ~2%.

Data availability The data and code underlying the figures of this research article are available online through `https://doi.org/10.4121/14376611`.

3.9. SUPPLEMENTARY INFORMATION

3.9.1. MULTIPLE P1 CENTERS

In this section we discuss multiple coupled P1 centers that simultaneously occupy the same nitrogen nuclear spin- and JT-state. For simplicity we discuss the case of two P1 centers - S1 and S2 - with significant couplings to the NV center, but this can be extended to more P1 centers. Given the measured coupling strengths in $|+1, D\rangle$ and the chosen interaction time 2τ as shown in Fig. 3.2c of the main text, the NV acquires a phase of approximately $\pm\pi$ ($\pm 4\pi/5$) due to S1 (S2) individually. For the case that both spins occupy the same $|m_I, i\rangle$ state, summation of coupling strengths and the number of repetitive measurements play a role for the observed effective phase. If both spins are in $|+1, D\rangle$, the total phase is given by the sum or difference of the individual phase contributions and depends on the parity of their electron spins. This results in phases of $\pm 1\pi/5$ or $\pm 9\pi/5$. However, because the P1 electron spin states relax rapidly under repeated measurement (see Supplementary Fig. 3.12b), for $K = 820$ the measured result is an average of the results generated by the phases of each possible two-spin state. In this case, this gives an effective phase of $1\pi/5$. The resulting signal is well separated from the cases of just S1 or S2, so that cases in which both P1s occupy the same state are removed by the initialization procedures used. Note also that the probability that two of the P1s (S1-S4) are in the same state simultaneously is small.

3.9.2. JT DEPENDENT COUPLING

Mainly due to the anisotropic hyperfine interaction of the P1 center, the effective NV-P1 dipolar coupling ν, which is the interaction observed in a DEER experiment (Supplementary Eq. (8.13)), varies depending on the JT axis. We numerically calculate ν as a function of angles θ and ϕ of the vector $\mathbf{r}$ between an NV and a P1 using an exemplary case. Supplementary Fig. 3.7a, shows the calculated $\nu/2\pi$ for different states $|m_I, i\rangle$ as a function of angle ϕ as in Supplementary Eq. (8.9) (here $\theta = 45°$). This figure demonstrates that the JT state can affect the effective dipolar coupling strength ν (Supplementary Eq. (8.13)). For a P1 center in the states $|+1, A\rangle, |+1, B\rangle$ and $|+1, C\rangle$ the principal axis of the hyperfine tensor is rotated 109.5° w.r.t. the $\mathbf{z}$ axis (NV axis) and thus varying ϕ has a substantial effect on ν. For a P1 center in $|+1, D\rangle$ the hyperfine tensor's principal axis is along $\mathbf{z}$ and therefore the dependence on ϕ is small. The observed dependence in the simulation for $|+1, D\rangle$ is explained by the purposely slightly tilted magnetic field. The tilted magnetic field also explains the differences in maximal and minimal values of ν for the states $|+1, A\rangle, |+1, B\rangle$ and $|+1, C\rangle$. The ϕ angles at which ν is at a maximum for these three states are shifted by $\Delta\phi \approx 120°$ w.r.t. each other as is expected from the three-fold rotational symmetry.

Supplementary Fig. 3.7b illustrates that the relative differences of ν for different states are largest near the magic angles $\theta = \pm 54.7°$. Note that information about the P1 positions can be obtained by combining the knowledge of which signal belongs to which P1 center for several $|m_I, i\rangle$ states (Fig. 2d main text) and measuring the NV-P1 dipolar
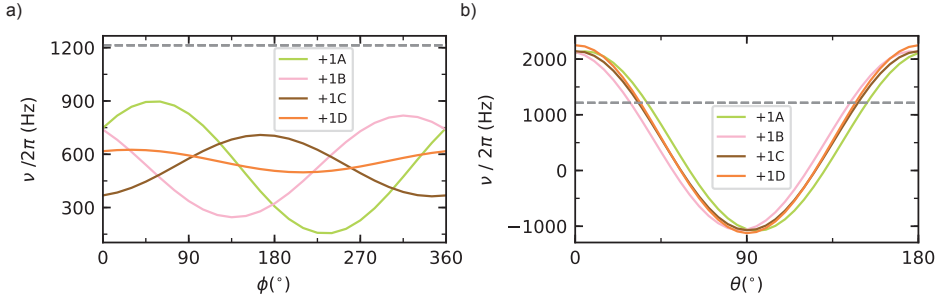
Figure 3.7: **Example showing JT dependent effective dipolar coupling ν. a)** Numerical simulation of $\nu/2\pi$ as a function of angle ϕ of the vector **r** between the NV and a P1. As an example we set $\theta = 45°$ and $|\mathbf{r}| = 35$ nm. The magnetic field **B** and hyperfine/quadrupole parameters as obtained from the fitted DEER spectrum (main text Fig. 1b) are used. Colored curves indicate the P1 center in different states $|+1, i\rangle$. The dashed grey line indicates the value of $\nu_{\text{dip}}/2\pi$ as in Supplementary Eq. (8.9). **b)** Similar to (a) but now as a function of θ ($\phi = 90°$).

coupling. This provides a future opportunity to determine the position of P1 centers (up to inversion symmetry) w.r.t. the NV.

3.9.3. Fitting the Hamiltonian parameters

This section describes the fitting procedure used to obtain the Hamiltonian parameters $A_\parallel$, $A_\perp$, P, B_x, B_y and B_z from the DEER spectroscopy (see Fig. 3.1b and Supplementary Fig. 3.8). We use parabolic fits of the measured dips to determine their center frequencies, and subsequently use a least squares method to minimize the difference between the measured frequencies and the frequencies resulting from diagonalization of the Hamiltonian (Supplementary Eq. (8.1)) for all 4 JT axes (see Supplementary Fig. 3.8b). This method requires that we can assign which measured frequency (dips in Supplementary Fig. 3.8a) belongs to which transition. We use a two step process. First, we take the four highest-energy transitions, which are well separated from any other transition, and use initial values for $A_\parallel$, $A_\perp$, P [41] to obtain an estimate of the magnetic field vector. Second, we select 11 well-isolated transitions and corresponding experimental dips to fit $A_\parallel$, $A_\perp$, P and the magnetic field vector.

To obtain an initial estimate of B_x, B_y and B_z, we first perform a brute force optimization. We sweep B_x and B_y between ± 4 G and B_z between 45 and 46 G in discrete steps and diagonalize the Hamiltonian (Supplementary Eq. (8.1)), where we use $\gamma_e = 2\pi \cdot$ 2.802495 MHz/G and $\gamma_n = -2\pi \cdot$ 0.3078 kHz/G. For every combination we sort the four highest frequencies (corresponding to $|+1, i\rangle$) and calculate $\Delta = \sum_{i=1}^{4} (f_{i,\text{exp}} - f_{i,\text{theo}})^2$, where $f_{i,\text{theo}}$ is the transition frequency obtained by diagonalization and $f_{i,\text{exp}}$ is the measured frequency. We find a minimum in Δ for $\mathbf{B} = (2.53, 1.39, 45.37)^T$ G.

We then use 11 dips that we can unambiguously assign to a well-isolated transition and measure these dips with high accuracy, see Supplementary Fig. 3.8b. We use this

data to extract $A_\parallel$, $A_\perp$, P and the magnetic field vector using a least squares fit. The fit obtains $\{A_\parallel, A_\perp, P_\parallel\} = \{114.0264(9), 81.312(1), -3.9770(9)\}$ MHz and $\mathbf{B} = \{2.437(2), 1.703(1), 45.5553(5)\}$ G. The vertical lines in Supplementary Fig. 3.8b are the 11 transition frequencies calculated with these values. In order to provide a more quantitative comparison we provide the experimentally measured frequencies of the 11 dips in Supplementary Table 3.1 alongside with their values calculated from Supplementary Eq. (8.1). Furthermore, by inspection, we identify 9 other dips in Supplementary Fig. 3.8a. We determine their center frequency and compare them to their closest transition frequency resulting from the fitted parameters, see Supplementary Table 3.1.
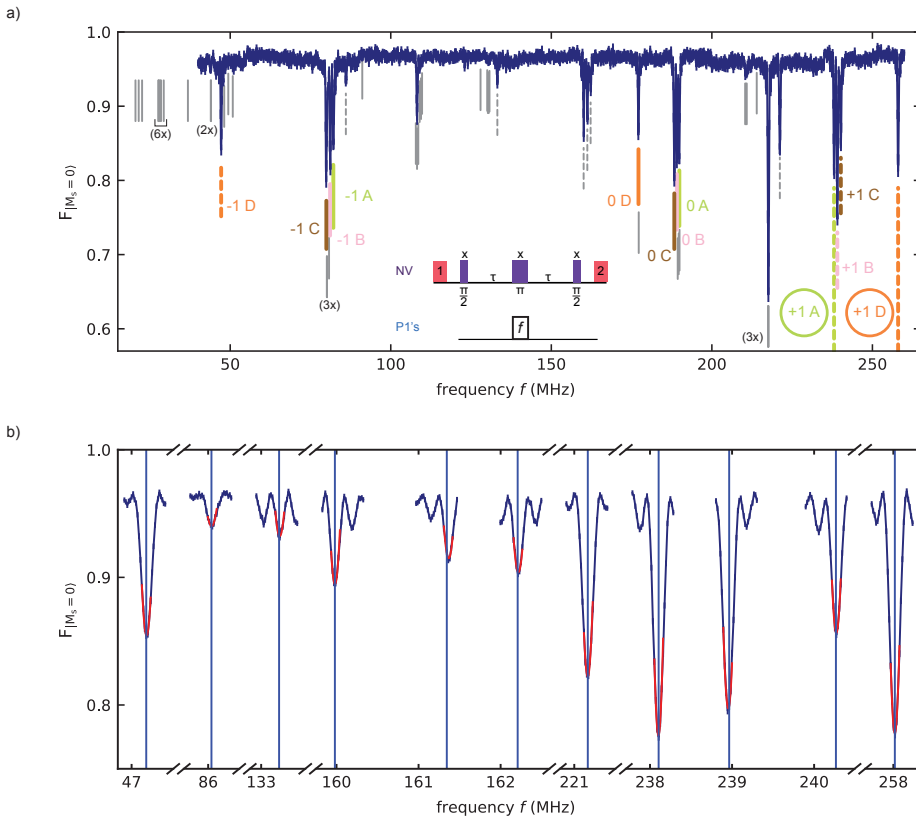
Figure 3.8: **Fitting the P1 Hamiltonian parameters.** a) Complete dataset corresponding to Fig. 3.1b (main text). No measurements were performed around the predicted transitions on the left. b) Measurement of 11 dips that are assigned to a well isolated transition (blue lines). Side lobes are due to Rabi oscillations. We fit a parabola (red) and extract the center frequency. Using a least squares fit of the center frequencies and the transitions, we extract the values of $\{A_\parallel, A_\perp, P_\parallel\}$ and $\mathbf{B}$. Error bars indicate one statistical standard deviation, with a typical value 2×10^{-3}, which is smaller than the data points.

Dip Nr	Experimental value (MHz)	Supplementary Eq. (8.1) (MHz)	$|m_I, i\rangle$ state
1	47.183(1)	47.179	$|-1, D\rangle$
2	86.042(2)	86.040	
3	133.227(2)	133.219	
4	159.9810(4)	159.980	
5	161.367(4)	161.344	
6	162.217(3)	162.208	
7	221.1641(7)	221.1648	
8	238.1027(6)	238.1051	$|+1, A\rangle$
9	238.954(1)	238.965	$|+1, B\rangle$
10	240.271(1)	240.266	$|+1, C\rangle$
11	258.0176(6)	258.018	$|+1, D\rangle$
12	79.898(4)	79.961	$|-1, C\rangle$
13	81.16(2)	81.10	$|-1, B\rangle$
14	82.106(8)	82.119	$|-1, A\rangle$
15	108.18(2)	108.20	
16	177.1167(2)	177.1476	$|0, D\rangle$
17	188.32(2)	188.32	$|0, C\rangle$
18	189.15(6)	189.11	$|0, B\rangle$
19	189.88(5)	189.88	$|0, A\rangle$
20	217.5783(8)	217.5709	

Table 3.1: Comparison of measured P1 transition frequencies (Supplementary Fig. 3.8b) with closest values from Supplementary Eq. (8.1). We include the 11 frequencies of Supplementary Fig. 3.8b used in the fitting, as well as 9 other identified dips in Supplementary Fig. 3.8a, which is taken at a slightly different magnetic field compared to Supplementary Fig. 3.8b.

3.9.4. Estimate of P1 concentration

In this section we estimate the P1 concentration surrounding the NV center. We calculate an expected concentration (C_d) based on decoherence of the NV electron spin. In the secular approximation the dipolar interaction of a number (N_d) of P1 centers and the NV (see Supplementary Eq. (8.9)) is given as:

$$H_{\text{int}} = J_z \sum_{k=1}^{N_d} 2\pi \cdot \nu_k \cdot (1 - 3\cos^2(\theta)) \cdot S_z = J_z \sum_{k=1}^{N_d} b_k \cdot S_z, \tag{3.15}$$

where $2\pi \cdot \nu_k = \frac{-\mu_0 \gamma_e \gamma_e \hbar}{4\pi r_k^3}$ and θ the polar angle in spherical coordinates. For a given concentration of P1 centers C_d, we consider a sphere around the NV center of radius R:

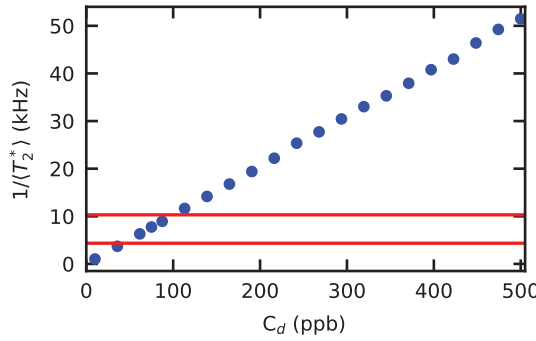$$R = \left(\frac{3 \cdot V_{\text{tot}}}{4\pi}\right)^{1/3}, \tag{3.16}$$

Figure 3.9: **Simulated $1/\langle T_2^* \rangle$.** Simulation based on m $= 10^4$ different defect configurations of $N_d = 40$ defects. The red vertical lines indicate estimated bounds for $1/\langle T_2^* \rangle$.

where $V_{\text{tot}} = \frac{N_d \cdot V_{\text{unit}}}{C_d \cdot 8}$ with V_{unit} the volume of a diamond crystal unit cell, and 8 denotes the number of atoms within one unit cell. Within such a sphere we generate a number of P1 centers ($N_d = 40$) at random positions and calculate T_2^* due to a Gaussian spin bath[72] as:

$$T_2^* = \frac{\sqrt{2}}{\frac{1}{2}\sqrt{\sum_{k=1}^{N_d} b_k^2}}. \tag{3.17}$$

We repeat this procedure to generate $m = 10^4$ different spatial configurations of P1 centers and calculate the average, $\langle T_2^* \rangle$.

The result of this simulation as a function of P1 concentration C_d is shown in Supplementary Fig. 3.9. For randomly positioned P1s, $1/\langle T_2^* \rangle$ scales linearly with C_d. Note the difference in scaling with the average number of P1 centers coupled to during a DEER measurement, $\langle n_{\text{spins}} \rangle$, which scales as $1/T_{2,\text{DEER}} \propto \sqrt{\langle n_{\text{spins}} \rangle}$ due to the fixed positions of the P1s[53]. We estimate the NV decoherence time due to coupling to P1s to be within two values (as indicated by the red vertical lines in Supplementary Fig. 3.9). The first value is the measured $T_{2,\text{NV}}^* = 97(3)$ µs ($1/T_{2,\text{NV}}^* \approx 10$ kHz). Here it is assumed that the P1 centers are the dominant spin bath and the effect of the ^{13}C bath, and other magnetic field noise sources, on the NV decoherence is small. The second value is extrapolated from the measured $T_{2,\text{DEER}} = 0.803(5)$ ms for $|+1, \text{D}\rangle$ and thus is given by $T_2^* \sim T_{2,\text{DEER}}/\sqrt{12} \approx 230$ µs ($1/T_2^* \approx 4$ kHz). Here we assume approximately equal coupling strength in all 12 $|m_I, i\rangle$ states and an equal probability of occurrence for each state. The concentration is expected to be within these values and thus we estimate $C_d \sim 75$ ppb.

Supplementary Fig. 3.10 shows the probability density of $b_k/2\pi$ for the first four P1 spins, given a concentration $C_d = 75$ ppb and the condition 4 kHz $\le 1/T_2^* \le 10$ kHz for the NV spin. These distributions demonstrate the expected values of $|b_k|$ to be close

Figure 3.10: **Simulated distributions of the coupling strengths for the most strongly coupled P1 spins.**
a),b),c),d) Distributions of $|b_k|/2\pi$ given 4 kHz $\leq 1/T_2^* \leq$ 10 kHz and a concentration C_d = 75 ppb.

to the measured values as stated in Methods (indicated by the vertical red lines). The
probability densities without a condition on $1/T_2^*$ are shown in Supplementary Fig. 3.11.
These plots show that given the concentration $C_d \sim$ 75 ppb, a large range of coupling
strengths are possible for the nearest spin (including the measured value |17.8(5)| kHz as
measured between S1 and S2).
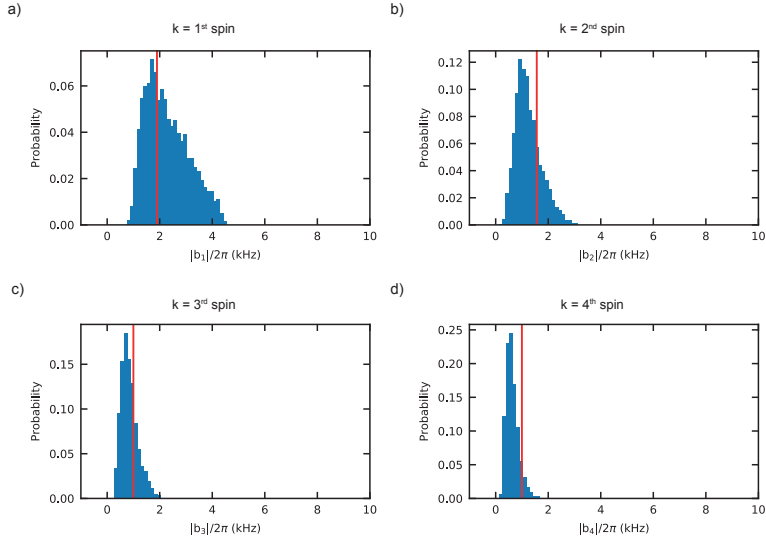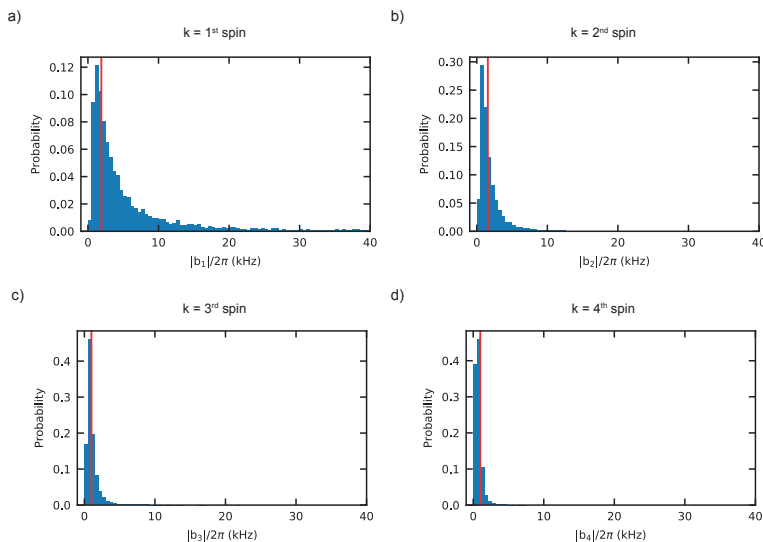
Figure 3.11: **Simulated distributions for the 4 most strongly coupled spins.** a),b),c),d) Distributions of $|b_k|/2\pi$ given a concentration C_d = 75 ppb.

3.9.5. RELAXATION TIMES OF S1 DURING REPETITIVE DEER MEASUREMENTS

This section characterizes the relaxation of the P1 $|+1, \text{D}\rangle$ state (Supplementary Fig. 3.12a) and the P1 electron spin in $|+1, \text{D}\rangle$ (Supplementary Fig. 3.12b) under repeated measurement sequences. We first prepare spin S1 in $|+1, \text{D}\rangle$ using DEER measurements (K=820) and subsequently apply 5 sequential sets of DEER measurements with K=820. We plot the result of each set in Supplementary Fig. 3.12a. We obtain a 1/e decay of ~19 sets, showing the $|+1, \text{D}\rangle$ state is stable over ~ 1.5×10^4 DEER repetitions (including optical 637 nm pulses).

To investigate the stability of the P1 electron state under repetitive DEER(y) measurements, we initialize S1 in $|+1, \text{D}\rangle$ and prepare its electron state in $|\uparrow\rangle$ using L=8 DEER(y) measurements. Subsequently we apply 51 sequential sets of DEER(y) measurements with L=8 and plot the result of each set in Supplementary Fig. 3.12b. We extract a 1/e decay for $|\uparrow\rangle$ of ~32 sets, showing a stability over ~250 DEER(y) repetitions. Comparing this with the 1/e decay of $|+1, \text{D}\rangle$ shows that a single sequence is much more destructive for the P1 electron state than for the combined nitrogen nuclear spin and JT state. This limits the amount of DEER(y) sequences L that can be used to initialize the P1 electron spin with high fidelity.
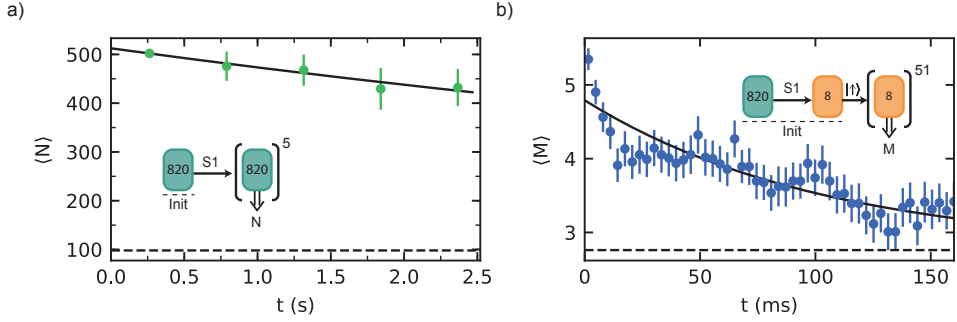
Figure 3.12: **Relaxation during repetitive readout.** a) Relaxation from the $|+1, D\rangle$ state while continuously performing DEER measurements. We fit (solid line) the curve to $o + A_0 \cdot e^{-t/T_{|+1,D\rangle\text{rep}}}$, where o is fixed to the uninitialized mean value (dashed line) and obtain $T_{|+1,D\rangle\text{rep}} = 10(4)$ s. This timescale corresponds to ~ 19 bins of DEER measurements with K=820 repetitions. b) Relaxation from the $|\uparrow\rangle$ state, we fit (solid line) the curve to $o_1 + A_1 \cdot e^{-t/T_{|\uparrow\rangle\text{rep}}}$, where o_1 is fixed to the uninitialized mean value (dashed line) and obtain $T_{|\uparrow\rangle\text{rep}} = 103(8)$ ms. This timescale corresponds to ~ 32 bins of DEER(y) measurements with L=8 repetitions.

3.9.6. PREPARATION OF P1 BATH CONFIGURATIONS BY ACTIVE OPTICAL RESET

Several of the experiments require initialisation of the charge, nitrogen nuclear spin and JT degrees of freedom for single P1 centers. To be able to distinguish the signals of the different P1 centers a large amount of measurement repetitions K is required, which limits the experimental repetition rate. In this section we describe how we increase the experimental rate fourfold by dynamically resetting the P1 center states based on outcomes of early measurement repetitions. The key ideas are: (1) cases for which none of the P1 centers start in the desired state can be identified already after a few repetitions, so that the sequence can be aborted, and (2) the state of the P1 centers can be rapidly reset by a laser pulse (515 nm) before re-attempting the initialization.

OPTIMIZATION TO INCREASE EXPERIMENTAL RATE

In various experiments, we initialize the nitrogen nuclear spin- and JT-state of selected P1 centers by using the outcome of $K = 420$ or $K = 820$ DEER measurements to herald the desired state (Fig. 3.2a of the main text and Supplementary Fig. 3.15). In Supplementary Fig. 3.13a, we plot the histogram of $\sim 3 \times 10^5$ DEER measurements in bins of K=420 on $|+1, D\rangle$. In this dataset we define a successful (unsuccessful) initialisation of either S1 or S2 in $|+1, D\rangle$ if the outcome N of K=420 DEER measurements fulfils $N > 180$ ($N \leq 180$), see the green (red) part of the distribution in Supplementary Fig. 3.13a. We find $\sim 11\%$ of the distribution in the green region which indicates the probability to find either S1 or S2 in $|+1, D\rangle$. This differs from a probability of $\sim 2 \cdot \frac{1}{12}$ and suggests that P1 centers occasionally ionize or preferentially occupy specific states. Research on all 12 nitrogen nuclear spin- and JT-states is required to provide more insight on the occupation of such states and provides a potential direction for future research. We note that from Supplementary Fig. 3.15 we extract $\sim 11\%$ of S1 or S2 being in $|+1, A\rangle$. Because of these low probabilities,

the success rate of initialising S1 or S2 is limited. In Supplementary Fig. 3.13b, we inspect the measurement outcome N1 of successful (green) and unsuccessful (red) initialisation attempts after the first $K=\Theta$ DEER sequences, where in this figure $\Theta = 5$. This shows that N1 is low for many unsuccessful cases (red), indicating that the experiment can be sped up by aborting the sequence after a few repetitions if N1 is below a threshold.

We implement a Monte Carlo method to determine a good set of parameters to increase the experimental rate. A schematic of the method is depicted in Supplementary Fig. 3.13d. We sample from the dataset in Supplementary Fig. 3.13a and check after Θ DEER measurements (DEER 1) whether the outcome N1 is below a threshold Λ. If so, we abort, sample again from the dataset and inspect DEER 1 again. If $N1 \geq \Lambda$, we continue until finishing 420 DEER measurements. If the outcome of the 420 DEER measurements is above 180, we accept it as a successful initialisation. We continuously sample from the dataset until we achieve 1000 successful runs ($N1 + N2 > 180$).

We now sweep Θ and Λ and calculate the average time $\langle T_{avg} \rangle$ required to finish one successful run, where we average over 1000 successful runs (see Supplementary Fig. 3.13d). Here we use that 1 DEER sequence takes 684 µs and we introduce an overhead time of 1 ms for resetting the P1 center states (experimentally done with a laser pulse, see subsection below). Two critical parameters that determine $\langle T_{avg} \rangle$ are 1) the probability $P(N1 \geq \Lambda)$ to pass the condition in DEER 1 and 2) the probability $P(N1 + N2 > 180 | N1 \geq \Lambda)$ to obtain $N1 + N2 > 180$ conditioned on passing the condition in DEER 1. These probabilities can be extracted from Supplementary Fig. 3.13a and b and are shown in Supplementary Fig. 3.13c for the example case of $\Theta = 5$. From Supplementary Fig. 3.13d we extract that $\Theta = 5$ and $\Lambda = 3$ are parameters where $\langle T_{avg} \rangle$ is small and we find an increase in experimental rate by a factor ~ 5. This shows that the experiment can be sped up by aborting the sequence after 5 repetitions already if N1 is below 3. Note, however, that this method assumes perfect randomization of the P1 center states by drawing random samples from the dataset.
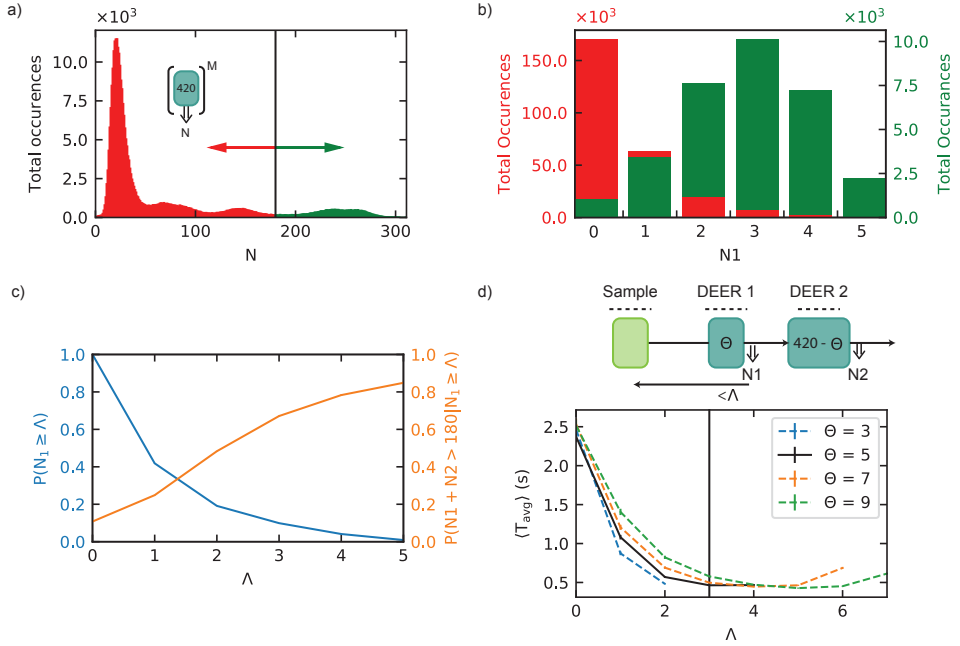
Figure 3.13: **Optimization to increase the experimental rate** a) The distribution of outcomes for $K = 420$ DEER measurements. We define successful (unsuccessful) initializations as $N > 180$ ($N \leq 180$) indicated by the green (red). b) Distribution of outcomes after Θ DEER measurements, where as an example we take $\Theta = 5$. Green (red) bars correspond to the green (red) datasets in (a). c) The probability P(N1 $\geq \Lambda$) to measure an outcome N1 $\geq \Lambda$ after 5 DEER measurements (blue) and the probability P(N1 + N2 > 180|N1 $\geq \Lambda$) to obtain $N > 180$ after 420 DEER measurements, conditioned on having N1 $\geq \Lambda$ in the first 5 DEER measurements. d) The average time ($\langle T_{\text{avg}} \rangle$) to complete one successful run of the method shown on top. A run is successful if N1 + N2 > 180. We calculate $\langle T_{\text{avg}} \rangle$ as a function of Λ for different settings of Θ. We find a factor 5 increase in experimental rate for $\Theta = 5$ and $\Lambda = 3$ compared to no thresholding ($\Lambda = 0$).

ACTIVE OPTICAL RESET

In this section we implement the method devised above to increase the experimental rate. We use photoexcitation[71] to efficiently randomize/reset the P1 center states after failed initialisation attempts. This method results in a fourfold increase of experimental rate. We observe a trade-off for the laser power, with higher laser power decreasing the rate due to spectral diffusion and ionization of the NV[73] and increasing the rate due to resetting the nitrogen nuclear spin and JT configuration of the P1 bath, and find an optimal working point.
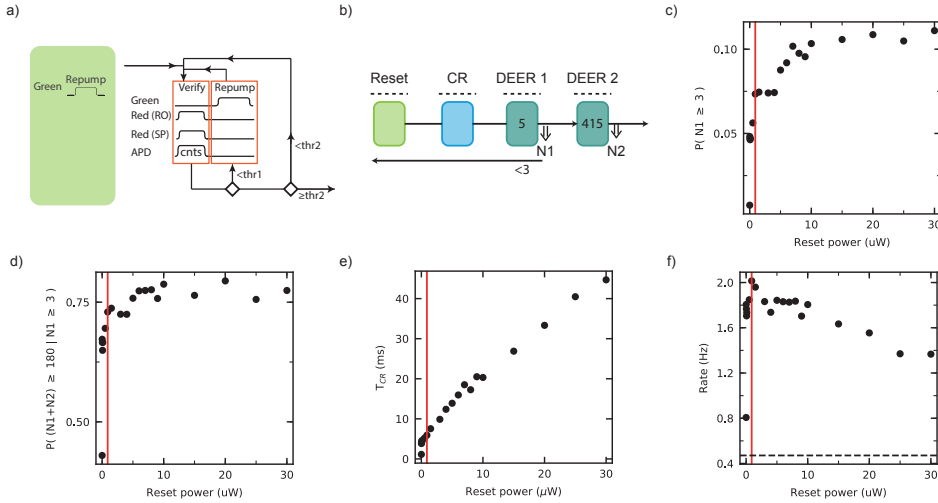
Figure 3.14: **Active optical reset of P1 bath.** a) Illustration of the green (515 nm) optical reset pulse (left). Logical sequence showing the charge and resonance verification (CR) for the NV center (right). We count the number of photons (cnts) while resonantly exciting the NV center simultaneously at its readout (RO) and spin-pump (SP) transitions. If cnts < thr1, the charge state is optically reset (repump, 30 µW). The experimental sequence is continued if cnts ≥ thr2 (thr2 > thr1). If thr1 ≤ cnts < thr2, a new verification step is entered. b) Schematic of the experimental sequence. An initial optical reset is performed (green, 5 µs) to excite the P1 bath [71]. Thereafter, the CR scheme (blue, see (a)) is implemented until the experimental sequence is continued. This scheme is followed by a DEER sequence (K=5, see main text). Based on the outcome of DEER 1 we either continue to DEER 2 (K=415) or go back to the start of the experimental sequence to apply an optical reset pulse. c),d) Plots of the probabilities to pass the desired threshold after DEER 1 and DEER 2, as a function of the optical reset pulse power. e) Average duration of the CR scheme (T_{CR}) as a function of optical reset pulse power. f) Experimental rate given the desired threshold (N1 + N2) ≥ 180. The dashed horizontal line marks the rate without optical reset pulse and without feedback based on the outcome N1. Vertical red lines in c),d),e),f) mark the reset power for maximal experimental rate.

Our experiments require that the NV centre is in the correct negative charge state and that its readout and spin-pump transitions are on resonance with the two 637 nm lasers. This is established by implementing a charge and resonance verification scheme (CR) [65]. Additional to this scheme, we use an optical pulse to reset the P1 center states. Supplementary Figs. 3.14a and b show the experimental sequence where the optical reset pulse is applied at the beginning. The CR scheme is thereafter implemented, followed by a short DEER sequence (DEER 1). At this point, feedback is implemented as the DEER 1 sequence provides information about the configuration of the P1 bath (see Supplementary Fig. 3.13b). Based on the method above, we apply an optical reset pulse if N1 < 3. In Supplementary Figs. 3.14c,d), an increase of the probability of passing the desired thresholds for both DEER 1 and DEER 2 as a function of reset pulse power is shown. This demonstrates the reset pulse to be fully effective at a power of ~10 µW.

We observe an increase of the duration of the CR scheme as a function of reset power (Supplementary Fig. 3.14e), likely due to spectral diffusion caused by photoexcitation of the P1 bath. The trade-off between optical reset and increased CR scheme duration

becomes apparent in Supplementary Fig. 3.14f, where the experimental rate is plotted as a function of optical reset power. The rate initially increases, followed by a decrease as the time required for CR verification becomes dominant. We find over a 4-fold increase of experimental rate at the optimal optical reset power of 0.9 μW. The observed increase in experimental rate here is close to theoretically predicted in the section above.

3.9.7. CORRELATION MEASUREMENTS FOR DIFFERENT JT AXES

In this section we provide the background for the correlation measurement on different JT axes (Fig. 3.2d, main text), and include an analysis of the complete dataset (additional to the selected data in the main text). We derive the expected correlation value C for a signal originating from a number n of P1 centers in such correlation measurements.

First, we define the regions of interest for the measurement outcomes in both JT axes ($N_{|+1,A\rangle}$ and $N_{|+1,D\rangle}$, see Supplementary Fig. 3.15). We fit the peaks in both distributions to Gaussian functions of the form $f = O + \sum_{q=1}^{q_{tot}} A_q \cdot e^{-(N-N_{q,0})^2/2\cdot\sigma_{q,0}^2}$, where N corresponds to either $N_{|+1,A\rangle}$ or $N_{|+1,D\rangle}$ and q_{tot} is either 1 or 3. From these fits (black lines, Fig. 3.15), we obtain the FWHM of each Gaussian, and use these to define the areas of interest as shown in Supplementary Fig. 3.16. Note that these ranges for $N_{|+1,D\rangle}$ ($N_{|+1,A\rangle}$) are also used in experiments described in the main text and supplementary information for initialisation of S1, S2 and S3/S4 in $|+1,D\rangle$ ($|+1,A\rangle$), unless mentioned otherwise.
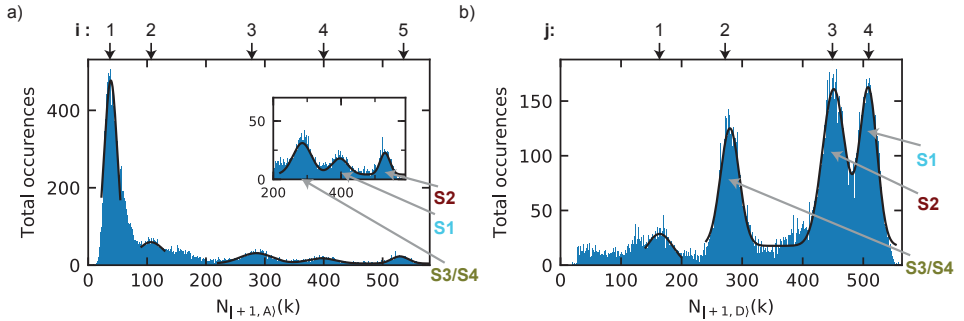
Figure 3.15: **Distributions of total occurrences.** a) All data from the measurement of Fig. 2d in the main text. The histogram shows the total occurrences plotted as a function of outcome $N_{|+1,A\rangle}$ (irrespective of the outcome $N_{|+1,D\rangle}$). The black solid line corresponds to the fit. Numbers corresponding to an index, indicate the center of each fitted Gaussian. Inset: enlarged view of the same histogram indicating S2, S1 and S3/S4. b) Similar to (a), but for measurements on $|+1,D\rangle$. The data in (b) is taken with an increased rate using the active optical reset method described in section 3.9.6, explaining why no peak at low counts is observed.

Second, we define the required probability functions. For outcome $N_{|+1,D\rangle}$, the probabilities for obtaining $N_D^{min} \leq N_{|+1,D\rangle} \leq N_D^{max}$ irrespective of $N_{|+1,A\rangle}$ are given by:

Figure 3.16: **Complete dataset corresponding to the measurement in Fig. 3.2d (main text).** The red rectangular areas illustrate the regions defined by the FWHM as obtained from the fitted curves in Supplementary Fig. 3.15. We denote each area by indices (i, j). The correlation values C corresponding to these areas are shown in Supplementary Table 3.2.

$$P(N_D^{min} \leq N_{|+1,D\rangle} \leq N_D^{max}) = P_D\big|_{min}^{max} = \int_{N_D^{min}}^{N_D^{max}} pdf_D \cdot dN_{|+1,D\rangle}, \tag{3.18}$$

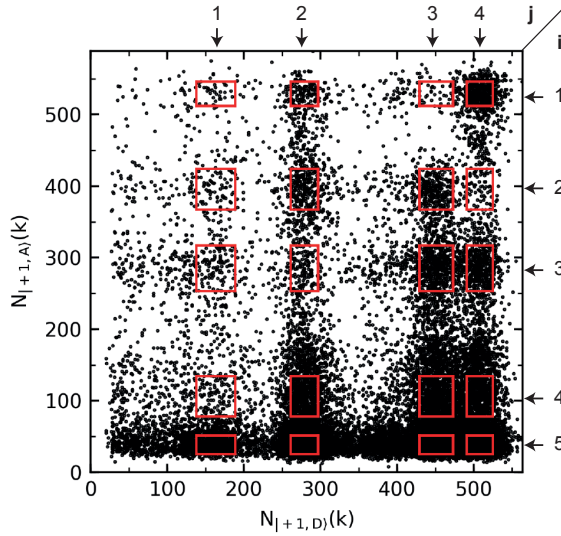and, for outcome $N_A^{min} \leq N_{|+1,A\rangle} \leq N_A^{max}$ irrespective of outcome $N_{|+1,D\rangle}$, this is given as:

$$P(N_A^{min} \leq N_{|+1,A\rangle} \leq N_A^{max}) = P_A\big|_{min}^{max} = \int_{N_A^{min}}^{N_A^{max}} pdf_A \cdot dN_{|+1,A\rangle}. \tag{3.19}$$

pdf_D and pdf_A are probability density functions. We additionally define a conditional probability

$$P((N_A^{min} \leq N_{|+1,A\rangle} \leq N_A^{max})|(N_D^{min} \leq N_{|+1,D\rangle} \leq N_D^{max})) = \overline{P_A}\big|_{min}^{max} = \int_{N_A^{min}}^{N_A^{max}} \overline{pdf_A} \cdot dN_{|+1,A\rangle}$$

$$\tag{3.20}$$

with $\overline{pdf_A}$ the probability density function for outcomes $N_{|+1,A\rangle}$ given $N_D^{min} \leq N_{|+1,D\rangle} \leq N_D^{max}$.

Finally, we derive a bound for the correlation function C. Consider n P1 centers, each of which generates signal within $N_D^{min} \leq N_{|+1,D\rangle} \leq N_D^{max}$ or within $N_A^{min} \leq N_{|+1,A\rangle} \leq N_A^{max}$ if they are in the corresponding state. The correlation C for consecutive measurements then satisfies:

$$C = \frac{\overline{P_A}\big|^{max}_{min}}{P_A\big|^{max}_{min}} \geq \frac{n-1}{n}. \tag{3.21}$$

The inequality in Supplementary Eq. (3.21) is derived as follows. We consider k P1 centers, each with an identical probability p to be in any of the states $|m_I, i\rangle$ (here p is approximately 1/12). We consider two signal regions $N_D^{min} \leq N_{|+1,D\rangle} \leq N_D^{max}$ and $N_A^{min} \leq N_{|+1,A\rangle} \leq N_A^{max}$, and assume that there are n ($n \leq k$) P1 centers with a coupling that results in a signal in those regions. Note that no signal is generated in the respective region if more than one P1 center is simultaneously in the state $|+1,D\rangle$ or $|+1,A\rangle$, as the NV then accumulates a different phase [1].

From the above, it follows that:

$$P_D\big|^{max}_{min} = P_A\big|^{max}_{min} = n \cdot p \cdot (1-p)^{k-1}. \tag{3.22}$$

The observation of a signal in the region $N_D^{min} \leq N_{|+1,D\rangle} \leq N_D^{max}$ means that one of the n spins is in state $|+1,D\rangle$ and thus conditional probability for the second measurement becomes:

$$\overline{P_A}\big|^{max}_{min} = (n-1) \cdot p \cdot (1-p)^{k-2} = \frac{n-1}{n} \cdot \frac{1}{1-p} \cdot P_A\big|^{max}_{min} \geq \frac{n-1}{n} \cdot P_A\big|^{max}_{min}, \tag{3.23}$$

which yields Supplementary Eq. (3.21). In a similar way it follows that $\overline{P_A}\big|^{max}_{min} \geq P_A\big|^{max}_{min} \geq \frac{n-1}{n}P_A\big|^{max}_{min}$, if the signal $N_A^{min} \leq N_{|+1,A\rangle} \leq N_A^{max}$ is generated by m spins that are not necessarily the same as the n spins that generate signal $N_D^{min} \leq N_{|+1,D\rangle} \leq N_D^{max}$.

The values of C obtained for all areas as indicated in Supplementary Fig. 3.16 (red rectangles) are shown in Supplementary Table 3.2. For the areas $(i, j) = (1,3)$ and $(2,4)$ (as in Fig. 2d in the main text) we obtain $C = 0.22(4)$ and $0.40(5)$ respectively, which indicates a single spin. For $(i, j) = (3,4)$ (as in Fig. 2d main text), $C = 0.47(4)$ indicating 1 or 2 spins. For areas such as $(i, j) = (5,1)$, $(5,2)$, $(5,3)$ and $(5,4)$ we find C ≈ 1 indicating a large number of spins n. For these areas one would indeed expect a larger number of spins because they correspond to weaker dipolar coupling to the NV. Interestingly, some areas have a C value that is significantly above unity such as $(1,4)$, $(2,1)$ and $(2,2)$. For the area $(1,4)$ the highest value is observed ($C = 2.2(2)$), this suggests that there might be preferred combinations of $|m_i, i\rangle$ states for S1 and S2.

---

[1] For two P1 centers (out of S1-S4) that simultaneously occupy the same state, summation of coupling strengths and electron spin relaxation play a role for the acquired phase and are discussed in section 3.9.1. Note also that the probability that two or more of the P1s considered here are in the same state simultaneously is small.

i\j	1	2	3	4
1	1.0(2)	1.0(1)	0.22(4)	2.2(2)
2	1.6(2)	1.5(1)	1.20(8)	0.40(5)
3	1.4(1)	0.47(4)	1.14(6)	1.15(6)
4	0.74(7)	1.17(5)	1.0(1)	0.94(4)
5	0.99(4)	0.94(2)	1.00(2)	0.97(2)

Table 3.2

C values for areas as shown in Supplementary Fig. 3.16

3.9.8. EFFECTIVE GYROMAGNETIC RATIO AND SPIN COHERENCE

Here we consider the effect of the electron-nuclear spin mixing due to a relatively large perpendicular hyperfine component ($\gamma_e|\mathbf{B}| \sim A_\perp$) on the expected coherence times. First we calculate the effective gyromagnetic ratios (labelled $\gamma_{n_{\text{eff}}}$ and $\gamma_{e_{\text{eff}}}$) of the two transitions used in the experiments of Fig. 5c, d (main text). We consider the six energy levels of a single P1 center distorted along the JT axis D at the experimental magnetic field, see dashed line Supplementary Fig. 3.17. Subsequently, we investigate the susceptibility of the energy levels to each component (B_i) of the magnetic field vector (**B**). We then determine the tangent of both energy levels connected to the green (blue) double headed arrows at the experimental value of B_i (see Supplementary Fig. 3.17) and calculate $\gamma_{n_{\text{eff}},i}$ ($\gamma_{e_{\text{eff}},i}$) as the difference between two tangents. The green (blue) arrow indicates the transition used in Fig. 5c(d) in the main text. We find $\gamma_{n_{\text{eff}},z}$ ($\gamma_{e_{\text{eff}},z}$) is more than 10 times larger than $\gamma_{n_{\text{eff}},x/y}$ ($\gamma_{e_{\text{eff}},x/y}$), and therefore we will only consider $\gamma_{n_{\text{eff}},z}$ and $\gamma_{e_{\text{eff}},z}$.
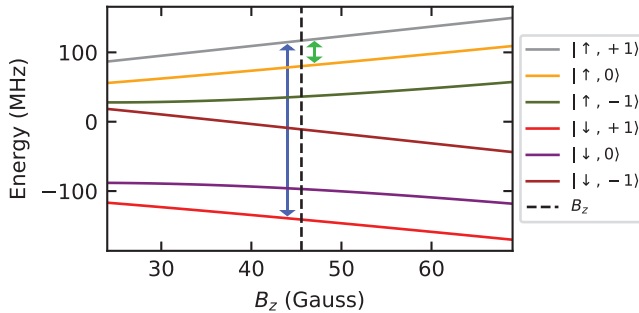
Figure 3.17: **Energy levels for a single P1 center in JT axis D**. Simulation of the six energy levels which are labelled according to their P1 electron and nitrogen nuclear spin state. The black dashed line denotes the experimental magnetic field value. The green (blue) double headed arrow indicates the transition used in the nitrogen (electron) coherence experiments (Fig. 5c,d)

With the approach above, we obtain $\gamma_{n_{\text{eff}},z} = 2\pi \cdot 0.206$ MHz/G ($\sim 700\gamma_n$) and $\gamma_{e_{\text{eff}},z} = 2\pi \cdot 2.60$ MHz/G ($\sim 0.93\gamma_e$). Defining $\Gamma = \gamma_{e_{\text{eff}},z}/\gamma_{n_{\text{eff}},z}$, we find $\Gamma = 12.6$. Thus, based on

the spin mixing, we would expect the nitrogen nuclear spin coherence to be a factor 12.6 larger than the electron spin coherence. For S3/S4, we find a ratio $T_{2N}^*/T_{2e}^* \sim 12$ between the nitrogen nuclear spin and electron coherence (see Supplementary Table 3.3), which agrees well. However, for spin S1 and S2 we find $T_{2N}^*/T_{2e}^* \sim 4$. The remaining discrepancy by a factor 3 is not yet understood.

3.9.9. COHERENCE TIMES OF S3/S4 IN $|+1, \mathrm{D}\rangle$

We use the same experimental sequence as in Fig. 3.5 of the main text to measure the T_1, T_2^* and T_2 of the electron and nitrogen nuclear spin of S3/S4 (see Supplementary Fig. 3.18a). The observed coherence times are presented in Supplementary Table 3.3, where also the coherence times of S1/S2 as measured in the main text are shown for completeness.
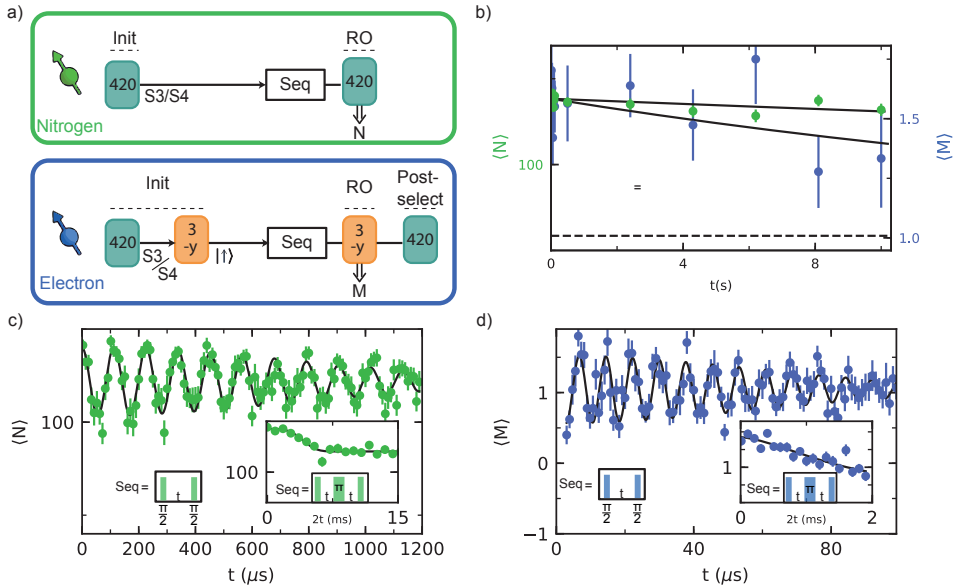
Figure 3.18: **Timescales S3/S4.** (a) Sequence for initialisation of S3/S4 in $|+1, \mathrm{D}\rangle$ (top) and sequence for initialisation of all degrees of freedom of S3/S4 (bottom). These sequences are used in b,c and d. b) Relaxation of a combination of: the nitrogen nuclear spin state, JT axis and charge state (green), and only the electron spin state (blue). We fit (solid lines) both curves to $o + A_0 e^{-t/T}$. c) Ramsey and spin echo (inset) experiments on the nitrogen nuclear spin. d) Ramsey and spin echo (inset) experiments on the electron spin. The obtained coherence times are shown in Supplementary Table 3.3. See Data analysis (section 3.8) for the complete fit functions of the Ramsey (Eq. 11) and spin echo (Eq. 12) experiments presented in this figure.

	S3/S4	S1/S2
$T_{|+1,D\rangle}$	104(38) s	40(4) s
T_{1e}	26(20) s	21(7) s
T_{2e}^*	82(10) μs	50(3) μs
T_{2N}^*	1.06(9) ms	0.201(9) ms
T_{2e}	1.5(1.2) ms	1.00(4) ms
T_{2N}	4.5(4) ms	4.2(2) ms

Table 3.3: Measured coherence and relaxation times of S3/S4 and S1/S2. For experimental data, see Supplementary Fig. 3.18 and main text Fig. 5 respectively.

3.9.10. ENTANGLEMENT SEQUENCE

In this section the entanglement generation sequence for S1 and S2 is explained in detail. We begin by initializing S1 and S2 in $|\Psi\rangle_{\text{init}} = |\uparrow, +1, D\rangle_{S1} |\downarrow, +1, A\rangle_{S2} = |\uparrow\downarrow\rangle$. Next we apply $U_1 = R_x(\pi/2)_{S1} R_x(\pi/2)_{S2}$, consisting of two $\frac{\pi}{2}$ pulses along x to obtain the state:

$$U_1 |\Psi\rangle_{\text{init}} = \frac{1}{2}\big(-i|\uparrow\uparrow\rangle + |\uparrow\downarrow\rangle - |\downarrow\uparrow\rangle - i|\downarrow\downarrow\rangle \big) \tag{3.24}$$

This state evolves for time t and accumulates phase due to dipolar coupling J, as $U_{zz}(t) = e^{-i \cdot J \cdot S_z S_z t}$:

$$U_{zz}U_1 |\Psi\rangle_{\text{init}} = \frac{1}{2}e^{i \cdot J \cdot t/4}\big(-i \cdot e^{-i \cdot J \cdot t/2}|\uparrow\uparrow\rangle + |\uparrow\downarrow\rangle - |\downarrow\uparrow\rangle - i \cdot e^{-i \cdot J \cdot t/2}|\downarrow\downarrow\rangle \big) \tag{3.25}$$

Thereafter, we apply $U_2 = R_x(\pi)_{S1} R_x(\pi)_{S2}$, consisting of two π pulses along X, followed by another free evolution time t:

$$|\Psi\rangle_{\text{final}} = U_{zz}U_2U_{zz}U_1 |\Psi\rangle = \frac{1}{2}e^{i \cdot J \cdot t/2}\big(i \cdot e^{-i \cdot J \cdot t}|\uparrow\uparrow\rangle + |\uparrow\downarrow\rangle - |\downarrow\uparrow\rangle + i \cdot e^{-i \cdot J \cdot t}|\downarrow\downarrow\rangle \big) \tag{3.26}$$

Rewriting $|S2\rangle$ in the X basis, where $|+\rangle = \frac{|\uparrow\rangle + |\downarrow\rangle}{\sqrt{2}}$ and $|-\rangle = \frac{|\uparrow\rangle - |\downarrow\rangle}{\sqrt{2}}$, results in:

$$|\Psi\rangle_{\text{final}} = \frac{1}{2}e^{i \cdot J \cdot t/2}\left[\left(\frac{i \cdot e^{-i \cdot J \cdot t}+1}{\sqrt{2}}\right)|\uparrow +\rangle + \left(\frac{i \cdot e^{-i \cdot J \cdot t}-1}{\sqrt{2}}\right)|\uparrow -\rangle + \left(\frac{i \cdot e^{-i \cdot J \cdot t}-1}{\sqrt{2}}\right)|\downarrow +\rangle + \left(\frac{-i \cdot e^{-i \cdot J \cdot t}-1}{\sqrt{2}}\right)|\downarrow -\rangle \right] \tag{3.27}$$

Note that at time $2t = \frac{\pi}{|J|}$, and a negative coupling J, this yields to the entangled state:

$$|\Psi\rangle_{\text{final}} = -e^{\frac{-i\pi}{4}} \frac{|\uparrow -\rangle + |\downarrow +\rangle}{\sqrt{2}} \tag{3.28}$$

3.9.11. OPTIMIZATION OF INITIALISATION/READOUT

^{14}N AND JT STATE

Here we explain the optimization of single-shot readout and initialisation of the ^{14}N and JT state of individual P1 centers. We define the fidelity of initialisation of S1 in $|+1, D\rangle$ and S2, S3/S4 not in that state as

$$F_{S1} = P(N(k+1) > N_{RO} | N(k) > N_{S1}), \tag{3.29}$$

whereas for a mixture of all other possibilities we define

$$F_{notS1} = P(N(k+1) \leq N_{RO} | N(k) \leq N_{notS1}). \tag{3.30}$$

In both cases $P(X|Y)$ is the probability to obtain X given Y. We define the combined initialisation and readout fidelity of these two cases as:

$$F = \frac{F_{S1} + F_{notS1}}{2}. \tag{3.31}$$

The correlation plot between two subsequent measurements of $K = 820$ binned DEER sequences is shown in Supplementary Fig. 3.19a. First, we find a threshold that separates S1 from other P1 centers by setting $N_{S1} = N_{notS1} = N_{RO}$ all equal to N_{sweep} and calculate the combined initialisation and readout fidelity F while we sweep this parameter. A local maximum $N_{opt} = 477$ is found separating spins S1 and S2 as shown in Supplementary Fig. 3.19b (red dashed line). Second, we set $N_{RO} = N_{notS1} = N_{opt}$ to distinguish between S1 and not S1 and vary N_{S1} as shown in Supplementary Fig. 3.19c. As a trade-off between the success rate and fidelity F we choose $N_{S1} = 522$ to maintain a success probability > 0.2. For Fig. 2f in the main text we have thus used $N_{notS1} = N_{RO} = 477$ and $N_{S1} = 522$.
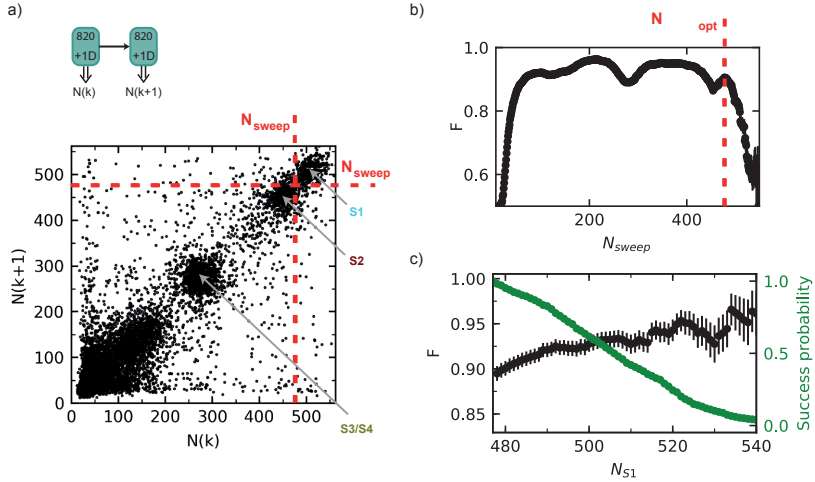
Figure 3.19: **Optimization of combined initialisation and readout of S1 in $|+1, D\rangle$. a)** Full correlation plot for consecutive measurement outcomes $N(k)$ and $N(k+1)$, both for $|+1, D\rangle$ (same dataset as Fig. 2e in the main text). We set the thresholds $N_{S1} = N_{notS1} = N_{RO}$ all equal to N_{sweep} (see main text Fig. 2e). Using these thresholds we calculate F as in Supplementary Eq. (3.31) for different values of N_{sweep}. **b)** Fidelity F as a function of N_{sweep}. The red dashed line indicates a local maximum of F (here $N_{sweep} = N_{opt} = 477$) that optimally separates between S1 and S2 under the given constraints ($N_{S1} = N_{notS1} = N_{RO} = N_{sweep}$). The same value ($N_{sweep} = N_{opt}$) is shown by the red dashed lines in (a). **c)** Further improvement of F at the cost of experimental rate is achieved by a stricter initialisation threshold N_{S1}. First we set $N_{notS1} = N_{RO} = N_{opt}$ and vary N_{S1}. The fidelity F is plotted as function of N_{S1} (black). The success probability of initialisation of S1 in $|+1, D\rangle$ as compared to when $N_{S1} = 477$ is plotted in green as a function of N_{S1}.

Electron spin initialisation and readout

We initialize and measure the electron spin state of P1 centers through a DEER(y) sequence following initialisation of the $|+1,D\rangle$ or $|+1,A\rangle$ state. Again, we use the correlation of consecutive measurements $M(k)$ and $M(k+1)$ to determine the combined initialisation and readout fidelity. First, we define the fidelity of preparing $|\uparrow\rangle$ as

$$F_{|\uparrow\rangle} = P(M(k+1) > M_{RO}|M(k) > M_{|\uparrow\rangle}), \tag{3.32}$$

and the fidelity of preparing $|\downarrow\rangle$ as

$$F_{|\downarrow\rangle} = P(M(k+1) \leq M_{RO}|M(k) \leq M_{|\downarrow\rangle}). \tag{3.33}$$

Again, the combined initialisation and readout fidelity is given as

$$F_{|\uparrow\rangle/|\downarrow\rangle} = \frac{F_{|\uparrow\rangle} + F_{|\downarrow\rangle}}{2}. \tag{3.34}$$
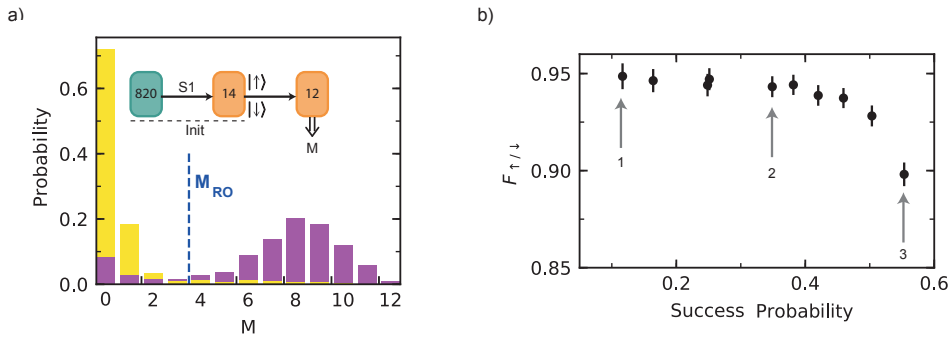

Figure 3.20: **Optimization of combined electron initialisation and readout fidelity.** We trade off fidelity and experimental success rate by setting the thresholds and bin sizes of the DEER(y) sequences used. For optimization, a large range of thresholds and bin sizes are explored. **a)** An exemplary case of probability distributions after initialisation. Here, after preparation of S1 in $|+1,D\rangle$, the electron spin is initialized through a DEER(y) ($L = 14$) with thresholds $M_{|\uparrow\rangle}$ (> 1) and $M_{|\downarrow\rangle}$ (≤ 1) before reading out ($L = 12$). The parameters in this exemplary case ensure a larger success probability (≈ 0.55) but lower $F_{|\uparrow\rangle/|\downarrow\rangle} = 0.90(1)$ as compared to those in Fig. 3d of the main text. **b)** The fidelity $F_{|\uparrow\rangle/|\downarrow\rangle}$ against the success probability of initialisation in $|\uparrow\rangle$. We calculate $F_{|\uparrow\rangle/|\downarrow\rangle}$ for a range of initialisation and readout bin sizes (L) and thresholds $M_{|\downarrow\rangle}$, $M_{|\uparrow\rangle}$ and M_{RO}. Only the maximum fidelities are shown, grouped over 10 intervals between 0.1 and 0.6 success probability. To ensure enough statistics, we only include intervals above 0.1 success probability. Numbered arrows indicate example cases: (1) parameters and probability histogram as shown in Fig. 3d in the main text; (2) $L = 14$ for initialisation, $L = 8$ for readout, $M_{|\uparrow\rangle}$ (> 8), $M_{|\downarrow\rangle}$ (≤ 1) and M_{RO} ($= 2$); (3) corresponds to panel (a).

We calculate $F_{|\uparrow\rangle/|\downarrow\rangle}$ for a large range of initialisation and readout bin sizes (L) and thresholds ($M_{|\downarrow\rangle}$, $M_{|\uparrow\rangle}$ and M_{RO}). In Supplementary Fig. 3.20b maximum values of $F_{|\uparrow\rangle/|\downarrow\rangle}$ are shown as a function of success probability. We trade-off $F_{|\uparrow\rangle/|\downarrow\rangle}$ against success probability to obtain a combined initialisation and readout fidelity of $F_{|\uparrow\rangle/|\downarrow\rangle} = 0.95(1)$ while maintaining a success probability above 0.1.

3

Optimization of sequential initialisation in $|+1, D\rangle$ **and** $|+1, A\rangle$

For entanglement generations of S1 and S2 we optimize for high total initialisation and readout fidelity while maintaining a fast experimental rate. To initialize the P1 centers in the desired $|m_I, i\rangle$ state, we use 4 sequential steps with real time logic. Firstly we use $K = 5$ DEER measurements on $|+1, A\rangle$ to quickly assess the likelihood of S2 in this state. If the outcome is below a threshold ($N_{|+1,A\rangle} = 3$), we apply fast logic: we abort the sequence, apply an optical reset (section 3.9.6) and start again. If the threshold is passed, we continue. Secondly we repeat this on $|+1, D\rangle$ to assess the likelihood of S1 in this state. If successful, we continue with DEER repetitions on $|+1, D\rangle$ and perform a third step after $K = 22$ to distinguish S1 from S3/S4. To finish the initialization of S1, we continue to $K = 820$, required to distinguish S1 from S2. Fourthly, we apply DEER sequences on $|+1, A\rangle$ and hereafter implement fast logic. With S1 initialized in $|+1, D\rangle$, S2 is more easily distinguished from S3/S4. Therefore we perform the logic after $K = 50$ DEER sequences. Because consecutive measurements can disturb earlier prepared states, the small number of repetitions for the initialisation of S2 is beneficial for the overall fidelity. The probability to have both P1 centers in the desired state is small, and this limits the experimental rate. By heralding and the use of subsequent fast logic, we significantly speed up because the initialization of S2 is not attempted if the initialization of S1 fails.

After initialisation of the JT and nitrogen state, we perform electron spin initialisation. For electron spin initialisation and readout we optimize in a similar way as described above. However, we now introduce additional measurements in order to take disturbance due to sequential measurements into account and find a best combined initialisation and readout fidelity for both spins. Finally, we optimize the sequential initialisation (S1 in $|\uparrow\rangle$ then S2 in $|\downarrow\rangle$) for a high rate and fidelity but minimal disturbance of the initialized state of the other P1 center.

3.9.12. NV fluorescence rate reference

In this section, we verify that the discrete jumps in the DEER time traces (Fig. 2a of the main text) are not due to the changes in the detected fluorescence rate of the NV itself (e.g. due to ionization, spatial or spectral drifts). As shown in Supplementary Fig. 3.21, we repeatedly apply the DEER sequence while alternating between opposite readout bases. We combine these measurements to obtain a continuous DEER signal and a reference of the detected NV fluorescence rate. The DEER signal shows discrete jumps. These jumps are not observed in the reference signal, thus excluding that they are caused by changes in the detected NV fluorescence rate.
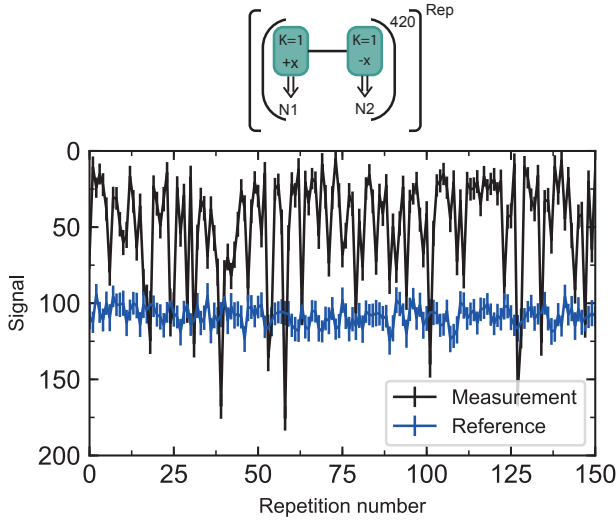
Figure 3.21: **Continuous DEER signal with reference signal.** Top: Experiment in which we alternate between a single DEER sequence (K=1, f_{+1D} as in main text Fig. 2b) with phase $+x$ and one with $-x$ for the final $\pi/2$ pulse. The outcomes N_1 and N_2 are summed in a bin size of 420 to obtain N_{bin1} and N_{bin2}. The reference signal for the NV fluorescence detection rate is defined as $N_{ref} = (N_{bin1} + N_{bin2})/2$. The measurement signal is given as $(2\langle N_{ref}\rangle - N_{bin1} + N_{bin2})/2$, here $\langle N_{ref}\rangle$ is the mean over the full dataset. Bottom: the measurement signal shows similar discrete jumps as in Fig. 2a of the main text, while the reference measurement remains approximately constant over time.

AUTHOR CONTRIBUTIONS

MJD, SJHL and THT devised the project and experiments. CEB, MJD, SJHL and HPB constructed the experimental apparatus. MJD and SJHL performed the experiments. MJD, SJHL, HPB, and THT analysed the data. ALM and MJD performed preliminary experiments. MM and DJT grew the diamond sample. MJD, SJHL and THT wrote the manuscript with input from all authors. THT supervised the project.

REFERENCES

[1] M. J. Degen *et al.*, *Entanglement of dark electron-nuclear spin defects in diamond,* Nature Communications **12**, 3470 (2021).

[2] C. Degen, F. Reinhard and P. Cappellaro, *Quantum sensing,* Reviews of Modern Physics **89**, 035002 (2017).

[3] G. Waldherr *et al.*, *Quantum error correction in a solid-state hybrid spin register,* Nature **506**, 204 (2014).

[4] J. Cramer *et al.*, *Repeated quantum error correction on a continuously encoded qubit by real-time feedback,* Nature Communications **7**, 11526 (2016).

[5] C. Bradley *et al.*, *A Ten-Qubit Solid-State Spin Register with Quantum Memory up to One Minute,* Physical Review X **9**, 031045 (2019).

[6] J. Cai, A. Retzker, F. Jelezko and M. B. Plenio, *A large-scale quantum simulator on a diamond surface at room temperature,* Nature Physics **9**, 168 (2013).

[7] Y. Wang *et al.*, *Quantum Simulation of Helium Hydride Cation in a Solid-State Spin Register,* ACS Nano **9**, 7769 (2015).

[8] H. Bernien *et al.*, *Heralded entanglement between solid-state qubits separated by three metres,* Nature **497**, 86 (2013).

[9] B. Hensen *et al.*, *Loophole-free Bell inequality violation using electron spins separated by 1.3 kilometres,* Nature **526**, 682 (2015).

[10] A. Sipahigil *et al.*, *An integrated diamond nanophotonics platform for quantum-optical networks,* Science **354**, 847 (2016).

[11] D. D. Awschalom, R. Hanson, J. Wrachtrup and B. B. Zhou, *Quantum technologies with optically interfaced solid-state spins,* Nature Photonics **12**, 516 (2018).

[12] M. Atatüre, D. Englund, N. Vamivakas, S.-Y. Lee and J. Wrachtrup, *Material platforms for spin-based photonic quantum technologies,* Nature Reviews Materials **3**, 38 (2018).

[13] S. Castelletto and A. Boretti, *Silicon carbide color centers for quantum applications,* Journal of Physics: Photonics **2**, 022001 (2020).

[14] M. H. Abobeih *et al.*, *One-second coherence for a single electron spin coupled to a multi-qubit nuclear-spin environment,* Nature Communications **9**, 2552 (2018).

[15] D. Sukachev *et al.*, *Silicon-Vacancy Spin Qubit in Diamond: A Quantum Memory Exceeding 10 ms with Single-Shot State Readout,* Physical Review Letters **119**, 223602 (2017).

[16] B. C. Rose *et al.*, *Observation of an environmentally insensitive solid-state spin defect in diamond,* Science **361**, 60 (2018).

[17] R. Nagy *et al.*, *Quantum Properties of Dichroic Silicon Vacancies in Silicon Carbide,* Physical Review Applied **9**, 034022 (2018).

[18] D. Simin *et al.*, *Locking of electron spin coherence above 20 ms in natural silicon carbide,* Physical Review B **95**, 161201 (2017).

[19] N. Bar-Gill, L. M. Pham, A. Jarmola, D. Budker and R. L. Walsworth, *Solid-state electronic spin coherence time approaching one second,* Nature Communications **4**, 1743 (2013).

[20] R. Nagy *et al.*, *High-fidelity spin and optical control of single silicon-vacancy centres in silicon carbide,* Nature Communications **10**, 1954 (2019).

[21] W. F. Koehl, B. B. Buckley, F. J. Heremans, G. Calusine and D. D. Awschalom, *Room temperature coherent control of defect spin qubits in silicon carbide,* Nature **479**, 84 (2011).

[22] S. Maity *et al.*, *Coherent acoustic control of a single silicon vacancy spin in diamond,* Nature Communications **11**, 193 (2020).

[23] B. L. Green *et al.*, *Electronic structure of the neutral silicon-vacancy center in diamond,* Physical Review B **99**, 161112 (2019).

[24] F. Dolde *et al.*, *Room-temperature entanglement between single defect spins in diamond,* Nature Physics **9**, 139 (2013).

[25] F. Dolde *et al.*, *High-fidelity spin entanglement using optimal control,* Nature Communications **5**, 3371 (2014).

[26] S. van Dam, J. Cramer, T. Taminiau and R. Hanson, *Multipartite Entanglement Generation and Contextuality Tests Using Nondestructive Three-Qubit Parity Measurements,* Physical Review Letters **123**, 050401 (2019).

[27] T. Unden, D. Louzon, M. Zwolak, W. Zurek and F. Jelezko, *Revealing the Emergence of Classicality Using Nitrogen-Vacancy Centers,* Physical Review Letters **123**, 140402 (2019).

[28] P.-Y. Hou *et al.*, *Experimental Hamiltonian Learning of an 11-Qubit Solid-State Quantum Spin Register*,* Chinese Physics Letters **36**, 100303 (2019).

[29] V. Vorobyov *et al.*, *Quantum Fourier transform for nanoscale quantum sensing,* npj Quantum Information **7**, 1 (2021).

[30] N. Kalb *et al.*, *Entanglement distillation between solid-state quantum network nodes,* Science **356**, 928 (2017).

[31] X. Xiao and N. Zhao, *Proposal for observing dynamic Jahn–Teller effect by single solid-state defects,* New Journal of Physics **18**, 103022 (2016).

3

[32] A. Cooper, W. K. C. Sun, J.-C. Jaskula and P. Cappellaro, *Environment-assisted Quantum-enhanced Sensing with Electronic Spins in Diamond,* Physical Review Applied **12**, 044047 (2019).

[33] G. Goldstein *et al.*, *Environment-Assisted Precision Measurement,* Physical Review Letters **106**, 140502 (2011).

[34] N. Y. Yao *et al.*, *Scalable architecture for a room temperature solid-state quantum information processor,* Nature Communications **3**, 800 (2012).

[35] Y. Ping, B. W. Lovett, S. C. Benjamin and E. M. Gauger, *Practicality of Spin Chain Wiring in Diamond Quantum Technologies,* Physical Review Letters **110**, 100503 (2013).

[36] N. Y. Yao *et al.*, *Quantum logic between remote quantum registers,* Physical Review A **87**, 022306 (2013).

[37] T. Gaebel *et al.*, *Room-temperature coherent coupling of single spins in diamond,* Nature Physics **2**, 408 (2006).

[38] R. Hanson, F. M. Mendoza, R. J. Epstein and D. D. Awschalom, *Polarization and Readout of Coupled Single Spins in Diamond,* Physical Review Letters **97**, 087601 (2006).

[39] R. Hanson and J. Wrachtrup, Private communication (2020).

[40] A. Dréau, J.-R. Maze, M. Lesik, J.-F. Roch and V. Jacques, *High-resolution spectroscopy of single NV defects coupled with nearby ^{13}C nuclear spins in diamond,* Physical Review B **85**, 134107 (2012).

[41] H. S. Knowles, D. M. Kara and M. Atatüre, *Observing bulk diamond spin coherence in high-purity nanodiamonds,* Nature Materials **13**, 21 (2014).

[42] H. S. Knowles, D. M. Kara and M. Atatüre, *Demonstration of a Coherent Electronic Spin Cluster in Diamond,* Physical Review Letters **117**, 100802 (2016).

[43] C. Belthangady *et al.*, *Dressed-State Resonant Coupling between Bright and Dark Spins in Diamond,* Physical Review Letters **110**, 157601 (2013).

[44] F. Shi *et al.*, *Quantum logic readout and cooling of a single dark electron spin,* Physical Review B **87**, 195414 (2013).

[45] A. Cooper, W. K. C. Sun, J.-C. Jaskula and P. Cappellaro, *Identification and Control of Electron-Nuclear Spin Defects in Diamond,* Physical Review Letters **124**, 083602 (2020).

[46] T. Yamamoto *et al.*, *Strongly coupled diamond spin qubits by molecular nitrogen implantation,* Physical Review B **88**, 201201 (2013).

[47] E. Rosenfeld, L. Pham, M. Lukin and R. Walsworth, *Sensing Coherent Dynamics of Electronic Spin Clusters in Solids,* Physical Review Letters **120**, 243604 (2018).

[48] M. S. Grinolds *et al.*, *Subnanometre resolution in three-dimensional magnetic resonance imaging of individual dark spins,* Nature Nanotechnology **9**, 279 (2014).

[49] W. K. C. Sun, A. Cooper and P. Cappellaro, *Improved entanglement detection with subspace witnesses,* Physical Review A **101**, 012319 (2020).

[50] W. V. Smith, P. P. Sorokin, I. L. Gelles and G. J. Lasher, *Electron-Spin Resonance of Nitrogen Donors in Diamond,* Physical Review **115**, 1546 (1959).

[51] R. Ulbricht *et al.*, *Single substitutional nitrogen defects revealed as electron acceptor states in diamond using ultrafast spectroscopy,* Physical Review B **84**, 165202 (2011).

[52] P. Deák, B. Aradi, M. Kaviani, T. Frauenheim and A. Gali, *Formation of NV centers in diamond: A theoretical study based on calculated transitions and migration of nitrogen and vacancy related defects,* Physical Review B **89**, 075203 (2014).

[53] G. de Lange *et al.*, *Controlling the quantum dynamics of a mesoscopic spin bath in diamond,* Scientific Reports **2**, 382 (2012).

[54] J. H. N. Loubser and J. A. v. Wyk, *Electron spin resonance in the study of diamond,* Reports on Progress in Physics **41**, 1201 (1978).

[55] M. I. Zaritskii and et al., *Spin-lattice relaxation of a jahn-teller nitrogen center in diamond,* Sov. Phys., Solid State **18** (1967).

[56] L. A. Shul'man, M. I. Zaritskii and G. A. Podzyarei, *Reorientation of the jahn- teller distortion in nitrogen impurity centers in diamond,* Sov. Phys., Solid State **8** (1967).

[57] C. A. J. Ammerlaan and E. A. Burgemeister, *Reorientation of Nitrogen in Type-Ib Diamond by Thermal Excitation and Tunneling,* Physical Review Letters **47**, 954 (1981).

[58] R. J. Cook and D. H. Whiffen, *Electron Nuclear Double Resonance Study of a Nitrogen Centre in Diamond,* Proceedings of the Royal Society of London. Series A, Mathematical and Physical Sciences **295**, 99 (1966).

[59] A. Dréau, P. Spinicelli, J. R. Maze, J.-F. Roch and V. Jacques, *Single-Shot Readout of Multiple Nuclear Spin Qubits in Diamond under Ambient Conditions,* Physical Review Letters **110**, 060502 (2013).

[60] G.-Q. Liu *et al.*, *Single-Shot Readout of a Nuclear Spin Weakly Coupled to a Nitrogen-Vacancy Center at Room Temperature,* Physical Review Letters **118**, 150504 (2017).

[61] P. Neumann *et al.*, *Single-Shot Readout of a Single Nuclear Spin,* Science **329**, 542 (2010).

[62] O. Gühne and G. Tóth, *Entanglement detection,* Physics Reports **474**, 1 (2009).

[63] L. Schlipf *et al.*, *A molecular quantum spin network controlled by a single qubit,* Science Advances **3**, e1701116 (2017).

3

[64] A. Reiserer *et al.*, *Robust Quantum-Network Memory Using Decoherence-Protected Subspaces of Nuclear Spins,* Physical Review X **6**, 021040 (2016).

[65] L. Robledo *et al.*, *High-fidelity projective read-out of a solid-state spin quantum register,* Nature **477**, 574 (2011).

[66] J. P. Hadden *et al.*, *Strongly enhanced photon collection from diamond defect centers under microfabricated integrated solid immersion lenses,* Applied Physics Letters **97**, 241901 (2010).

[67] W. Pfaff *et al.*, *Unconditional quantum teleportation between distant solid-state quantum bits,* Science **345**, 532 (2014).

[68] T. K. Yeung, D. Le Sage, L. M. Pham, P. L. Stanwix and R. L. Walsworth, *Anti-reflection coating for nitrogen-vacancy optical measurements in diamond,* Applied Physics Letters **100**, 251111 (2012).

[69] L. M. K. Vandersypen and I. L. Chuang, *NMR techniques for quantum control and computation,* Reviews of Modern Physics **76**, 1037 (2005).

[70] W. S. Warren, *Effects of arbitrary laser or NMR pulse shapes on population inversion and coherence,* The Journal of Chemical Physics **81**, 5437 (1984).

[71] F. J. Heremans, G. D. Fuchs, C. F. Wang, R. Hanson and D. D. Awschalom, *Generation and transport of photoexcited electrons in single-crystal diamond,* Applied Physics Letters **94**, 152102 (2009).

[72] G. de Lange, Z. H. Wang, D. Ristè, V. V. Dobrovitski and R. Hanson, *Universal Dynamical Decoupling of a Single Solid-State Spin from a Spin Bath,* Science **330**, 60 (2010).

[73] L. Robledo, H. Bernien, I. Van Weperen and R. Hanson, *Control and Coherence of the Optical Transition of Single Nitrogen Vacancy Centers in Diamond,* Physical Review Letters **105**, 177403 (2010).

3

4

QUANTUM-NETWORK NODES WITH REAL-TIME NOISE MITIGATION USING SPECTATOR QUBITS

S.J.H. Loenen, Y. Wang, N. Demetriou, C.E. Bradley, M. Markham, D.J. Twitchen, B.M. Terhal, T.H. Taminiau

Quantum networks have the potential to unlock advanced quantum communication and modular quantum computing protocols. Solid-state defects are promising platforms because they simultaneously provide an efficient optical interface for entanglement distribution and a nuclear-spin register to store and process quantum information. The capability to generate quantum states faster than they are lost would enable efficient scaling of quantum networks. Here, we employ additional nuclear spins associated to an NV-center as spectator qubits to mitigate correlated noise induced while running entanglement generation protocols. Upon completion of the protocol, measurements on the spectator qubits reveal information about the phase of the memory qubit. We correct for dephasing in real time. Additional dephasing due to imperfections of the spectator measurements limits the effectiveness of the spectator approach. We bypass this limitation by introducing a gate-based scheme that avoids measurements. Finally, we analyse the impact of spectator qubits for different entanglement generation success probabilities and identify spectator qubits as a promising approach for near-term solid-state testbeds for quantum networks.

4.1. INTRODUCTION

Quantum networks hold promise for a multitude of applications, ranging from secure communication and quantum sensor networks to distributed quantum computation[1–4]. A potential architecture to establish such a quantum network consists of many isolated quantum nodes that each possess a qubit register that provides quantum processing power, quantum memories, and an optical interface to establish entangled links between different nodes[5]. The NV center, like other solid state defect systems in e.g. diamond and silicon carbide[6–9], complies with these requirements. This system provides an electronic spin that can be interfaced with photonic qubits so that entanglement can be established[10,11]. In addition, the defect host material provides long-lived nuclear-spin qubits that can be used as robust quantum memories as well as processing qubits via their interaction with the electronic spin[12].

Following pioneering work on two-node quantum networks in different platforms[11,13–15], currently the largest quantum network able to run quantum protocols, such as entanglement swapping and quantum teleportation, consists of three solid-state defect nodes[6,16]. To efficiently create large networks, it is desirable to faithfully store previously generated entangled states while generating new entangled links. Nuclear-spin qubits provide a robust memory in that respect. However, their decoherence rate under entanglement generation is still larger than the rate at which new entangled states are generated[6], which is captured by an active link efficiency smaller than 1[17]. On the one hand, a substantial amount of work is dedicated to improving the entanglement generation rate by incorporating defects into cavities[7,18–20]. On the other hand, the memory has been made more robust against entanglement generation attempts by reducing the duration of entanglement generation attempts[6], as well as by reducing the effective coupling of the memory to the noise[17,21,22]. This work focuses on an alternative complementary approach to improve the memory decoherence rate, which is based on sensing the noise experienced by the memory qubit during entanglement generation using ancillary qubits referred to as spectator qubits[23–30].

The underpinning idea behind the paradigm of spectator qubits is that ancillary qubits (spectator qubits) are prepared in a state that is sensitive to the noise process of interest. Measurements on these spectator qubits reveal information about the imparted noise. Real-time feed-forward, in combination with knowledge of how noise on the spectators correlates to the noise on the memory qubit, enables to mitigate the loss of quantum information stored in that memory qubit. A difference with respect to using multiple nuclear spins in a decoherence protected subspace, or an error-corrected logical qubit approach, to mitigate correlated noise[21,31], is that the spectator qubit approach investigated here does not require the preparation of nuclear spins in an entangled state. A second advantage, as we will discuss in this work, is that the decision to employ the information accumulated on the spectators can be made after the successful entanglement distribution. This avoids overhead and loss of fidelity in cases where little noise was created. In comparison, decoherence-protected subspaces or error correction require encoding before the entanglement process. Related approaches

with spectator qubits in different settings have previously been introduced for real-time system calibration in trapped-ion qubits[23], monitoring energy injection events in superconducting qubits[24], mid-circuit error correction in hybrid cold atoms arrays[25], and inspired work on photonic spectator modes[26].

In this work, we investigate the spectator qubit approach for its application in a quantum network setting as demonstrated in figure 4.1. We demonstrate that the usage of multiple spectator qubits can extend the coherence time of a quantum memory during a sequence that emulates entanglement generation attempts. We use a thoroughly characterized NV-center system[32] as our quantum node, where the nuclear spin register provides access to a quantum memory and spectator qubits. The NV center's associated electronic spin serves as an optical interface to distribute entanglement over different nodes. During the entanglement generation sequence, the electron undergoes stochastic evolution. Because of the always-on hyperfine coupling to the nuclear spins, this imposes spatially correlated dephasing on the memory and spectator qubits.

We investigate different strategies on how to use the spectator qubits. We demonstrate that the overhead required to extract the spectator information imparts noise onto the system of interest and hence find a trade-off as to when it is beneficial to use spectator qubits. We identify that the readout of the spectator qubit itself is one of these noise sources, and mitigate this by employing a gate-based implementation of the spectator protocol. Based on these results we demonstrate what spectator strategies to use given an entanglement success probability per entanglement generation trial. Additionally, we elaborate on the limitations provided by our system architecture in the framework of spectator qubits and how to improve on them. These results indicate that employing nuclear spins as spectator qubits provides a viable way to extend the memory coherence time when the noise experienced is dominantly spatially correlated.

4.2. BAYESIAN INFERENCE OF THE PHASE

We investigate the spectator qubit approach in the well-characterized NV system described by Abobeih et al[32] where a single electronic spin couples to a register of nuclear spin qubits. The dynamics of nuclear spin "i" is described by

$$H_{n_i} = \omega_l I_z |0\rangle \langle 0|_e + \left[(\omega_l - A_{\|_i}) I_z + A_{\perp_i} I_x \right] |1\rangle \langle 1|_e, \qquad (4.1)$$

where ω_l is the nuclear Larmor frequency, $\{A_\|,\ A_\perp\}$ the hyperfine coupling parameters to the electron spin qubit and $|m_s\rangle_e$ denotes the electron spin state. We implement the experimental sequence of figure 4.1b, where the spectators are initialized in a phase-sensitive state while the memory qubit holds the quantum state of interest. Subsequently, we execute N_{LDE} long-distance entanglement attempts. The stochastic evolution of the electron during these attempts introduces a random walk type of decoherence on the nuclear spin qubits. First we consider the limit where $\frac{A_{\perp_i}}{\omega_l \pm A_{\|_i}} << 1$. In this case, the two electron spin-conditioned nuclear dynamics (see eq. (4.1)) commute and the decoherence is purely described as dephasing. Additionally, the correlation of
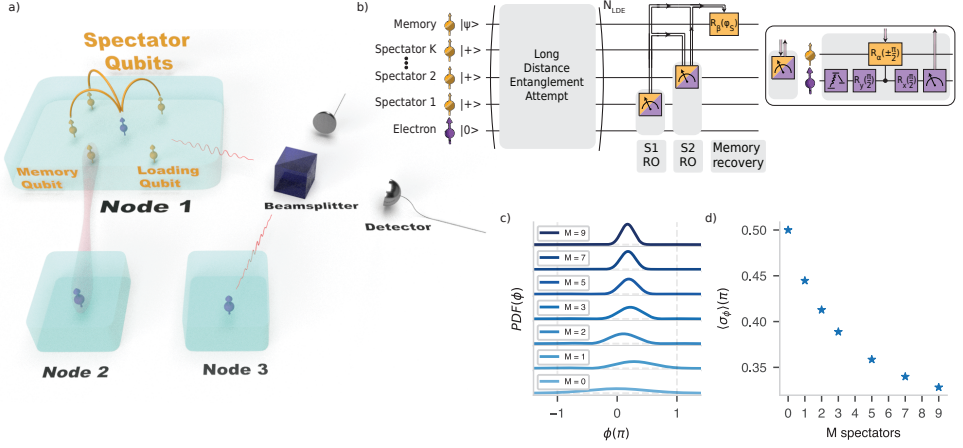
Figure 4.1: **Concept: spectator qubits for network nodes. a)** Schematic of the spectator qubit protocol in a quantum network setting. Blue blocks indicate separate network nodes that each hold a communication qubit (purple) that is used as an optical interface. Ancillary qubits are present (only drawn in node 1) that interact with the communication qubit and can serve different purposes, e.g. as memory, loading or spectator qubits. As an example, we show here a case in which entanglement was generated between the communication qubit of node 1 and node 2. Subsequently, to free up the communication qubit of node 1, the entanglement was swapped to an ancillary qubit that serves as a quantum memory (memory qubit). Spectator qubits are initialized before the entanglement generation between node 1 and node 3 is attempted. The stochastic evolution of the communication spin during these attempts will accumulate a random phase on the state stored in the memory qubit. The spectator qubits serve to "spectate" the evolution of the communication qubit. On node 1, there is a loading qubit that serves to store an entangled state generated between node 1 and 3. **b)** Example sequence of remote entanglement attempts with spectator qubits. The memory qubit holds a quantum state and one or multiple spectator qubits are initialized in a phase-sensitive state. After running N remote entanglement attempts, spectator qubits are optionally measured to obtain information about the evolution of the communication qubit. The spectator readout basis that provides maximum information depends on the readout outcomes of previous spectators. After all desired spectators are measured, we recover the state in the memory qubit. **c)** Exemplary narrowing of the memory qubit phase probability density distribution for a specific readout syndrome of M spectators. The perpendicular hyperfine component ($A_\perp$) is assumed to be zero for all qubits, and the parallel hyperfine component ($A_\parallel$) of all spectators is identical to the memory qubit. For M=0 (blue line), the state of the memory qubit is $\left|\psi\right\rangle = \frac{1}{2}\left[\left|0\right\rangle + e^{-i\phi}\left|1\right\rangle\right]$, with $P(\phi) = \frac{1}{\sigma\sqrt{2\pi}}\exp\left(-\frac{1}{2}\frac{\phi^2}{\sigma^2}\right)$ and $\sigma = \frac{1}{2}\pi$. Each distribution is offset to the others for clarity. In this calculation, gates and measurements are ideal. **d)** Standard deviation of the memory qubit phase distribution averaged over all spectator readout syndromes.

the phase evolution of the nuclear-spin qubits is then set by their parallel hyperfine components $A_\parallel$.

Measurements on the spectator qubits reveal these correlations and facilitate a Bayesian update (see SI section 4.7.2) of the memory qubit's phase distribution according to

$$P(\phi|\mathcal{M}_n) \propto \prod_{i=1}^{n} \frac{1 + (-1)^{m_i}\cos\left(g_i\phi - \theta_i\right)}{2} P_0(\phi). \tag{4.2}$$

Here $P(\varphi|\mathcal{M}_n)$ is the memory qubit phase distribution given a string $\mathcal{M}_n$ of n spectator readout outcomes m_i. $g_i = \frac{A_{\parallel_i}}{A_{\parallel_m}}$ is the ratio of the parallel hyperfine couplings of spectator i ($A_{\parallel_i}$) and the memory qubit ($A_{\parallel_m}$), θ_i denotes the basis in the XY-plane of the Bloch sphere along which spectator i is read out, and $P_0(\phi)$ is the memory qubit phase distribution prior to any spectator measurements. Figure 4.1c exemplifies the narrowing of the memory qubit phase distribution after measuring M spectators, where each spectator is measured in a basis perpendicular to its predicted Bloch vector (SI section 4.7.3), $P(\phi)$ is a normal distribution with $\sigma_\phi = \frac{1}{2}\pi$, $g_i = 1$ and the readout outcome of spectator i is given by $(-1)^{i+1}$. Figure 4.1d demonstrates that for this situation, increasing the number of spectator qubits reduces the standard deviation averaged over all spectator readout syndromes and hence reduces the memory qubit's dephasing.

4.3. SPECTATOR QUBITS IN LONG-DISTANCE ENTANGLEMENT PROTOCOLS

We now apply this approach in an experimental setting where we emulate a sequence of N_{LDE} entanglement attempts after initializing M spectator qubits in the X-basis, as depicted in figure 4.2a, with M=2. The emulated entanglement primitives start with a stochastic optical electron spin re-initialization followed by a microwave (MW) $\frac{\pi}{2}$ pulse. While in actual entanglement protocols a subsequent optical π-pulse follows[6,11,33], we omit this here because of hardware limitations. The entanglement primitive ends with a waiting time t_e that e.g. allows entanglement heralding signals to be received before a subsequent electron re-initialization. To rephase quasi-static fluctuations, we implement a nuclear spin-echo after $\frac{N_{LDE}}{2}$ entanglement attempts.

Upon completion of all attempts, the state of the electron can be transferred to a loading qubit (see figure 4.1a) to free up the electron for subsequent spectator qubit readouts. As we focus on the dephasing process, and do not generate an actual entangled state, the loading qubit is omitted in this work. Therefore, at the end of the emulated entanglement generation sequence, we directly read out K ≤ M spectators sequentially via the electron-spin qubit. Note that we can decide in real-time how many spectators we read out. This allows to only use a spectator at the end of the entanglement generation process if its use improves the ability to preserve the quantum state stored in the memory qubit, which we can calibrate (see discussion below and figure 4.2d). The spectator readout basis is set in real-time based on the measurement syndrome of previously measured spectators, and set perpendicular to the expected Bloch vector of the spectator, see equation (4.2).

The electron-spin state during the re-initialisation process depends on the optical cycling of the electron, where stochastic decays occur from the excited state directly, or through the meta-stable state, to the ground state. In addition, the re-initialisation projects the superposition state created on the electron-spin qubit by the MW pi/2 pulse with respective probabilities to the $|0\rangle_e$ or $|1\rangle_e$ state. Over many attempts, these
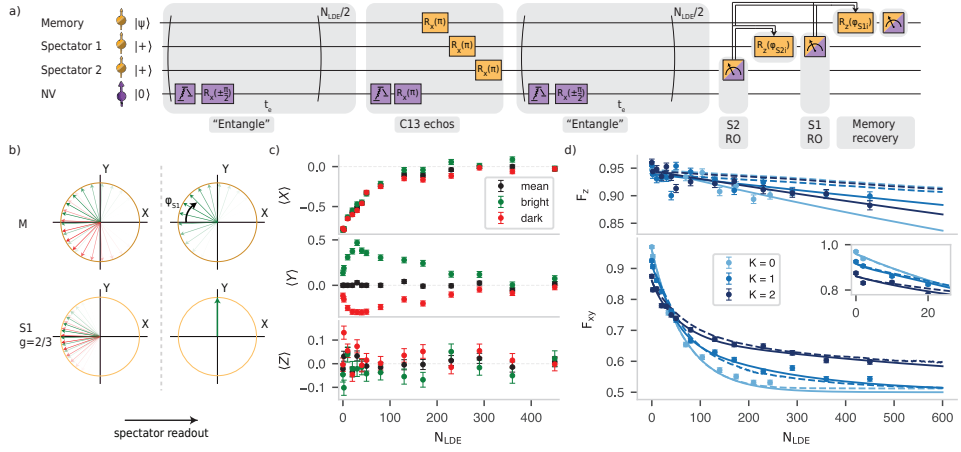
Figure 4.2: **Spectator readout and real-time feed-forward in an entanglement generation setting. a)** Exemplary experimental sequence with $M = 2$ spectator qubits. The memory qubit is prepared in the state $|\psi\rangle$, which is to be protected. All spectator qubits are initialized in the X-basis ($|+\rangle$), which is a phase-sensitive state. The entanglement sequence consists of N_{LDE} entanglement generation attempts ("Entangle") divided into two equal blocks of $\frac{N}{2}$ repetitions separated by nuclear spin echos to rephase quasi-static noise. The re-initialization of the electron is inherently stochastic. Upon completion of N entanglement attempts, K spectators are read out starting with spectator number M (K=M=2 in the sequence shown). To maximize the information gain, the readout basis of each spectator (set by a $R_Z(\phi)$ rotation), is determined in real-time by the combined measurement syndrome of previously read-out spectators (see SI section 4.7.3). **b)** Bloch plane visualisation of spectator method. For illustrative purposes, we use the example case that the spectator qubit's $A_\parallel$ is $\frac{2}{3}$ the one of the memory qubit, such that $g = \frac{2}{3}$ (also, we use $A_\perp = 0$). (left) The phase distributions of the memory qubit (top) and spectator qubit (bottom) are correlated via their electron-nuclear hyperfine couplings, as indicated by the red and green arrows. A subsequent (electron-mediated) readout of the spectator qubit along the Y-axis updates the knowledge about the phase distribution on the memory qubit (top) and projects the spectator qubit (bottom). **c)** Experimental data of the evolution of the memory qubit $\langle X\rangle$, $\langle Y\rangle$ and $\langle Z\rangle$ after running the protocol in (a) with the memory qubit initialized in the $|+X\rangle$ state and a spectator g-factor of 1.49. Data is conditioned on obtaining a bright (green) or dark (red) readout on the first spectator. Initially, correlation during the entanglement attempts increases, but for longer entanglement attempts the correlation reduces due to $g \neq 1$ and non-zero $A_\perp$. **d)** Impact of spectator qubits on the fidelity of the final state after the protocol in (a) with respect to the initial state of the memory qubit. (top) Initial state is $|0\rangle$. (bottom) average over data with initial states in $|+X\rangle$ and $|+Y\rangle$. K indicates the amount of spectators that are initialized and read out (M=K). For low N_{L}DE, the measurement of the spectators impart more dephasing noise on the memory qubit than the amount of dephasing that can be compensated (see inset). For large N, the net effect of spectators is positive. Solid lines are fits and dashed lines are simulations. For a detailed explanation of the fit and simulations, see section 4.7.4 and 4.7.6 respectively.

processes generate dephasing on the nuclear-spin qubits, which is correlated by the nuclear spin hyperfine parameters.

Figure 4.2b graphically depicts the phase-narrowing of the spectator method. In the top left, a phase distribution on the memory qubit is shown. The left bottom shows the correlated phase distribution of the spectator qubit, after the spectator qubit Y-axis is mapped to the electron-spin eigenstate basis (Z-axis) to prepare it for readout. The color coding corresponds to the posterior phase distributions for different measurement

outcomes on the electron spin in the +Z basis. We have set $A_{\parallel S1} = \frac{2}{3} A_{\parallel m}$, with $A_{\parallel m} (A_{\parallel S1})$ the parallel hyperfine component of the memory (spectator) qubit. The perpendicular hyperfine component is set to zero for both qubits. After the electron-spin readout, see right side of figure 4.2b, the electron-spin qubit is in a pure state and the phase distribution on the memory qubit is displaced by ϕ_{S1} and has a smaller standard deviation, which we experimentally illustrate in figure 4.2c and figure 4.2d respectively.

For the data in figure 4.2c, we use two nuclear spins labelled C0 and C1 with respective hyperfine parameters $\{A_{\parallel}, A_{\perp}\}$ given by $\{24.4, 24.8\}$ and $\{-36.3, 26.6\}$ kHz[32]. All data in this chapter is taken with a magnetic field of 404 G along the NV symmetry axis. We execute the sequence in figure 4.2a with C0 as the memory qubit (initialized in $|+X\rangle$, $|+Y\rangle$ or $|0\rangle$) and C1 as spectator 1 (always initialized in $|+X\rangle$) ('Spectator 2' is not used). The dephasing on both qubits is correlated via their hyperfine parameters and increases for increasing N_{LDE} (more stochastic electron evolution). We plot the expectation values $\langle X\rangle$, $\langle Y\rangle$ and $\langle Z\rangle$ of the memory qubit at the end of the sequence. We show data conditioned on a bright or dark readout of the spectator qubit in the -Y basis. We observe that for a bright (dark) readout, the memory qubit is found more towards the +Y (-Y) basis, which demonstrates the correlation between the spectator and memory qubit.

To quantify the corresponding spectator mediated reduction of dephasing on the memory qubit, we consider the memory fidelity corresponding to the remaining coherence (Bloch vector length, BVL), $F_{xyz} = \frac{1}{2}\sqrt{\langle X\rangle^2 + \langle Y\rangle^2 + \langle Z\rangle^2} + \frac{1}{2}$ in figure 4.2d. Here we have included C2 ($\{A_{\parallel}, A_{\perp}\} = \{20.6, 41.5\}$) as spectator 2. Correspondingly, the g-values of the spectator qubits are $|g_{C1}| = 1.49$ and $|g_{C2}| = 0.84$. We calibrate the readout axis $\theta_{i_{\mathcal{M}}}$ of spectator i given a readout syndrome $\mathcal{M}$ on previous spectators, to be perpendicular to the angular expectation value $\langle\theta_i\rangle = \arctan\frac{\langle\sin(\theta_i)\rangle}{\langle\cos(\theta_i)\rangle}$ of spectator i, see SI section 4.7.3.

In the top panel of figure 4.2d, we show the data for using K=M=0,1,2 spectators with the memory qubit initialized in the Z-basis, while in the bottom panel we show the averaged data with the initial states in the X- or Y-basis. Solid lines are a fit through the data that assumes $A_{\perp} = 0$ and usage of only one spectator qubit, see the analysis in SI section 4.7.4. This analysis also confirms that for the memory qubit initialised in the XY-plane, the spectator 2 provides a more significant improvement in memory fidelity because of it's g-value that is closer to 1 than for spectator 1. The spectators do not provide a prolonged storage of memory-qubit states along the Z-axis as the spectator approach implemented here is tailored to dephasing noise. We confirm our understanding by comparing the experimental and fitted data sets with a simulation that models the sequence of figure 4.2a, where the SPAM errors are included based on the fits. See SI section 4.7.6 for a detailed discussion on the simulation.

Importantly, the spectator initialization and readout can be imperfect. On the one hand, this compromises information gain upon a spectator measurement. On the other hand, this can impart additional dephasing on other qubits via crosstalk of the gates involved, as well as via stochastic optical cycling of the electron in the spectator initiali-

sation and readout procedure. Hence, a spectator is only desired if the net information gain outweighs the additional dephasing. While the latter is independent of the amount of entanglement attempts N_{LDE} executed, the former depends on N_{LDE}. Consequently, the optimal strategy related to which spectators to read out depends on N_{LDE}, which is demonstrated in figure 4.2d. For low N_{LDE}, see inset, the strategies involving spectator qubits provide a lower memory fidelity compared not using spectators. We mainly attribute this to additional dephasing induced by the spectator readout (see SI section 4.7.5) and will now discuss a gate-based spectator qubit implementation that bypasses the spectator readout.

4.4. GATE BASED SPECTATOR QUBIT IMPLEMENTATION

Imperfect electron mediated spectator readout reduces the overall spectator qubit performance through two distinct mechanisms. First, a faulty spectator readout outcome leads to an incorrect phase update of the memory qubit, reducing the gain from the spectator qubit. Secondly, stochastic electron spin flips during the readout lead to an additional unknown phase on the nuclear-spin qubits, causing additional dephasing. We bypass these limitations by employing a gate-based, rather than a measurement-based, implementation of the spectator protocol, see figure 4.3a.

We now explain the implementation of this protocol in more detail for our system. After N_{LDE} repetitions of the remote entanglement sequence, we prepare the electron-spin qubit into an eigenstate. Now the goal is to revert the (unknown) phases picked up by all the nuclear-spin qubits. For convenience, we regard the nuclear spins in their respective rotating frames with frequency $f_r = \frac{1}{2}(f_{|0\rangle_e} + f_{|1\rangle_e})$, where the hyperfine parameters determine whether $f_{|0\rangle_e} < f_{|1\rangle_e}$ or $f_{|0\rangle_e} > f_{|1\rangle_e}$. The larger frequency of the two will thus impart a positive phase, while the smaller frequency will impart a negative phase. To achieve the reversal of the nuclear spin phases, we take two steps. First, we implement a spectator-controlled electron bit flip that correlates a $+\frac{\pi}{2}$ ($-\frac{\pi}{2}$) spectator phase with the electron state that induces a negative (positive) phase on that spectator (right panel figure 4.3a). Second, we apply a waiting time δ_t that generates the phase reversal evolution. The efficiency of the phase reversal depends on correctly timing δ_t (see figure 4.3b). A too long δ_t overcompensates the obtained unknown nuclear-spin qubit phase and therefore effectively imparts additional dephasing.

We experimentally demonstrate this in figure 4.3c, where we plot the BVL for different δ_t. δ_t corresponding to the first maximum of the BVL and is set by the stochastic phase acquisition during entanglement generation attempts. Timings of subsequent maxima, which are possible because of the 2π periodicity of the phase, depend on the specific hyperfine couplings of individual nuclear spins (spectators as well as memory qubit). Therefore, only at the first maxima all nuclear spins simultaneously experience the optimal phase reversal. More entanglement attempts (N_{LDE}) will induce more stochastic dephasing and correspondingly require a longer waiting time to achieve optimal phase reversal. This is illustrated by figure 4.3d, where the optimal waiting time

($\delta_{t,opt}$) is plotted against the number of entanglement generation attempts. For each N_{LDE}, a dataset such as in figure 4.3c is obtained from which $\delta_{t,opt}$ is extracted through a sinusoidal fit.
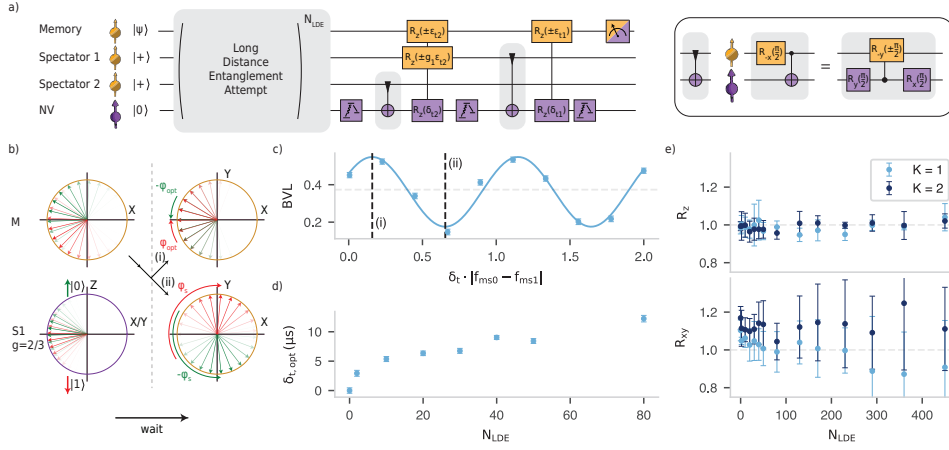

Figure 4.3: **Gate-based spectator implementation a)** Experimental sequence of gate-based spectator scheme. Before memory retrieval, the state of a spectator qubit is mapped to the electron and a waiting time is applied that implements an electron-controlled $R_Z(\theta)$ operation on the nuclear spin qubits (see SI section 4.7.7 for the $R_Z(\theta)$ rotation). Since the electron state is correlated with the nuclear spin qubits, the electron-controlled $R_Z(\theta)$ partially rephases those nuclear spins if correctly timed, see (b). The use of multiple spins provides an accumulated rephasing. **b)** (left) The state of the memory qubit correlates with the spectator qubit state that has been mapped to the electron eigenstates. The leading (retarded) part of the spectator phase distribution (red (green)) is mapped to the electron state that gives a smaller (larger) spectator precession frequency. (right) A subsequent waiting time rotates the phase distributions to overlap and hence partially rephases the nuclear phase distributions (top). Incorrectly timing the waiting overrotates the distributions and dephases the nuclear phase distributions (bottom). **c)** Implementation of the sequence in (a), with N=30 and C0 as the memory qubit and C1 as the spectator qubit, where the waiting time after the nuclear-conditioned electron rotation is swept. The memory qubit Bloch vector length as a function of the waiting time. The waiting time is normalized over the difference in electron-state dependent precession frequencies of the memory qubit, which is the frequency with which the green and red distribution in (b) evolve relative to each other. Timing the waiting time correctly (i) allows to compensate correlated dephasing, while waiting suboptimally (ii) introduces additionally dephasing. **d)** The optimal waiting time as a function of the number of entanglement attempts. **e)** Quantification of the improvement of the gate-based implementation over the measurement-based implementation. Using the same qubits as in figure 4.2, the scheme in figure 4.2a and 4.3a is executed for different implementations of these qubits (acting as spectators or memory qubit). Averaged over these implementations, we plot the ratio of the memory qubit Bloch vector length for the memory qubit initialized in $|0\rangle$ (R_z top) and averaged over $|+X\rangle$ and $|+Y\rangle$ (R_{xy}). No effect is observed in the R_z, while a considerable effect is observed in R_{xy}, confirming the dephasing noise introduced by the spectator readout.

We now implement the gate-based approach in the sequence of figure 4.3, where we have calibrated δ_{t2} and δ_{t1} for both spectators and compare this to the measurement based implementation of figure 4.2. We make the comparison between the two approaches by implementing the two schemes for different settings of C0, C1 and C2 (memory or spectator qubits). For each setting, we measure the ratio R of the gate-based BVL over the measurement-based BVL after N_{LDE} entanglement generation sequences

and with K spectator qubits in figure 4.3d. Subsequently, for different initial states of the memory qubit, we take the average R obtained over the different settings and plot the standard deviation as the uncertainty. In the top panel R_z is plotted when the memory qubit is initialized in the Z-basis, while in the bottom panel R_{xy} is shown as the average over the data with the memory qubit initialized in the X- and Y-basis. R_z remains close to 1, while (specifically at low N_{LDE}) R_{xy} is considerably larger than 1. This confirms that that the spectator readout introduces dephasing and that the gate-based implementation provides an improvement over the measurement-based approach.

Importantly, the gate-based implementation simultaneously reverts dephasing induced by the entanglement generation attempts on all nuclear spin qubits in a way that correlates to the phase the spectator qubit obtained. As a result, nuclear spins that did not acquire a dephasing that was correlated to the spectator qubit (e.g. the loading qubit of figure 4.1a) will experience dephasing during the waiting time δ_t. A decoupling pulse at $\frac{1}{2}\delta_t$ on these nuclear spins can however decouple from this dephasing. Note that, unlike other applications of spectator qubits[23–26], here two-qubit interactions between the spectator/memory qubits and the source of dephasing (the electron-spin qubit) are naturally present. This enables replacing the measurement based scheme in combination with classical feed-forward, with a gate-based scheme. Combined, these findings make the use of a gate-based spectator scheme in practical entanglement generation experiments using solid-state defects interesting.

4.5. SPECTATOR MEDIATED MEMORY FIDELITY FOR DIFFERENT ENTANGLEMENT SUCCESS PROBABILITIES

In the previous sections, we analyzed the impact of spectator qubits as a function of N_{LDE} entanglement generation sequences. Such an entanglement generation attempt is probabilistic, and for a probability p to successfully generate entanglement, the likelihood to successfully generate entanglement at attempt N_{LDE} is given by $P(N_{LDE}) = (1-p)^{N_{LDE}-1} \cdot p$. We now analyze the use of spectator qubits as a function of p by considering what the expected fidelity ($\overline{F}$) of the memory qubit is with respect to its initial state prior to the entanglement generation sequence. We calculate the expected fidelity by weighing the memory fidelity F_{xyz} at attempt N_{LDE} with $P(N_{LDE})$.

In figure 4.4, we investigate and execute the gate-based implementation with the spectator and memory qubits identical to the ones used for figure 4.3. We consider the situation where, after completion of N_{LDE} entanglement sequences, we use the phase-information contained in each spectator that was initialized and analyse the cases with 0, 1 or 2 spectators initialised. Figure 4.4a shows the memory fidelity F_{xyz} averaged over datasets with the memory qubit initialized in the X-, Y- and Z-basis. In addition, we have analyzed datasets with the memory qubit initialized in the -Z-basis, which showed no significant difference from data with the memory qubit initialized in the +Z-basis. We fit the data using the fit-function for a single spectator (see SI section 4.7.4), where we fit the SPAM error such that the fit overlaps with the data at $N_{LDE} = 0$.
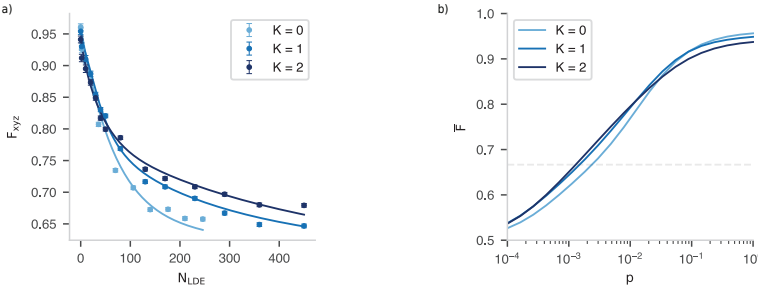
Using these fits, we calculate $\overline{F}$.

Figure 4.4: **Memory fidelity** F_{xyz} **for different entanglement generation success probabilities using spectator qubits. a)** Memory fidelity F_{xyz} after N_{LDE} entanglement generation attempts in the gate-based implementation using K spectators, averaged over the memory initial states $|0\rangle$, $|+X\rangle$ and $|+Y\rangle$. **b)** Using the fits (solid lines in a, see SI section 4.7.4), we extract the expected average fidelity ($\overline{F}$) for different number of K spectators used, weighted over the expected distribution of the required entanglement attempts until success, given an entanglement success probability p.

For low p, there is a relatively high likelihood to generate entanglement at large N_{LDE}, where using spectators considerably outperforms not using spectators. This explains the regime in figure 4.4b where using spectators (K$\neq$0) outperforms using no spectators. On the contrary, for p $\approx$ 1, low numbers of N_{LDE}, where little correlated noise is built up, dominate $\overline{F}$. Therefore, at low N_{LDE}, using spectators is not expected to provide a significant improvement over not using spectators. This is reflected by $\overline{F}$ that is slightly lower for K>0 than for K=0, likely because of a (small) overhead associated with the gate-based scheme.

A further optimisation strategy is to decide in real time, for each spectator and based on N_{LDE} for taht instance, to use the information contained or not, e.g. to apply the measurement- or gate-based scheme. As the spectator qubit initialisation comes at little costs (see SI figure 4.7), an optimal strategy could be to always initialise multiple spectators and only use certain spectators if entanglement is generated after a certain amount of entanglement sequence repetitions. This also allows to use qubits with relatively poor fidelities, which might not be suitable to serve other purposes, as we can always decide not to use them in case they are not expected to ameliorate memory qubit fidelity. For follow-up work in the context of figure 4.4, we will consider the case where we make real-time decisions on which spectator qubit to use.

4.6. CONCLUSION AND OUTLOOK

Using an NV center in diamond in the context of entanglement generation in a quantum network setting, we have demonstrated a method based on correlated noise sensing using spectator qubits to complement the toolbox of memory lifetime extension under repeated entanglement generation. Measurements performed on the spectator qubits

reveal partial information of the noise imposed on the memory qubit, and we can use this information in real-time to partially compensate for the memory qubit dephasing. The results however also demonstrated that the measurement of a spectator qubit imparts additional noise on the memory qubit while the initialisation of multiple spectators was not associated with much additional memory qubit dephasing. As the decision on whether or not to read out a spectator qubit can be made in real-time, it can be beneficial to always initialise a spectator, but only read it out if enough correlated noise is built up.

The correlated noise in the NV-center network configuration considered here predominantly originates from the electron spin. The intrinsically available two-qubit gate between the nuclear spectator qubits and the electron spin enabled a gate-based implementation of the spectator protocol. Here, we perform a spectator-controlled electron rotation and, instead of an optical electron readout, we apply a carefully chosen wait time that partially rephases the memory and remaining spectator qubits via an electron-controlled phase gate. This avoids the electron-mediated readout and corresponding additional dephasing on the memory qubit. We showed that, specifically at low number of entanglement attempts, the gate-based scheme outperformed the measurement-based scheme.

Finally, for the NV under investigation and the entanglement protocol in figure 4.2 and 4.3, we identified in what regime of entanglement generation success probabilities different spectator qubit strategies could provide an advantage over only using a memory qubit. We limited the considered strategies to ones where all initialised spectators are used. Future work will include strategies where real-time decisions are made whether or not to use a spectator qubit. Besides, we will run simulations at high magnetic fields, where the role of the parallel hyperfine coupling $A_\perp$, is expected to be negligible which likely increases the degree of correlation between the spectator qubit and memory qubit phase. Lastly, we will also consider entanglement generation sequences that include an electron pi-pulse at half the waiting time of each entanglement generation attempt.

4.7. SUPPLEMENTARY INFORMATION

4.7.1. CORRELATION OF NUCLEAR SPIN EVOLUTION

In this section, we demonstrate that for zero $A_\perp$ and the electron spin as the only fluctuator, the memory and spectator qubit evolutions are completely correlated by their parallel hyperfine component $A_\parallel$. Following equation (4.1), we can write the evolution Hamiltonian of nuclear spin i in the case the electron is in $|0\rangle$ and $|1\rangle$:

$$H_{0_i} = \omega_l I_z \tag{4.3}$$
$$H_{1_i} = (\omega_l + A_{\parallel_i})I_z + A_{\perp_i}I_x. \tag{4.4}$$

For stochastic electron evolution events, nuclear spin i experiences H_{0_i} and H_{0_i} back to back for random times. For M stochastic electron spin states, where the time the electron spends in each state is random, the total nuclear spin evolution equals

$$U_i(T) = \prod_j^M \exp\left\{\left(-iH_{\alpha_{M-j_i}}t_j\right)\right\}, \tag{4.5}$$

where $\alpha_{M-j} \in \{0,1\}$ and $\sum t_j = T$. If $A_\perp = 0$, then H_{0_i} and H_{1_i} commute. Therefore, following the Baker-Campbell-Hausdorff lemma, we can express as

$$U_i(T) = \exp\left\{(-i[\omega_l T + A_{\parallel_i}T_1]I_z)\right\}, \tag{4.6}$$

where $T_1 \leq T$ is the total time the electron spent in the $|1\rangle$ state. The time ordering of when the electron is in state $|0\rangle$ and $|1\rangle$ is thus not important. From this equation we see that for two nuclear spins which only differ by their $A_\parallel$, the phase of two nuclear spins is completely correlated. Namely, relative to $\omega_l T$, if the phase of nuclear spin 1 is given by $\phi_1 = A_{\parallel_1}$, then the phase of nuclear spin 2 equals $\frac{A_{\parallel_2}}{A_{\parallel_1}}\phi_1$.

In case $A_\perp \neq 0$, then H_{0_i} and H_{1_i} do not commute and the time ordering of when the electron is in the state $|0\rangle$ and the state $|1\rangle$ thus matters. Therefore, we cannot generally write equation (4.5) in a simple form as equation (4.6) and express a simple general relation between the evolution of different nuclear spins. For high magnetic fields however, the precession axis of H_{0_i} and H_{1_i} asymptotically overlap and hence equation (4.6) is retrieved. In our experiments the typical $A_\perp \approx 20$ kHz which for our magnetic field of ~403 Gauss gives a small tilt of the precession axis of ~2.7 degrees. The simulations in figure 4.2d, that include non-zero $A_\perp$ have been repeated with $A_\perp = 0$ and little difference was observed, confirming that in our experiments $A_\perp$ is not substantially deteriorating the effectiveness of the spectator qubit approach.

4.7.2. BAYESIAN INFERENCE

According to Bayes' theorem[34], a the posterior probability density distribution $P(H|E)$ of a parameter H given that a evidence m has been observed, is given by

$$P(H|m) = \frac{P(m|H) \cdot P(H)}{P(m)}, \tag{4.7}$$

where $P(m|H)$ the probability to obtain evidence m given a parameter H, $P(H)$ is the prior probability density function and $P(m) = \int P(m|H)P(H)dH$.

For a quantum state given by $|\psi\rangle = \frac{1}{\sqrt{2}}\left(|0\rangle + \exp(ig\phi)\right)$, a measurement in a basis θ in the XY-plane obtains an outcome $m = \pm 1$ with probability $\frac{1}{2} + (-1)^m \cos(g\phi - \theta)$. By induction, for n spectators, this gives equation (4.2).

4.7.3. Spectator readout basis and phase compensation

Dephasing is optimally mitigated if the uncertainty of the memory qubit phase probability density function (PDF) $P(\theta)$ is minimized. The uncertainty over a cyclic variable is described by the Holevo phase variance[35,36]:

$$V[P(\theta)] = S[P(\theta)]^{-2} - 1 \equiv \left|\int e^{i\theta} P(\theta)d\theta\right|^{-2} - 1, \tag{4.8}$$

with $S[P(\theta)] \in [0,1]$ the *sharpness* parameter. One can show that for a small phase variance $V[P(\theta)] \approx \langle(\theta - \langle\theta\rangle)^2\rangle$, being the usual variance for a non-cyclic parameter[36]. The optimal readout phase ϕ_m of the m'th spectator is the one that, given a prior distribution defined by previous measurement outcomes $x[m-1]$, maximizes the sharpness parameter of the posterior PDF averaged over the possible readout outcomes x_m:

$$\phi_m^{\text{opt}} = \underset{\phi_m}{\arg\max}\left\{S_{posterior}(\phi_m)\right\} = \underset{\phi_m}{\arg\max}\left\{\sum_{x_m=0,1} P_{\phi_m}(x_m|x[m-1]) \cdot S[P_{\phi_m}(\theta|x[m])]\right\}. \tag{4.9}$$

Here $P_{\phi_m}(x_m|x[m-1])$ is the probability of obtaining measurement outcome x_m on the m'th measurement in a readout basis defined by ϕ_m given a measurement outcome $x[m-1]$ of previous measurements in bases defined by $\{\phi_1,...,\phi_{m-1}\}$, which we assume to be fixed. $P_{\phi_m}(\theta|x[m])$ is the PDF of θ conditioned on measurement outcomes $x[m]$. Using Bayes rule and the conditional probability identity $P(C|AB) = P(CB|A)/P(B|A)$ we write[35]

$$\begin{aligned} P_{\phi_m}(\theta|x[m]) &= \frac{P(\theta|x[m-1]) \cdot P_{\phi_m}(x_m|\theta, x[m-1])}{P_{\phi_m}(x_m|x[m-1])} \\ &= \frac{P(\theta|x[m-1]) \cdot P_{\phi_m}(x[m]|\theta)}{P_{\phi_m}(x_m|x[m-1]) \cdot P(x[m-1]|\theta)}. \end{aligned} \tag{4.10}$$

Inserting equation (4.10) into equation (4.9) leads to:

$$\phi_m^{\text{opt}} = \underset{\phi_m}{\arg\max} \sum_{x_m=0,1} \left|\int e^{i\theta} \frac{P(\theta|x[m-1]) \cdot P_{\phi_m}(x[m]|\theta)}{P(x[m-1]|\theta)} d\theta\right|. \tag{4.11}$$

Given a set of measurement bases $\phi = \{\phi_i\}$ and a state with angle θ, the measurement results of each measurement are independent and hence

$$P_{\phi_m}(x[m]|\theta) = \prod_{i=1}^{m} P_{\phi_i}(x_i|\theta) = \prod_{i=1}^{m} \cos^2\left(\frac{\theta - \phi_i}{2} + x_i \frac{\pi}{2}\right),$$ (4.12)

where the measurement result x_i is either 0 or 1. Similarly equation (4.12) holds up for $P(x[m-1]|\theta)$ and hence equation (4.11) reduces to

$$\phi_m^{\text{opt}} = \underset{\phi_m}{\arg\max} \left\{ S_{posterior}(\phi_m) \right\}$$

$$= \underset{\phi_m}{\arg\max} \left\{ \sum_{x_m=0,1} \left| \int e^{i\theta} \cdot P(\theta|x[m-1]) \cdot \cos^2\left(\frac{\theta - \phi_m}{2} + x_m \frac{\pi}{2}\right) d\theta \right| \right\}.$$ (4.13)

If $P(\theta)$ is a normal distribution with a expectation value $\langle\theta\rangle = \arctan\frac{\langle\sin\theta\rangle}{\langle\cos\theta\rangle} = \arctan\frac{\langle Y\rangle}{\langle X\rangle}$, then $\phi_m^{\text{opt}} = \langle\theta\rangle \pm \frac{\pi}{2}$. The stochastic electron spin evolution during the entanglement attempts imparts a random walk-like correlated evolution on the nuclear spins where the step-size is related to the electron reinitialisation dynamics (SI figure 4.10). For large numbers of entanglement attempts, the central limit theorem provides a normally distributed nuclear phase probability density function. For the first spectator qubit, this justifies the choice of a readout basis perpendicular to the Bloch vector angle. We also use this strategy for spectator $M > 1$, which according to equation (4.13) is not necessarily optimal. However, for the second spectator, the difference in sharpness parameter between the most optimal readout basis and a readout bases set by $\langle\theta\rangle + \frac{\pi}{2}$ is minor. This is illustrated in figure 4.5 where the initial PDF is a normal distribution with $\sigma = 1$.

Having obtained a measurement result, the real-time feedback allows to apply a phase rotation ϕ_c on the memory qubit and on the other spectator qubits. We want to choose ϕ_c to optimally recover the memory qubit state, which we express by its fidelity with respect to the X-axis ($\theta = 0$). A single spectator measurement gives two measurement outcome-dependent PDFs on which an independent phase rotation can be applied. Hence the fidelity we target to maximize is described as

$$F(\{\phi_{c_i}\}) = P_{\phi_m}(0) \int_{-\infty}^{\infty} \frac{1}{2} \left[1 + \cos(\theta)\right] \cdot P_{\phi_m}(\theta - \phi_{c_0}|0) d\theta$$

$$+ P_{\phi_m}(1) \int_{-\infty}^{\infty} \frac{1}{2} \left[1 + \cos(\theta)\right] \cdot P_{\phi_m}(\theta - \phi_{c_1}|1) d\theta,$$ (4.14)

where $P_{\phi_m}(\theta|i)$ is the posterior PDF of $P(\theta)$ after performing a measurement along basis ϕ_m and obtaining measurement outcome "i". $P_{\phi_m}(i)$ is the probability to obtain measurement outcome "i" and ϕ_{c_i} is the corresponding phase rotation. Using Bayes' theorem (see section 4.7.2) we can write

$$P_{\phi_m}(\theta|i) = \frac{\frac{1}{2}\left[1 + \cos(\theta - \phi_m + i\pi)\right] \cdot P(\theta)}{P_{\phi_m}(i)},$$ (4.15)
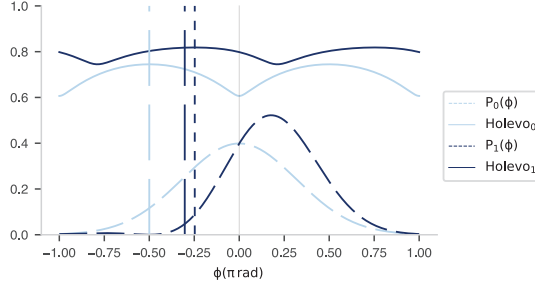
Figure 4.5: **Optimal spectator readout angle.** Dashed curves correspond to phase PDFs $P(\phi)$ and the solid lines correspond to $S_{posterior}(\phi)$. Large-dashed vertical lines indicate $\langle\phi\rangle + \frac{\phi}{2}$ (see below equation (4.13)). The small-dashed vertical line indicates ϕ_m^{opt}. The underlying PDFs are $P(\phi) = \frac{1}{\sqrt{2\pi}\sigma} e^{-\frac{\phi^2}{2\sigma^2}}$ (light blue) and the posterior PDF after a measurement in a basis $\langle\phi\rangle + \frac{\phi}{2}$ (see equation (4.2), given by $P(\phi) = \frac{1}{\sqrt{2\pi}\sigma} e^{-\frac{\phi^2}{2\sigma^2}} \cdot (1 + \cos(\phi - \frac{\pi}{2}))$ (dark blue). In the data shown here $\sigma = 1$. For the light blue data, the dashed and dotted line overlap. For the dark blue data, the readout perpendicular to $\langle\phi\rangle$ is sub-optimal, but the decrease in the sharpness parameter $S_{posterior}(\phi)$ is minor.

and hence for a chosen ϕ_m the most optimal set $\{\phi_{c_i}^{\text{opt}}\}$ of phase compensation angles is given by

$$
\phi_{c_i}^{\text{opt}} = \underset{\phi_{c_i}}{\arg\max}\left\{F(\{\phi_{c_i}\})\right\}
$$

$$
= \underset{\phi_{c_i}}{\arg\max}\left\{\sum_i \int_{-\infty}^{\infty} \frac{1}{2}\left[1 + \cos(\theta)\right] \cdot \frac{1}{2}\left[1 + \cos(\theta - \phi_{c_i} - \phi_m + i\pi)\right] \cdot P(\theta - \phi_{c_i})\, d\theta\right\}.
$$

(4.16)

For a symmetric phase PDF $P(\theta)$ it holds that $\phi_{c_1} = -\phi_{c_0}$. Considering a normal phase PDF $P(\theta)$ and an optimal readout angle $\phi_m = \frac{\pi}{2}$, equation (4.16) gives $\phi_{c_0} = \arctan\left(-e^{-\frac{\sigma^2}{2}}\sinh(\sigma^2)\right)$, with σ the standard deviation of the normal distribution.

4.7.4. SINGLE SPECTATOR EFFECT: ANALYTICAL EXPRESSIONS

In this section we will derive an analytical expression for the memory qubit fidelity upon using a single spectator after running N_{LDE} entanglement sequences as given in figure 4.2a. We will assume that both the memory and spectator qubit have zero $A_\perp$ and their parallel hyperfine components are related by $g = \frac{A_{\parallel,s}}{A_{\parallel,m}}$. Additionally, we assume perfect gates and instantaneous electron reinitialisation. Correspondingly, the only source of dephasing is given by the projection of the electron-spin qubit to the $|0\rangle$ or $|1\rangle$ state after each entanglement attempt with respective probabilities p_0 and $p_1 = 1 - p_0$. Here we will use $p_0 = \frac{1}{2}$, which corresponds to a $\frac{\pi}{2}$ pulse to generate an electron-spin superposition state at the start of the entenglement sequence.

Generally, the fidelity of a quantum state in the XY-plane with a phase probability density $P(\phi)$ is given by

$$F_\theta = \int_{-\infty}^{\infty} \frac{1}{2} \left[1 + \cos(\phi - \theta) \right] P(\phi) \, d\phi, \tag{4.17}$$

where θ defines the angle in the XY plane along which the fidelity is measured. In the following, we target to determine $P(\phi)$ and θ_c, the optimal angle along which to measure the fidelity. We will start with with $P(\phi)$ and consider each nuclear-spin qubit in their respective rotating frames with the respective frequency being the average of the two electron-spin-dependent frequencies ($f = \frac{1}{2}(f_{m_s=0} + f_{m_s=1})$). Following the assumptions above, the nuclear-spin qubits pick up a phase $\pm \frac{1}{2} A_\parallel t_e$ at each entanglement attempt, such that after N (here N=N$_{LDE}$) entanglement attempts the phase distribution is given by:

$$P(\phi, N) = \sum_{M=0}^{N} \frac{1}{2^M} \frac{N!}{M!(N-M)!} \delta \left(\phi - M A_\parallel t_e \right). \tag{4.18}$$

For large N, this binomial distribution is expressed as

$$P(\phi, N) = \sqrt{\frac{2}{\pi N A_\parallel^2 t_e^2}} \exp\left(-2 \frac{\phi^2}{N A_\parallel^2 t_e^2} \right) = \frac{1}{\sigma \sqrt{2\pi}} \exp\left(-\frac{\phi^2}{2\sigma^2} \right), \tag{4.19}$$

with $\sigma = \sqrt{N} A_\parallel t_e$.

After measuring a spectator with a g-value equal to "g", the posterior phase distribution is given by (see equation (4.2)) $P(\phi|H) = \left[1 + (-1)^H \cos(g\phi - \chi) \right]$, with H the spectator-measurement outcome and χ the spectator readout phase, for which we use $\chi = \langle g\phi \rangle + \frac{\pi}{2}$ (see section 4.7.3) calculated using the phase distribution prior to a spectator readout. The spectator measurement both narrows and shifts the memory phase distribution, such that the expected spectator-dependent memory-qubit phase ($\langle \phi_H \rangle$) is non-zero. Experimentally, we target to measuring the memory qubit fidelity along $\theta_c = \langle \phi_H \rangle$, where

$$\langle \phi_H \rangle = \arctan \left(\frac{\langle \sin(\phi) \rangle}{\langle \cos(\phi) \rangle} \right) \tag{4.20a}$$

$$\langle \sin(\phi) \rangle = \int_{-\infty}^{\infty} \sin(\phi) \left[1 + (-1)^H \sin(g\phi) \right] \frac{1}{\sigma \sqrt{2\pi}} \exp\left(-\frac{\phi^2}{2\sigma^2} \right) \tag{4.20b}$$

$$\langle \cos(\phi) \rangle = \int_{-\infty}^{\infty} \cos(\phi) \left[1 + (-1)^H \sin(g\phi) \right] \frac{1}{\sigma \sqrt{2\pi}} \exp\left(-\frac{\phi^2}{2\sigma^2} \right). \tag{4.20c}$$

Evaluating these integrals gives

$$\langle \phi_H \rangle = (-1)^H \arctan \left(\frac{1}{2} \exp\left(-\frac{1}{2} g (2+g) \sigma^2 \right) \cdot \left(-1 + \exp\left(2g\sigma^2 \right) \right) \right), \tag{4.21}$$

such that the fidelity averaged over both spectator-measurement outcomes equals

$$F_\theta = \sum_H \frac{1}{2} \int_{-\infty}^{\infty} \frac{1}{2} \left[1 + \cos\left(\phi - \langle\phi_H\rangle\right) \right] \cdot \left[1 + (-1)^H \sin\left(g\phi\right) \right] \frac{1}{\sigma\sqrt{2\pi}} \exp\left(-\frac{\phi^2}{2\sigma^2}\right) d\phi. \quad (4.22)$$

Evaluating this expressing allows to rewrite F_θ in a simpler form given by

$$F_\theta = \frac{1}{2} + \frac{1}{4}\sqrt{\rho}\exp\left(-\frac{1}{2}\sigma^2\right) \tag{4.23a}$$

$$\rho = 4 + \frac{(\nu - 1)^2}{\mu\nu} \tag{4.23b}$$

$$\nu = \exp\left(2g\sigma^2\right) \tag{4.23c}$$

$$\mu = \exp\left(g^2\sigma^2\right), \tag{4.23d}$$

which reduces to $F_\theta = \frac{1}{2} + \frac{1}{2}\exp\left(-\frac{1}{2}\sigma^2\right)$ for $g = 0$, being equal to the spectator-less situation.

In figure 4.6a, we plot the equation (4.23b) for different g-values and $\sigma = 1$. We observe that for g=1, so a spectator qubit identical to the memory qubit, the fidelity can be restored from $\frac{1}{2}$ to $\frac{3}{4}$. In light and dark blue, we plot the fidelity for $g = g_e$ and $g = \frac{1}{g_e}$ from which a larger improvement is observed for $g = \frac{1}{g_e}$. We hypothesise that the quick initial decay is related to the memory qubit $A_\parallel$, while the following slower decay is related to timescale needed for the difference between the parallel hyperfine components of the memory and spectator qubit to acquire a phase on the order of 2π which prohibits unique identification of the memory phase upon measuring the spectator qubit phase.
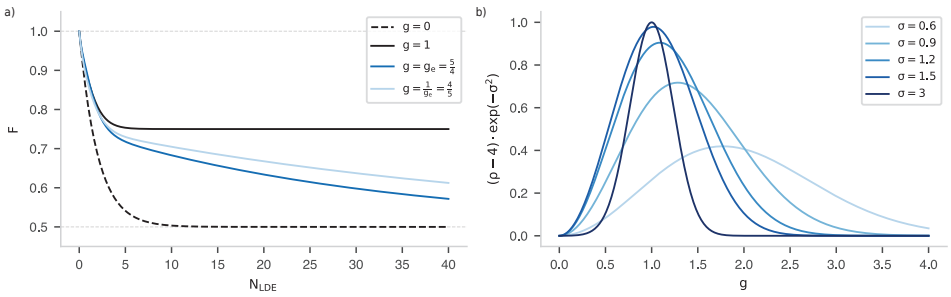
Figure 4.6: **Single spectator effect. a)** Fidelity of the memory qubit after running N_{LDE} entanglement attempts and using one spectator with different g-values. The gate sequence of each attempt is shown in figure 4.2a. The fidelity is the fidelity measured in the XY plane with the memory qubit initialized in the XY plane. **b)** The term in the fidelity responsible for the improvement over the case without a spectator. For memory distributions with a small dephasing, larger g-values are desirable, whereas for large dephasing, g-values equal to 1 become preferential.

In figure 4.6b, $(\rho - 4)\exp(-\sigma^2)$ is plotted. This effectively describes the possible improvement possible in F_θ as a function of g, plotted for different values of σ. The plot shows that for low σ one benefits from a larger g-value, as then the spectator is susceptible to the small phases picked up by the memory qubit. However, for larger σ, the optimal g-value approaches g=1, to avoid a 2π phase wrapping following from the differences of the memory and spectator $A_\parallel$.

FITTING EXPERIMENTAL DATA

To fit the data measured in this chapter where the memory qubit was initialized in the XY plane, we modify the function of equation (4.23b) to include SPAM errors. As the spectator approach is designed to compensate correlated dephasing, we use an exponential decay as a fit function for data with the memory qubit initialized in the Z-basis. Correspondingly, for these two cases, the fit functions are given by

$$F_{xy} = \frac{1}{2} + \frac{1}{4}(1 - A_{SPAM})\sqrt{\rho}\exp\left(-\frac{1}{2}\sigma^2\right) \tag{4.24a}$$

$$F_z = (1 - A_{SPAM_z})\exp\left(-\frac{N_{LDE}}{N_{1/e}}\right) + a, \tag{4.24b}$$

where we substitute $\sigma = \sqrt{N_{LDE}A_\parallel t_e}$. We consider $A_\parallel t_e$ as a single fit parameter. For the fits of F_{xy}, we fix the g-value to 0 if no spectator is used, to the g-value of the spectator if a single spectator is used and leave it as a free parameter if more than one spectator are used. For F_z, we fix $a = \frac{1}{2}$.

The fit parameters of the measurement-based data in figure 4.2d shown in table 4.1:

K spectators	A_{SPAM}	g	$A_\parallel t_e$	χ^2_{xy}
K = 0	0.082 ± 0.007	fixed, g = 0	0.0271 ± 0.0003	5.06
K = 1	0.168 ± 0.007	fixed, g = 1.49	0.0309 ± 0.0004	2.18
K = 2	0.279 ± 0.008	0.68 ± 0.02	0.025 ± 0.001	2.91
K spectators	A_{SPAM_z}	a	$N_{1/e}$	χ^2_z
K = 0	0.105 ± 0.008	fixed, a = 0.5	2.1e3 ± 0.3e3	1.66
K = 1	0.122 ± 0.005	fixed, a = 0.5	4.4e4 ± 0.7e3	3.60
K = 2	0.110 ± 0.005	fixed, a = 0.5	3.1e3 ± 0.3e3	2.13

Table 4.1: fit parameters of fits through data in figure 4.2d.

The fit parameters of the gate-based data in figure 4.4a shown in table 4.2:

K spectators	A_{SPAM}	g	$A_{\parallel}t_e$	χ^2_{xy}
K = 0	fixed, 0.066	fixed, 0	0.0271 ± 0.0002	9.53
K = 1	fixed, 0.081	fixed, 1.49	0.0314 ± 0.0002	5.01
K = 2	fixed, 0.125	0.588 ± 0.009	0.0300 ± 0.0004	8.15
K spectators	A_{SPAM_z}	a	$N_{1/e}$	χ^2_z
K = 0	fixed, 0.1033	fixed, a = 0.5	$1.95e3 \pm 0.09e3$	34.62
K = 1	fixed, 0.1141	fixed, a = 0.5	$3.0e3 \pm 0.1e3$	10.05
K = 2	fixed, 0.0961	fixed, a = 0.5	$2.6e3 \pm 0.1e3$	3.04

Table 4.2: fit parameters of fits through data in figure 4.4a.

4.7.5. MEASUREMENT-INDUCED DEPHASING

The experimental dataset shown in figure 4.2d only shows data where M = {0, 1, 2} spectator qubits are initialised and read out. The BVL at N_{LDE}=0 decreases for an increasing amount of spectators used. Thus, the initialisation and read out of the spectators provide an additional dephasing mechanism. Here, alongside the data shown in figure 4.2d, we show a complementary dataset where we initialise M spectators and read out K≤M spectators. The data is shown in figure 4.7. C0 is the memory qubit, C1 spectator qubit 1 and C2 spectator qubit 2 (see figure 4.2a). Points indicated with circles represent data where only the memory qubit is read out. Points represented by diamonds represent data where only spectator 1 and the memory qubit are read out, and crosses represent data where subsequently spectator 2, spectator 1 and the memory qubit are read out. For the light blue data only the memory qubit is initialised, while for the blue data also spectator 1 is initialised and for the dark blue data both spectators are initialised. The data shows that initialising more spectators does not significantly reduce the memory qubit BVL, but reading out more spectators does reduce the memory qubit BVL.
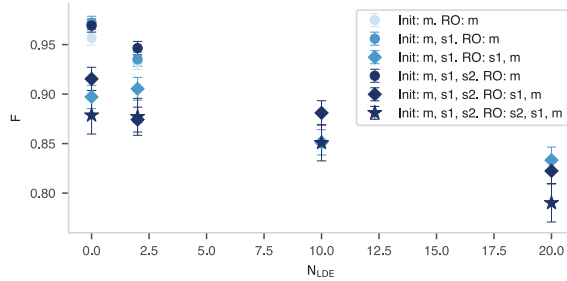
Figure 4.7: **Readout induced dephasing.** Fidelity with the +X basis of the memory qubit initialized in the $|+X\rangle$ state after N_{LDE} entanglement generation attempts for different spectator initialisation and readout strategies. The data is part of the dataset in figure 4.2d. The coding in legend uses 'm' for memory qubit, 'sx' for spectator x, 'Init' to indicate which qubits are initialised and 'RO' to indicate which qubits are read out. Initialising additional spectator qubits barely affects the memory qubit fidelity at small N, while the readout of these spectators does decrease the fidelity.

4.7.6. SIMULATION BACKGROUND

We adopt a density matrix formalism approach to simulate the spectator qubit approach. In general, an entanglement sequence starts with an electron spin initialisation to $|0\rangle$ followed by an (unbalanced) microwave π pulse that prepares the electron spin in a superposition required for spin-photon entanglement. Following this MW pulse, an optional electron decoupling is applied (not done the experiments presented). Finally a set of spectator qubits is read out based on which real-time feedback is applied on other spectator qubits and the memory qubit, see figure 4.8.
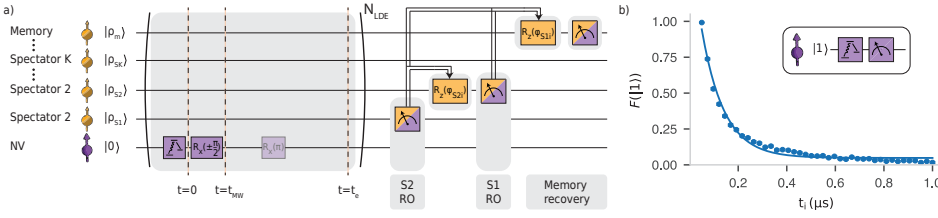

Figure 4.8: **General entanglement sequence and spectator qubit implementation.** **a)** Upon the start of an entanglement sequence, the electron is initialized in $|0\rangle$ and subsequently rotated to an (unbalanced) superposition state to allow spin-photon entanglement (we omit the optical pi-pulse here). Subsequent coherent rotations on the electron can be performed, as indicated by the transparent π-pulse. Upon completion of N_{LDE} entanglement attempts, a set of spectators is read out and feedforward is applied. **b)** Fidelity with respect to the $|1\rangle$ state of the electron-spin qubit upon applying a repump laser for time t_i after initializing the electron in $|1\rangle$. The dataset shown here uses a repump power of 600 nW, alike all measurements presented in the main text. We fit a single exponential decay $F(|1\rangle) = A \exp\{(-t/t_i)\} + a$ and extract $t_i = 92 \pm 4$ns.

Upon the start of the sequence the total density matrix equals $\rho_{t=0,N=0} = \prod_i \rho_{Si} \otimes \rho_m \otimes |0\rangle_e \langle 0|_e$, where the product refers to a tensor product of different Hilbert spaces, ρ_{Si} to the density matrix of spectator number i, ρ_m to the memory qubit density matrix and the subscript e to the electron state. We define the start of the entanglement sequence ($t = 0$) after the electron reinitialisation (see figure 4.8). The subsequent MW pulse along the X-axis is modelled as an instantaneous pulse and creates an unbalanced superposition defined by α on the electron-spin qubit. The MW pulse modifies the density matrix to

$$\rho(t = t_{MW}) = \rho_{t=0,N=0} \otimes$$
$$\left[|\alpha|^2 |0\rangle_e \langle 0|_e - i\alpha\sqrt{1-|\alpha|^2} |0\rangle_e \langle 1|_e + i\alpha^\dagger\sqrt{1-|\alpha|^2} |1\rangle_e \langle 0|_e + (1-|\alpha|^2) |1\rangle_e \langle 1|_e \right].$$
$$(4.25)$$

After the MW pulse, there is a free evolution of time t_e followed by the application of a laser pulse of time t_i that targets to reinitialise the electron to $|0\rangle$. This reinitialisation is stochastic and at each N_{LDE} we sample the time τ_N at which the $|1\rangle$ state is reinitialised to $|0\rangle$ from a single exponential decay with decay constant τ_d, see figure 4.8b. While the decay is more accurately described by a sum of two exponential decays (see figure 4.10),

the single exponential decay can be easily inverted to sample τ. The density matrix in our model at time $T = t_e + \tau_N$ after the MW-pulse is hence described by

$$U_{evo,T} = U_{0,T} \otimes |0\rangle_e \langle 0|_e + U_{1,T} \otimes |1\rangle_e \langle 1|_e \tag{4.26a}$$

$$\rho_{t=(t_e+\tau_N)} = |\alpha|^2 U_{0,T} \rho_{t=0,N=0} U_{0,T}^\dagger |0\rangle_e \langle 0|_e - i\alpha\sqrt{1-|\alpha|^2} U_{0,T} \rho_{t=0,N=0} U_{1,T}^\dagger |0\rangle_e \langle 1|_e +$$
$$i\alpha^\dagger \sqrt{1-|\alpha|^2} U_{1,T} \rho_{t=0,N=0} U_{0,T}^\dagger |1\rangle_e \langle 0|_e + (1-|\alpha|^2) U_{1,T} \rho_{t=0,N=0} U_{1,T}^\dagger |1\rangle_e \langle 1|_e, \tag{4.26b}$$

where U_i only acts on the nuclear spins Hilbert space and is determined by the electron spin state during the entanglement attempt and equation (4.1). Subsequently, we model the electron reinitialisation by tracing out the electron state in equation (4.26b) and a free evolution time of $T_0 = t_i - \tau_N$ with the electron in the $|0\rangle$ state. Therefore, after one entanglement generation sequence ($N_{\text{LDE}}=1$), we have

$$\rho_{t=0,N_{\text{LDE}}=1} = U_{0,T_0} \left[|\alpha|^2 U_{0,T} \rho_{t=0,N=0} U_{0,T}^\dagger + (1-|\alpha|^2) U_{1,T} \rho_{t=0,N=0} U_{1,T}^\dagger \right] U_{0,T_0}^\dagger |0\rangle_e \langle 0|_e. \tag{4.27}$$

The final density matrix $\rho_{N_{\text{LDE}}}$ after N_{LDE} repetitions of the entanglement sequence is given by iterating through the protocol from equation (4.25) to (4.27) N_{LDE} times. This can be straightforwardly done by substituting $\rho_{t=0,N_{\text{LDE}}=0}$ in equation (4.25) for the output of equation (4.27).

After having obtained ρ_f, we proceed by implementing the spectator protocol. The target is to read out spectator k in a basis perpendicular to the measurable expectation value $\langle\theta\rangle_k$ (see SI section 4.7.3). We calculate $\langle\theta\rangle_k$ from ρ_N, apply a $R_z(\phi - \langle\theta\rangle_k)$ rotation on spectator k and subsequently read out spectator k in the Y-basis. In case of perfect readout, the probability (P_{k_i}) and corresponding density matrices (ρ_{k_i}) conditioned on obtaining a bright/dark measurement outcome on spectator k are given by

$$\rho_{k_b} = P_{k_b}^{-1} \left(\rho_{k_y} \otimes I_{i \neq k} \right) \rho_f \left(\rho_{k_y} \otimes I_{i \neq k} \right) \quad \text{with} \quad P_{k_b} = \text{Tr}\left\{ \left[\rho_f \left(\rho_{k_y} \otimes I_{i \neq k} \right) \right] \right\} \tag{4.28a}$$

$$\rho_{k_d} = P_{k_d}^{-1} \left(\rho_{k_{-y}} \otimes I_{i \neq k} \right) \rho_f \left(\rho_{k_{-y}} \otimes I_{i \neq k} \right) \quad \text{with} \quad P_{k_d} = \text{Tr}\left\{ \left[\rho_f \left(\rho_{k_{-y}} \otimes I_{i \neq k} \right) \right] \right\} \tag{4.28b}$$

where $\rho_{k_{\pm y}}$ is the density matrix of spectator qubit k in the $\pm Y$ state and $I_{i \neq k}$ the identity on the Hilbert space of all remaining qubits. Using these density matrices and probabilities, we can calculate the BVL averaged over different spectator readout outcomes.

The analysis above assumed a perfect readout. We now include the single shot readout fidelity given by $F_{\text{RO}} = \begin{pmatrix} F_{00} & F_{10} \\ F_{01} & F_{11} \end{pmatrix}$, where F_{ij} is the probability to obtain outcome j if the state was i. This provides the experimental probabilities to measure different spectator readout outcomes and their corresponding post measurement density matrices:

$$\rho_{k_b}^e = \frac{1}{\rho_{k_b}^e} \left[F_{00} \cdot P_{k_b} \cdot \rho_{k_b} + F_{10} \cdot P_{k_d} \cdot \rho_{k_d} \right] \quad \text{with} \quad \rho_{k_b}^e = F_{00} \cdot P_{k_b} + F_{10} \cdot P_{k_d} \tag{4.29a}$$

$$\rho_{k_d}^e = \frac{1}{\rho_{k_d}^e} \left[F_{01} \cdot P_{k_b} \cdot \rho_{k_b} + F_{11} \cdot P_{k_d} \cdot \rho_{k_d} \right] \quad \text{with} \quad \rho_{k_d}^e = F_{01} \cdot P_{k_b} + F_{11} \cdot P_{k_d}. \tag{4.29b}$$

The simulation procedure above does not include SPAM-related errors that induce dephasing on the memory qubit and other spectator qubits. As a result, the simulations always provide a BVL equal to 1 for N=0, which is not what is observed in figure 4.2d and figure 4.7. We compensate for this by rescaling the BVL obtained from the simulation by the fitted SPAM errors obtained from a fit through the data that the simulation targets to describe (see section 4.7.4).

To encapsulate these SPAM-related errors in the simulations independently from experimentally obtained datasets, in the future we can target to simulate the quantum circuit used for initialisation and readout and characterise the fidelities of the involved operations. An near-term improvement, that does not require additional characterisation measurements, is to include dephasing induced on nuclear-spin qubits from an electron-mediated spectator qubit readout. Namely, in our experiments, we employ a low power electron-spin readout (50 pW) for a long time (~100 μs), such that we switch off the readout laser upon photon detection to prevent a subsequent electron spin excitation and corresponding potential spin-flip. As a consequence, if a spin-flip occurs before we detect a photon, there is a large uncertainty about the time at which the spin-flip happened. This relates to F_{10}. In the future, we can model this by assuming complete dephasing on the nuclear spins in such cases and hence replace $F_{01} \cdot P_{k_b} \cdot \rho_{k_b}$ by $F_{01} \cdot P_{k_b} \cdot \rho_{mixed}$, with ρ_{mixed} the density matrix of a mixed state on the nuclear spins. Likewise we replace $F_{10} \cdot P_{k_d} \cdot \rho_{k_d}$ by $F_{10} \cdot P_{k_d} \cdot \rho_{mixed}$.

For the simulations corresponding to the measurement-based spectator implementation presented in the main text, we use $F_{RO} = \begin{pmatrix} 0.88 & 0 \\ 0.12 & 1 \end{pmatrix}$ as we use a 100 pW readout laser power (see figure 4.10, SI section 4.7.9). For the gate-based implementation, we completely omit the electron readout, and hence effectively use $F_{RO} = \begin{pmatrix} 1 & 0 \\ 0 & 1 \end{pmatrix}$.

4.7.7. ELECTRON CONTROLLED PHASE ROTATION

In this section we provide the mathematical background for the electron-controlled phase rotation of the nuclear spins used in the gate-based spectator protocol (see figure 4.3). We neglect intra-nuclear couplings (~Hz[32]) as their effect is small on the timescale of the controlled gate ($< \omega_l \approx 2.3$ μs). In that case, all nuclear spin evolutions do not depend on each other and only on the electron spin state. Following equation (4.1), we can write the electron-conditioned evolution of K nuclear spins as

$$H_0 = \prod_{i=1}^{K} \omega_l I_{z,i} \tag{4.30}$$

$$H_1 = \prod_{i=1}^{K} (\omega_l - A_{\parallel,i}) I_{z,i} + A_{\perp,i} I_{x,i} \approx \prod_{i=1}^{K} (\omega_l - A_{\parallel,i}) I_{z,i}, \tag{4.31}$$

where the product is a tensor product of the Hilbert spaces of the nuclear spins, and the approximation in equation (4.31) follows from $\omega_l - A_{\parallel,i} \gg A_{\perp,i}$. Thus, each nuclear spin experiences an electron-controlled $R_Z(\theta)$ rotation if the electron is left idle. Here the control is the eigenstates of the electron (the Z basis eigenstates). In the gate-based implementation of figure 4.3, the phase the electron picks up during the waiting time (indicated by δ_{ti} in figure 4.3) is irrelevant and is reset by the electron spin reinitialisation that follows the waiting time.

4.7.8. GATE-BASED PHASE COMPENSATION

To alleviate electron readout induced dephasing, a gate-based implementation of the spectator approach can be employed. Here, we target to reduce the phase uncertainty of the nuclear spin qubits. After the electron is initialized to $|0\rangle_e$, we perform a spectator controlled electron flip followed by a waiting time that imprints an electron-spin dependent phase on the nuclear spins (see figure 4.3). This section provides insight in the mathematical background underlying this gate based approach. We first derive the gate-based effect considering a pure state ($P(\theta) = \delta(\theta)$) of the nuclear spin qubits in the XY plane of the Bloch sphere, and use that result to generalize for a nuclear spin qubit phase probability density function.

Given a phase θ on the memory and a phase correlation between spectator qubit i and the memory given by $\theta_i = g_i \cdot \theta$ we write

$$|\psi\rangle = \prod_{(i \neq k)} \left(\frac{1}{\sqrt{2}} \left[|0\rangle_i + e^{ig_i\theta} |1\rangle_i \right] \right) \otimes \frac{1}{\sqrt{2}} \left[|0\rangle_k + e^{ig_k\theta} |1\rangle_k \right] \otimes \frac{1}{\sqrt{2}} \left[|0\rangle_m + e^{i\theta} |1\rangle_m \right] \otimes |0\rangle_e, \tag{4.32}$$

where the indices refer to the memory qubit (m) or the spectator qubits (i & k). SI section 4.7.3 showed that for a normally distributed phase probability density function centered at $\theta = 0$, the optimal spectator readout angle is $\pm\frac{\pi}{2}$. Hence, here we perform a spectator k controlled electron flip where we flip the electron if the spectator is in $|-Y\rangle$. This modifies $|\psi\rangle$ to

$$|\psi\rangle = \prod_{(i\neq k)} \left(\frac{1}{\sqrt{2}} \left[|0\rangle_i + e^{ig_i\theta} |1\rangle_i \right] \right) \otimes \frac{1}{\sqrt{2}} \left[|0\rangle_m + e^{i\theta} |1\rangle_m \right]$$

$$\otimes \frac{1}{2\sqrt{2}} \left(1 - i e^{ig_k\theta} \right) \left[|0\rangle_k + i |1\rangle_k \right] \otimes |0\rangle_e +$$

$$\prod_{(i\neq k)} \left(\frac{1}{\sqrt{2}} \left[|0\rangle_i + e^{ig_i\theta} |1\rangle_i \right] \right) \otimes \frac{1}{\sqrt{2}} \left[|0\rangle_m + e^{i\theta} |1\rangle_m \right]$$

$$\otimes \frac{1}{2\sqrt{2}} \left(1 + i e^{ig_k\theta} \right) \left[|0\rangle_k - i |1\rangle_k \right] \otimes |1\rangle_e . \tag{4.33}$$

In the rotating frame of the nuclear spins with the electron in the $|0\rangle$ state, a subsequent waiting time t_w imprints a phase $\phi_c = (\omega_1 - \omega_0) t_w$ on the nuclear spin qubits correlated with the electron $|1\rangle$ state:

$$|\psi\rangle (\phi_c) = \prod_{(i\neq k)} \left(\frac{1}{\sqrt{2}} \left[|0\rangle_i + e^{ig_i\theta} |1\rangle_i \right] \right) \otimes \frac{1}{\sqrt{2}} \left[|0\rangle_m + e^{i\theta} |1\rangle_m \right]$$

$$\otimes \frac{1}{2\sqrt{2}} \left(1 - i e^{ig_k\theta} \right) \left[|0\rangle_k + i |1\rangle_k \right] \otimes |0\rangle_e$$

$$+ \prod_{(i\neq k)} \left(\frac{1}{\sqrt{2}} \left[|0\rangle_i + e^{ig_i(\theta+\phi_c)} |1\rangle_i \right] \right) \otimes \frac{1}{\sqrt{2}} \left[|0\rangle_m + e^{i(\theta+\phi_c)} |1\rangle_m \right]$$

$$\otimes \frac{1}{2\sqrt{2}} \left(1 + i e^{ig_k\theta} \right) \left[|0\rangle_k - i e^{ig_j\phi_c} |1\rangle_k \right] \otimes |1\rangle_e . \tag{4.34}$$

The subsequent electron reinitialisation mathematically translates to tracing out the electron state of equation (4.34). This leaves the nuclear spins in state $|\psi\rangle_0$ with probability $P(0)$ and in state $|\psi\rangle_1$ with probability $P(1)$, with

$$|\psi\rangle_0 = \frac{1}{P(0)} \prod_{(i\neq k)} \left(\frac{1}{\sqrt{2}} \left[|0\rangle_i + e^{ig_i\theta} |1\rangle_i \right] \right) \otimes \frac{1}{\sqrt{2}} \left[|0\rangle_m + e^{i\theta} |1\rangle_m \right]$$

$$\otimes \frac{1}{2\sqrt{2}} \left(1 - i e^{ig_k\theta} \right) \left[|0\rangle_k + i |1\rangle_k \right] \tag{4.35a}$$

$$P(0) = \frac{1}{2} \left[1 + \sin (g_k\theta) \right]$$

$$|\psi\rangle_1 = \frac{1}{P(1)} \prod_{(i\neq k)} \left(\frac{1}{\sqrt{2}} \left[|0\rangle_i + e^{ig_i(\theta+\phi_c)} |1\rangle_i \right] \right) \otimes \frac{1}{\sqrt{2}} \left[|0\rangle_m + e^{i(\theta+\phi_c)} |1\rangle_m \right]$$

$$\otimes \frac{1}{2\sqrt{2}} \left(1 + i e^{ig_k\theta} \right) \left[|0\rangle_k - i e^{ig_j\phi_c} |1\rangle_k \right] \tag{4.35b}$$

$$P(1) = \frac{1}{2} \left[1 - \sin (g_k\theta) \right] .$$

Equations (4.35) show two important observations: 1) there is no phase correlation between the state of spectator k and the other qubits, which corroborates that the gate-based implementation effectively implements a measurement on the phase of spectator k. 2) the post gate-based approach probability density function of the phase θ is $\frac{1}{2}[1 + \sin(g_k\theta)]\delta(\theta) + \frac{1}{2}[1 - \sin(g_k\theta)]\delta(\theta - \phi_c)$. For a general initial phase distribution $P(\theta)$, the posterior phase distribution $P(\theta|k_-)$ after the gate-based spectator approach is given by equation (4.36). Here k_- indicates that an electron flip was executed for the state correlated to the -Y state of spectator k. Execution of the electron flip correlated to the +Y state of spectator k is equivalent to replacing ϕ_c for $-\phi_c$ in equation (4.36):

$$P(\theta, \phi_c|k_-) = \frac{1}{2}\left[1 + \sin(g_k\theta)\right]P(\theta) + \frac{1}{2}\left[1 - \sin(g_k\theta)\right]P(\theta - \phi_c). \qquad (4.36)$$

In figure 4.9a, $P(\theta, \phi_c|k_-)$ and $P(\theta, \phi_c|k_+)$ are depicted for a normal distribution of $P(\theta)$ with $\sigma = 1$ and $\phi_c = 0.34$. In line with figure 4.3, to narrow the phase distribution, it is crucial to choose the right spectator state (+Y or -Y) based on which an electron flip is executed. Note that experimentally only the magnitude of ϕ_c can be chosen. Namely $t_w \geq 0$ and the sign is determined by $\omega_1 - \omega_0$. The narrowing of $P(\theta, \phi_c|k_-)$ with respect to $P(\theta)$ is reflected in an increased BVL as demonstrated by figure 4.9b. The blue dashed line reflects the optimal angle ϕ_c for which the plots in figure 4.9a are generated. The ϕ_c values for which the BVL is zero correspond to the situation shown in the right top of figure 4.3b. Increasing ϕ_c will move the BVL through a discontinuity at 0. This discontinuity is explained as upon the zero crossing the Bloch vector obtains a π phase shift.
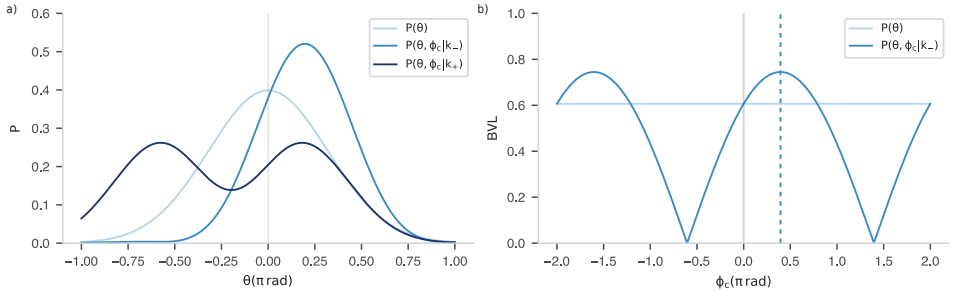

Figure 4.9: **Gate based spectator implementation. a)** Initial normally distributed PDF P(θ) with standard deviation $\sigma = 1$ (light blue). The posterior PDF if an electron flip is correlated with the -Y state on spectator k: P($\theta, \phi_c|k_-$) (blue) and when correlated with the +Y state P($\theta, \phi_c|k_+$) (dark blue). ϕ_c in this figure is set to the dashed line in b), which maximizes the BVL corresponding to P($\theta, \phi_c|k_-$)). **b)** BVL for the prior (P(θ), light blue) and posterior (P($\theta, \phi_c|k_-$)), blue) PDF as a function of ϕ_c.

4.7.9. OPTICAL DYNAMICS IN SPECTATOR QUBIT MEASUREMENTS

In this section, we first provide insight in the powers and duration used for the electron repump during the entanglement generation sequence. Secondly, we do this for the power and duration involved in the spectator readout. In figure 4.10a, we plot the fidelity of the electron spin with respect to the $|1\rangle$ state after having the electron spin initialized in the $|1\rangle$ state and applying a resonant repump laser for a time t_{repump} for
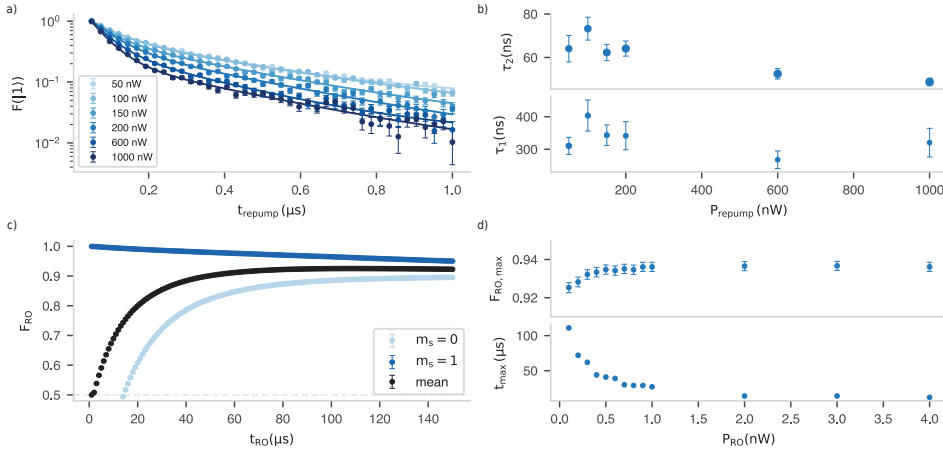
Figure 4.10: **Electron optical dynamics. a)** Depletion of the population in $|1\rangle$ under constant illumination of the repump laser for different a laser powers. Fitted line is $F(|1\rangle) = A_1 \exp\left\{\left(-\frac{t}{\tau_1}\right)\right\} + A_2 \exp\left\{\left(-\frac{t}{\tau_2}\right)\right\} + a$. **b)** Fitparameters for the curves in (a). The size of the markers reflects $\frac{A_1}{A_1+A_2}$ (bottom) $\left(\frac{A_2}{A_1+A_2}\right)$ (top). **c)** Exemplary single-shot readout curve. The applied readout power here is 100 pW. The light (dark) blue curve indicates the probability to (not) have detected a photon after applying the RO laser for a time t_{RO} if the initial state is $|0\rangle$ ($|1\rangle$). Black is the average readout fidelity, averaged over the light and dark blue data. **d)** Maximum readout fidelities and corresponding t_{RO} at which these maxima are achieved for different readout powers. The readout power used in the spectator measurements in this work is 100 pW. Upon photon detection, we turn off the readout laser, and otherwise terminate the readout after 98 µs.

different powers. We fit a double exponential decay (see figure caption) and plot the extracted timescales in figure 4.10b. The longer the decay timescales, the longer the electron undergoes continuous optical cycles and the longer the electron experiences a stochastic evolution. In the experimental results in this work, we set the repump power to 600 nW and the repump time to ~500 ns. A longer spin-pump time would improve the electron reinitialisation fidelity, at the cost of a longer sequence time. Infidelities in the electron spin reinitialisation act as correlated noise, which the spectator qubit approach can mitigate.

In the spectator qubit readout, we want to simultaneously optimize the probability to obtain the right readout outcome and the probability that the post-measurement state is equal to the measured state. We read out by selectively addressing the $|0\rangle$ electron state[37]. In case the electron is in the $|0\rangle$ state, the electron cycles through the excited state, thereby emitting photons. Photon detection measures the electron spin state $|0\rangle$. In this process, spin-flips in the excited state can change the electron spin state. To minimize such spin flips, we avoid unnecessary excitations by using a weak laser power, such that a feedback signal (1 µs clock cycle) can be used to rapidly turn off the laser upon detection of a photon[31,38].

In figure 4.10c, we show the probability to (not) measure a photon in case the

electron was prepared in the $|0\rangle$ ($|1\rangle$) state upon application of a 100 pW laser pulse for duration t_{RO}. From this, we can extract what the maximum achievable fidelity averaged over the $|0\rangle$ and $|1\rangle$ is, and at what t_{RO} we obtain this fidelity. We do this for different laser powers and plot these numbers in figure 4.10d. For lower repump powers, we barely observe a drop in the maximum attainable fidelity. Therefore we pick a low readout power in our experiments (100 pW) to benefit the ability to turn off the readout laser upon photon detection.

AUTHOR CONTRIBUTIONS

SJHL took and analyzed all experimental data and simulations with input from THT and YW. SJHL, YW, BMT and THT set up the theoretical background. SJHL, YW and THT devised the project and experiments. CEB assisted in analyzing and taking preliminary data. BMT and THT supervised the project. SJHL wrote this chapter with input mainly from THT and also input from YW and BMT. The sample was grown by MM and DJT.

REFERENCES

[1] S. Wehner, D. Elkouss and R. Hanson, *Quantum internet: A vision for the road ahead,* Science **362**, eaam9288 (2018).

[2] L. Jiang, J. M. Taylor, A. S. Sørensen and M. D. Lukin, *Distributed quantum computation based on small quantum registers,* Physical Review A **76**, 062323 (2007).

[3] N. H. Nickerson, Y. Li and S. C. Benjamin, *Topological quantum computing with a very noisy network and local error rates approaching one percent,* Nature Communications **4**, 1756 (2013).

[4] N. H. Nickerson, J. F. Fitzsimons and S. C. Benjamin, *Freely Scalable Quantum Technologies Using Cells of 5-to-50 Qubits with Very Lossy and Noisy Photonic Links,* Physical Review X **4**, 041041 (2014).

[5] H. J. Kimble, *The quantum internet,* Nature **453**, 1023 (2008).

[6] M. Pompili *et al., Realization of a multinode quantum network of remote solid-state qubits,* Science **372**, 259 (2021).

[7] C. Nguyen *et al., Quantum Network Nodes Based on Diamond Qubits with an Efficient Nanophotonic Interface,* Physical Review Letters **123**, 183602 (2019).

[8] C. Babin *et al., Fabrication and nanophotonic waveguide integration of silicon carbide colour centres with preserved spin-optical coherence,* Nature Materials **21**, 67 (2022).

[9] D. D. Awschalom, R. Hanson, J. Wrachtrup and B. B. Zhou, *Quantum technologies with optically interfaced solid-state spins,* Nature Photonics **12**, 516 (2018).

[10] H. Bernien *et al., Heralded entanglement between solid-state qubits separated by three metres,* Nature **497**, 86 (2013).

[11] P. C. Humphreys *et al., Deterministic delivery of remote entanglement on a quantum network,* Nature **558**, 268 (2018).

[12] C. Bradley *et al., A Ten-Qubit Solid-State Spin Register with Quantum Memory up to One Minute,* Physical Review X **9**, 031045 (2019).

[13] R. Stockill *et al., Phase-Tuned Entangled State Generation between Distant Spin Qubits,* Physical Review Letters **119**, 010503 (2017).

[14] L. Stephenson *et al., High-Rate, High-Fidelity Entanglement of Qubits Across an Elementary Quantum Network,* Physical Review Letters **124**, 110501 (2020).

[15] C. M. Knaut *et al., Entanglement of Nanophotonic Quantum Memory Nodes in a Telecommunication Network,* (2023), arXiv:2310.01316 [quant-ph].

[16] S. L. N. Hermans *et al., Qubit teleportation between non-neighbouring nodes in a quantum network,* Nature **605**, 663 (2022).

[17] C. E. Bradley *et al.*, *Robust quantum-network memory based on spin qubits in iso-topically engineered diamond,* npj Quantum Information **8**, 1 (2022).

[18] A. Faraon, P. E. Barclay, C. Santori, K.-M. C. Fu and R. G. Beausoleil, *Resonant en-hancement of the zero-phonon emission from a colour centre in a diamond cavity,* Nature Photonics **5**, 301 (2011).

[19] M. Ruf, M. Weaver, S. van Dam and R. Hanson, *Resonant Excitation and Purcell Enhancement of Coherent Nitrogen-Vacancy Centers Coupled to a Fabry-Perot Microcavity,* Physical Review Applied **15**, 024049 (2021).

[20] D. M. Lukin *et al.*, *4H-silicon-carbide-on-insulator for integrated quantum and non-linear photonics,* Nature Photonics **14**, 330 (2020).

[21] A. Reiserer *et al.*, *Robust Quantum-Network Memory Using Decoherence-Protected Subspaces of Nuclear Spins,* Physical Review X **6**, 021040 (2016).

[22] H. Bartling *et al.*, *Entanglement of Spin-Pair Qubits with Intrinsic Dephasing Times Exceeding a Minute,* Physical Review X **12**, 011048 (2022).

[23] S. Majumder, L. Andreta de Castro and K. R. Brown, *Real-time calibration with spec-tator qubits,* npj Quantum Information **6**, 1 (2020).

[24] J. L. Orrell and B. Loer, *Sensor-Assisted Fault Mitigation in Quantum Computation,* Physical Review Applied **16**, 024025 (2021).

[25] K. Singh *et al.*, *Mid-circuit correction of correlated phase errors using an array of spectator qubits,* Science **380**, 1265 (2023).

[26] A. Lingenfelter and A. A. Clerk, *Surpassing spectator qubits with photonic modes and continuous measurement for Heisenberg-limited noise mitigation,* npj Quantum In-formation **9**, 1 (2023).

[27] R. S. Gupta, L. C. G. Govia and M. J. Biercuk, *Integration of spectator qubits into quantum computer architectures for hardware tune-up and calibration,* Physical Review A **102**, 042611 (2020).

[28] A. Youssry, G. A. Paz-Silva and C. Ferrie, *Noise detection with spectator qubits and quantum feature engineering,* New Journal of Physics **25**, 073004 (2023).

[29] H. Song, A. Chantasri, B. Tonekaboni and H. M. Wiseman, *Optimized mitigation of random-telegraph-noise dephasing by spectator-qubit sensing and control,* Physical Review A **107**, L030601 (2023).

[30] B. Tonekaboni, A. Chantasri, H. Song, Y. Liu and H. M. Wiseman, *Greedy versus map-based optimized adaptive algorithms for random-telegraph-noise mitigation by spectator qubits,* Physical Review A **107**, 032401 (2023).

[31] M. H. Abobeih *et al.*, *Fault-tolerant operation of a logical qubit in a diamond quan-tum processor,* Nature **606**, 884 (2022).

[32] M. H. Abobeih *et al.*, *Atomic-scale imaging of a 27-nuclear-spin cluster using a quantum sensor,* Nature **576**, 411 (2019).

[33] S. L. N. Hermans *et al.*, *Entangling remote qubits using the single-photon protocol: an in-depth theoretical and experimental study,* New Journal of Physics **25**, 013011 (2023).

[34] Wikipedia, *Bayesian inference,* (2024).

[35] B. M. Terhal and D. Weigand, *Encoding a qubit into a cavity mode in circuit QED using phase estimation,* Physical Review A **93**, 012315 (2016).

[36] D. W. Berry, H. M. Wiseman and J. K. Breslin, *Optimal input states and feedback for interferometric phase estimation,* Physical Review A **63**, 053804 (2001).

[37] L. Robledo *et al.*, *High-fidelity projective read-out of a solid-state spin quantum register,* Nature **477**, 574 (2011).

[38] J. Cramer *et al.*, *Repeated quantum error correction on a continuously encoded qubit by real-time feedback,* Nature Communications **7**, 11526 (2016).

4

5

SPECTRAL-DIFFUSION DYNAMICS OF LIFETIME-LIMITED OPTICAL TRANSITIONS IN COMMERCIALLY AVAILABLE BULK SILICON CARBIDE

S.J.H. Loenen[*]**, G.L. van de Stolpe**[*]**, L.J. Feije**[*]**, G.M. Timmer, A. Das, T.H. Taminiau**

Solid-state single-photon emitters are a versatile platform for the realisation of a multitude of quantum technologies, among which optically-connected quantum networks. Many of these technologies place stringent requirements on the optical coherence of the emitters. However, the dynamics of surrounding charge impurities may cause spectral diffusion of optical transitions, in particular when the sample is exposed to laser illumination. Here, we introduce a high-bandwidth 'check-probe' measurement scheme that enables the quantitative measurement of spectral diffusion and ionisation rates, and allows for determining the homogeneous transition linewidth of single quantum emitters in spectrally diffusive environments. We apply this technique to the V2 center in commercially available bulk 4H-silicon carbide. Despite observing significant diffusion under laser illumination ($\gtrsim$ GHz s^{-1}), the optical transitions are narrow (~ 35 MHz), and remain stable in the dark. Moreover, through the observation of Landau-Zener-Stückelberg interference, we determine the optical coherence time to be lifetime limited (17(3) ns), further establishing the V2 center as promising candidate for quantum networking experiments. These results advance our understanding of spectral diffusion of quantum emitters in semiconductor materials, and might have applications for studying charge dynamics across other platforms.

5.1. INTRODUCTION

Optically active solid-state defects have enabled pioneering experiments in the field of quantum computation[1–3] and quantum networks[4,5]. Proof-of-principle experiments have demonstrated primitives for quantum error correction[1–3] and the realisation of a three-node network[6,7]. Key to these advances is the ability to connect multiple emitters via their coherent spin-optical interface, with many applications requiring narrow, stable optical transitions[5,6].

However, a major challenge for preserving optical coherence is posed by the presence of fluctuating charge impurities, either within the bulk material, or at the surface[8]. Such impurities can cause spectral diffusion of the optical transitions at timescales ranging from the sub-nanosecond to second timescale, especially when emitters are integrated in nanostructures[8,9]. Moreover, optical pulses that are used to probe and manipulate the emitter typically exacerbate spectral diffusion, further complicating reliable operation[8]. Experimental techniques that enable the systematic, quantitative study of spectral diffusion are of key importance, as they provide unique insight in the environment charge dynamics, and allow for targeted optimisation of material properties and fabrication processes. However, frequently used methods for probing spectral diffusion, such as photoluminescence (PLE) scans or autocorrelation measurements suffer from several challenges. For example, PLE scans only provide a limited bandwidth set by the time of a single scan[10–12] and might disturb the system with continuous laser illumination, complicating the extraction of underlying diffusion rates[9]. Autocorrelation-type measurements provide higher bandwidth, but face limited flexibility for probing diffusion under external perturbations and do not easily distinguish between diffusion and ionisation processes.

Here, we introduce a toolbox for characterising the spectral diffusion of solid-state emitters, based on charge-resonance check protocols[6,13], which we dub the *check-probe* scheme. Our methods offer high bandwidth, allow for the distinction between diffusion and ionisation processes, and can be used without disturbing the system with external perturbations (such as laser pulses). Moreover, they enable measurements of the optical coherence of single centers, even in heavily diffusive environments, while only introducing limited laser-induced disturbance.

To benchmark our method, we apply it to a system that is of specific interest to quantum networks: the cubic lattice site silicon vacancy (V2) center in silicon carbide[14,15]. In particular, we study the diffusion and ionisation dynamics of a single V2 center embedded in a nanopillar[16], etched in commercially available bulk 4H-silicon carbide. This system exhibits a high degree of spectral diffusion (> 1 GHz linewidth, when time-averaged), typical for single quantum emitters in commercially available bulk materials[17–19]. We introduce a protocol based on charge-resonance checks[6,13], which we exploit to quantitatively determine the spectral diffusion rates, both under application of laser illumination and in the dark. We use this knowledge to prepare specific spectral configurations and thereby tune the defect emission frequency while

simultaneously realizing a near-lifetime-limited linewidth that can be stored for over a second and accessed on-demand. Finally, through the observation of Landau-Zener-Stückelberg interference, we determine the optical coherence time to be $T_2 = 17(3)$ ns, representing the life-time limit for these defects [14].

Our observation of (near-)lifetime limited linewidths in nanostructures in commercially available silicon carbide hints towards the possibility of using commercially mass-fabricated material for quantum technology applications, although a more likely path is to use high-purity epitaxial grown layers that provide a starting point with less spectral diffusion [10,14,20]. Nevertheless, the techniques developed here might enable the targeted optimisation of material and fabrication recipes, and can be readily transferred to other platforms [17,19,21,22].
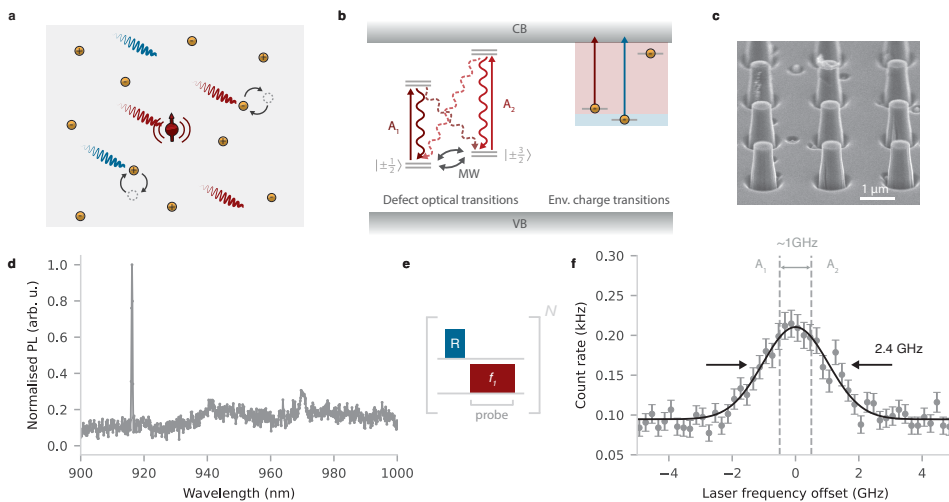

Figure 5.1: **Defect optical properties under laser-induced charge dynamics. a)** Schematic of the system. A single V2 defect is surrounded by charges (yellow circles) associated to residual defects intrinsic to the silicon carbide material [23]. Under laser illumination, these charges can be mobilised after excitation to (from) the conduction (valence) band, indicated by blue and red wiggly lines. **b)** Energy diagram, depicting the V2 center's optical transitions (left) and possible laser-induced charge dynamics of the (unknown) impurities in the environment (right). The spin-dependent A_1 and A_2 transitions can be excited with a tunable, near-infrared (NIR) laser (916 nm, red arrow), while a high energy repump laser (785 nm, blue arrow) is used to scramble the charge state of the V2 center and its environment. The ground-state spin ($S = \frac{3}{2}$) can be manipulated with microwave (MW) radiation. **c)** Scanning-electron-microscopy image of the sample used in this work. We study V2 centers in samples diced from a 100 mm commercially available 4H-SiC bulk wafer. Nanopillars (~ 500 nm diameter) are fabricated to improve the photon collection efficiency. **d)** Representative emission spectrum of a V2 center when exciting it with the repump laser. **e)** Photoluminescence-excitation spectroscopy (PLE) sequence. The frequency f_1 of the NIR laser (red) is scanned over the V2 zero-phonon line, while emission in the phonon sideband is collected. The repump laser (blue) is used to scramble the defect charge state before every repetition (total N). **f)** Measured PLE spectrum. Averaging over many charge-environment configurations results in a single, broad peak (~ 2.4 GHz FWHM). The A1 and A2 transition (seperated by ~ 1 GHz) of the V2 defect are located within the broad peak. The laser frequency is offset from 327.10 THz

5.2. INHOMOGENEOUS LINEWIDTH

Spectral diffusion occurs when the spatial configuration of charges, for example associated to material impurities or surface defects, changes. This leads to fluctuating electric fields that, via the Stark shift[24,25], modify the optical transition frequency of a nearby quantum emitters. Although charge dynamics are largely frozen at cryogenic temperatures, studies have shown that charges can still be mobilised through laser illumination used for the controlled optical driving of the quantum emitter[8,9,19,26]. Figure 5.1a depicts these dynamics in the system under study in this work: the V2 center in commercially available bulk silicon carbide. A single V2 center is surrounded by (mobile) charges associated to residual defects and shallow dopants (concentrations $\sim 10^{15} cm^{-3}$) that are naturally created during the growth process[23]. Resonant optical operation of the V2 center typically requires the use of two types of lasers. A high-power (~ 10 μW) 785 nm laser for V2 charge-state reinitialisation and low-power (~ 10 nW frequency-tunable near-infrared (NIR) lasers close to the emitter's zero-phonon line (916 nm), to access the spin-dependent optical transitions A_1 and A_2 (figure 5.1b). Under such laser illumination, the surrounding charges can be excited via a single-photon process if the energy difference between the occupied charge state and the conduction (or valence) band is smaller than the associated energy of the laser frequency (indicated by the red (blue) window for the NIR (repump) laser in figure 5.1b).

We investigate individual V2 defects at 4K. To mitigate the effects of the unfavourable dipole orientation in c-plane 4H-SiC, we fabricate nanopillars that enhance the optical collection efficiency (Fig. 5.1c, Methods). In about one in every 10 pillars, we observe a (low temperature) spectrum with a characteristic zero-phonon line at 916 nm(Fig. 5.1d), hinting at the presence of single V2 centers confined in the nanopillars. The dimensions of the nanopillar, a diameter of ~ 500 nm and a height of ~ 1.2 μm, prevents the exclusion of surface-related effects on the optical properties the studied V2 centers.

We investigate the V2 optical absorption linewidth by repeatedly interleaving repump pulses ('R', 10 μs, 10 μW) with NIR pulses (10 μs, 10 nW) at frequency f_1, see figure 1e. We register the count rate averaged over N repetitions and repeat this procedure for multiple frequencies, varying f_1 over across the absorption line. In a system without spectral diffusion, we would expect to see signal at two distinct peaks separated by $\Delta \approx 1$ GHz[27], corresponding to the separation of the A_1 and A_2 transitions, with homogeneous linewidhts of ~ 22.5 MHz[14]. However, we observe a broad (~ 1 GHz, see figure 5.1f) peak instead, hinting at high degrees of spectral diffusion, consistent with comparable experiments in commercially available bulk materials[17,19].

In order to resolve the individual A_1 and A_2 transitions within the broad inhomogeneously broadened line, we first employ a two-laser photoluminescence excitation (PLE) scan[17]. Compared to the sequence in figure 5.1e, we now fix frequency f_1 close to the middle of the broad resonance (Fig. 5.1f) and add a second NIR laser at frequency f_2 (Fig. 5.2a). We observe a significant increase in the detected count rate when the two-laser-detuning satisfies: $f_2 - f_1 \approx \Delta$. This can be explained by the fact that optical

pumping, which otherwise quickly diminishes the signal, is effectively reduced when both the A_1 and A_2 transitions are on resonance with the f_1 and f_2 laser frequencies respectively (see also Fig. 5.1b). Importantly, the relatively narrow resonance (≈ 90 MHz) observed in Fig. 5.2b suggests that the homogenous emitter linewidth is much narrower than the inhomogeneous line measured in Fig. 5.1f.

Next, we fix the two-laser detuning to Δ and record the counts per experimental repetition (Fig. 5.2c). We obtain a telegraph-like signal, consistent with a single V2 center spectrally diffusing at timescales on the order of the length of a single repetition (5 ms in Fig. 5.2c). Interestingly, such a signal allows for the implementation of a charge-resonance check[13,21], which probes whether the V2 center is in the right (negative) charge state, and its transitions are resonant with the NIR lasers. If the number of detected counts passes some set minimum threshold $T \geq 1$ (e.g. the grey dashed line in Fig. 5.2c), we conclude that the defect was on resonance in that specific experimental repetition, allowing for post-selection (or pre-selection) of the data based on this fact. In the following, we will explore how we can use such post-selection tactics to gain insights in the spectral dynamics.
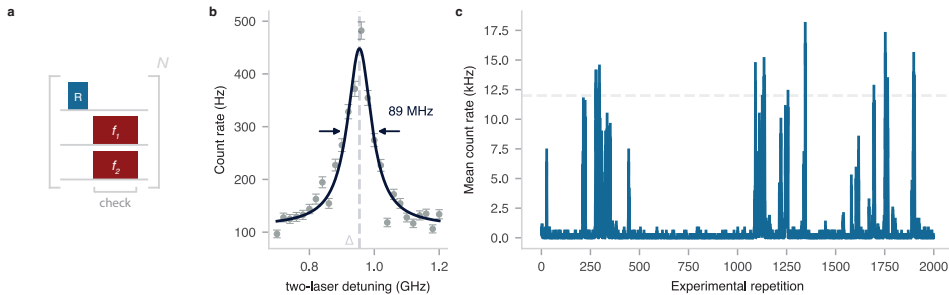

Figure 5.2: **Charge-resonance check. a)** Experimental sequence. A short (10 μs, 10 μW) high-energy (785 nm) repump laser pulse (denoted 'R') is used to scramble the V2 charge state. Next, emission from the defect is collected while two NIR lasers at frequencies f_1 and f_2 are turned on (approximately resonant with the broad peak in Fig. 5.1g at ≈ 916 nm). We refer to this sequence element as the 'check' block. **b)** We vary the detuning between the two NIR lasers ($\Delta = f_1 - f_2$) and observe an increase in count rate if the two lasers are approximately 1 GHz apart, which equals the difference between the A_1 and A_2 transitions. A Lorentzian fit obtains a FWHM of 89 MHz. **c)** Detected mean count rate per experimental repetition, when the NIR lasers are turned on for 200 ms. In most repetitions, the defect is off-resonant with the lasers and (almost) no counts are detected. However, in some cases, when the A_1 and A_2 transitions coincide with laser frequencies f_1 and f_2, we observe significant emission (> 1 kHz). Thresholding (dashed line) on the detected counts can be employed to prepare specific spectral configurations of the V2 defect.

5.3. Ionisation and spectral diffusion dynamics

Next, we develop a method to measure the charge and spectral dynamics of the defect. Currently, various experimental techniques exist, based either on tracking the transition frequency with subsequent PLE scans[8,10,11], or on autocorrelation-type

measurements[9,28]. The former method struggles with measuring dynamics faster than the acquisition timescale of a single scan[12], while the latter, although fast, offers limited flexibility for probing diffusion under external perturbations, and generally does not distinguish between emitter ionisation and spectral diffusion.

Here, we take a different approach, conceptually similar to autocorrelation-type measurements, but based explicitly on the post-selection of specific spectral configurations via the 'check' block introduced in Fig.5.2a. In particular, we consider an experimental sequence of the form sketched in Fig. 5.3a. After a charge-reinitialisation (repump) step, a 'check' and a 'probe' block are executed (as in Fig.5.2a), separated by a perturbation of the system (grey block marked 'X') of varying length t (delay time). During these blocks, significant emission is only expected when the emitter is in the correct (i.e. negative) charge state and the A_1 and A_2 transitions are resonant with f_1 and f_2 (a *bright* state). Therefore, by post-selecting the data based on passing a minimum counts threshold ($T \geq 1$) in the first block (denoted 'check'), we effectively initialise the emitter in the *bright* state at the start of the sequence. By measuring the mean number of detected counts in the second block (denoted 'probe'), we can track the evolution of the emission under the application of an external perturbation. Alternatively, we can post-select the data on passing the threshold in the second block, and observe the brightness in the first block, effectively tracking the evolution of brightness backward in time (delay times $t < 0$). Figure 5.3b shows theoretical example curves for diffusion-, or ionisation-dominated perturbation processes.

We derive an analytical expression for the acquired signal, taking into account spectral diffusion and ionisation processes, assuming the thresholding procedure initialises the defect in the *bright state* at delay time $t = 0$. Spectral diffusion is described as a time-inversion-symmetric process, governed by an effective diffusion rate γ_d (in $Hz\,s^{-1}$), leading to a (symmetric) reduction in observed counts for both positive and negative delay times t as the emitter drifts off resonance (top curve in Fig. 5.3b). We quantitatively capture this behaviour using the spectral propagator, which describes the evolution of the spectral probability density function in time, and is commonly used in the field of single-molecule spectroscopy[29]. The detected emission at time t can then be calculated by considering the expected emission when the laser and emitter are off-resonance (Lorentzian lineshape with homogeneous linewidth Γ (FWHM)), and integrating over the spectral probability density (see SI section 5.8.1).

In our system in particular, diffusion is mainly caused by laser-induced reorientation of charges surrounding the defect, whose dynamics can effectively be described by a bath of fluctuating electric dipoles[26]. In this case, the spectral propagator has an analytical solution, given by a Lorentzian whose linewidth $\gamma(t)$ increases linearly with time: $\gamma(t) = \gamma_d\, t$[29]. Note that this description is valid only at short timescales ($\gamma_d\, t \ll \sigma$), as the spectral probability density should eventually converge to the inhomogeneous distribution observed in Fig. 5.1g[29].

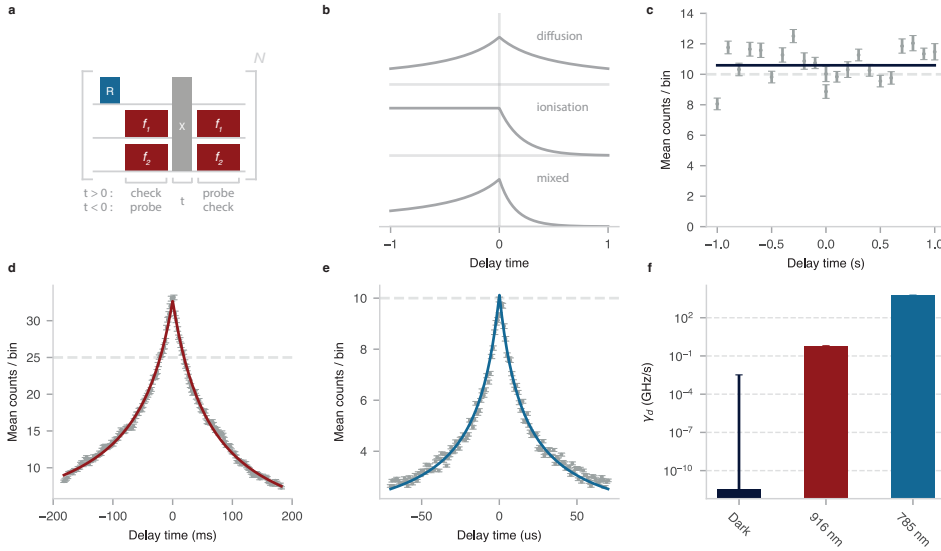Finally, ionisation (charge recapture) of the emitter is modelled as an exponential

Figure 5.3: **Spectral diffusion dynamics. a)** Experimental sequence. A resonance-check block checks whether the defect starts out on resonance. Next, a diffusion-inducing block (marked 'X') is inserted, which consist either of turning off the lasers (c), turning on the resonant lasers (d), or turning on the repump laser (e). Finally, a second resonance-check blocks probes whether the defect is still on resonance or has diffused away. We post-select the data by imposing a minimum-counts threshold (T), heralding the emitter in the bright state in the first (second) block and computing the mean number of counts in the second (first) block, which encodes the emitter brightness at future (past) times. **b)** Schematic illustrating the expected mean number of counts (according to Eq. 5.1), when either ionisation or spectral diffusion is dominant. **c)** No significant spectral diffusion or ionisation is observed when the lasers are turned off. The solid line is a fit to the data using Eq. 5.1. Dashed grey line denotes the set threshold (in a 2 ms window). **d)** Experiment and fit under 20 nW of resonant laser excitation (916 nm). **e)** Experiment and fit under 1 μW of repump laser excitation. **f)** Extracted saturation diffusion rates, obtained at laser powers of ~ 20 nW (resonant) and ~ 5 μW (repump). See supplementary Fig. 5.8 for underlying data and error analysis.

decay of fluorescence, governed by ionisation (recapture) rate γ_i (γ_r). Then, the mean number of observed counts at delay time t can be described by (see SI section 5.8.1):

$$\bar{C}(t) = \begin{cases} \bar{C}_0 \left(1 + \gamma_d\, t/\Gamma\right)^{-1} e^{-\gamma_i t}, & \text{if } t > 0. \\ \bar{C}_0 \left(1 - \gamma_d\, t/\Gamma\right)^{-1} e^{-\gamma_r t}, & \text{otherwise.} \end{cases} \tag{5.1}$$

where $\bar{C}_0$ is the mean number of observed counts at $t = 0$ and $\gamma_d, \gamma_i, \gamma_r > 0$. Note that Eq. 5.1 in general does not obey time-inversion symmetry (for $\gamma_i \neq \gamma_r$), and in specific cases allows for a clear distinction between ionisation and diffusion processes (if $\gamma_r = 0$). Next to that, the functional form of Eq. 5.1 also captures information about the type of processes at play (exponential decay for emitter charge dynamics and a power law dependence for diffusion).

Next, we experimentally implement the sequence drawn in Fig. 5.3a for three distinct perturbations: no laser illumination (Fig. 5.3c), illumination with the two NIR

lasers (20 nW, Fig. 5.3d), and illumination with the repump laser (1 μW, Fig. 5.3e). We observe a wide range of dynamics, from the microsecond to second timescale, and observe excellent agreement between the data and fits based on Eq. 5.1 (solid lines). Interestingly, when the lasers are turned off, almost no diffusion (or ionisation) is present, confirming that diffusion is mainly caused by laser illumination in the material. For the NIR-lasers perturbation, a slight asymmetry between positive and negative delay times can be seen, hinting at a small contribution of ionisation to the dynamics. When applying the repump laser, we observe a (approximately symmetric) quickly decaying signal (μs timescale).

To quantitatively extract the ionisation and diffusion rates under the various perturbations, we set $\Gamma = 36$ MHz, (independently determined in section 5.4). We find that extracted rates are weakly dependent on the set threshold value, resulting from non-perfect initialisation on-resonance, but converge for higher T. Averaging over a range of threshold values, we find diffusion rates $\gamma_d = 0.00(2)\,\text{GHz}\,\text{s}^{-1}, 0.60(2)\,\text{GHz}\,\text{s}^{-1}, 2.4(2) \times 10^3$ $\text{GHz}\,\text{s}^{-1}$, for the data in Fig 5.3c, d and e respectively (SI section 5.8.2). In the dark, the fit only converges if we set $\gamma_i, \gamma_r = 0$, which is a reasonable assumption as defect charge dynamics are expected to be frozen at 4 K[26]. Furthermore, ionisation effects are only observed under NIR-lasers illumination, due to the short diffusion timescale during the repump-laser perturbation (resulting in divergent fit results for γ_i and γ_r). From the data in Fig. 5.3d, we extract $\gamma_i = 1.0(2)\,\text{GHz}\,\text{s}^{-1}$ and $\gamma_r = 0.03(4)\,\text{GHz}\,\text{s}^{-1}$. Correcting for reduced ionisation when the V2 center is off-resonance with the NIR lasers results in an ionisation rate $\gamma_i^0 = 3(1)$ Hz (see SI section 5.8.1). Finally, we repeat the experiments for various laser powers, and observe a saturation of the diffusion rates, both under NIR-lasers and repump laser excitation (SI Fig. 5.8). The higher saturation-diffusion rate measured for the repump laser is likely due to the larger fraction of charge traps that can be ionised via a single-photon process (Fig.5.1b and Fig. 5.3f).

5.4. FAST OPTICAL SPECTROSCOPY

Having established the spectral diffusion timescales, the next step is to characterise the homogeneous linewidth when minimal (laser-induced) disturbance is present. To this end, we use a fast optical spectroscopy method (similar to Ref.[30]) that, in our system, only requires laser illumination on timescales shorter than the laser-induced diffusion timescales.

First, we execute an alternative implementation of the 'check' block (compared to Figs 5.2a and 5.3a), that consists of a single NIR-laser pulse at f_1, together with a MW pulse that mixes the spin states, see Fig. 5.4a. By post-selecting on high counts (here $T = 7$), either the A_1 or A_2 transition is initialised on-resonance with f_1. Then, a second laser is used to probe the defect emission at a frequency f_2 immediately after the charge-resonance check (~ μs timescale, limited by the experiment hardware). By studying the mean number of counts during the f_2 pulse, (an upper bound for) the homogenous linewidth can be extracted (Fig. 5.4b).
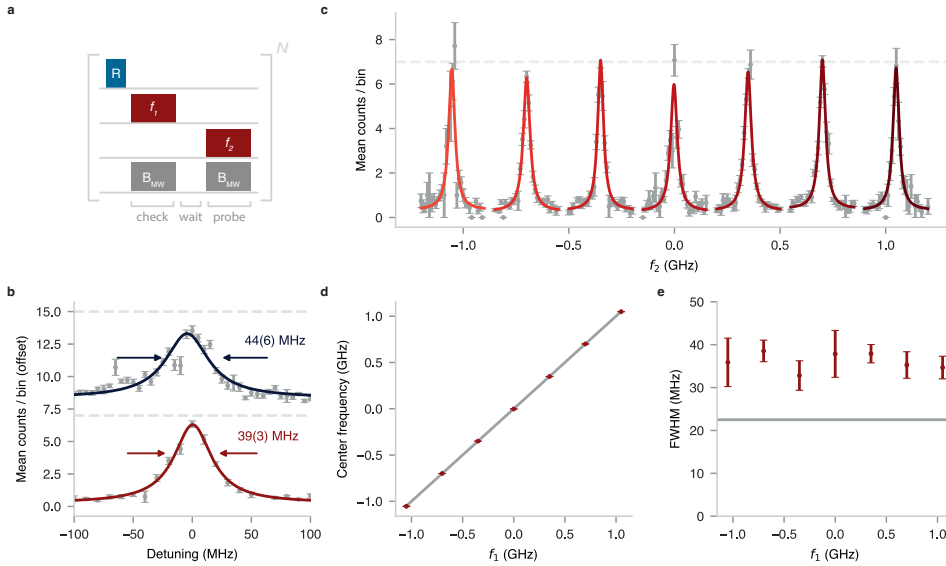
Figure 5.4: **Fast optical spectroscopy a)** Experimental sequence. A resonant laser at f_1 and a microwave (MW) pulse resonant with the ground-state spin transition (3 V) act as a resonance check, initialising the optical transition at f_1. Next, a laser at f_2 (detuned from f_1) immediately probes the defect emission slightly off-resonance (for 2 ms), yielding a measurement of the (instantaneous) homogeneous line width with minimal disturbance. **b)** Experimental data showing near-lifetime-limited optical transitions, with the bottom (top) data corresponding to a waiting time of 5 µs (40 ms) between the f_1 and f_2 laser pulses (offset for clarity). Data are fitted to a Lorentzian with a FWHM of 39(3) MHz (44(6) MHz). The threshold is set to $T = 7$ during the f_1 pulse. **c)** Data and fits as in (b)(bottom), scanning f_2 around f_1, when f_1 is set at different frequencies (various shades of red) within the broad inhomogeneous line measured in Fig. 5.1g (arbitrary offset on x-axis). **d)** Measured f_2 center frequency as a function of the set f_1 frequency. The defect emission frequency can effectively be tuned over a 2 GHz range. **e)** Corresponding homogeneous linewidth extracted from (c), showing near-lifetime-limited coherence across the full range.

Our method minimally disturbs the system, which is different compared to commonly used methods involving scanning a laser over the transition. For such scanning methods, laser-induced diffusion can result in distorted lineshapes[10], or inaccurate (or even unphysical) linewidths due to limited photon statistics[8]. In our method, the minimum time the system is perturbed by the laser, is set by the length of the 'check'-(probe-)block required to obtain enough photon statistics to reliable discern the targeted spectral configuration from other configurations (2 ms in our experiments). Hence, the set time of the 'check'-block introduces a trade-off between the ability to discern such configurations and the amount of spectral diffusion introduced within this block. Independent characterisation of the diffusion rates (as in Fig. 5.3), allows for an informed decision on this trade-off.

We demonstrate the fast spectroscopy method on the same V2 center as used in Figs. 5.2 and 5.3 (Methods) and observe near-lifetime limited transitions (~ 39 MHz

versus predicted 22 MHz[14]), see fig. 5.4. Note that these numbers are not corrected for power broadening (optical Rabi frequencies are estimated to be ∼ 30 MHz, see Fig. 5.5). Additionally, to verify our previous inference that spectral diffusion is virtually absent in the dark (Fig. 5.3c), we insert a 40 ms waiting time between the f_1 and f_2 pulses (Fig. 5.4b, top), which does not increases the line width within the fit error. Importantly, this allows for the preparation of the transition at a specific frequency, 'storing' it in the dark, so that it can be used to produce coherent photons at a later time. Furthermore, the broad nature of the inhomogeneous line depicted in Fig. 5.1f, enables probabilistic tuning of the emission frequency over a 2 GHz range[21]. We demonstrate this by varying the f_1 frequency, initialising the emitter at different spectral locations, and probing the transition with the NIR laser at frequency f_2 (Fig. 5.4c, d and e). Such tuning of the V2 emission frequency without the need for externally applied electric fields[25,31], might open up new opportunities for optically interfacing multiple centers.

5.5. Landau-Zener-Stückelberg interference

Finally, we use the fast spectroscopy method to resolve Landau-Zener-Stückelberg (LZS) interference fringes in the optical spectrum[32]. Such fringes demonstrate coherent control of the orbital states of the V2 defect using MW frequency electric fields, and allow for the independent determination of the optical coherence and Rabi frequency[32], allowing for the separation of their contributions to the linewidths measured in Fig. 5.4.

LZS interference fringes can arise when a strong AC electric field shifts the optical transition across the laser frequency multiple times within the coherence time of the emitter[25,33]. Each time a crossing occurs, the emitter is excited with a small probability amplitude and associated 'Stückelberg' phase. These amplitudes can interfere constructively or destructively, creating interference fringes (see Ref. Shevchenko et al[32] for an extensive review on the phenomenon).

In our setup, MW radiation is applied by running an AC current through a (aluminum alloy) wire spanned across the sample (Fig. 5.5a). The original purpose of the wire is to enable mixing of the ground-state spin in the 'check' and 'probe' blocks used in Fig. 5.4. However, this geometry also creates significant *electric* fields at microwave frequencies(Fig. 5.5a). Taking the defect ground and excited states as basis states ($|g\rangle = |0\rangle$ and $|e\rangle = |1\rangle$), we can describe the effect of the electric field by considering the Hamiltonian (in the rotating frame of the emitter)[33]:

$$H = \frac{\Omega}{2}\sigma_x + \frac{\delta + A\cos(\omega t)}{2}\sigma_z,\qquad(5.2)$$

where Ω is the optical Rabi frequency, δ is the detuning between the optical transition and the laser frequency, A is the stark-shift amplitude (dependent on the electric field amplitude), ω is the MW driving frequency and σ_x, σ_z are the Pauli spin matrices. For the experimental parameters used in this work, the system is considered to be in the 'fast-passage' regime (defined as $A\omega \gg \Omega^2$[32]), meaning the excitation probability amplitude during a single crossing is small (Methods). In this regime, the spectral response of the
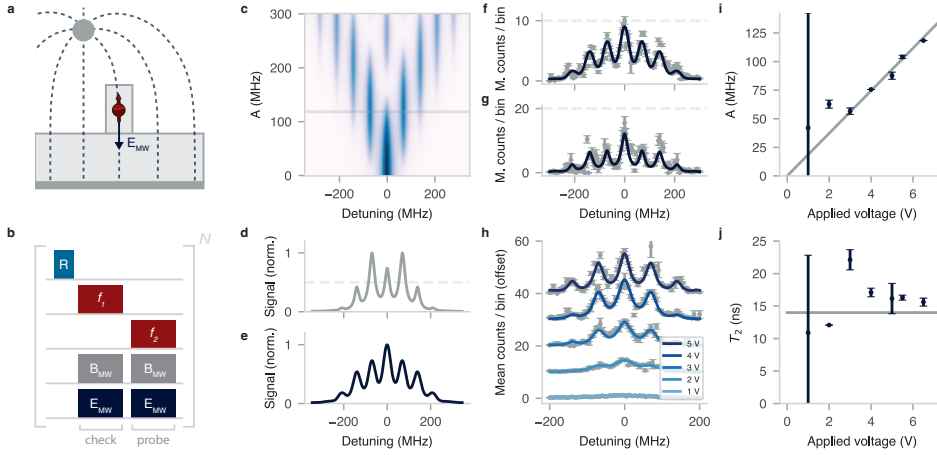
Figure 5.5: **Landau-Zener-Stückelberg (LZS) interference. a)** Schematic showing the electric-field lines generated by the MW drive, connecting the bond wire and ground plane (dark grey, not drawn to scale). The electric field can generate a significant stark shift of the V2 center. **b)** Sequence schematic, as in Fig. 5.4a, but now explicitly including the electric field components (E_{MW}). **c)** Characteristic LZS interference pattern (theory) as function of the laser detuning from resonance, and the electric field strength A. At higher electric fields, multiple side bands emerge, at multiples of the driving frequency $\omega = 70$ MHz. **d)** Line cut through (c) for $A = 118$ MHz. The dashed line denotes an example set threshold T. **e)** Experimental signal that would be observed from (d). The minimum counts threshold is passed also when one of the side bands (at ± 70 MHz) is on resonance with f_1, modulating the signal. **f)** Mean detected counts as a function of the two-laser detuning when the MW amplitude is set to 6.5 V, approximately equal to the value in (d). The threshold ($T = 10$) is set to about half the maximum amplitude, as in (d). The fit function (solid line) is obtained by fitting the dataset for a range of threshold values (see Supplementary Fig. 5.9). **g)** Same dataset as in (f), but with $T = 20$. The changing signal shape with the set threshold is well-captured by the fit. **h)** Experimental data (grey) and fit (solid lines) as in (f), varying the applied voltage ($T = \{2, 7, 11, 14, 16\}$). Data are offset by 10 counts for clarity. **i)** Extracted electric field strength A as a function of the applied voltage. Solid grey line is a linear guide to the eye. **j)** Extracted optical coherence time T_2. Solid grey line denotes the life-time limit for $T_1 = 7$ ns.

emitter (i.e. the time-averaged excitation probability), is given by[32]:

$$P_e = \frac{1}{2} \sum_k \frac{\Omega_k^2}{\frac{1}{T_1 T_2} + \frac{T_2}{T_1}(k\omega - \delta)^2 + \Omega_k^2},$$ (5.3)

where $\Omega_k = \Omega\, J_k\left(\frac{A}{\omega}\right)$, with J_k the Bessel function, and T_1, T_2 the emitter's optical relaxation and coherence time respectively. Figure 5.5c shows the optical spectrum as a function of A, obtained by evaluating Eq. 5.3 for our sample parameters. At higher electric field amplitudes (i.e. higher A), multiple characteristic interference fringes, spaced by the driving frequency ω (here 70 MHz) arise next to the central resonance, creating a complex optical spectrum.

Measuring such complex spectra with the fast optical spectroscopy method requires taking into account signal distortions resulting from the minimum-threshold setting. To see why this is the case, we refer to an exemplary theoretical spectrum plotted in Fig. 5.5d (for $A = 118$ MHz, grey line in figure 5.5c), where the threshold T is set to

about half the maximum signal amplitude (dashed line in Fig. 5.5d). Such a threshold is passed not only when the central peak is on resonance with f_1, but also when one of the nearest fringes is on resonance with the laser. Averaging over these possible configurations creates a distorted, convoluted spectrum, as shown in Fig. 5.5e. Note that this mapping is generally not unique, and retrieving the original signal may be challenging. Nevertheless, by varying the set threshold in post-processing, and accounting for the expected distortion, we can reduce such ambiguity, and retrieve the underlying signal (see Supplementary Fig. 5.9).

To experimentally measure the LZS interference signal, we execute the sequence drawn in Fig. 5.5b. Note that the electric field components generated by the MW drive are now explicitly included in the schematic. These components were also (implicitly) present in previously discussed experiments (Fig. 5.4), but their effects could largely be neglected under the condition: $\omega > A$[32]. We set the MW driving frequency ω to $\Delta_{GS} = 70$ MHz, so that the magnetic field components efficiently mix the spin states[14,34], and set the (peak-to-peak) MW amplitude between the wire and the ground plane to 6.5 V. Figures 5.5f and g show the measured spectrum for a threshold of $T = 10$ and $T = 20$ respectively. The former corresponds roughly to the example threshold in Fig. 5.5d, and the observed signal matches well with the expected (distorted) spectrum in Fig. 5.5e. However, setting $T = 20$ significantly alters the measured spectrum, highlighting the interplay between the set threshold and corresponding distortion. The solid lines correspond to a single fit of the complete dataset using Eq. 5.3, incorporating the distortion of the signal for a range of threshold values ($1 < T < 21$, post-processed).

We repeat this procedure while varying the MW amplitude (Fig 5.5h) and extract A and the optical T_2 coherence time from the fit (Figs 5.5i and j), fixing the optical relaxation time to 7 ns[14] and ω to 70 MHz. For amplitude values above 2 V we observe a linear relation between the MW amplitude and A, as expected. For lower values, a significant deviation is observed, possibly because the system is no longer well-described by the fast-passage limit (i.e.: $A\omega \sim \Omega^2$). Indeed, from the > 2 V data points, the optical Rabi frequency is estimated to be 30(6) MHz, on the order of $\sqrt{A\omega}$ (brackets denote Std.). Finally, examining the values for the optical coherence in the same way, we find $T_2 = 17(3)$ ns, approximately equal to the lifetime-limit set by: $T_2 = 2\,T_1 \approx 14$ ns[14].

The observation of lifetime-limited optical coherence in commercially available material highlights the potential of the V2 center, and the silicon carbide platform, for quantum-photonic technologies. Next to that, the ability to modulate the spectral response of the emitter, as demonstrated here, might enable its use as an MW-to-optical interface[33].

5.6. DISCUSSION AND CONCLUSION

In this work, we introduced a high-bandwidth *check-probe* scheme that allows for characterisation of spectral diffusion and ionisation processes under the influence

of external perturbations. Moreover, it enables measurements of the homogeneous transition linewidth of single quantum emitters, while only introducing minimal system disturbance. The systematic, quantitative investigation of diffusion and ionisation rates demonstrated here, provides insights in the quality of host materials and fabricated nanostructures in which solid-state defects live.

Furthermore, the observation of optical coherence of the V2 center in commercially available silicon carbide, further establishes it as promising next-generation candidate for quantum-networking experiments. Despite of the high levels of spectral diffusion under laser illumination, we find that that optical transitions are stable in the dark, and can be preserved over second timescales. In fact, we showed that the reconfigurable charge environment can be used as a resource, enabling probabilistic tuning of the defect emission frequency over a few gigahertz range, without the need for strong applied electric fields[21,25,31]. Finally, our methods can be readily transferred to other platforms where spectral diffusion forms a natural challenge, such as rare-earth doped crystals[35] or semiconductor quantum dots[22], and might enable new insights in the charge-environment dynamics of such systems.

5

5.7. Methods

5.7.1. Sample parameters

The sample was diced directly from a 4 inch High-Purity Semi-Insulating (HPSI) wafer obtained from the company Wolfspeed, model type W4TRF0R-0200. We note that the HPSI terminology originates from the silicon carbide electronics industry. In the quantum technology context considered here, this material has a significant amount of residual impurities (order $\sim 10^{15}\,\mathrm{cm}^{-3}$ according to Son et al.[23]) and is hence considered low purity with respect to a concentration of $\sim 10^{13}\,\mathrm{cm}^{-3}$ typical for epitaxially grown layers on the c-axis of silicon carbide[10,36]. On a different sample, diced from a wafer with the same model type, a Secondary-Ion Mass Spectroscopy (SIMS) measurement determined the concentration of nitrogen donors as $[\mathrm{N}] = 1.1 \times 10^{15}\,\mathrm{cm}^{-3}$. In addition to intrinsic silicon vacancies, we generate additional silicon vacancies through a 2 MeV electron irradiation with a fluence of $5 \times 10^{13}\,\mathrm{cm}^{-2}$. We study individual centers in a confocal microscope setup. To enhance the optical collection efficiency and mitigate the unfavourable V2 dipole orientation for confocal access along the SiC growth axis (c-axis), we fabricate nanopillars. We deposit 25 nm of Al_2O_3 and 75 nm of nickel on lithographically defined disks. A subsequent SF_6/O_2 ICP-RIE etches the pillars, see figure 5.1c. The nanopillars have a diameter of 450 nm at the top and 650 nm at the bottom and are 1.2 µm high.

5.7.2. Magnetic field

For the fast optical spectroscopy measurements in Fig. 5.4, we apply an external magnetic field of ≈ 1 mT along the defect symmetry axis (c-axis). All other experiments are performed at approximately zero field. We apply the field by placing a permanent neodymium magnet outside the cryostat. We align it by performing the sequence depicted in Fig. 5.1e, with f_1 set at the center frequency of the broad resonance (Fig. 5.1f), and monitoring the average photoluminescence (f_1 pulse is set to 2 ms). A (slightly) misaligned field causes spin-mixing between the $m_s = \pm\frac{3}{2}$ and $m_s = \pm\frac{1}{2}$ subspace, which increases the detected signal. Minimising for the photoluminescence thus optimises the field alignment along the symmetry axis.

5.7.3. Fast-passage regime (LZS)

The fast-passage regime is defined by: $A\omega \gg \Omega^2$ [32], with $\omega = 70$ MHz. From the measurements in Fig. 5.4, we can estimate: $\Omega < 40$ MHz. Furthermore, we can get a rough estimate for A by approximating the electric field at the defect to be: $E \approx \frac{U}{d}(\epsilon + 2)/3$, with U the applied voltage, $d \approx 500$ µm the distance between the wire and the ground plane and $\epsilon \approx 10$ the dielectric constant of silicon carbide (using the local field approximation[25]). There is some debate on the value of the Stark-shift coefficient[25,31]. Here, we take the value from Ref.[25]: $3.65\,\mathrm{GHz\,m\,MV^{-1}}$ and estimate $A \approx 29$ MHz for an applied voltage of 1 V. Hence, $A\omega > \Omega^2$ for $U > 1$ V, and the fast-passage requirement is satisfied for most measurements in Fig. 5.5. The excellent agreement between the data and our

model (especially for higher values of U) and the corresponding extracted values for Ω and A further the justify using the fast-passage solution of the LZS Hamiltonian.

5.8. SUPPLEMENTARY INFORMATION

5.8.1. SPECTRAL DYNAMICS MODEL DERIVATION

The Lorentzian spectral propagator is given by[29]:

$$P_f(t) = \pi^{-1} \frac{\frac{1}{2}\gamma(t)}{f^2 + \left(\frac{1}{2}\gamma(t)\right)^2}, \tag{5.4}$$

where f is the detuning from resonance. The FWMH $\gamma(t)$ is linear in time[29]:

$$\gamma(t) = \gamma_d\, t. \tag{5.5}$$

The mean counts obtained from a defect as a function of detuning f from the defect's resonance is described by:

$$\lambda_d(f) = \frac{\Gamma \bar{C}_0}{2} \frac{\frac{1}{2}\Gamma}{f^2 + \left(\frac{1}{2}\Gamma\right)^2}, \tag{5.6}$$

with $\bar{C}_0$ the observed counts on resonance and Γ the emitters homogeneous line width (FWHM). This Lorentzian is normalised such that $\lambda(0) = C_0$. We can add the effect of ionisation by describing the ionisation probability as:

$$P_i(t) = 1 - e^{-\gamma_i t}, \tag{5.7}$$

Here, γ_i is assumed to be independent of emitter detuning. However, if ionisation is caused by a two-photon process, we would expect the ionisation rate to scale with the square of the excitation rate:

$$\gamma_i(f) = \gamma_i^0 \left(\frac{(\frac{1}{2}\Gamma)^2}{f^2 + (\frac{1}{2}\Gamma)^2} \right)^2, \tag{5.8}$$

where γ_i^0 is the ionisation rate on resonance. Then,

$$\gamma_i = \int_{-\infty}^{\infty} P_f \gamma_i(f) df = \frac{\gamma_0}{2} \frac{\Gamma\gamma(t) + 2\Gamma^2}{(\gamma(t) + \Gamma)^2}. \tag{5.9}$$

The mean counts can then be calculated as:

$$\lambda(f, t) = (1 - P_i(t))\, \lambda_d(f), \tag{5.10}$$

Next, we integrate over the spectral density:

$$\bar{C}(t) = \int_{-\infty}^{\infty} P_f(t)\, \lambda(f, t)\, df, \tag{5.11}$$

which can be solved to yield:

$$\bar{C}(t) = \bar{C}_0 \frac{1}{1 + \gamma_d\, t/\Gamma} e^{-\gamma_i t}. \tag{5.12}$$

where we can either decide to model γ_i as a constant, or by equation (5.9). Additionally, if we neglect the recapture or de-ionisation rate, then for values of $t < 0$, effectively $\gamma_i = 0$.

5.8.2. MODEL PERFORMANCE AND DEPENDENCE ON SET COUNTS THRESHOLD

The model presented in the main text describes spectral diffusion caused by a macroscopic bath of fluctuating dipoles (described by the spectral propagator in Eq. 5.4). We can compare the performance of this model compared to other versions of the model, which restric certain parameters, for example one that assumes that no spectral diffusion (or ionisation) occurs. Supplementary Table 5.1 presents the description of the models we fitted to the data.

Sweeping the counts threshold value T, we observe that all models saturate to a range of values for higher T, consistent with the intuition that stringent thresholds initialise the emitter more precisely on resonance with the lasers. At very high tresholds ($T \gtrsim 35$), only very little data is available, and rates obtained with all models start to fluctuate heavily (due to the noisy data). Hence, we emperically determine a convergence region: $20 \leq T \leq 27$ (grey solid lines in Supplementary Fig. 5.6 and $12 \leq T \leq 21$ in Supplementary Fig. 5.7), over which we average to obtain the rates presented in the main text.

Comparing various goodness of fit metrics (reduced χ-squared, AIC, BIC), we learn that the model described in the main text (denoted Full), describes the data best (Supplementary Fig. 5.6j-l), providing insight in the nature of the defect charge environment and its dynamics.

5.8.3. DIFFUSION POWER DEPENDENCE

Here we plot the diffusion rates extracted by the method in figure 5.3 for different resonant and NIR laser powers. The data in figure 5.3 was averaged over the powers corresponding to the last two data points in figure 5.8a and b for the repump and NIR laser respectively.
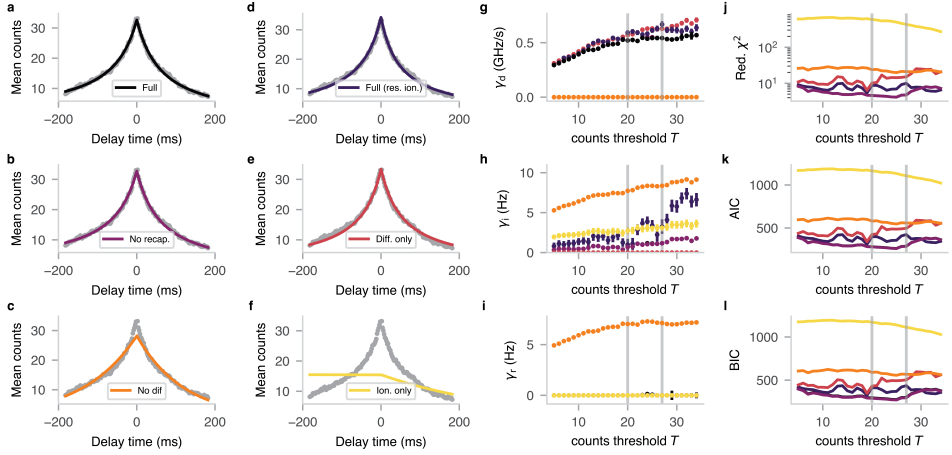
Figure 5.6: *Comparison of models for perturbation by the NIR lasers.* **a-f)** Data from Fig. 5.3d, overlayed with the various models, which are described in Supplementary Table 5.1. **g-i)** Estimated rates $\gamma_d, \gamma_i^0, \gamma_r$ as a function of counts threshold T for the different models. We observe a saturating behaviour for high T, as the defect is initialised in a more specific frequency range. For very high treshold values, the lack of data creates large fluctuations in the obtained rates. To determine the rate values in Supplementary Table 5.1, we take an average over the values indicated by the grey solid lines and take the standard deviation as uncertainty. **j-l)** Various goodness of fit models (reduced χ-squared, AIC, BIC) indicate that the model presented in the main text (Std.) captures the data best. Here, we also observe a saturation behaviour, where the sudden drop for very high T is attributed to overfitting due to lack of data. Colors in (g-l) match the models described in (a-f). Errorbars are based on photon shot noise (grey data), or represent fit uncertainties (panels g-i).
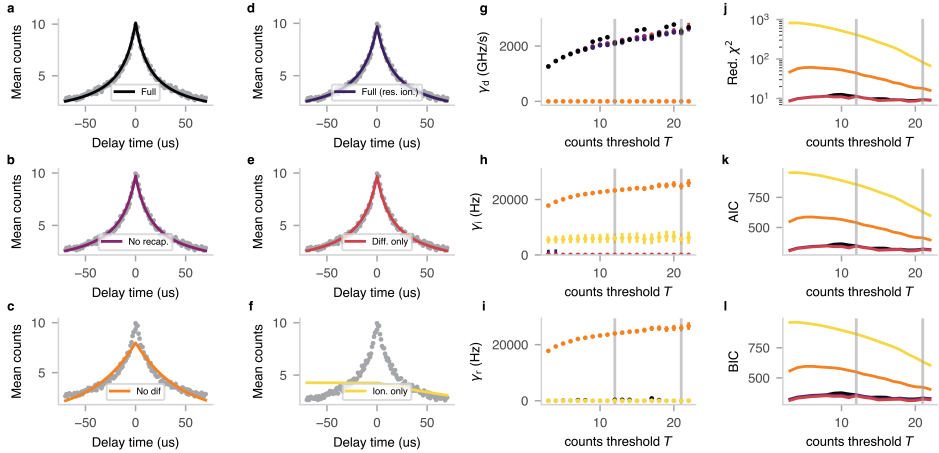

Figure 5.7: *Comparison of models for perturbation by the repump laser.* **a-i)** Same as Supplementary Fig.5.6, but for the data presented in Fig. 5.3e.

Table 5.1: Models used for fitting in Supplementary Figs. 5.6 and 5.7

Model name	Description
Full	$\bar{C}(t)/\bar{C}_0 = \begin{cases} \left(1+\gamma_\mathrm{d}\,t/\Gamma\right)^{-1}\,e^{-\gamma_\mathrm{i}t}, & \text{if } t > 0. \\ \left(1-\gamma_\mathrm{d}\,t/\Gamma\right)^{-1}\,e^{\gamma_\mathrm{r}t}, & \text{otherwise.} \end{cases}$
Full (res. ion.)	$\bar{C}(t)/\bar{C}_0 = \begin{cases} \left(1+\gamma_\mathrm{d}\,t/\Gamma\right)^{-1}\,e^{-\frac{\gamma_\mathrm{i}^0}{2}\frac{\Gamma\gamma(t)+2\Gamma^2}{(\gamma(t)+\Gamma)^2}\,t}, & \text{if } t > 0. \\ \left(1-\gamma_\mathrm{d}\,t/\Gamma\right)^{-1}\,e^{\gamma_\mathrm{r}t}, & \text{otherwise.} \end{cases}$
No recap.	$\bar{C}(t)/\bar{C}_0 = \begin{cases} \left(1+\gamma_\mathrm{d}\,t/\Gamma\right)^{-1}\,e^{-\gamma_\mathrm{i}t}, & \text{if } t > 0. \\ \left(1-\gamma_\mathrm{d}\,t/\Gamma\right)^{-1}, & \text{otherwise.} \end{cases}$
Diff. only	$\bar{C}(t)/\bar{C}_0 = \begin{cases} \left(1+\gamma_\mathrm{d}\,t/\Gamma\right)^{-1}, & \text{if } t > 0. \\ \left(1-\gamma_\mathrm{d}\,t/\Gamma\right)^{-1}, & \text{otherwise.} \end{cases}$
No diff.	$\bar{C}(t)/\bar{C}_0 = \begin{cases} e^{-\gamma_\mathrm{i}t}, & \text{if } t > 0. \\ e^{\gamma_\mathrm{r}t}, & \text{otherwise.} \end{cases}$
Ion. only	$\bar{C}(t)/\bar{C}_0 = \begin{cases} e^{-\gamma_\mathrm{i}t}, & \text{if } t > 0. \\ 1, & \text{otherwise.} \end{cases}$
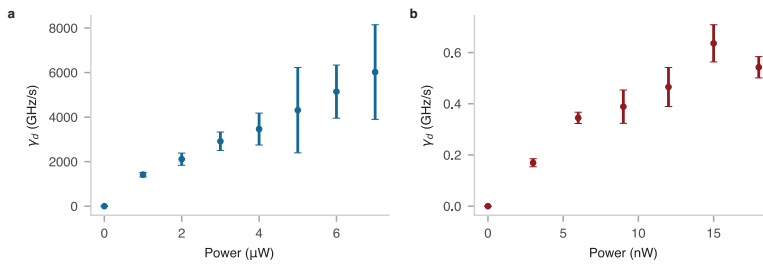
Figure 5.8: *Diffusion rates as function of laser power.* **a)** Diffusion rate γ_d as a function of applied repump laser power (785 nm, as in Fig. 5.3c). Data from 8-10 μW are omitted as the CR-check was not passed, due to drifting of the objective (leading to a diminished collection efficiency). **b)** Diffusion rate γ_d as a function of applied resonant laser power (916 nm, single laser). Data points for both panels are an average over fits with thresholds $T = \{10, 14, 18\}$, and error bars denote the standard deviation of the extracted rates. Laser powers are measured at the entrance of the objective. The rates presented in Fig. 5.3d are an average of the two final (saturation) data points for both panels (with their standard deviation as error bar).

5.8.4. LZS INTERFERENCE SIGNAL THRESHOLD DEPENDENCE

Here we show the experimental data that underlies the fitted parameters in figure 5.5i and j. For each voltage value, all data is fitted simultaneously, as mentioned in the main text.
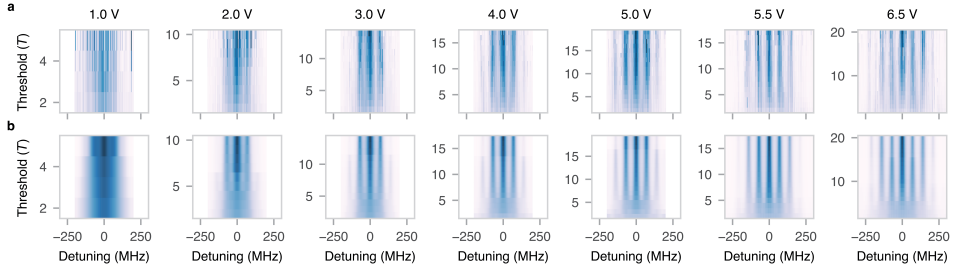

Figure 5.9: **LZS interference signal threshold dependence. a)** Experimental data underlying the extracted parameters presented in Fig. 5.5i and j (applied voltage annotated), as a function of the two-laser detuning $(f_2 - f_1)$ and the set threshold T. **b)** Fit of the data in (a), using only three free fit parameters: A, Ω and T_2, together with a general scaling and offset. The fixed fit parameters ω and T_1 are set to 70 MHz and 7 ns, respectively. The dependence on T is fixed by the model.

5.8.5. LITERATURE REVIEW ON SILICON CARBIDE QUANTUM EMITTER LINEWIDTHS

In this section we provide an overview of the work done using silicon vacancies and divacancies in silicon carbide in the context of optical coherence. In table 5.2, we report on multiple parameters that can impact the optical coherence. These parameters include the defect generation method, the annealing strategy, the measured optical absorption linewidth, material parameters of the layer that contains the investigated defect, and the use of a potential nanostructure for efficient light extraction.

Work	Defect	Defect generation	Annealing	PLE linewidth	Sample parameters in the defect layer	Nanostructure
Banks 2019[34]	V2	e: 1e12 cm⁻², 2 MeV	-	~65 MHz	18µm n-doped epi layer. [N]=~3e14 cm⁻³	-
Nagy 2019[36]	V1	e: 1e12 cm⁻², 2 MeV	30 m, 600°C	~60 MHz	110µm [²⁸Si]>99.85%, [¹³C]>99.98% epi layer. [N] = ~3.5e13 cm⁻³	SIL
Udvarhelyi 2020[27]	V1 & V2	e: 1e13 cm⁻², 2 MeV	30 m, 600°C	~100 MHz	110µm [²⁸Si]>99.85%, [¹³C]>99.98% epi layer. [N]=~3.5e13 cm⁻³	SIL
Nagy 2021[37]	V2	e: 1e13 cm⁻², 2 MeV	-	~300 MHz*	[N]=~5e13 cm⁻³	-
Babin 2022[14]	V2	He⁺: 1e11 cm⁻², 6 keV	30 m, 600°C	~25-40 MHz	110µm [²⁸Si]>99.85%, [¹³C]>99.98% epi layer. [N]=~4e13 cm⁻³	-
Babin 2022[14]	V2	e: 5e11 cm⁻², 2 MeV	30 m, 600°C	Best: ~30 MHz	28µm [²⁸Si]>99.85%, [¹³C]>99.98% epi layer. [N]=~3e15 cm⁻³	Triangular waveguides
Lukin 2020[25]	V2	e: 1e13 cm⁻², 2 MeV	30 m, 300°C	~100 MHz	100µm ²⁸Si¹³C epi layer.	-
Lukin 2020[25]	V2	e: 5e12 cm⁻², 23 MeV	30 m, 300°C	~100 MHz	100µm ²⁸Si¹³C epi layer.	-
Lukin 2023[38]	V2	e: 1e13 cm⁻², 2 MeV	2 h, 550°C†	~40 MHz	20µm n-doped epi layer. [N]=~2e13 cm⁻³	Disk resonator
Fang 2023[20]	V1	e: 2.3e12 cm⁻², 10 MeV	30 m, 500°C	~60 MHz	80µm epi layer. [N]=~2e13 cm⁻³	SIL
Christle 2017[39]	VV	e: 5e12 cm⁻², 2.5 MeV	30 m, 750°C	~2 GHz	730 µm sublimation epitaxially grown 3C-SiC layer. [N]~5e15 cm⁻³	-
Christle 2017[39]	VV	e: 5e12 cm⁻², 2 MeV	30 m, 745°C	~100 MHz	120 µm 4H-SiC epi layer. [N]<5e13 cm⁻³	-
Miao 2019[33]	VV	e: 3e12 cm⁻², 2 MeV	30 m, 850°C	~21 MHz	20µm i-type epi layer. [N]<1e15 cm⁻³	-
Anderson 2019[19]	VV	-	-	~31 MHz	-	-
Crook 2020[40]	VV	e: 1e16 cm⁻², 2 MeV	30 m, 850°C	~4 GHz	n-p-n-i-n epi layers. ([N_n]=1e18, [Al_p]=1e18, [N_i]<1e15) cm⁻³	Photonic crystal cavity
Anderson 2022[41]	VV	e: 1e13 cm⁻², 2 MeV	810°C	<0.5 GHz	90µm [²⁸Si]>99.85%, [¹³C]>99.98% epi layer. [N]=~6e13 cm⁻³	No nanostructure

Table 5.2: Sample parameters on literature publications that demonstrated PLE measurements with silicon vacancy ($V1$, $V2$) defects and divacancy (VV) defects in silicon carbide. A dash (-) indicates the information is not specified in the respective publication. *: Increased linewidth attributed to global sample properties, such as an increased Fermi level due to the elevated [N], rather than defect density. †: Annealing tailored to HSQ bonding for sample preparation.

5

5

REFERENCES

[1] G. Waldherr *et al.*, *Quantum error correction in a solid-state hybrid spin register,* Nature **506**, 204 (2014).

[2] J. Cramer *et al.*, *Repeated quantum error correction on a continuously encoded qubit by real-time feedback,* Nature Communications **7**, 11526 (2016).

[3] M. H. Abobeih *et al.*, *Fault-tolerant operation of a logical qubit in a diamond quantum processor,* Nature **606**, 884 (2022).

[4] M. Pompili *et al.*, *Experimental demonstration of entanglement delivery using a quantum network stack,* npj Quantum Information **8**, 1 (2022).

[5] C. M. Knaut *et al.*, *Entanglement of Nanophotonic Quantum Memory Nodes in a Telecommunication Network,* (2023), arXiv:2310.01316 [quant-ph].

[6] M. Pompili *et al.*, *Realization of a multinode quantum network of remote solid-state qubits,* Science **372**, 259 (2021).

[7] S. L. N. Hermans *et al.*, *Qubit teleportation between non-neighbouring nodes in a quantum network,* Nature **605**, 663 (2022).

[8] L. Orphal-Kobin *et al.*, *Optically Coherent Nitrogen-Vacancy Defect Centers in Diamond Nanostructures,* Physical Review X **13**, 011042 (2023).

[9] J. Wolters, N. Sadzak, A. W. Schell, T. Schröder and O. Benson, *Measurement of the Ultrafast Spectral Diffusion of the Optical Transition of Nitrogen Vacancy Centers in Nano-Size Diamond Using Correlation Interferometry,* Physical Review Letters **110**, 027401 (2013).

[10] J. Heiler *et al.*, *Spectral stability of V2-centres in sub-micron 4H-SiC membranes,* (2023), arXiv:2310.12617 [physics, physics:quant-ph].

[11] M. K. Koch, V. Bharadwaj and A. Kubanek, *Limits for coherent optical control of quantum emitters in layered materials,* (2023), arXiv:2312.11090 [quant-ph].

[12] T. Basché, ed., *Single-molecule optical detection, imaging and spectroscopy* (VCH, Weinheim, 1997).

[13] H. Bernien *et al.*, *Heralded entanglement between solid-state qubits separated by three metres,* Nature **497**, 86 (2013).

[14] C. Babin *et al.*, *Fabrication and nanophotonic waveguide integration of silicon carbide colour centres with preserved spin-optical coherence,* Nature Materials **21**, 67 (2022).

[15] D. M. Lukin, M. A. Guidry and J. Vučković, *Integrated Quantum Photonics with Silicon Carbide: Challenges and Prospects,* PRX Quantum **1**, 020102 (2020).

5

[16] B. J. M. Hausmann *et al.*, *Fabrication of diamond nanowires for quantum information processing applications,* Diamond and Related Materials Proceedings of Diamond 2009, The 20th European Conference on Diamond, Diamond-Like Materials, Carbon Nanotubes and Nitrides, Part 1, **19**, 621 (2010).

[17] D. B. Higginbottom *et al.*, *Optical observation of single spins in silicon,* Nature **607**, 266 (2022).

[18] E. R. MacQuarrie *et al.*, *Generating T centres in photonic silicon-on-insulator material by ion implantation,* New Journal of Physics **23**, 103008 (2021).

[19] C. P. Anderson *et al.*, *Electrical and optical control of single spins integrated in scalable semiconductor devices,* Science **366**, 1225 (2019).

[20] R.-Z. Fang *et al.*, *Experimental Generation of Spin-Photon Entanglement in Silicon Carbide,* (2023), arXiv:2311.17455 [physics, physics:quant-ph].

[21] J. M. Brevoord *et al.*, *Heralded initialization of charge state and optical transition frequency of diamond tin-vacancy centers,* (2023), arXiv:2311.11962 [quant-ph].

[22] R. G. Neuhauser, K. T. Shimizu, W. K. Woo, S. A. Empedocles and M. G. Bawendi, *Correlation between Fluorescence Intermittency and Spectral Diffusion in Single Semiconductor Quantum Dots,* Physical Review Letters **85**, 3301 (2000).

[23] N. T. Son and I. G. Ivanov, *Charge state control of the silicon vacancy and divacancy in silicon carbide,* Journal of Applied Physics **129**, 215702 (2021).

[24] M. Ruf, N. H. Wan, H. Choi, D. Englund and R. Hanson, *Quantum networks based on color centers in diamond,* Journal of Applied Physics **130**, 070901 (2021).

[25] D. M. Lukin *et al.*, *Spectrally reconfigurable quantum emitters enabled by optimized fast modulation,* npj Quantum Information **6**, 1 (2020).

[26] D. R. Candido and M. E. Flatté, *Suppression of the Optical Linewidth and Spin Decoherence of a Quantum Spin Center in a p - n Diode,* PRX Quantum **2**, 040310 (2021).

[27] P. Udvarhelyi *et al.*, *Vibronic States and Their Effect on the Temperature and Strain Dependence of Silicon-Vacancy Qubits in 4H-SiC,* Physical Review Applied **13**, 054017 (2020).

[28] L. Fleury, A. Zumbusch, M. Orrit, R. Brown and J. Bernard, *Spectral diffusion and individual two-level systems probed by fluorescence of single terrylene molecules in a polyethylene matrix,* Journal of Luminescence **56**, 15 (1993).

[29] G. Zumofen and J. Klafter, *Spectral random walk of a single molecule,* Chemical Physics Letters **219**, 303 (1994).

[30] S. L. N. Hermans *et al.*, *Entangling remote qubits using the single-photon protocol: an in-depth theoretical and experimental study,* New Journal of Physics **25**, 013011 (2023).

[31] M. Rühl, L. Bergmann, M. Krieger and H. B. Weber, *Stark Tuning of the Silicon Vacancy in Silicon Carbide,* Nano Letters **20**, 658 (2020).

[32] S. Shevchenko, S. Ashhab and F. Nori, *Landau–Zener–Stückelberg interferometry,* Physics Reports **492**, 1 (2010).

[33] K. C. Miao *et al.*, *Electrically driven optical interferometry with spins in silicon carbide,* Science Advances **5**, eaay0527 (2019).

[34] H. B. Banks *et al.*, *Resonant Optical Spin Initialization and Readout of Single Silicon Vacancies in 4H-SiC,* Physical Review Applied **11**, 024013 (2019).

[35] C. Thiel, T. Böttger and R. Cone, *Rare-earth-doped materials for applications in quantum information storage and signal processing,* Journal of Luminescence **131**, 353 (2011).

[36] R. Nagy *et al.*, *High-fidelity spin and optical control of single silicon-vacancy centres in silicon carbide,* Nature Communications **10**, 1954 (2019).

[37] R. Nagy *et al.*, *Narrow inhomogeneous distribution of spin-active emitters in silicon carbide,* Applied Physics Letters **118**, 144003 (2021).

[38] D. M. Lukin *et al.*, *Two-Emitter Multimode Cavity Quantum Electrodynamics in Thin-Film Silicon Carbide Photonics,* Physical Review X **13**, 011005 (2023).

[39] D. J. Christle *et al.*, *Isolated Spin Qubits in SiC with a High-Fidelity Infrared Spin-to-Photon Interface,* Physical Review X **7**, 021046 (2017).

[40] A. L. Crook *et al.*, *Purcell Enhancement of a Single Silicon Carbide Color Center with Coherent Spin Control,* Nano Letters **20**, 3427 (2020).

[41] C. P. Anderson *et al.*, *Five-second coherence of a single spin with single-shot readout in silicon carbide,* Science Advances **8**, eabm5912 (2022).

5

6

Outlook: Coupled electron-spin clusters and photonic crystal cavities in silicon carbide

S.J.H. Loenen, G.L. van de Stolpe, L.J. Feije, G.M. Timmer, T.W. de Jong, A. Das, T.H. Taminiau

Electron-spin clusters are promising systems for multi-qubit registers and robust quantum memories for optically connected quantum networks. Additionally, they form a test bed to study the decoherence of a central spin due to the dynamics of a coupled electron-spin bath, and provide opportunities for enhanced sensing. A challenge for such electron-spin clusters is the ability to control the constituent spins as individual qubits. In this chapter, we propose and simulate an architecture to realise an electron-spin cluster based on individually controllable and dipolarly coupled V2 defects in a silicon carbide nanopillar. We consider He^+-ion irradiation for defect creation and micromagnets in close proximity to the nanopillar to create a local magnetic field gradient that allows individual qubit control. We conclude the first section by discussing the fabrication recipe and results of a sample fabricated to study such electron-spin clusters.

In the second part of this chapter, we study the integration of V2 defects in photonic crystal cavities to create Purcell enhancement. This is a key requirement for the efficient use of these defects in scalable quantum networks. We first demonstrate simulations on alligator-type photonic crystal cavities to create high-Q-over-V cavities for optical dipoles that couple to transverse magnetic modes, such as the V2 defect. We then finalize the chapter by discussing the development of a silicon-carbide-on-insulator platform, as well as the fabrication of photonic crystal cavities from this platform.

6.1. COUPLED ELECTRON-SPIN CLUSTER

Solid-state defects with a central electron spin and adjacent individually controllable nuclear-spin qubits form an interesting system for optically connected quantum network nodes[1–4]. Individual control of multiple electron-spin qubits provides an avenue to larger qubit registers (see also chapter 3) and nuclear-spin qubits coupled to these electron spins can provide robust quantum memories. Many approaches that maintain individual electron-spin qubit addressability rely on indirect qubit-qubit interactions via a quantum channel to establish two-qubit quantum logic. These include physical transport of qubits[5–7], or exploiting a photonic interface provided by the qubits[8–11]. While these approaches circumvent the typically short-range direct qubit interaction, they are not necessarily native to the quantum system under study, require additional hardware components, and can lead to additional losses stemming from the interface of the qubit with the quantum channel.

Electron-spin clusters coupled via intrinsic interactions form an interesting complementary method[12–14]. A advantage is the ability to use the same hardware for both individual spin control as well as two-qubit logic. Additionally, such clusters open up possibilities for quantum sensing[15,16], quantum simulations[17] and spin-chains[18–21]. A central challenge is the engineering of strong qubit-qubit coupling while maintaining individual addressability[14,16]. In this chapter, we propose an architecture for realising individually controllable dipolarly coupled electronic-spin qubits associated to V2 defects in silicon carbide. The architecture is based on a small number of V2 defects embedded in a nanopillar created via localized He*-ion irradiation, where individual control is achieved via proximal micromagnets. We first outline three configurations and corresponding use cases which we target to study in the context of quantum networks, and provide simulations on the required irradiation parameters and the corresponding projected qubit-qubit couplings. Based on this, we determine the required micromagnet configuration. With these insights, we present the fabrication of a device to study the three different configurations and corresponding use cases.

6.1.1. THREE ELECTRON SPIN-CLUSTER CONFIGURATIONS

In order to establish electron-spin clusters for quantum networks and robust quantum memories, we regard the three cluster configuration as depicted in figure 6.1. Using these configurations we target to develop and demonstrate control techniques and multi-qubit interactions that underpin the use of V2 defect clusters in quantum networks. In general, all configurations consider V2 spins embedded in nanopillars to boost the optical collection efficiency. Additionally, micromagnets (black bars in figure 6.1) are placed next to the nanopillars in order to create a magnetic field gradient over the nanopillar that detunes the ground-state transition frequencies of the spin-cluster defects. To drive the electron-spin qubits, we use a gold stripline (gold bar extending out of the configurations in figure 6.1). In the following, we will more concretely define the goals we set per configuration in line with the development of electron-spin clusters for quantum network. After discussing the goals, we provide simulations on the defect creation strategy and micromagnet placement in order to enable the realisation of these
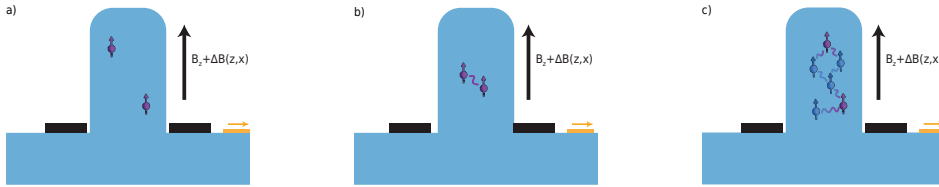
goals.

Figure 6.1: **Three different spin cluster configurations in nanopillars, not to scale. a)** Two optically addressible V2 defects (purple) in one nanopillar. The defects are spatially well separated so that their dipolar coupling is negligible and the micro-magnets (black) can create a large magnetic field gradient such to address these spins individually using a gold stripline (gold, extending out of the figure). **b)** Two dipolarly coupled electron spins with a spatial separation on the order of 10 nm. The micro-magnet allows for individual driving of the different spins. **c)** Extension of (b) to a spin cluster of multiple coupled, and magnetically individually addressable, electron spins. Two non-neighbouring electron spins are optically accessible spins (V2 defects). The other spins (blue) can serve as qubits or a quantum bus.

(a) **Configuration a):** This configuration consists of two (or more) V2 defect spins that are within a diffraction limited spot and not magnetically coupled. The goals here serve to develop intermediate steps for control techniques that we will use in multi-qubit registers. We will target to achieve the following three goals: 1) Demonstrate that we can optically address individual V2 centers, such that even if they would be close together, we can do selective optical state preparation and measurement. The different local environment of the V2 centers can detune their optical transition frequencies through which selective control is enabled[22]. 2) Eventually, we want to use micromagnets to detune the transition frequency of different V2 defects for individual control. This configuration serves as a testbed to show individual qubit Rabi driving, T_2^* and T_2 measurements in the presence of micromagnets. To avoid potential complex mulit-spin dynamics, the distance between multiple V2 defects is large such that their dipolar coupling can be neglected. 3) We target to control a small register of nuclear spins associated with one of the defects[23].

(b) **Configuration b):** This configuration consists of two optically individually addressable V2 electron spins within roughly 10 nm separation such that their dipolar coupling is on the order of 10 kHz. To make multiple electron spins operate as a quantum register, and to allow the transfer of quantum states on the electron-spin to nuclear spins associated with another electron spin, we need to demonstrate two-qubit logic. Building on the goals in configuration (a), we here target to 4) use one electron spin to sense the presence of another electron spin. This can potentially be done using the double-electron-electron-resonance technique explained in chapter 2 and used in chapter 3. 5) Having sensed a coupled electron spin, the next step is to demonstrate an electron-electron two-qubit gate, such as a controlled phase gate. Following the two-qubit gate, goal number 6) is to the generation of an entangled state distributed over the two electron spins[12,13,24] (see

also chapter 3). This demonstrates the ability to combine individual control, two-qubit control, initialisation and readout, all which are key ingredients for faithful operation of an electron spin cluster in a quantum network. Finally, 7) we want to combine the electron-electron two qubit gate with the developed nuclear-spin control to demonstrate the storage of an arbitrary quantum state in a nuclear spin qubit associated with an electron spin that is robust to stochastic evolution of another electron spin (see chapter 4).

(c) **Configuration c):** A spin cluster of dipolarly coupled electron spins of which at least two are optically addressable spins. Here these spins are associated to a V2 defect, but this is extendable to other optically addressible defects in silicon-carbide such as the V1 defect or the divacancy. Inspired by the ability to map the intra-nuclear-spin couplings[25–27] and electron-spin couplings[28–31] goal 8) is to map and characterise the electron-electron coupling strengths and positions. This information could be used to establish many-to-many qubit interactions, which relates to the final goal: 9) initialise an arbitrary quantum state on the first optically addressable spin, and transfer this state via intermediary electron spins to the other optically addressable electron spin[32,33]. Tomography can then be performed via direct optical readout of the qubit that holds the transferred state.

6.1.2. CLUSTER GENERATION SIMULATION

In this section, we explain how we propose to realise a cluster of coupled electron spins. First, we outline three requirements that we impose on the spin-cluster and subsequently show simulations with respect to the defect creation strategy and micromagnet configuration on how to achieve these requirements. For the defect creation, we propose to generate V2 defects via He^+-ion irradiation. Previous work demonstrated promising work on localized V2 defect generation with near-lifetime limited optical linewidths using this method[34]. The three requirements that we set for our spin cluster are the following:

1. To accompany individual optical addressability of different defects, we target to generate at maximum ~10 V2 defects per nanopillar. These defects are expected to cover a spectral distribution of ± 10 GHz[34].

2. Individual ground-state spin manipulation roughly requires $\delta_\omega = \omega_i - \omega_j > \frac{1}{T_2^*}$, where $\omega_i (\omega_j)$ is the transition frequency of electron spin $i(j)$ and T_2^* the minimum of their natural dephasing times. For moderate magnetic fields ($B > 300$ G), T_2^* times for V2 defects in SiC vary from ~1 μs to ~50 μs depending on the nuclear spin isotope concentration[35–37].
Additionally, a maximum gate time of t_{gate} with limiting crosstalk requires $\delta_\omega > \frac{1}{t_{gate}}$. We define a $\delta_\omega > 5$ MHz and thus allow gate times of ~1 μs.

3. To exploit double electron-electron resonance techniques for two-qubit controlled phase gates, the intra-electron couplings should exceed $\frac{1}{T_2}$. For V2 and similar defects created via electron irritation with fluences of $5e^{11}$-$1e^{12}$ in epitaxially grown layers, T_2 typically is ~ 1 ms[34,36]. Only recently we gained access to epi-

taxially grown layers in which purification is possible, while we already had commercially available bulk samples to our disposal. Therefore, the research proposed in this chapter is based our commercially available bulk samples. These have a natural nuclear spin concentration and a nitrogen concentration of [N]=1.1e^{15} as determined by secondary-ion mass spectroscopy. According to Bourassa et al[38], this gives T_2 times of 1 ms at fields of 500 Gauss. So we require the ZZ-coupling between electrons to exceed 10 kHz.

Based on the V2 creation yield of 8.5% reported for He$^+$-ion irradiation[34], we plot the mean number of V2 defects created by He*-ion irradiation on a masked silicon carbide sample for different irradiation doses in figure 6.2a. In this study we investigate circular masks with diameters of 60, 80 and 100 nm. While likely also other defects such as the V1 center and carbon vacancies are created, we here first just investigate the creation of V2 defects as that aligns with research goals (a) and (b). Knowledge of the creation yield of other paramagnetic defects easily allows to extend the data in figure 6.2 to incorporate those defects.
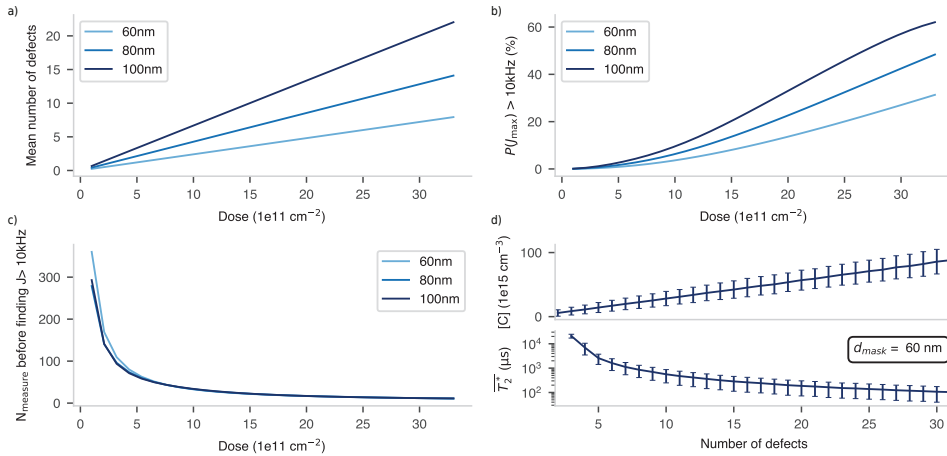
Figure 6.2: **Cluster parameters at different irradiation doses. a)** Mean number of defects per irradiation mask as a function of the irradiation dose for different irradiation mask diameters. **b)** Probability that at least one coupling in a spin cluster is larger than 10 kHz. **c)** Expected number of defects to investigate before a defect is found with a coupling larger than 10 kHz. **d)** Concentration of created defects and the associated dephasing timescale $\left(\overline{T_2^*}\right)$ purely caused by them. See the main text for the calculation of $\overline{T_2^*}$.

Subsequently we investigate what the probability is to find a V2-V2 dipolar coupling stronger than 10 kHz and correspondingly the number of defect to consider before a spin with that coupling is found. We simulate cases where we created N V2 defects and create many (2000) clusters for each N. We sample the lateral position of the defects such that the defect concentration is maximum in the middle of the mask and drops off radially following a Gaussian distribution with $\sigma_{xy} = r_{mask}$. For the irradiation depth, we also adopt a Gaussian distribution of defect generation with $\sigma_z = 25$ nm[34]. For each

cluster, we calculate all the dipolar couplings and the difference in position coordinates δ_x, δ_y and δ_z of the spins involved in the coupling. For each spin-cluster we calculate the probability to find a V2-V2 dipolar coupling stronger than 10 kHz.

The irradiation creates a Poisson distribution of the number of defects per irradiation spot[34], based on which we convert the data for spin clusters of N defects to the plots in figure 6.2b and c. Figure 6.2c indicates the mean number of defects to investigate before finding a defect that couples stronger than 10 kHz. We calculate this by the inverse of the probabilities shown in figure 6.2b multiplied by the quotient of the mean number of unique spins in a cluster that couple stronger than 10 kHz and the mean number of spins in a cluster.

Requirements 2 and 3 are based on T_2^* and T_2 times obtained from literature. In figure 6.2d, we analyse the dephasing purely caused by electron spins created in the irradiation process and call the associated timescale $\overline{T_2^*}$. To more easily incorporate the effect of creating additional defects alongside V2 defects, we analyse $\overline{T_2^*}$ based on the number of defects created in a cluster rather than the irradiation dose. We consider a regime where the quantisation axis of the electron spins associated with the created defects is set by the external magnetic field, treat the electrons as spin $\frac{1}{2}$ particles and calculate $\overline{T_2^*}$ of spin j as $\frac{2}{\sqrt{\sum_{i=1}^{N} A_{ij}^2}}$ with A_{ij} the zz-coupling between between spin i and j (see appendix 8.2.1). We correct for strongly coupled spins by rejecting all $A_{ij} > \frac{1}{2\pi \overline{T_2^*}}$ and recalculate $\overline{T_2^*}$ with the remaining A_{ij}. The results in figure 6.2d show that the dephasing $\overline{T_2^*}$ caused by the defects created by the irradiation process (up to ~30 created defects) is not expected to limit the dephasing time in experiments.

We calculate the electron spin concentration in the irradiation area by dividing the created number of defects by the volume of a cylinder with radius r_{mask} and height $2\sigma_z$. According to Cluster Correlation Expension (CCE) simulations by Bourassa et al[38], for natural isotope samples, paramagnetic spins start linearly decreasing T_2 below 1 ms from concentrations close to 1×10^{16} cm^{-3}. Already for 20 defects in the irradiation volume, the electron spin concentration is well above 1×10^{16} cm^{-3} and hence for such clusters the electron spins are expected to significantly contribute to the T_2 time. Using multi pulse decoupling schemes one might be able to extend the coherence time such that double electron-electron resonance techniques still allow high-fidelity controlled phase gates for electron-spin couplings of 10 kHz.

To individually manipulate the ground-state spin levels of individual defects that couple stronger than 10 kHz, we plan to use the magnetic field gradients created by micromagnets (see figure 6.1) to establish two well-separated transition frequencies of the involved defects. The required magnetic field gradient, and corresponding micromagnet design, is set by the typical electron-electron distance in a spin cluster. In figure 6.3a we plot the distribution of difference in x-position (δ_x) and z-position (δ_z) for the defects involved in couplings that are larger than 10 kHz. We omit the difference
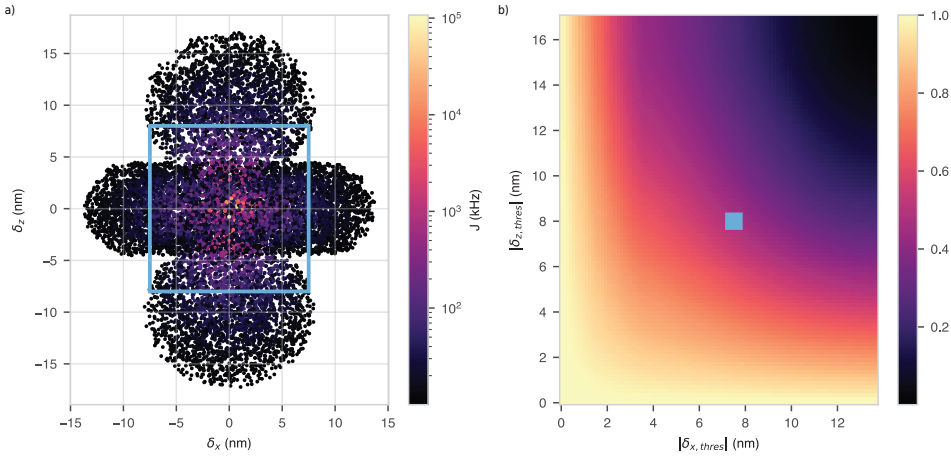
Figure 6.3: **Intra-spin distances for couplings > 10 kHz. a)** The distribution of δ_x- and δ_z-position for spins that couple stronger than 10 kHz. The colorbar indicates the coupling strength corresponding to the data-points. δ_y is not considered as our sample architecture (figure 6.4) does not create a magnetic field gradient in the y-direction. **b)** Given the data points in (a), the density plot defines what the probability is that, given one measures a coupling larger than 10 kHz, the electron spins involved in the coupling are individually address-able. Individually addressable is defined such that either over a distance $|\delta_{x,thres}|$ or over a distance $|\delta_{z,thres}|$ a transition frequency difference bewteen the two electron spins can be created that is larger than the thresh-old δ_ω required for individual control (see point 2 of the main text). The blue filled square (probability $\approx$ 50%) indicates the probability that a randomly sampled coupling of figure (a) lies outside of the blue window of figure (a).

6

in y-position (δ_y) as our micromagnet architecture does not generate a field gradient in the y-direction.

A realistic experimental situation is that we find access to a randomly placed defect within the spin cluster. Using that spin, we will set out to measure whether there is a coupling stronger than 10 kHz to another spin. We now target to get an estimate of what the likelyhood is that a measured coupling larger than 10 kHz involves two electron-spin qubits that are individually controllable. Electron-spin qubits are individually con-trollable if their transition frequency difference (δ_ω) is larger than a certain threshold (e.g. 5 MHz, see point 2 above). The transition frequency difference relates to the integral of the magnetic field gradient, created by the micromagnets, over the difference in position of the electron spins involved in the coupling. While the total transition frequency difference is set by an integral over both δ_z and δ_x, here we consider the simpler situation that a transition frequency difference is created purely by δ_x or purely by δ_z. This means that two spins are individually controllable if either their $|\delta_z|$ is above a threshold ($|\delta_{z,thres}|$), or if their $|\delta_x|$ is above a threshold ($|\delta_{x,thres}|$). These thresholds follow from the micromagnet configuration. In figure 6.3b we plot the probability that, if a coupling > 10 kHz is measured, the electron spins involved in that coupling have either $|\delta_z| > |\delta_{z,thres}|$ or $|\delta_x| > |\delta_{x,thres}|$. To balance the ability to generate well-separated transition frequencies (large δ_x, δ_z) while maintaining strong coupling (small δ_x, δ_z), we

target to develop a micromagnet configuration that can create a transition frequency difference larger than δ_ω over a distance $\{|\delta_x|, |\delta_z|\} \gtrsim 8$ nm, such that probabilities in figure 6.3b are around 50%, see blue square in figure 6.3b.
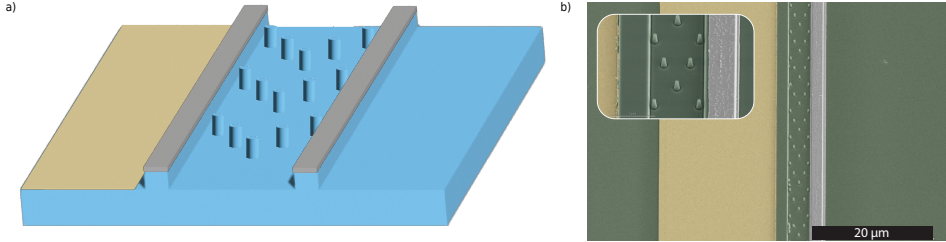

Figure 6.4: **Prototype of the proposed device. a)** 5 rows of nanopillars are embedded between two mirco-magnets (grey) residing on a ridge that is level with the nanopillars in order to maximally create B_z gradients near the top of the nanopillars, where defects are formed via He$^+$-ion irradiation. The stripline adjacent to one of the micromagnet serves to conduct electromagnetic fields that we plan to use to drive qubit transitions. **b)** Colored SEM image of the proposed architecture in (a), where only one 2 μm wide and 50 nm thick nickel micromagnet is deposited. The stripline (width 20 μm) material is gold. The nanopillars diameter and height are 300 nm and 600 nm respectively. The distance between the nanopillar edges is at least 2 μm to prevent confocal excitation/collection from unwanted nanopillars.

A schematic of the proposed device to simultaneously generate a frequency gradient, a driving field and sufficient optical collection is shown in figure 6.4a. Rows (5 in the schematic) of nanopillars are fabricated between two ridges of equal height as the nanopillars. The nickel (grey) deposited on the ridges serve as micromagnets to generate a transition frequency difference for closely spaced electron spins. The B_z gradient benefits from having the micromagnets level with the z-position of the defects, which for the He$^+$-ion irradiation we propose is ~40 nm alike what was shown by Babin et al.[34]. On the side of one ridge, a gold stripline enables electron spin driving. The edges of the nanopillars are separated by at least 2 μm to prevent optical excitation/collection from undesired defects. Figure 6.4b shows a colored SEM image of a prototype test sample, with only one nickel micromagnet deposited. The reader is referred to section 6.1.3 for the fabrication recipe.

In figure 6.5 we simulate the B_z and B_x field and their gradients for a configuration where the micromagnets are 2 μm wide, 100 nm thick and their centers are separated by 2 μm. From this we calculate the Hamiltonian terms in the z-direction $H_z = \gamma_e B_z$ and the x-direction $H_x = \gamma_e B_x$, with γ_e the electron gyromagnetic ratio. The simulations assume an external B_z field that exceeds the coercivity field of nickel (0.056 to 23kAm^{-1}, $\lesssim 300$ G[39]). In red, we show the B_x field generated by the 20 μm wide gold stripline left from the micromagnet ridges. This field is on par with B_x values on NV centers embedded in a SIL ~3 μm below the surface with a 20 μm stripline adjacent to the SIL. Hence the stripine is expected to allow likewise Rabi-frequencies. The green dotted lines represent the proposed center locations of the nanopillars with the He$^+$-ion irradiated V2 defects. At these locations we obtain gradients $\frac{dH_z}{dz} \approx 1$ MHznm^{-1} and $\frac{dH_z}{dx} \approx 2$ MHznm^{-1},

which enables selective driving for spins separated by 8-10 nm in the x- or z-direction.

Note that while also the H_x gradients are in the MHznm^{-1} range, the total H_x components remains below 100 MHz. Lower H_x values can be obtained by trading off for lower H_z and H_z gradients. Also, high external magnetic fields aligned with the z-axis reduce spin mixing caused by H_x. For some applications, such as photo luminescence excitation experiments without microwave control, off-axis magnetic fields serve an advantage [40]. The degree to which off-axis magnetic fields are acceptable for the research goals outlined in section 6.1.1 is for future studies. The framework and simulations presented here serve as a useful tool to investigate whether configurations are possible that e.g. simultaneously allow large transition frequency gradients with low off-axis fields.

To conclude this section, we developed a simulation tool that provides insight into the expected intra-electron coupling and position-differences within spin clusters created using He$^+$-ion irradiation. We used these couplings and position-differences to define a minimal distance of 8-10 nm over which micromagnets need to create a transition frequency difference δ_ω of two electron spins, such that they are individually addressable ($\delta_\omega > 5$ MHz), while maintaining a considerable likelyhood to obtain intra-electron coupling strengths above 10 kHz. We found that two nickel micromagnets of 2 μm wide, 100 nm thick and with their centers separated by 2 μm are promising to enable that for spin-clusters embedded in nanopillars between the micromagnets.

6

6.1.3. FABRICATION OF ELECTRON SPIN CLUSTER SAMPLES

The fabrication process of the sample in figure 6.4b is described in figure 6.6. We commence the fabrication by deposition of a tungsten height ring and markers. The markers enable precise overlay of multiple subsequent fabrication steps. The height ring is 0.5 mm wide and spans the entire circumference of the sample (with gaps to allow control lines originating from the edge of the sample). It allows the accurate determination of the sample surface via optical reflectometry measurements of the e-beam, which is not possible directly on the transparent 4H-SiC sample using the alignment tool in the used electron beam lithography tool. A 210 nm thick 200K PMMA A6 (AllResist 642.06) layer with holes of 60-100 nm serves as a mask for V2 defect generation by He$^+$-ion irradiation.
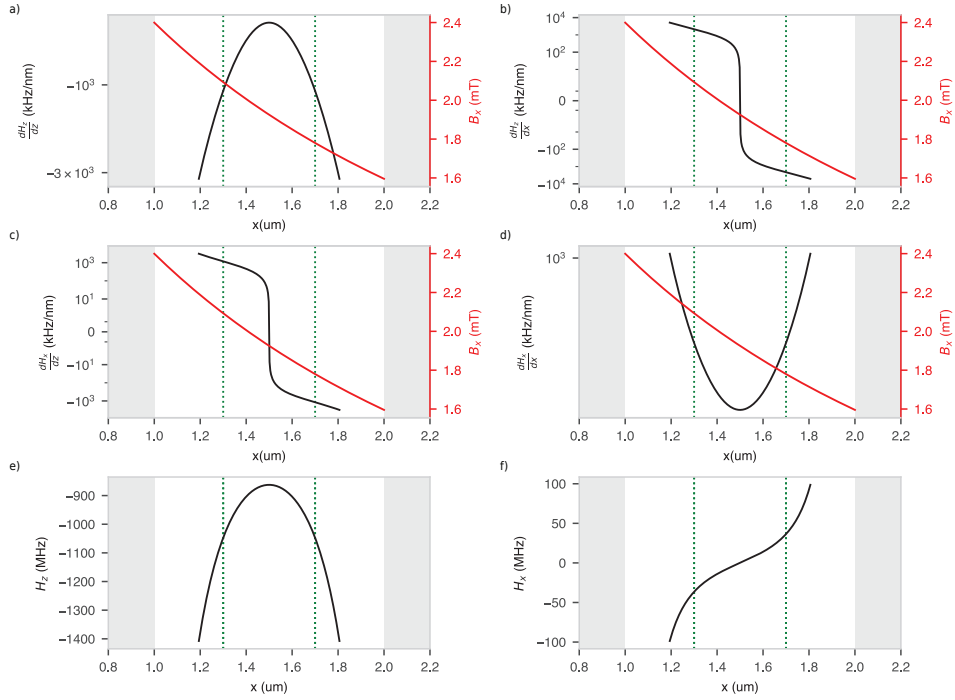
Figure 6.5: **Micromagnet Hamiltonian terms and gradients thereof (black), and B_x-field generated by the stripline (red).** Gradients of the H_z and H_x Hamiltonian terms in the x- and z-direction (a,b,c,d) and absolute H_z and H_x Hamiltonian terms (e,f) generated by two 2 μm wide, 100 nm thick micromagnets. The green dotted lines are the x-positions of the proposed nanopillars. The grey shaded area is the x-position of the micromagnet. The red line in (a,b,c,d) is the B_x field generated by the 20 μm wide stripline next to the left micromagnet (see figure 6.4). The B_x values are on par with B_x values on NV centers embedded in a SIL ~3 μm below the surface with a 20 μm stripline adjacent to the SIL.

Projected nanopillar and micromagnet locations are masked with a double layer hard mask of Al_2O_3 and nickel lithographically defined on the SiC sample before a subsequent SF_6/O_2 etch. The height ring and markers are maintained on the sample during the etch by also masking them with the double layer. The main purpose of the Al_2O_3 layer is to allow lift-off of the nickel hard mask to prevent nickel contamination on the nanopillars. Namely, nickel can potentially diffuse into the nanopillars and thereby hinder optical collection and create spurious magnetic fields as nickel is a ferromagnet. Nickel is removed in a HNO_3 wet etch and Al_2O_3 in a $H_2O : HF$ wet etch with a volume ratio of 7:1. Subsequently, see figure 6.6e, gold markers alongside a gold stripline are deposited. We use a 5 nm Titanium layer to ensure the gold layers adhere to the silicon carbide. The gold markers replace the tungsten markers that are etched away during a thorough piranha clean. In the last fabrication step, nickel micromagnets are deposited.

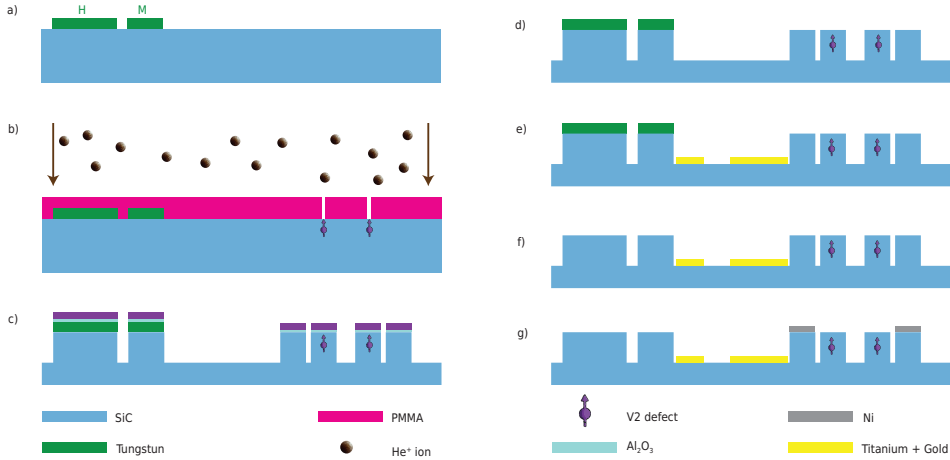Figure 6.6: **Fabrication of electron spin cluster sample (not to scale). a)** A Tungstun height ring (H) and markers (M) are deposited on the transparent silicon carbide sample. The height ring permits optical reflectometry measurements for the e-beam to accurately focus on the sample surface for subsequent steps. **b)** Irradiation holes ($60 - 100$nm diameter) are written in a PMMA mask followed by He$^+$-ion irradiation to generate V2 defects. **c)** The height ring, markers, nanopillar locations and mircomagnet ridges are covered with a double layer of Al_2O_3 and nickel before a subsequent SF_6/O_2 etch. **d)** Nickel and Al_2O_3 are stepwise removed by a HNO_3 and $H_2O : HF$ (volume ratio 7:1) wet etch respectively. The sacrificial Al_2O_3 prevents the nickel hard mask from sticking to the sample in the cleaning process. **e)** Deposition of the gold stripline. A 5 nm Titanium layer adheres the deposited gold. Additional gold markers are written to replace the Tungstun makers that etch away in step f). **f)** Piranha clean. **g)** Nickel micromagnet deposition.

Currently, a test sample (see figure 6.4b) is fabricated with the recipe of figure 6.6, excluding the He$^+$-ion irradiation step. The next steps involve the characterisation of the magnetic field gradients created by the micromagnets. This can first be done using electron spin resonance measurements on spins in different nanopillars created by electron irradiation, which is more easily accessible for us. Note that we have 5 rather than 2 nanopillars in figure 6.4. Electron irradiated samples also already allow to demonstrate all the goals listed in configuration (a) of section 6.1.1. We then plan to implement the lessons learned from these tests and demonstrations, and fabricate two samples according to the sample design of figure 6.5. One sample we plan to use for the goals outlined to configuration (b), and the other sample for the goals outlined according to configuration (c) of section 6.1.1.

6.2. NANOPHOTONIC INTEGRATION OF V2 DEFECTS

Modular optically interconnected quantum nodes in the architecture of figure 1.1 demand a coherent spin-photon interface for the efficient interference of indistinguishable zero-phonon line (ZPL) photons, required to distribute entanglement over the network. That means spectral tuning, high quantum efficiency, high Debye-Waller factor (DWF) and (near) Fourier linewidth-limited optical transition should be simultaneously satisfied[41]. However, the V2 defect suffers from a low DWF (8-9%[42]) and a

significant non-radiative decay rate that limits the cyclicity to about 8 photons[43,44]. This strongly motivates the integration of these defects in high-Q-over-V cavities, such that both the quantum efficiency and the DWF are Purcell enhanced[45]. In this section, we first briefly review demonstrations where the V2 defect was integrated in nanophotonic structures. Secondly, we present a cavity design, along with corresponding simulations, that has the potential to simultaneously achieve high Q-factors and low mode volumes for the V2 defect. Thirdly, we present the fabrication of these cavities using a silicon-carbide-on-insulator platform. We conclude by outlining different mechanims to tune both the cavity resonance and the V2 optical frequency such that Purcell enhancement of multiple indistinguishable emitters can be realized.

In the past years, building blocks towards efficient cavity integration of V2 centers have been demonstrated. Babin et al., integrated V2 defects in apexes of triangular waveguides while preserving narrow optical lines[34]. The large mode volume of those waveguides however limits the potentially achievable Purcell enhancement. Lukin et al. have demonstrated integration of the V1 center, which is similar the V2 center, in a small mode volume photonic crystal cavity[46]. However, their cavity design was optimized to boost optical dipoles that couple to optical modes with a transverse electric (TE) orientation, while the V2 defect possesses a dipole moment that couples to the transverse magnetic (TM) optical mode. Purcell enhancement of V2 defect centers was realized with micro-disk resonators that are optimised for optical dipoles that couple to a TM mode[40]. While these disk resonators enjoy high quality factors, they also have large mode volumes compared to photonic crystal cavities. In the following, we first simulate and then fabricate alligator-type photonic crystal cavities that have the potential to simultaneously realize high Q-factors and low mode volumes. Recently, a theoretical and experimental discussion on these cavities has been published[47,48].

Photonic crystal cavities consist of a region enclosed by the periodic modulation of high- and low-refractive-index material. This modulation creates optical bandgaps, much alike the electronic bandgaps in semi-conductor materials, that function as mirrors for optical frequencies of a certain mode. A theoretical architecture suitable for a large TM mode bandgap consists of floating pillars[50]. This is an inverse design with respect to the more common perforated waveguide structure, which boost large TE mode bandgaps[50 45 51].

However, floating pillars are extremely challenging to fabricate. While one could try to embed pillars of silicon carbide in a low refractive index material, here we pursue a homogeneous solution. We connect the pillars via a bridge and deform the pillars to ovals in order to maintain high Q-factors despite the connecting bridge. The unit cell of our proposed design is shown in figure 6.7a. We set the connecting bridge width $c_y = 50$ nm, close to the fabrication limit[52]. We now consider different geometries to create a large TM bandgap around the ZPL emission wavelength of the V2 defect (917 nm). Consequently, these regions serve as a mirror for the V2 ZPL emission. After a non-exhausitive optimization, we find the that the following geometry creates a large TM bandgap. The small axis of the oval is $b_x = 125$ nm, the long axis of the oval is
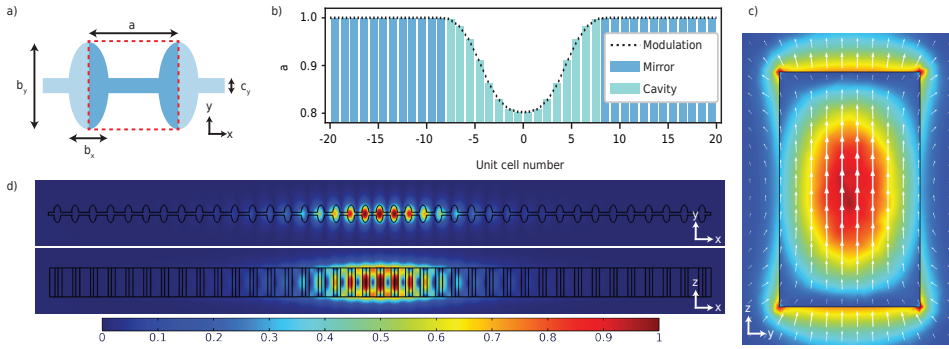
Figure 6.7: **Alligator photonic crystal cavity simulations. a)** Unit cell of the alligator-type cavity. A TM bandgap around 917 nm is created for $b_x = 125$ nm, $b_y = 300$ nm and $a = 311$ nm. $c_y = 50$ nm is the minimum set by the achievable fabrication. **b)** A cavity region is created by gradual modulation of the inter-oval spacing a. The y-axis indicates the a parameter relative to 311 nm as a function of the unit cell number. 917 nm propagation is allowed in the cavity region. See De Jong et al [49] for the modulation function. **c)** Electric field profile in a y-z crossection of a the middle of the cavity (unit cell number 0). **d)** Electric field profile and confinement in the alligator-type cavity defined by a) and b).

$b_y = 300$ nm and the inter-oval distance equals $a = 311$ nm [49].

We now present how we use the this geometry to realize a cavity for light of 917 nm. We achieve this by concatenating the unit cell in figure 6.7a and by adiabatically varying the inter-oval distance as shown in figure 6.7b. This simultaneously creates a region where 917 nm light is allowed and minimizes scattering at the mirror interfaces. The resulting electric field profile and intensities at the center of the cavity are shown in figure 6.7c and 6.7d. The extracted simulated quality factor and mode volume are 2.4×10^6 and $0.82(\lambda/n)^3$ respectively, with $\lambda = 917$ nm and n the silicon carbide refractive index at that wavelength. These numbers are comparable to simulations of TE-like photonic crystal cavities in silicon carbide [53].

Crucially light needs to be coupled in and out of these cavities. Effectively, this means the introduction of an additional loss channel, that, for an efficient coupling, should be more dominant than the other loss channels. This will reduce the (simulated) Q-factor. An in-depth study of optical in/out-coupling designs is an interesting future avenue. Potential strategies include 1) one-sided tapered fiber and waveguide coupling where one of the mirrors is made less reflective [54], 2) double-sided fiber coupling [55] and 3) evanescent coupling to an adjacent waveguide [56]. Coupling light in could alternatively be done confocally. If the cavity contains an emitter, the emitter can also be excited by a mode perpendicular to the allowed cavity mode.

In figure 6.8 we describe a wafer-scale compatible process we pursued to create the alligator-type cavities discussed above. This process was a joint effort with the Quantum Materials and Nanostructures group of the Fraunhofer IISB institute in Erlangen in Germany (from now on referred to as Fraunhofer) and NovaSiC (France). First, Fraunhofer
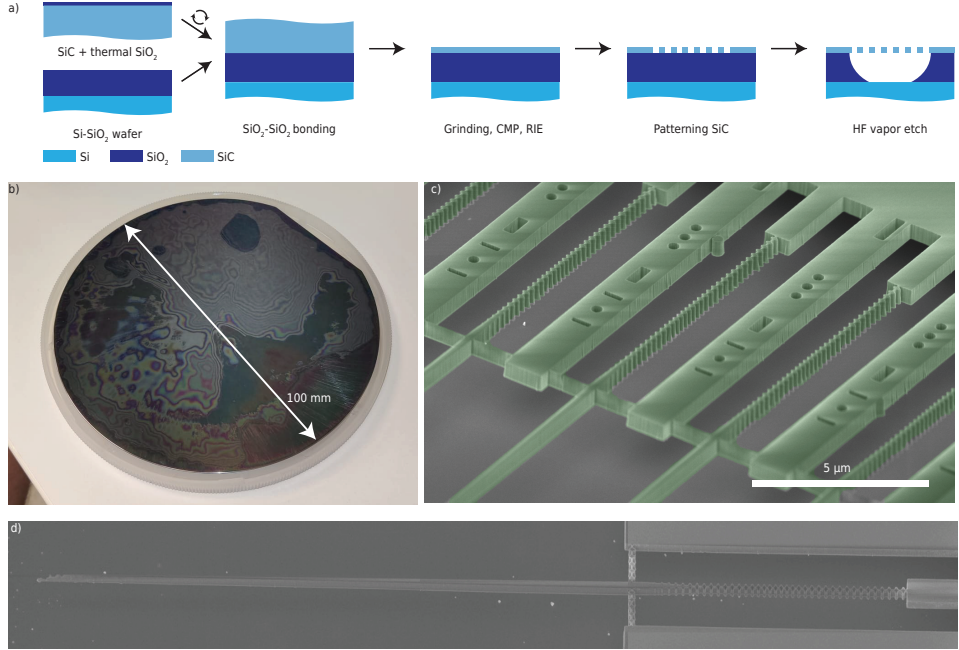
Figure 6.8: **Alligator photonic crystal cavity fabrication on SiCOI. a)** Fabrication process of a silicon carbide on insulator (SiCOI) wafer. After the grinding, chemical mechanical polishing and reactive ion etching, the wafer is thinned down to a desired thickness. The wafer is diced into smaller samples on which nanofabrication is performed. Undercutting patterns is enabled by a HF vapor etch of the sacrificial SiO_2 layer. **b)** SiCOI after grinding and CMP. The interference fringes signify different SiC thicknesses. The CMP of this wafer lead to a lot of SiC being delaminated from the SiO_2. **c)** Alligator photonic crystal cavities fabricated using the recipe in (a) and an Al_2O_3 + nickel hard mask. The squares and holes in the rectangles are purely used as cavity identifiers. **d)** Zoom in of one alligator cavity with adjacent tapered waveguide to allow fiber coupling.

created a 100 mm diameter silicon-carbide on insulator (SiCOI) wafer (see figure 6.8b), inspired by Lukin et al[46]. 30 nm SiO_2 was grown on a commercial 500 μm thick silicon-carbide wafer and subsequently this was bonded to a $Si - SiO_2$ wafer stack. Successively, NovaSiC grinded and chemically mechanically polished (CMP) the stack such that a few μm of SiC was left. We then use a reactive ion etch to thin down the silicon carbide to the desired cavity thickness before we pattern the cavity using a hard mask. The cavities in figure 6.8c are created using a nickel hard mask. Free-standing cavities are obtained via a vertical SF_6/O_2 etch of the silicon carbide and a HF vapor etch of the SiO_2 layer. To couple light in and out of the cavity, we fabricate a tapered waveguide on the cavity, see figure 6.8d. Figure 6.8b shows a SiCOI wafer after grinding and CMP of our first batch. The interference pattern indicates different SiC thicknesses on the sample. Also, during the CMP step a lot of SiC was delaminated from the SiO_2, which rendered part of the wafer useless. The next steps involve optimisation of the SiCOI wafer production and tests of the cavity performance in terms of the cavity Q-factor, mode volume and resonance frequency, parameters which are influenced by fabrication imperfections.

To realize Purcell enhancement of the ZPL emission, the cavity resonance should overlap with the ZPL frequency of the V2 defect. Additionally, we desire to tune the ZPL frequency to realize spectral overlap of multiple V2 centers. Therefore, we now list mechanisms that allow independent tuning of the ZPL frequency and the cavity resonance. A promising approach to modify the V2 emission frequency is based on the application of external DC electric fields (Stark tuning). Using this approach, the emission frequency has been tuned by ~100 GHz[57,58]. Additionally, strain fields modify the spectral position of Tin-Vacancy centers in diamond[59], which can potentially be used for V2 centers[42]. On the cavity side, gas tuning can be exploited[40,46,60]. Here the cavity resonance is modified as a result of the refractive index difference between the deposited gas and vacuum. A potential second approach relies on the Pockels effect, which modifies the silicon carbide refractive index via electric fields[61]. Finally, a third possibility relies on cavity resonance shifting through evanescent field pertubation. This has e.g. been demonstrated by modifying the spatial position of an auxiliary cavity with respect to the cavity that is to be tuned using a microelectromechanical system (MEMS)-driven system[62]. The mechanisms discussed here are non-exhausitive and potential alternative approaches might provide similar tuning abilities.

In conclusion, we designed a silicon-carbide alligator-type photonic crystal cavity to boost optical dipoles that couple to TM-modes at 917 nm. We obtained a simulated Q-factor of 2.4×10^6 and a mode volume of $0.82(\lambda/n)^3$. In collaboration with Fraunhofer and NovaSiC, we developed a SiCOI wafer that we used to fabricate the first batch of these cavities. Future steps involve the realisation of an efficient fiber-cavity interface to couple light in and out. Thanks to the work of Daniel Bedialauneta Rodríguez[63], a former master student in our group, fibers have been simulated, fabricated and used for reflection-based experiments on the cavities of figure 6.8. A one-way fiber-coupling efficiency between 80% and 97% was simulated. The experimental one-way fiber-coupling efficiency was measured at 10% and was limited by the large waveguide tapes that were used. Improvements, such as reducing the thickness of the SiC layer in the SiCOI stack, were recommended to achieve higher fiber-coupling efficiencies. Using these improved fiber-coupling efficiencies, in the short-term we target to characterisation the experimental Q-factors and resonance frequencies via reflection or transmission measurements[51], and use the results in a feedback loop to optimize the cavities to have their center resonance at 917 nm and to optimise the fabrication for high Q-factors. In the longer-term, we plan to embed V2 defect centers in these cavities either by electron irradiation[36], He^+-ion irradiation[34] or laser writing[64] and show Purcell enhancement. The final goal is to use this Purcell enhancement for direct single-shot readout of V2 center electron-spin qubit[65], to demonstrate spin-photon entanglement using the V2 center[37,66] and entanglement between two V2 center electron spins[8,66].

AUTHOR CONTRIBUTIONS

SJHL performed the spin-cluster simulations. GLvdS helped with preliminary simulations. All other authors provided input to the simulations. SJHL and GMT fabricated the spin-cluster sample. TWdJ performed simulations on the photonic crystal cavities under

6

REFERENCES

[1] C. Bradley, *Order from Disorder: Control of Multi-Qubit Spin Registers in Diamond*, Ph.D. thesis, Delft University of Technology (2021).

[2] M. Pompili *et al.*, *Realization of a multinode quantum network of remote solid-state qubits*, Science **372**, 259 (2021).

[3] S. L. N. Hermans *et al.*, *Qubit teleportation between non-neighbouring nodes in a quantum network*, Nature **605**, 663 (2022).

[4] C. Nguyen *et al.*, *Quantum Network Nodes Based on Diamond Qubits with an Efficient Nanophotonic Interface*, Physical Review Letters **123**, 183602 (2019).

[5] A. Zwerver *et al.*, *Shuttling an Electron Spin through a Silicon Quantum Dot Array*, PRX Quantum **4**, 030303 (2023).

[6] J. M. Pino *et al.*, *Demonstration of the trapped-ion quantum CCD computer architecture*, Nature **592**, 209 (2021).

[7] D. Bluvstein *et al.*, *A quantum processor based on coherent transport of entangled atom arrays*, Nature **604**, 451 (2022).

[8] P. C. Humphreys *et al.*, *Deterministic delivery of remote entanglement on a quantum network*, Nature **558**, 268 (2018).

[9] L. Stephenson *et al.*, *High-Rate, High-Fidelity Entanglement of Qubits Across an Elementary Quantum Network*, Physical Review Letters **124**, 110501 (2020).

[10] T. van Leent *et al.*, *Entangling single atoms over 33 km telecom fibre*, Nature **607**, 69 (2022).

[11] S. Daiss *et al.*, *A quantum-logic gate between distant quantum-network modules*, Science **371**, 614 (2021).

[12] F. Dolde *et al.*, *Room-temperature entanglement between single defect spins in diamond*, Nature Physics **9**, 139 (2013).

[13] F. Dolde *et al.*, *High-fidelity spin entanglement using optimal control*, Nature Communications **5**, 3371 (2014).

[14] Z. Xu, Z.-q. Yin, Q. Han and T. Li, *Quantum information processing with closely-spaced diamond color centers in strain and magnetic fields [Invited]*, Optical Materials Express **9**, 4654 (2019).

[15] A. Cooper, W. K. C. Sun, J.-C. Jaskula and P. Cappellaro, *Environment-assisted Quantum-enhanced Sensing with Electronic Spins in Diamond*, Physical Review Applied **12**, 044047 (2019).

[16] J. Lee *et al.*, *Dressed-state control of effective dipolar interaction between strongly-coupled solid-state spins*, npj Quantum Information **9**, 1 (2023).

6

[17] J. Randall *et al.*, *Many-body–localized discrete time crystal with a programmable spin-based quantum simulator,* Science **374**, 1474 (2021).

[18] S. Bose, *Quantum Communication through an Unmodulated Spin Chain,* Physical Review Letters **91**, 207901 (2003).

[19] N. Y. Yao *et al.*, *Quantum logic between remote quantum registers,* Physical Review A **87**, 022306 (2013).

[20] A. Ajoy and P. Cappellaro, *Perfect quantum transport in arbitrary spin networks,* Physical Review B **87**, 064303 (2013).

[21] P. Cappellaro, *Implementation of State Transfer Hamiltonians in Spin Chains with Magnetic Resonance Techniques,* in *Quantum State Transfer and Network Engineering,* Quantum Science and Technology, edited by G. M. Nikolopoulos and I. Jex (Springer, Berlin, Heidelberg, 2014) pp. 183–222.

[22] R. Nagy *et al.*, *Narrow inhomogeneous distribution of spin-active emitters in silicon carbide,* Applied Physics Letters **118**, 144003 (2021).

[23] T. H. Taminiau *et al.*, *Detection and Control of Individual Nuclear Spins Using a Weakly Coupled Electron Spin,* Physical Review Letters **109**, 137602 (2012).

[24] M. J. Degen *et al.*, *Entanglement of dark electron-nuclear spin defects in diamond,* Nature Communications **12**, 3470 (2021).

[25] M. H. Abobeih *et al.*, *Atomic-scale imaging of a 27-nuclear-spin cluster using a quantum sensor,* Nature **576**, 411 (2019).

[26] K. S. Cujia, K. Herb, J. Zopes, J. M. Abendroth and C. L. Degen, *Parallel detection and spatial mapping of large nuclear spin clusters,* Nature Communications **13**, 1260 (2022).

[27] G. L. van de Stolpe *et al.*, *Mapping a 50-spin-qubit network through correlated sensing,* (2023), arXiv:2307.06939 [cond-mat, physics:quant-ph].

[28] A. Cooper, W. K. C. Sun, J.-C. Jaskula and P. Cappellaro, *Identification and Control of Electron-Nuclear Spin Defects in Diamond,* Physical Review Letters **124**, 083602 (2020).

[29] E. Rosenfeld, L. Pham, M. Lukin and R. Walsworth, *Sensing Coherent Dynamics of Electronic Spin Clusters in Solids,* Physical Review Letters **120**, 243604 (2018).

[30] H. S. Knowles, D. M. Kara and M. Atatüre, *Demonstration of a Coherent Electronic Spin Cluster in Diamond,* Physical Review Letters **117**, 100802 (2016).

[31] H. P. Bartling *et al.*, *Control of individual electron-spin pairs in an electron-spin bath,* (2023), arXiv:2311.10110 [cond-mat, physics:quant-ph].

[32] N. Y. Yao *et al.*, *Robust Quantum State Transfer in Random Unpolarized Spin Chains,* Physical Review Letters **106**, 040505 (2011).

[33] G. Gualdi, V. Kostak, I. Marzoli and P. Tombesi, *Perfect state transfer in long-range interacting spin chains,* Physical Review A **78**, 022325 (2008).

[34] C. Babin *et al.*, *Fabrication and nanophotonic waveguide integration of silicon carbide colour centres with preserved spin-optical coherence,* Nature Materials **21**, 67 (2022).

[35] L.-P. Yang *et al.*, *Electron Spin Decoherence in Silicon Carbide Nuclear Spin Bath,* Physical Review B **90**, 241203 (2014).

[36] R. Nagy *et al.*, *High-fidelity spin and optical control of single silicon-vacancy centres in silicon carbide,* Nature Communications **10**, 1954 (2019).

[37] R.-Z. Fang *et al.*, *Experimental Generation of Spin-Photon Entanglement in Silicon Carbide,* (2023), arXiv:2311.17455 [physics, physics:quant-ph].

[38] A. Bourassa *et al.*, *Entanglement and control of single nuclear spins in isotopically engineered silicon carbide,* Nature Materials **19**, 1319 (2020).

[39] Wikipedia, *Coercivity,* (2023), accessed: 2023-12-15. Page Version ID: 1185821408.

[40] D. M. Lukin *et al.*, *Two-Emitter Multimode Cavity Quantum Electrodynamics in Thin-Film Silicon Carbide Photonics,* Physical Review X **13**, 011005 (2023).

[41] M. Ruf, N. H. Wan, H. Choi, D. Englund and R. Hanson, *Quantum networks based on color centers in diamond,* Journal of Applied Physics **130**, 070901 (2021).

[42] P. Udvarhelyi *et al.*, *Vibronic States and Their Effect on the Temperature and Strain Dependence of Silicon-Vacancy Qubits in 4H-SiC,* Physical Review Applied **13**, 054017 (2020).

[43] H. B. Banks *et al.*, *Resonant Optical Spin Initialization and Readout of Single Silicon Vacancies in 4H-SiC,* Physical Review Applied **11**, 024013 (2019).

[44] D. Liu *et al.*, *The silicon vacancy centers in SiC: determination of intrinsic spin dynamics for integrated quantum photonics,* (2023), arXiv:2307.13648 [quant-ph].

[45] M. Ruf, *Cavity-enhanced quantum network nodes in diamond,* Ph.D. thesis, Delft University of Technology (2021).

[46] D. M. Lukin *et al.*, *4H-silicon-carbide-on-insulator for integrated quantum and nonlinear photonics,* Nature Photonics **14**, 330 (2020).

[47] J. M. Bopp *et al.*, *'Sawfish' Photonic Crystal Cavity for Near-Unity Emitter-to-Fiber Interfacing in Quantum Network Applications,* (2022), arXiv:2210.04702 [physics, physics:quant-ph].

[48] T. Pregnolato *et al.*, *Fabrication of Sawfish photonic crystal cavities in bulk diamond,* (2023), arXiv:2311.03618 [physics, physics:quant-ph].

6

[49] T. W. de Jong, *Simulated enhancement of optical properties V_{Si} defects in 4H-SiC through nanophotonic structures*, Master thesis (TU Delft), TU Delft (2022).

[50] J. D. Joannopoulos, ed., *Photonic crystals: molding the flow of light*, 2nd ed. (Princeton University Press, Princeton, 2008).

[51] M. J. Burek *et al.*, *High quality-factor optical nanocavities in bulk single-crystal diamond*, Nature Communications **5**, 5718 (2014).

[52] G. Timmer, *Exploring nanofabrication in rH-SiC for optical enhancement of the Vsi*, Master thesis (TU Delft), TU Delft (2022).

[53] D. O. Bracher, X. Zhang and E. L. Hu, *Selective Purcell enhancement of two closely linked zero-phonon transitions of a silicon carbide color center*, Proceedings of the National Academy of Sciences **114**, 4060 (2017).

[54] M. J. Burek *et al.*, *Fiber-Coupled Diamond Quantum Nanophotonic Interface*, Physical Review Applied **8**, 024026 (2017).

[55] B. Khanaliloo *et al.*, *Single-Crystal Diamond Nanobeam Waveguide Optomechanics*, Physical Review X **5**, 041051 (2015).

[56] F. O. Afzal, S. I. Halimi and S. M. Weiss, *Efficient side-coupling to photonic crystal nanobeam cavities via state-space overlap*, JOSA B **36**, 585 (2019).

[57] D. M. Lukin *et al.*, *Spectrally reconfigurable quantum emitters enabled by optimized fast modulation*, npj Quantum Information **6**, 1 (2020).

[58] M. Rühl, L. Bergmann, M. Krieger and H. B. Weber, *Stark Tuning of the Silicon Vacancy in Silicon Carbide*, Nano Letters **20**, 658 (2020).

[59] X. Guo *et al.*, *Microwave-based quantum control and coherence protection of tin-vacancy spin qubits in a strain-tuned diamond membrane heterostructure*, (2023), arXiv:2307.11916 [cond-mat, physics:quant-ph].

[60] E. R. Schmidgall *et al.*, *Frequency Control of Single Quantum Emitters in Integrated Photonic Circuits*, Nano Letters **18**, 1175 (2018).

[61] R. Wang, J. Li, L. Cai and Q. Li, *Investigation of the electro-optic effect in high-Q 4H-SiC microresonators*, Optics Letters **48**, 1482 (2023).

[62] X. Chew *et al.*, *Dynamic tuning of an optical resonator through MEMS-driven coupled photonic crystal nanocavities*, Optics Letters **35**, 2517 (2010).

[63] D. B. Rodríguez, *Fiber-coupled photonic crystal cavities for the V2 defect in 4H-SiC*, Master thesis (TU Delft), TU Delft (2023).

[64] A. M. Day, J. R. Dietz, M. Sutula, M. Yeh and E. L. Hu, *Laser writing of spin defects in nanophotonic cavities*, Nature Materials **22**, 696 (2023).

[65] L. Robledo, H. Bernien, I. Van Weperen and R. Hanson, *Control and Coherence of the Optical Transition of Single Nitrogen Vacancy Centers in Diamond,* Physical Review Letters **105**, 177403 (2010).

[66] H. Bernien *et al., Heralded entanglement between solid-state qubits separated by three metres,* Nature **497**, 86 (2013).

6

7

CONCLUSIONS AND OUTLOOK

In this chapter, I first summarize the key findings of this thesis in the context of the three requirements for solid-state based quantum network outlined in chapter 1. In the second part, I will put these results in the context of the state-of-the-art and provide directions for future research for each of these three areas.

7.1. SUMMARY

This thesis describes advances made in the understanding of the spin and optical properties of solid-state defects in the context of quantum networks and was motivated by the 3 quantum-network requirements outlined in Chapter 1. To recap, these requirements were 1) An efficient qubit-photon interface for entanglement generation, 2) A high-fidelity quantum memory under network operation, and 3) A qubit register with high-fidelity control. In this section, I will first summarize the achievements of this thesis chapter by chapter, and place each chapter in the context of these requirements. Secondly, I will provide an outlook for future advancements in the road towards (scalable) quantum networks with solid-state defect centers. I will do this separately for the three requirements.

- **Chapter 2** provided a background on the three electron spin defects investigated in this thesis, as well as the nuclear spin bath around them. The three defects comprise the nitrogen-vacancy (NV) center in diamond, the P1 center (substitutional nitrogen atom) in diamond, and the V2 defect in silicon carbide (SiC). In addition, the chapter elaborated on the control techniques, timescales, parameters, and photonic structures used for the experiments in this thesis.

- A better understanding of the spin environment of the solid-state defect center both contributes to the ability to decouple from environmental noise, and to establish control over environmental spins. This aids in better control fidelities and can add a new layer of qubits to the available qubit register (requirement 3). In **chapter 3**, we demonstrated a detailed understanding and control of individual P1 centers within an electronic spin bath. We exploited projective measurements to prepare the multiple degrees of freedom of the P1 center, such as the charge state, Jahn-Teller axis, nuclear spin and electron spin. We demonstrated initialisation, control and single-shot readout. Using these techniques we generated an entangled state between two individual P1 centers. This chapter provides a proof-of-principle towards dark electron-nuclear spin defects, including those with more favourable properties than the P1 center, as qubits for quantum sensing and quantum networks.

- The ability to protect quantum states while multiple entangled states are distributed over a network, or while running computations on the network, will benefit the realisation of a useful quantum network. In chapter **4**, we use nuclear-spin spectator qubits to demonstrate the protection of an arbitrary quantum state stored within a nuclear-spin memory qubit associated with an NV center while applying pulse sequences that emulate remote entanglement generation. The spectator qubits experience noise correlated to the memory qubit. Measurements on the spectator qubits, in combination with real-time feed-forward, enable to mitigate correlated noise. We identify the that the electron-mediated spectator readout imparts additional dephasing, and realize a gate-based implementation of the protocol that alleviates the necessity to read out the electron. We demonstrate that the gate-based protocol indeed outperforms the measurement-based

protocol. Finally, we analyze the impact of the spectator qubit approach as a function of the probability to generate entanglement per attempt. We find that, for the NV center under investigation, the spectator qubits are expected to improve the ability to protect an arbitrary quantum state for a range of probabilities.

The results of this chapter show spectator qubits are a promising way to mitigate correlated dephasing. Especially, as the initialisation of spectator qubits can be done with little additional dephasing, and it can be decided in real-time whether to use the spectator qubits at the end of the sequence. The latter allows to omit the extraction of the information contained in the spectators if that process introduces more dephasing than what can be mitigated. Besides, spectator qubits do not necessarily require high-fidelity operation. Therefore, qubits that are not considered useful for more advanced protocols, can still be used as spectator qubits in parallel with these advanced protocols.

- **chapter 5**, investigates the laser-induced spectral diffusion dynamics of a single silicon vacancy embedded in nanopillars fabricated in commercially available bulk silicon carbide. Using a 'check-probe' scheme, we initialize the system in specific spectral configurations in the 'check' block. The 'probe' block allows to investigate the influence on the spectral dynamics of arbitrary perturbations between the 'check' and 'probe' blocks. This technique allows to separate the contribution ionisation and diffusion. Additionally, we present a photoluminescence experiment that imposes minimal disturbance to the system under study and measure near Fourier-linewidth limited optical transitions within an inhomogeneously broadened spectrum of about 50 times this Fourier limit. Via Landau-Zener-Stückelberg interference we confirm the (near-)Fourier limited linewidths. This observation of (nearly) lifetime-limited linewidths of single defects in commercially available bulk silicon carbide highlights the potential of the V2 defect, and silicon carbide as a host, for quantum network applications.

- In **Chapter 6**, we propose the controlled generation of an electron-spin cluster in SiC nanopillars (requirement 3). We propose to use He^+-ion irradiation for the defect generation and micromagnets to detune the ground-state transitions of the spins in the cluster to allow individual optical and magnetic addressability of the electron spins in the cluster. We simulate what irradiation and micromagnet parameters we require to achieve this multi-defect electron-spin cluster. The results of this chapter indicate that the use of He^+-ion irradiation and micromagnets enables the realisation of clusters with individually addressable electron-spin qubits that have a dipolar coupling of 10 kHz or larger. Future steps involve optimization in the fabrication of the device and to actually perform the He^+-ion irradiation. Using these devices, we target to demonstrate an entangled state distributed over two V2 defect centers. In addition, we plan to transfer a quantum state from one electron-spin qubit (qubit 1) to a nuclear-spin qubit associated with another electron-spin qubit (qubit 2). Following this, we characterize the robustness of this nuclear-spin qubit against dephasing induced by qubit 1. This

potentially allows for robust quantum state storage during remote entanglement generation.

The second part of **Chapter 6** demonstrates simulations on, and progressions of the fabrication of, photonic crystal cavities to boost the optical properties of V2 defects in SiC (requirement 1). We design alligator-type photonic crystal cavities tailored to the optical dipole orientation of the V2 center and simulate high Q-factors (2.4×10^6) and low mode volumes $(0.82(\lambda/n)^3)$. We fabricate the first batch of these cavities using a silicon-carbide-on-insulator platform. The simulation results indicate that these cavities are promising to realize Purcell enhanced V2 defects in silicon carbide, and our fabrication efforts using a silicon-carbide-on-insulator platform demonstrate initial steps towards this Purcell enhancement. Near-term steps involve optimizing the cavity fabrication and the fiber coupling interface to these cavities. Subsequently, we plan to measure, and optimize for, the cavity Q-factors and resonance wavelength. In the long-term, the goal is to demonstrate direct single-shot readout of the V2 defect, spin-photon entanglement and remote V2-V2 entanglement.

The results in this thesis contribute to the realisation of next-generation quantum network experiments. In the following, I will discuss the outlook of this work in the context of the requirements for quantum networks based on optically interfaced solid-state defects.

7.2. ENHANCING THE SPIN-PHOTON INTERFACE

PHOTONIC INTEGRATION AND FREQUENCY TUNING

Currently, the most advanced quantum networks of the type considered in this thesis are based on bulk NV centers embedded in solid-immersion lenses (SILs) in diamond[1]. The rate of entanglement generation relies on an efficient collection, and a high rate of emission of (near-)Fourier linewidth-limited indistinguishable zero-phonon-line (ZPL) photons from different emitters[2]. Bulk NV centers only emit ~3% in the ZPL[3] and the SIL collection efficiency is typically around ~5%[4]. Both can be improved by embedding the defect in an optical cavity. Purcell enhancement increases the ZPL transition rate and hence the fraction of ZPL emission, and funnels the light in a well-defined spatial mode, such as the one of a waveguide, that can be efficiently collected[5,6]. E.g. over 90% coupling efficiencies of waveguide-fiber interfaces have been demonstrated in diamond and SiC[7,8]. The susceptibility of the NV center to electrical charges associated with cavity surface defects has hindered efficient integration in photonic crystal cavities[9]. While NV center integration in Fabry-Perot cavities has been demonstrated[10,11], photonic crystal cavities are likely preferred because of their compatibility with photonic integrated circuits.

This has stimulated the search for defects that maintain a coherent optical interface while integrated in a photonic crystal cavity, while simultaneously possessing spin-properties likewise to the NV center. This formed the motivation for the SiC research in

this thesis and has also motivated research into Group-IV defects in diamond. These Group-IV defects show good intrinsic optical properties and are to first order insensitive to charge noise because of their inversion symmetry[12–15]. Recently, cavity-integrated silicon-vacancy centers in diamond have demonstrated coherent cooperativities of ∼100[16], memory-enhanced quantum communication[17] and two-node entanglement over a telecommunication fiber network diamond[18]. The orbital-doublet spin-doublet ground-state structure of group IV defects[19,20] imposes challenges for the temperature operation regime and spin control[21–23], including dynamical decoupling based gates[24]. Future research into spin-control techniques, such as DDRF driving[25], is key for the establishment of Group-IV defects as future nodes for quantum networks.

For the V2 defect, as well as other defects in SiC, demonstrations alike the ones for Group-IV centers in diamond are yet to be realised. The low ZPL emission fraction (∼8%) and poor cyclicity (8 cycles before a spin flip) underpin the necessity of cavity integration, both for direct single-shot electron readout and entanglement protocols[26–28]. A next milestone is to integrate defects in suitable cavity designs (see chapter 6) and demonstrate two-node entanglement based on V2-defects. Free hanging cavities with integrated defects have already been fabricated using doping-selective etching[29,30], Faraday-cage triangular etching[31,32] and silicon-carbide-on-insulator platforms[33]. V2 centers in triangular cavities showed near-Fourier linewidth-limited resonant absorption lines[32], while at the same time stark tuning over ∼100 GHz has been realized[34]. It is an interesting avenue to understand the underpinning physics that allows this combination. Potentially the ability of SiC to form oxides removes the presence of surface-related dangling bonds and hence increases the electrostatic stability for cavity integrated defects[35].

Purcell enhancement is maximal if the defect spatially overlaps with the anti-node of the cavity. This can be achieved by first identifying the positions of randomly oriented defect centers and subsequent cavity fabrication. A more scalable approach is to generate defects at targeted positions. This can e.g. be achieved through ion-irradiation[32,36] or laser writing[37,38]. Ion-irradiation can however generate lattice damage that can lead to poor spectral properties, as observed for nitrogen implanted NV-centers[36]. He$^+$-ion irradiated V2 defects maintained near-Fourier linewidth-limited optical transitions in bulk. A future challenge is to apply this technique for V2 generation in cavities.

Another open challenge, not specific to SiC, relates to cavity fabrication. Currently, cavity fabrication methods routinely achieve Q-factors ∼10^4, two orders of magnitude lower than simulated[39]. This is partially explained by a combination of surface roughness[16] and deviations from the expected device cross-section[40]. Potentially, etching methods lead to sub-surface crystal damage that hinders high Q-factors. Plasma-polished dry etching (PPDE) techniques have been developed for SiC, that can effectively remove sub-surface damage and improve the surface roughness of SiC[41,42]. This motivates the introduction of a PPDE recipe for SiC quantum photonics. In addition, the sensitivity of cavities to the fabrication process leads to a spread in cavity resonance wavelength of ∼5 nm across devices[39]. This can be overcome by

cavity tuning mechanisms, such as gas tuning[33,43], spatially controlled proximity of a dielectric material[44], or potentially using the non-linear electro-optical effect (available in SiC)[45]. Spectral cavity-emitter overlap can alternatively be achieved by tuning the emitter wavelength, by e.g. Stark tuning[33,46,47], or potentially via strain tuning[48–50]. Precise overlap of the ZPL frequency of multiple emitters likely requires both cavity and emitter tuning. An alternative is to use frequency conversion to interfere to spectrally distinguishable emitters[51].

One of the advantages of photonic crystal cavities is their compatibility with photonic integrated circuits (PICs), which is appealing for scalability reasons. PICs typically have a small footprint beneficial for dense integration, and consist of low-loss on-chip components, such as waveguides, filters and switches. A review of the state-of-the-art PIC technologies in the context of quantum networks is provided by Harris et al.[52] and Bogaerts et al.[53]. On-chip phase modulators can implement on-chip routing of photons[53], thereby paving the way to complex on-chip qubit-to-qubit connectivity. This is, amongst others, interesting for quantum error correction protocols[54]. PICs benefit from high refractive index contrast to confine light[55]. In that respect, the ability to fabricate silicon-carbide-on-insulator is an appealing motivation to foster the field of SiC PICs. A potential challenge here is the degree to which a uniform film thickness can be achieved after polishing[56]. Another exciting recent achievement is the integration of triangular quantum photonic devices with on-chip photon detectors in SiC[57]. Additionally, first demonstrations of electro-optic modulators[58] and single-emitter frequency tuning[33] in SiC have been demonstrated. A review on quantum information processing with integrated SiC photonics is provided by Majety et al.[56].

CHARGE ENVIRONMENT STABILISATION

Solid-state defect quantum technologies typically rely on stable optical transitions of a specific charge state of the defect. In that respect, it is important to understand how to stabilize the charge-state and the electrostatic/strain environment of the defect, as well as lattice damage associated with defect creation[12]. Defects are routinely created by high-energy irradiation, followed by high-temperature annealing to recover strain-inducing lattice damage from the irradiation process[32,36,59]. However, this annealing does not guarantee a full recovery of the solid-state lattice[36]. A potential way to circumvent this in diamond, is to use shallow, low-energy, ion-irradiation and subsequent overgrowth, which reduces lattice damage[60,61]. This however is not applicable to SiC due to the large epitaxial growth temperature required[56].

Fermi-level engineering allows to modify the electrostatic environment and thereby control the preferential charge state of the defect[62–64]. Fermi-level tuning is effective in samples with high-doping concentration ($> 10^{13} - 10^{15} \mathrm{cm}^{-3}$), where doping-related defects dominate over additional charge traps[63] and has been achieved in diamond using phosphorous doping[65]. SiC offers industrially mature doping processes and Fermi-level tuning in SiC has been proposed by Zhang et al.[66]. Finally, the electrostatic environment can be engineered using external bias voltages, which has allowed stable near Fourier-linewidth limited transitions of the neutral divacancy charge state in a

p-i-n-junction in SiC[67].

Future research directed to the optimal combination of defect creation, doping strategy and gate tuning for defects in nanophotonic cavities can provide pivotal impact in terms of the stabilisation of the desired charge state, which is important for to maintain a stable efficient optical interface.

7.3. QUANTUM MEMORY UNDER NETWORK OPERATION

An outstanding challenge for optically connected solid-state quantum networks is the realisation of robust data qubits under network operation. In entanglement protocols that are currently being used[68,69], the data qubits dephase because of a combination of the always-on hyperfine interaction with the communication qubit (electron spin) and uncontrolled dynamics of the electron spin during the entanglement generation protocol[2,70–72]. The uncontrolled dynamics results from control infidelities and the stochastic optical cycling during electron-spin reinitialisation. In this section, I will revise different approaches to improve the protection of arbitrary quantum states during entanglement generation attempts. These approaches mainly rely on either reducing the duration of network protocols, such as entanglement generation, or the reduction of the effective coupling between the data qubit and the electron spin.

Operating at a high magnetic field was proposed by Kalb et al.[70], and implemented by Pompili et al.[69], in order to reduce the duration per entanglement attempt, thereby decreasing the time over which data qubits are susceptible to stochastic electron-spin evolutions. As a result, the data qubit (a ^{13}C nuclear spin in this case) was not limited by the noise imparted by the entanglement generation attempts, but by intrinsic dephasing. Consequently, decoupling of the nuclear spin further extended the coherence time under network operation[71]. In addition, higher magnetic fields are also projected to benefit the spectator qubit approach. At these fields, the influence of the perpendicular electron-nuclear hyperfine coupling decreases, which provides a more straightforward correlation between the phase distribution of different nuclear-spin qubits (see chapter 4). Stochastic electron evolution is also reduced via improved fidelity of microwave echo pulses and active microwave power stabilisation[73–76], as well as shorter electron initialisation times.

Promising routes to reduce the effective coupling of the data qubit to the electron spin (communication qubit) involve the encoding of a data qubit in a decoherence protected subspace. E.g., two nuclear spins with similar hyperfine couplings can be employed in a state defined by $\alpha\,|01\rangle + \beta\,|10\rangle$ such that the electron-state dependent interaction is reduced[77]. Another approach to reduce the hyperfine coupling between addressable nuclear spins and the electron spin relies on isotopic purification. This approach enabled $\sim 10^5$ entanglement attempts before decoherence of an arbitrary quantum state[78], compared to ~ 500 attempts in a sample with a natural isotope concentration[1]. A challenge for weakly coupled carbon spins, is to unify long coherence

times with fast two-qubit gates, as both scale with the hyperfine coupling to the electron spin.

In this respect, coupled electron-spin defects potentially provide a solution[79,80]. Here, an electron spin, with an associated nuclear spin register, is coupled to the communication qubit. This electron spin serves as a 'bus' qubit to transfer information between the communication qubit and the nuclear spins associated with this 'bus' qubit. Compared to the electron-spin 'bus' qubit, the nuclear spins themselves couple $\frac{\gamma_N}{\gamma_e} = O(1^{-3})$ less strongly to the communication qubit. This potentially allows to unify robust memories with fast two-qubit gates. First demonstrations of coupled electron-spin defects have been demonstrated in the form of NV-NV entanglement[81] and NV-P1 entanglement (chapter 3). However, for NV-NV based systems, individual addressability is challenging, and for e.g. P1 centers the many degrees of freedom make initialisation slow. Additionally, the strong electron-nuclear hyperfine coupling of the intrinsic P1 nuclear spin leads to significant spin-mixing at low magnetic fields (see chapter 3), thereby making the nuclear spin more susceptible to the dynamics of the communication qubit. An interesting future avenue is to use environmental nuclear spins associated to the 'bus' electron-spin qubit. In e.g. SiC, this is potentially enabled by the multitude of electron-spin defects.

7.4. MULTI-QUBIT REGISTER WITH HIGH-FIDELITY OPERATION

Lastly in this outlook, I consider the construction of a multi-qubit register associated with each communication qubit. In this section, I will first focus on the advancements related to nuclear-spin qubits and second on electron-spin-based registers. Detection of nuclear spins via dynamical decoupling[82–84] propelled efforts to use these spins as qubits. In 2019, a 10-qubit register containing nine nuclear spins was established based on dynamical decoupling and radio-frequency driving[25]. A GHZ state involving six nuclear spins, as well as entanglement between any nuclear-spin pair, along with electron-nuclear control fidelities of ~98% (~ms gate times), and coherence times above 10 seconds has been demonstrated. This nuclear-spin register has also been used for primitives of fault-tolerant computation[85] and time-crystal simulations[86]. A challenge here, is that all nuclear-spin qubits can only be addressed via the electron spin, complicating parallel addressing and slowing down computations.

Improvements in gate fidelity, and likely gate speeds, are desired for large-scale quantum network protocols. The gate-times are limited by the electron-nuclear hyperfine interaction. Intrinsic nuclear spins, such as the nitrogen spin in NV centers, have ~MHz coupling strengths. While at the same time such spin is more susceptible to electron-induced dephasing, they also offer ~µs gate speeds. Using gate-set tomography (GST), 99.999% single-qubit and 99.9% two-qubit gate fidelities have been demonstrated using the nitrogen spin associated to an NV center in diamond[87]. This work identified coherent gate errors and electron-spin dephasing as dominant noise sources, which stimulates further investigation of these sources. Potentially, outcomes

of a GST analysis can be used to optimize a combination of both gate speed and fidelity of ^{13}C nuclear spins in diamond. In SiC, both ^{13}C as well as ^{29}Si nuclear spins are present, potentially offering a more abundant controllable nuclear-spin register[32]. Recently, nuclear spins strongly coupled to a single V2 defect in SiC with initialisation and control fidelities reaching 98% were demonstrated, and in natural abundance samples, 5 strongly coupled nuclear spins were observed[88]. In future research, GST analysis could be applied to such SiC-based system in order to realize a high-fidelity, high-speed nuclear-spin register associated to a single electron spin. Still, the strong coupling to the electron can induce dephasing during optical driving of the electron. A strong coherent defect-cavity interaction potentially offer routes to initialise and read-out the electron spin based on photon reflection, instead of photon emission, thereby alleviating the need to optically drive the electron spin[17].

As demonstrated in chapter 3, electron spins associated to optically addressable defects provide a qubit register[89]. For magnetic coupling between the same types of electronic defects, one outstanding challenge is to achieve high-fidelity individual electron-spin control, both in the microwave domain as well as the optical domain (see chapter 6). For systems consisting of different electronic defects, such as the NV-P1 system in chapter 3, this difficulty was bypassed at the cost of the rich P1 level structure that complicates qubit initialisation. In chapter 6, we provide a detailed outlook for future research into individually controllable, optically addressable, magnetically coupled electron-spin defects. This study mainly focuses on electron spins associated to identical defects, but can be fairly easily adapted to investigate systems consisting of different electronic defects. Outstanding challenges here are the non-deterministic fabrication, and simultaneous realisation of individual addressability and magnetic coupling.

7

REFERENCES

[1] M. Pompili *et al.*, *Experimental demonstration of entanglement delivery using a quantum network stack,* npj Quantum Information **8**, 1 (2022).

[2] S. L. N. Hermans *et al.*, *Entangling remote qubits using the single-photon protocol: an in-depth theoretical and experimental study,* New Journal of Physics **25**, 013011 (2023).

[3] A. Faraon, P. E. Barclay, C. Santori, K.-M. C. Fu and R. G. Beausoleil, *Resonant enhancement of the zero-phonon emission from a colour centre in a diamond cavity,* Nature Photonics **5**, 301 (2011).

[4] H. Bernien, *Control, measurement and entanglement of remote quantum spin registers in diamond,* Ph.D. thesis, Delft University of Technology (2014).

[5] A. Reiserer and G. Rempe, *Cavity-based quantum networks with single atoms and optical photons,* Reviews of Modern Physics **87**, 1379 (2015).

[6] E. Janitz, M. K. Bhaskar and L. Childress, *Cavity quantum electrodynamics with color centers in diamond,* Optica **7**, 1232 (2020).

[7] M. J. Burek *et al.*, *Fiber-Coupled Diamond Quantum Nanophotonic Interface,* Physical Review Applied **8**, 024026 (2017).

[8] M. Krumrein *et al.*, *Precise characterization of a silicon carbide waveguide fiber interface,* (2024), arXiv:2401.06096 [physics, physics:quant-ph].

[9] A. Faraon, C. Santori, Z. Huang, V. M. Acosta and R. G. Beausoleil, *Coupling of Nitrogen-Vacancy Centers to Photonic Crystal Cavities in Monocrystalline Diamond,* Physical Review Letters **109**, 033604 (2012).

[10] D. Riedel *et al.*, *Deterministic Enhancement of Coherent Photon Generation from a Nitrogen-Vacancy Center in Ultrapure Diamond,* Physical Review X **7**, 031040 (2017).

[11] M. Ruf, M. Weaver, S. van Dam and R. Hanson, *Resonant Excitation and Purcell Enhancement of Coherent Nitrogen-Vacancy Centers Coupled to a Fabry-Perot Microcavity,* Physical Review Applied **15**, 024049 (2021).

[12] M. Ruf, N. H. Wan, H. Choi, D. Englund and R. Hanson, *Quantum networks based on color centers in diamond,* Journal of Applied Physics **130**, 070901 (2021).

[13] C. Bradac, W. Gao, J. Forneris, M. E. Trusheim and I. Aharonovich, *Quantum nanophotonics with group IV defects in diamond,* Nature Communications **10**, 5625 (2019).

[14] R. E. Evans, A. Sipahigil, D. D. Sukachev, A. S. Zibrov and M. D. Lukin, *Narrow-Linewidth Homogeneous Optical Emitters in Diamond Nanostructures via Silicon Ion Implantation,* Physical Review Applied **5**, 044010 (2016).

7

[15] M. E. Trusheim *et al.*, *Transform-Limited Photons From a Coherent Tin-Vacancy Spin in Diamond*, Physical Review Letters **124**, 023602 (2020).

[16] C. T. Nguyen *et al.*, *An integrated nanophotonic quantum register based on silicon-vacancy spins in diamond*, Physical Review B **100**, 165428 (2019).

[17] M. K. Bhaskar *et al.*, *Experimental demonstration of memory-enhanced quantum communication*, Nature **580**, 60 (2020).

[18] C. M. Knaut *et al.*, *Entanglement of Nanophotonic Quantum Memory Nodes in a Telecommunication Network*, (2023), arXiv:2310.01316 [quant-ph].

[19] C. Hepp *et al.*, *The electronic structure of the silicon vacancy color center in diamond*, Physical Review Letters **112**, 036405 (2014).

[20] M. Ruf, *Cavity-enhanced quantum network nodes in diamond*, Ph.D. thesis, Delft University of Technology (2021).

[21] D. Sukachev *et al.*, *Silicon-Vacancy Spin Qubit in Diamond: A Quantum Memory Exceeding 10 ms with Single-Shot State Readout*, Physical Review Letters **119**, 223602 (2017).

[22] E. Takou and S. E. Economou, *Optical control protocols for high-fidelity spin rotations of single SiV^- and SnV^- centers in diamond*, Physical Review B **104**, 115302 (2021).

[23] R. Debroux *et al.*, *Quantum control of the tin-vacancy spin qubit in diamond*, Physical Review X **11**, 041041 (2021).

[24] C. Nguyen *et al.*, *Quantum Network Nodes Based on Diamond Qubits with an Efficient Nanophotonic Interface*, Physical Review Letters **123**, 183602 (2019).

[25] C. Bradley *et al.*, *A Ten-Qubit Solid-State Spin Register with Quantum Memory up to One Minute*, Physical Review X **9**, 031045 (2019).

[26] H. B. Banks *et al.*, *Resonant Optical Spin Initialization and Readout of Single Silicon Vacancies in 4H-SiC*, Physical Review Applied **11**, 024013 (2019).

[27] P. Udvarhelyi *et al.*, *Vibronic States and Their Effect on the Temperature and Strain Dependence of Silicon-Vacancy Qubits in 4H-SiC*, Physical Review Applied **13**, 054017 (2020).

[28] D. Liu *et al.*, *The silicon vacancy centers in SiC: determination of intrinsic spin dynamics for integrated quantum photonics*, (2023), arXiv:2307.13648 [quant-ph].

[29] D. O. Bracher, X. Zhang and E. L. Hu, *Selective Purcell enhancement of two closely linked zero-phonon transitions of a silicon carbide color center*, Proceedings of the National Academy of Sciences **114**, 4060 (2017).

[30] A. L. Crook *et al.*, *Purcell Enhancement of a Single Silicon Carbide Color Center with Coherent Spin Control*, Nano Letters **20**, 3427 (2020).

7

[31] B.-S. Song *et al.*, *High-Q-factor nanobeam photonic crystal cavities in bulk silicon carbide,* Applied Physics Letters **113**, 231106 (2018).

[32] C. Babin *et al.*, *Fabrication and nanophotonic waveguide integration of silicon carbide colour centres with preserved spin-optical coherence,* Nature Materials **21**, 67 (2022).

[33] D. M. Lukin *et al.*, *4H-silicon-carbide-on-insulator for integrated quantum and nonlinear photonics,* Nature Photonics **14**, 330 (2020).

[34] D. M. Lukin *et al.*, *Spectrally reconfigurable quantum emitters enabled by optimized fast modulation,* npj Quantum Information **6**, 1 (2020).

[35] C. P. Anderson, Private communication (2023).

[36] S. B. van Dam *et al.*, *Optical coherence of diamond nitrogen-vacancy centers formed by ion implantation and annealing,* Physical Review B **99**, 161203 (2019).

[37] Y.-C. Chen *et al.*, *Laser writing of individual nitrogen-vacancy defects in diamond with near-unity yield,* Optica **6**, 662 (2019).

[38] A. M. Day, J. R. Dietz, M. Sutula, M. Yeh and E. L. Hu, *Laser writing of spin defects in nanophotonic cavities,* Nature Materials **22**, 696 (2023).

[39] S. Mouradian, N. H. Wan, T. Schröder and D. Englund, *Rectangular photonic crystal nanobeam cavities in bulk diamond,* Applied Physics Letters **111**, 021103 (2017).

[40] N. H. Wan, S. Mouradian and D. Englund, *Two-dimensional photonic crystal slab nanocavities on bulk single-crystal diamond,* Applied Physics Letters **112**, 141102 (2018).

[41] H. Deng, K. Endo and K. Yamamura, *Damage-free finishing of CVD-SiC by a combination of dry plasma etching and plasma-assisted polishing,* International Journal of Machine Tools and Manufacture Far East Innovations in super-fine finishing of complex optics, **115**, 38 (2017).

[42] M. D. P. Emilio, *Plasma Polish Dry Etch Brings Next-Level SiC Quality,* (2022).

[43] E. R. Schmidgall *et al.*, *Frequency Control of Single Quantum Emitters in Integrated Photonic Circuits,* Nano Letters **18**, 1175 (2018).

[44] C. Errando-Herranz *et al.*, *MEMS for Photonic Integrated Circuits,* IEEE Journal of Selected Topics in Quantum Electronics **26**, 1 (2020).

[45] R. Wang, J. Li, L. Cai and Q. Li, *Investigation of the electro-optic effect in high-Q 4H-SiC microresonators,* Optics Letters **48**, 1482 (2023).

[46] D. M. Lukin *et al.*, *Two-Emitter Multimode Cavity Quantum Electrodynamics in Thin-Film Silicon Carbide Photonics,* Physical Review X **13**, 011005 (2023).

[47] S. Aghaeimeibodi, D. Riedel, A. E. Rugar, C. Dory and J. Vuckovic, *Electrical tuning of tin-vacancy centers in diamond,* Physical Review Applied **15**, 064010 (2021).

[48] S. Meesala *et al.*, *Strain engineering of the silicon-vacancy center in diamond,* Physical Review B **97**, 205444 (2018).

[49] Y.-I. Sohn *et al.*, *Controlling the coherence of a diamond spin qubit through its strain environment,* Nature Communications **9**, 2012 (2018).

[50] B. Machielse *et al.*, *Quantum interference of electromechanically stabilized emitters in nanophotonic devices,* Physical Review X **9**, 031022 (2019).

[51] A. Stolk *et al.*, *Telecom-Band Quantum Interference of Frequency-Converted Photons from Remote Detuned NV Centers,* PRX Quantum **3**, 020359 (2022).

[52] N. C. Harris *et al.*, *Linear programmable nanophotonic processors,* Optica **5**, 1623 (2018).

[53] W. Bogaerts *et al.*, *Programmable photonic circuits,* Nature **586**, 207 (2020).

[54] D. Bluvstein *et al.*, *Logical quantum processor based on reconfigurable atom arrays,* Nature **626**, 58 (2024).

[55] X. Chen *et al.*, *The Emergence of Silicon Photonics as a Flexible Technology Platform,* Proceedings of the IEEE **106**, 2101 (2018).

[56] S. Majety, P. Saha, V. A. Norman and M. Radulaski, *Quantum information processing with integrated silicon carbide photonics,* Journal of Applied Physics **131**, 130901 (2022).

[57] S. Majety *et al.*, *Triangular quantum photonic devices with integrated detectors in silicon carbide,* Materials for Quantum Technology **3**, 015004 (2023).

[58] K. Powell *et al.*, *Integrated silicon carbide electro-optic modulator,* Nature Communications **13**, 1851 (2022).

[59] J. Görlitz *et al.*, *Spectroscopic investigations of negatively charged tin-vacancy centres in diamond,* New Journal of Physics **22**, 013048 (2020).

[60] T. Staudacher *et al.*, *Enhancing the spin properties of shallow implanted nitrogen vacancy centers in diamond by epitaxial overgrowth,* Applied Physics Letters **101**, 212401 (2012).

[61] A. E. Rugar *et al.*, *Generation of Tin-Vacancy Centers in Diamond via Shallow Ion Implantation and Subsequent Diamond Overgrowth,* Nano Letters **20**, 1614 (2020).

[62] L. C. Bassett, A. Alkauskas, A. L. Exarhos and K.-M. C. Fu, *Quantum defects by design,* Nanophotonics **8**, 1867 (2019).

[63] G. Wolfowicz *et al.*, *Quantum guidelines for solid-state spin defects,* Nature Reviews Materials **6**, 906 (2021).

7

[64] P. Deák, B. Aradi, M. Kaviani, T. Frauenheim and A. Gali, *Formation of NV centers in diamond: A theoretical study based on calculated transitions and migration of nitrogen and vacancy related defects,* Physical Review B **89**, 075203 (2014).

[65] T. Murai *et al.*, *Engineering of Fermi level by nin diamond junction for control of charge states of NV centers,* Applied Physics Letters **112**, 111903 (2018).

[66] C. Zhang, F. Gygi and G. Galli, *Engineering the formation of spin-defects from first principles,* Nature Communications **14**, 5985 (2023).

[67] C. P. Anderson *et al.*, *Electrical and optical control of single spins integrated in scalable semiconductor devices,* Science **366**, 1225 (2019).

[68] P. C. Humphreys *et al.*, *Deterministic delivery of remote entanglement on a quantum network,* Nature **558**, 268 (2018).

[69] M. Pompili *et al.*, *Realization of a multinode quantum network of remote solid-state qubits,* Science **372**, 259 (2021).

[70] N. Kalb, P. C. Humphreys, J. J. Slim and R. Hanson, *Dephasing mechanisms of diamond-based nuclear-spin memories for quantum networks,* Physical Review A **97**, 062330 (2018).

[71] S. L. N. Hermans *et al.*, *Qubit teleportation between non-neighbouring nodes in a quantum network,* Nature **605**, 663 (2022).

[72] H. K. C. Beukers *et al.*, *Tutorial: Remote entanglement protocols for stationary qubits with photonic interfaces,* (2023), arXiv:2310.19878 [quant-ph].

[73] F. Dolde *et al.*, *High-fidelity spin entanglement using optimal control,* Nature Communications **5**, 3371 (2014).

[74] X. Rong *et al.*, *Experimental fault-tolerant universal quantum gates with solid-state spins under ambient conditions,* Nature Communications **6**, 8748 (2015).

[75] P. Rembold *et al.*, *Introduction to quantum optimal control for quantum sensing with nitrogen-vacancy centers in diamond,* AVS Quantum Science **2**, 024701 (2020).

[76] C. H. Yang *et al.*, *Silicon qubit fidelities approaching incoherent noise limits via pulse engineering,* Nature Electronics **2**, 151 (2019).

[77] A. Reiserer *et al.*, *Robust Quantum-Network Memory Using Decoherence-Protected Subspaces of Nuclear Spins,* Physical Review X **6**, 021040 (2016).

[78] C. E. Bradley *et al.*, *Robust quantum-network memory based on spin qubits in isotopically engineered diamond,* npj Quantum Information **8**, 1 (2022).

[79] M. J. Degen, *On the creation, coherence and entanglement of multi-defect quantum registers in diamond*, Ph.D. thesis, Delft University of Technology (2021).

7

[80] C. Bradley, *Order from Disorder: Control of Multi-Qubit Spin Registers in Diamond*, Ph.D. thesis, Delft University of Technology (2021).

[81] F. Dolde *et al.*, *Room-temperature entanglement between single defect spins in diamond*, Nature Physics **9**, 139 (2013).

[82] T. H. Taminiau *et al.*, *Detection and Control of Individual Nuclear Spins Using a Weakly Coupled Electron Spin*, Physical Review Letters **109**, 137602 (2012).

[83] S. Kolkowitz, Q. P. Unterreithmeier, S. D. Bennett and M. D. Lukin, *Sensing Distant Nuclear Spins with a Single Electron Spin*, Physical Review Letters **109**, 137601 (2012).

[84] N. Zhao *et al.*, *Sensing single remote nuclear spins*, Nature Nanotechnology **7**, 657 (2012).

[85] M. H. Abobeih *et al.*, *Fault-tolerant operation of a logical qubit in a diamond quantum processor*, Nature **606**, 884 (2022).

[86] J. Randall *et al.*, *Many-body–localized discrete time crystal with a programmable spin-based quantum simulator*, Science **374**, 1474 (2021).

[87] H. P. Bartling, *Quantum control of interacting nuclear and electron spins in diamond*, Ph.D. thesis, Delft University of Technology (2023).

[88] E. Hesselmeier *et al.*, *Measuring nuclear spin qubits by qudit-enhanced spectroscopy in Silicon Carbide*, (2023), arXiv:2310.15557 [physics, physics:quant-ph].

[89] Z. Xu, Z.-q. Yin, Q. Han and T. Li, *Quantum information processing with closely-spaced diamond color centers in strain and magnetic fields [Invited]*, Optical Materials Express **9**, 4654 (2019).

7

8

APPENDIX

This appendix consists of two parts. Part 1 complements the results reported in chapter 3, which presents entanglement of dark electron-nuclear spin defects in diamond. The second part provides background to the simulation of T_2^* values reported in chapter 6.

8.1. APPENDIX CHAPTER 3

8.1.1. P1 HAMILTONIAN

In this note we describe the Hamiltonian of a system consisting of a P1 center and an NV center in diamond.

P1 CENTER
The Hamiltonian of the P1 center is given by[1]:

$$H_{P1_i} = \gamma_e \mathbf{B} \cdot \mathbf{S} + \mathbf{S} \cdot \hat{\mathbf{A}}_i \cdot \mathbf{I} + \gamma_n \mathbf{B} \cdot \mathbf{I} + \mathbf{I} \cdot \hat{\mathbf{P}}_i \cdot \mathbf{I}, \tag{8.1}$$

where γ_e ($\approx 2\pi \cdot 2.802$ MHz/G) and γ_n ($\approx -2\pi \cdot 0.3078$ kHz/G) are the electron and ^{14}N gyromagnetic ratio respectively. $\mathbf{B}$ is the external magnetic field vector and $\mathbf{S}$ and $\mathbf{I}$ are the electron spin-1/2 and nuclear spin-1 operator vectors. The P1 center exhibits a JT distortion along the axis of one of the four carbon-nitrogen bonds (denoted by $i \in$ {A,B,C,D}). This JT axis defines the principal axis of the hyperfine interaction and the quadrupole interaction.

The hyperfine tensor ($\hat{\mathbf{A}}_i$) and quadrupole tensor ($\hat{\mathbf{P}}_i$) can be obtained in any coordinate frame via a transformation of the diagonal hyperfine tensor, $\mathbf{A_{diag}} = \text{diag}[A_x, A_y, A_z]$ and diagonal quadrupole tensor, $\mathbf{P_{diag}} = \text{diag}[P_x, P_y, P_z]$:

$$\hat{\mathbf{A}}_i = R^T \cdot \mathbf{A_{diag}} \cdot R \tag{8.2}$$

and

$$\hat{\mathbf{P}}_i = R^T \cdot \mathbf{P_{diag}} \cdot R. \tag{8.3}$$

Here R is the rotation matrix from the principal axis of the P1 center to any other coordinate frame defined by Euler angles $\{\alpha, \beta, \gamma\}$:

$$R(\alpha, \beta, \gamma) = \begin{pmatrix} \cos(\gamma)\cos(\beta)\cos(\alpha) - \sin(\gamma)\sin(\alpha) & \cos(\gamma)\cos(\beta)\sin(\alpha) + \sin(\gamma)\cos(\alpha) & -\cos(\gamma)\sin(\beta) \\ -\sin(\gamma)\cos(\beta)\cos(\alpha) - \cos(\gamma)\sin(\alpha) & -\sin(\gamma)\cos(\beta)\sin(\alpha) + \cos(\gamma)\cos(\alpha) & \sin(\gamma)\sin(\beta) \\ \sin(\beta)\cos(\alpha) & \sin(\beta)\sin(\alpha) & \cos(\beta) \end{pmatrix}. \tag{8.4}$$

Due to the axial symmetry of the P1 center in its principal axis coordinate frame ($A_x = A_y$ and $P_x = P_y$), this can be reduced to:

$$R(\beta, \alpha) = \begin{pmatrix} \cos(\beta)\cos(\alpha) & \cos(\beta)\sin(\alpha) & -\sin(\beta) \\ -\sin(\alpha) & \cos(\alpha) & 0 \\ \sin(\beta)\cos(\alpha) & \sin(\beta)\sin(\alpha) & \cos(\beta) \end{pmatrix}. \tag{8.5}$$

For any of the four JT axes, the hyperfine (quadrupole) tensor $\hat{\mathbf{A}}_i$ ($\hat{\mathbf{P}}_i$) in the coordinate frame of the symmetry axis of the NV center is obtained via a transformation with angles $(\beta, \alpha)_i$, where $(\beta, \alpha)_i \in \{(109.5°, 240°)_C, (109.5°, 120°)_B, (109.5°, 0°)_A, (0°, 0°)_D\}$.

NV-P1 SYSTEM

The Hamiltonian of a coupled NV-P1 system (in the frame of the symmetry axis of the NV center) is given by the terms corresponding to the NV, the P1 and the terms describing their dipolar coupling:

$$H_{\text{tot}} = H_{\text{NV}} + H_{\text{P1}} + H_{\text{dipole}}. \tag{8.6}$$

For the NV we only consider the electron spin of the NV center:

$$H_{\text{NV}} = \Delta J_z^2 + \gamma_e \mathbf{B} \cdot \mathbf{J}. \tag{8.7}$$

where $\Delta = 2\pi \cdot 2.877$ GHz is the zero-field splitting and $\mathbf{J}$ is the electron spin 1 vector. If we consider a point dipole coupling between the NV and the electron spin of the P1 center, separated by a vector $\mathbf{r}$, the dipole term can be written as:

$$H_{\text{dipole}} = \nu_{\text{dip}} \cdot \left(3(\mathbf{J} \cdot \hat{\mathbf{r}})(\mathbf{S} \cdot \hat{\mathbf{r}}) - \mathbf{J} \cdot \mathbf{S}\right), \tag{8.8}$$

where $\nu_{\text{dip}} = \frac{-\mu_0 \gamma_e \gamma_e \hbar}{4\pi r^3}$, $r = |\mathbf{r}|$ and $\hat{\mathbf{r}} = \mathbf{r}/r$. Transforming to spherical coordinates using the definitions $r_x = r\sin(\theta)\cos(\varphi)$, $r_y = r\sin(\theta)\sin(\varphi)$ and $r_z = r\cos(\theta)$, gives

$$
\begin{aligned}
H_{\text{dipole}} = \nu_{\text{dip}} \cdot \Big[& J_x S_x \left(3\sin^2(\theta)\cos^2(\varphi) - 1\right) + J_y S_y \left(3\sin^2(\theta)\sin^2(\varphi) - 1\right) + J_z S_z \left(3\cos^2(\theta) - 1\right) \\
& + (J_y S_x + J_x S_y)3\sin^2(\theta)\cos(\varphi)\sin(\varphi) + (J_z S_x + J_x S_z)3\cos(\theta)\sin(\theta)\cos(\varphi) \\
& + (J_z S_y + J_y S_z)3\cos(\theta)\sin(\theta)\sin(\varphi) \Big].
\end{aligned}
$$
$$\tag{8.9}$$

Due to the large difference between electron and ^{14}N gyromagnetic ratio ($\gamma_e/\gamma_n \sim 9000$) we expect the electron-nuclear NV-P1 dipolar coupling to be negligible and omit this term in the Hamiltonian.

8

ORIENTATION IN THE CRYSTAL LATTICE

In the diamond lattice, the P1 defect is located in a tetrahedral geometry with four surrounding carbon atoms. A single carbon atom can be positioned either directly above (orientation 1) or below (orientation 2) the P1 center's nitrogen atom, and the other three carbon atoms at 109.5° bond angles below or above respectively.

If we consider the JT distortions along the **z** axis (JT axis D) for these two orientations, the nitrogen atom either distorts in the -**z** direction or the +**z** direction. Therefore, these two orientations correspond to two spin Hamiltonians as in Supplementary Eq. (8.6): $H_{\text{tot},1}$ with $\hat{\mathbf{A}}_\mathbf{D} = \mathbf{A_{diag}}$ and $H_{\text{tot},2}$ with $\hat{\mathbf{A}}_\mathbf{D} = R(180°, 0°)^T \cdot \mathbf{A_{diag}} \cdot R(180°, 0°)$ (similar for $\hat{\mathbf{P}}_\mathbf{D}$). From Supplementary Eq. (8.5) it is evident that $R(180°, 0°)^T \cdot \mathbf{A_{diag}} \cdot R(180°, 0°) = \mathbf{A_{diag}}$, and thus $H_{\text{tot},1} = H_{\text{tot},2}$. Therefore, in the experiments performed in this work, we cannot distinguish between these two different orientations of P1 centers.

8.1.2. DEER AND DEER(Y) SEQUENCE

Here a more detailed description is given for the experimental sequences shown in Figs. 3.2b and 3.2b of the main text. We consider an idealized case of a single NV, a single P1 center and their magnetic dipolar coupling. In a diagonalized frame, the energy eigenstates and eigenvalues of the system are labelled as $\left|m_s, m_{\uparrow/\downarrow}, m_I\right\rangle$ and $\lambda_{m_s, m_{\uparrow/\downarrow}, m_I}$ respectively. The eigenstates form a 12-dimensional Hilbert space (the subspace $m_s = \{0, -1\}$ of the NV, the electron spin 1/2 of the P1 center and its ^{14}N spin 1).

DEER

We consider the sequence of unitary operations as applied during a DEER sequence with a single repetition $K=1$ (see Fig. 2b in the main text). First we apply $U_{\mathrm{NV},1} = R_x(\pi/2)_{\mathrm{NV}} \otimes \mathbb{1}_{\mathrm{P1}}$, a $\pi/2$ rotation on the NV with phase x, followed by an evolution time $U_{\mathrm{evo}}(\tau)$, which is given by $\mathrm{diag}[e^{-i\lambda_{0,\uparrow,+1}\cdot\tau}, e^{-i\lambda_{0,\uparrow,0}\cdot\tau}, \ldots, e^{-i\lambda_{m_s, m_{\uparrow/\downarrow}, m_I}\cdot\tau}, \ldots, e^{-i\lambda_{-1,\downarrow,-1}\cdot\tau}]$. This is followed by a π pulse on the NV; $U_{\mathrm{NV},2} = R_x(\pi)_{\mathrm{NV}} \otimes \mathbb{1}_{\mathrm{P1}}$. Simultaneously, we apply a π pulse on the P1 electron spin conditional on its ^{14}N state $|m_I\rangle = |+1\rangle$. This operation is described by $U_{\mathrm{P1}} = \mathbb{1}_{\mathrm{NV}} \otimes R_x(\pi)_{\mathrm{P1,e}} \otimes |+1\rangle\langle+1| + \mathbb{1}_{\mathrm{NV}} \otimes \mathbb{1}_{\mathrm{P1,e}} \otimes |0\rangle\langle 0| + \mathbb{1}_{\mathrm{NV}} \otimes \mathbb{1}_{\mathrm{P1,e}} \otimes |-1\rangle\langle-1|$. Then there is another evolution time $U_{\mathrm{evo}}(\tau)$ and finally a $\pi/2$ pulse $U_{\mathrm{NV},3} = R_{-x}(\pi/2)_{\mathrm{NV}} \otimes \mathbb{1}_{\mathrm{P1}}$ with phase $-x$. We assume perfect π and $\pi/2$ pulses between energy eigenstates. For an initial state ρ_1, we obtain a final state given by:

$$\rho_{f,1}(\tau) = U_{\mathrm{NV},3} U_{\mathrm{evo}}(\tau) U_{\mathrm{P1}} U_{\mathrm{NV},2} U_{\mathrm{evo}}(\tau) U_{\mathrm{NV},1} \rho_1 U_{\mathrm{NV},1}^\dagger U_{\mathrm{evo}}(\tau)^\dagger U_{\mathrm{NV},2}^\dagger U_{\mathrm{P1}}^\dagger U_{\mathrm{evo}}(\tau)^\dagger U_{\mathrm{NV},3}^\dagger$$

(8.10)

For the NV initialized in $|0\rangle$ but mixed P1 electron and ^{14}N spin states, the initial density matrix is given as:

$$\rho_1 = \frac{1}{6} |0\rangle\langle 0| \otimes \mathbb{1}_{\mathrm{P1}}$$

(8.11)

The reduced density matrix of the NV as a function of interaction time is given by:

$$\rho_{\mathrm{NV}}(\tau) = \sum_{m_{\uparrow,\downarrow}, m_I} \left\langle m_{\uparrow,\downarrow}, m_I \middle| \rho_{f,1}(\tau) \middle| m_{\uparrow,\downarrow}, m_I \right\rangle = \frac{1}{6}\cos(\nu\cdot\tau)\left[|-1\rangle\langle-1| - |0\rangle\langle 0|\right] + \frac{1}{6}|0\rangle\langle 0| + \frac{5}{6}|-1\rangle\langle-1|.$$

(8.12)

Here the effective NV-P1 dipolar coupling (ν) is given as

$$\nu = \lambda_{-1,\downarrow,+1} - \lambda_{0,\downarrow,+1} - (\lambda_{-1,\uparrow,+1} - \lambda_{0,\uparrow,+1}).$$

(8.13)

Note that at $\tau = \pi/|\nu|$ we obtain the highest probability of measuring $|0\rangle_{\mathrm{NV}}$. Upon measurement of $|0\rangle_{\mathrm{NV}}$ we obtain the state:

$$\rho_{m_s=0} = \frac{|0\rangle\langle 0| \rho_{f,1}(\tau) |0\rangle\langle 0|}{\mathrm{Tr}\left(|0\rangle\langle 0| \rho_{f,1}(\tau)\right)} = \frac{1}{2}|0\rangle\langle 0| \otimes \mathbb{1}_{\mathrm{P1,e}} \otimes |+1\rangle\langle+1|,$$

(8.14)

and thus initialize the ^{14}N state of the P1 center in $|+1\rangle$.

8.1.3. DEER(Y)

Now we consider DEER(y) (see main text Fig. 3b), which is sensitive to the P1 electron spin state. This sequence is the DEER sequence with the phase of the final $\pi/2$ pulse changed from $-x \rightarrow -y$, or $-x \rightarrow +y$. For an initial state ρ_2 and the phase of the final $\pi/2$ pulse as $-y$, we obtain the final state $\rho_{f,2}$ by:

$$\rho_{f,2}(\tau) = U_{\mathrm{NV},4} U_{\mathrm{evo}}(\tau) U_{\mathrm{P1}} U_{\mathrm{NV},2} U_{\mathrm{evo}}(\tau) U_{\mathrm{NV},1} \rho_2 U_{\mathrm{NV},1}^\dagger U_{\mathrm{evo}}(\tau)^\dagger U_{\mathrm{NV},2}^\dagger U_{\mathrm{P1}}^\dagger U_{\mathrm{evo}}(\tau)^\dagger U_{\mathrm{NV},4}^\dagger. \tag{8.15}$$

Note that the final operator has been changed to $U_{\mathrm{NV},4} = R_{-y}(\pi/2)_{\mathrm{NV}} \otimes \mathbb{1}_{\mathrm{P1}}$ with phase $-y$. If we consider the NV initialized in $|0\rangle$ and the ^{14}N state of the P1 in $|+1\rangle$, the initial density matrix is given as:

$$\rho_2 = \frac{1}{2} |0\rangle \langle 0| \otimes \mathbb{1}_{\mathrm{P1,e}} \otimes |+1\rangle \langle +1|. \tag{8.16}$$

The reduced density matrix of the NV as a function of interaction time is now given by:

$$\rho_{\mathrm{NV}}(\tau) = \sum_{m_{\uparrow,\downarrow}, m_I} \langle m_{\uparrow,\downarrow}, m_I | \rho_{f,2}(\tau) | m_{\uparrow,\downarrow}, m_I \rangle = \tfrac{1}{2} \cos(\nu \cdot t) \big[|0\rangle \langle -1| + |-1\rangle \langle 0| \big] + \tfrac{1}{2} |0\rangle \langle 0| + \tfrac{1}{2} |-1\rangle \langle -1|. \tag{8.17}$$

Upon measurement of $|0\rangle_{\mathrm{NV}}$ we obtain the state:

$$\rho_{m_s=0} = \frac{|0\rangle \langle 0| \rho_{f,2}(\tau) |0\rangle \langle 0|}{\mathrm{Tr}\big(|0\rangle \langle 0| \rho_{f,2}(\tau)\big)} = \tfrac{1}{2} (1 + \sin(\nu \cdot \tau)) |0,\uparrow,+1\rangle \langle 0,\uparrow,+1| + \tfrac{1}{2} (1 - \sin(\nu \cdot \tau)) |0,\downarrow,+1\rangle \langle 0,\downarrow,+1| \tag{8.18}$$

Note that at interaction time $\tau = \pi/(2|\nu|)$, the initialized state is either $|0,\downarrow,+1\rangle$ or $|0,\uparrow,+1\rangle$ depending on the sign of ν. Applying a phase $+y$ instead of $-y$ in the final $\pi/2$ pulse effectively changes the signs in front of the $\sin(\nu \cdot \tau)$ terms in Supplementary Eq. (8.18), which is used in Fig. 3.4b of the main text.

8.1.4. NV-P1 DIPOLAR COUPLING SIGN IN $|+1, \mathrm{A}\rangle$

This section demonstrates coherent control of the ^{14}N spin and extracts the sign of the NV-P1 dipolar coupling for the electron spin of S1, S2 and S3/S4 in the $|+1, \mathrm{A}\rangle$ state (similar as in Fig. 4b of the main text for $|+1, \mathrm{D}\rangle$). First, we choose an initialisation sequence with a low K ($K=6$), which with high probability prepares either S1, S2 or S3/S4 in $|+1, \mathrm{A}\rangle$. Then we calibrate a π pulse that implements a CNOT between the electron (control) and nitrogen nuclear spin (target) for a P1 in the $|+1, \mathrm{A}\rangle$ state, see Supplementary Fig. 8.1a. This pulse is only resonant with the $m_I = +1 \leftrightarrow 0$ transition, if the P1 electron spin is in the $|\uparrow\rangle$ state.

We use the same experimental procedure as in the main text for $|+1, \mathrm{D}\rangle$, to determine the NV-P1 coupling signs (Supplementary Fig. 8.1b). The value R is defined as:

$$R = \frac{P_{(+y)} - P_{(-y)}}{P_{(+y)} + P_{(-y)}}, \tag{8.19}$$

with $P_{(+y)}$ ($P_{(-y)}$) the probability that the outcome of the DEER readout sequence is within the FWHM range corresponding to S1, S2 or S3/S4 (see section 3.9.7), and the subscript +y (-y) indicates the readout basis of the DEER(y) sequence used to initialize the electron spin. The result shows that spin S1 and S3/S4 have a positive coupling sign, whereas it is negative for S2. Note that S1, S2 and S3/S4 have the same NV coupling sign in $|+1, A\rangle$ and $|+1, D\rangle$.
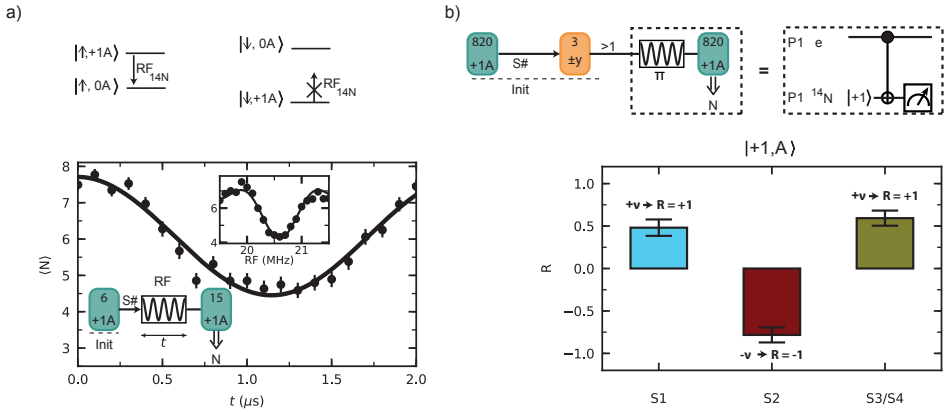

Figure 8.1: **Coupling sign of NV-P1 dipolar interaction for different P1 centers in the $|+1, A\rangle$ state.** a) Top: energy level structure of the P1 electron spin in the {0A, +1A} subspace. Bottom: A short initialisation sequence (K=6) prepares either S1, S2 or S3/S4 in $|+1, A\rangle$ (without knowledge of which P1 is prepared in which run) and the length t of a pulse at frequency RF = RF$_{14N}$ = 20.55 MHz is varied. The nitrogen nuclear spin is driven conditionally on the electron spin state (top). Inset: NMR spectrum obtained by varying the frequency (RF) for a fixed pulse duration t. b) Value of R (see Methods) measured for the P1s in $|+1, A\rangle$. Positive values correspond to a positive coupling sign.

8

8.1.5. NV-P1 COUPLING IN $|+1, A\rangle$

In Fig. 3a of the main text the effective NV-P1 dipolar coupling (Supplementary Eq. (8.13)) for S1, S2, S3/S4 in $|+1, D\rangle$ is measured. Here, we measure the effective dipolar coupling of these spins in $|+1, A\rangle$, see Supplementary Fig. 8.2. We initialize each P1 center by setting the requirement that the outcome of the DEER initialisation sequence is within the range for $|+1, A\rangle$ (see Supplementary Fig. 3.15a).

We obtain effective dipolar couplings ν of $2\pi \cdot 1.35(2)$, $2\pi \cdot 2.006(9)$ and $2\pi \cdot 1.06(2)$ kHz for S1, S2 and S3/S4 respectively, using the fit function in eq. 11 (see Methods). A comparison with the couplings for $|+1, D\rangle$ (Fig. 3a in the main text) shows that the effective NV-P1 dipolar coupling strength differs for the two JT axes (see section 3.9.2 for the theoretical treatment).
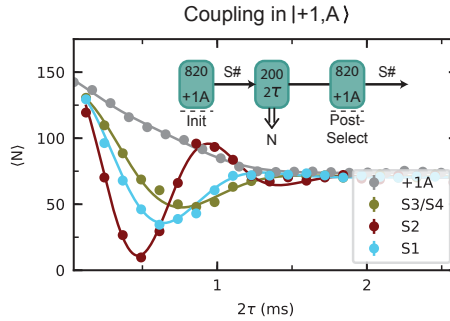
Figure 8.2: **Measuring NV-P1 coupling strength in $|+1,A\rangle$.** We initialize S1, S2 or S3/S4 in $|+1,A\rangle$ and vary the interaction time 2τ of a DEER sequence (K=200). To improve the signal, the results are post-selected on again obtaining $|+1,A\rangle$. Inset: experimental sequence. Grey: without P1 initialisation (data from Fig. 1c main text).

8.1.6. Magnetic field stability

Here we describe the magnetic field stabilisation used during the Ramsey and entanglement experiments in this manuscript, as well as during the data in Supplementary Fig. 3.8b. We use three permanent magnets on motorized linear translation stages to create a static magnetic field. To compensate for magnetic field fluctuations we repeatedly measure the NV $|0\rangle \leftrightarrow |-1\rangle$ frequency (f_{NV}) and this signal is fed back to one of the magnet stages until (f_t - 1.5 kHz $\leq f_{NV} \leq f_t$ + 1.5 kHz), with target frequency $f_t = 2.749692$ GHz. We interleave this protocol (typically every 20 minutes) with repetitions of an experimental sequence.

Supplementary Fig. 8.3a shows the time trace of f_{NV} before and after interleaved experiments. The two red lines indicate $f_t \pm 1.5$ kHz. The magnetic field can freely drift during the experimental sequences, but right before starting the next run the field is stabilized. From the histogram we infer that on average f_{NV} fluctuates with $\sigma = 4.07$ kHz around $f = 2.749690$ GHz during feedback.

To monitor the complete magnetic field vector $\mathbf{B} = (B_x, B_y, B_z)$ during experiments with the stabilization protocol interleaved, we measure $f_{+1A}, f_{+1B}, f_{+1C}$ and f_{+1D} (see Fig. 1b main text). In a similar approach as in section 3.9.3, we fit a parabola to the four frequencies and use the residuals consisting of the difference of the four fitted frequencies and the corresponding frequencies obtained from Supplementary Eq. (8.1) to perform a least-squares minimization to find $\mathbf{B}$.

The obtained values for B_x, B_y and B_z are shown in Figs. 8.3b,c,d. The standard deviations of these histogram verify a magnetic field stability during this protocol with $\sigma_{B_x} = 20$ mG, $\sigma_{B_y} = 16$ mG and $\sigma_{B_z} = 3$ mG. Note that the average values of $\mathbf{B}$ from Supplementary Fig. 8.3 show a discrepancy with the values obtained from the fit in the main text and section 3.9.3, indicating that these measurements have been taken under slightly different conditions.
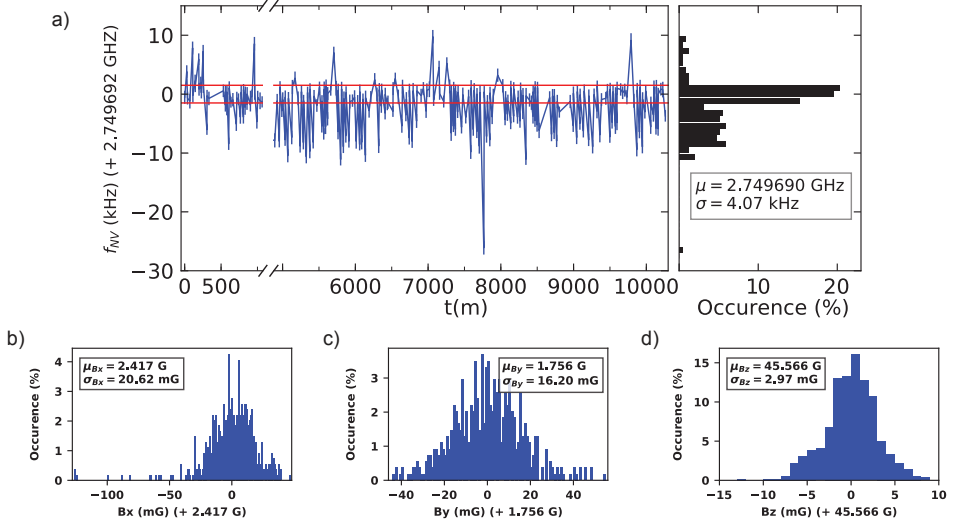
Figure 8.3: **Magnetic field stability.** (a) Time trace of all measured NV resonance frequencies before and after performing repetitions of an experimental sequence. The red lines indicate the region ($\pm$ 1.5 kHz) to within which we stabilize before each measurement. (b,c,d) Distribution of measured B_x, B_y and B_z during 220 hours, while stabilizing f_{NV}.

8.2. APPENDIX CHAPTER 6

8.2.1. NATURAL DEPHASING TIME CALCULATION

In this section, we derive the relation between the T_2^* of a central electron spin and the hyperfine components between this spin and spins in a surrounding spin bath. We assume that the quantisation axis of the central spin is dominated by the external magnetic field, and that the spin projection of the spins in the spin bath are completely random. We will derive that $T_2^* = \frac{2}{\sqrt{\sum_{i=1}^{N} A_i^2}}$, where A_i is the hyperfine interaction component along the direction of the magnetic field between the central electron spin and spin i. We first considering a spin bath of 1 spin, and extend this to an arbitrary number of spins N. Subsequently, in the absence of couplings stronger than the T_2^* of the central spin, we use a Taylor expansion to derive at the final result.

For a spin bath of a single spin with hyperfine coupling A_i, the probability at time t to measure the central electron spin in the X-basis in a Ramsey experiment is given by

$$P(|+\rangle) = \cos\left(\frac{1}{2}A_1 t\right), \tag{8.20}$$

where we adopted the rotating frame of the Larmor frequency of the central electron spin. If the bath consists of two spins, then the precession frequency in the rotating

frame is either the sum, or the difference, of the hyperfine components such that

$$P(|+\rangle) = \frac{1}{2}\cos\left(\frac{1}{2}(A_1 + A_2)t\right) + \frac{1}{2}\cos\left(\frac{1}{2}(A_1 - A_2)t\right) = \cos\left(\frac{1}{2}A_1 t\right)\cos\left(\frac{1}{2}A_2 t\right). \quad (8.21)$$

Extending this to N spins gives

$$P(|+\rangle) = \prod_{i=1}^{N}\cos\left(\frac{1}{2}A_i t\right), \quad (8.22)$$

with A_i defined as explained in the top of this section.

If none of the A_i values generates a visible oscillation in $P(|+\rangle)$, then there is no strongly coupled spin, and hence for a time equal to $t = T_2^*$ the value $A_i t \ll 1$. Therefore, we Taylor-expand the cosine expressions as $\cos\left(\frac{1}{2}A_i t\right) \approx 1 - \frac{1}{2}\left(\frac{1}{2}A_i t\right)^2$. Subsequently, we take the 'log ()' of the left and right side of equation (8.22) to obtain

$$\log(P(|+\rangle)) = \log\left(\prod_{i=1}^{N}\left[1 - \frac{1}{2}\left(\frac{1}{2}A_i t\right)^2\right]\right) = \sum_{i=1}^{N}\log\left(1 - \frac{1}{2}\left(\frac{1}{2}A_i t\right)^2\right). \quad (8.23)$$

Again, we make a Taylor expansion, using $\log(1 + x) \approx x$ and $\frac{1}{2}\left(\frac{1}{2}A_{ij}t\right) \ll 1$. Substituting this in equation (8.23), and taking the exponent on either side, gives

$$P(|+\rangle) = \exp\left\{-\sum_{i=1}^{N}\frac{1}{8}A_i^2 t^2\right\}. \quad (8.24)$$

Rewriting this as $P(|+\rangle) = \exp\left\{-\frac{1}{2}\left(\frac{t}{T_2^*}\right)^2\right\}$ gives

$$T_2^* = \frac{2}{\sqrt{\sum_{i=1}^{N}A_i^2}}. \quad (8.25)$$

8

REFERENCES

[1] W. V. Smith, P. P. Sorokin, I. L. Gelles and G. J. Lasher, *Electron-Spin Resonance of Nitrogen Donors in Diamond,* Physical Review **115**, 1546 (1959).

8

9

ACKNOWLEDGEMENTS

November 1st, 2019: My PhD commenced, the start of a journey.
148.221.000.000.000.000 nanoseconds later, the clock marks the start of my defense. During the time that light has traveled a distance equal to 26931 2π rotations around the world, the beadle comes in to end my defense. I've become a doctor now.

Tim, thanks a lot for having allowed me to pursue my master thesis in your group and for giving the chance to pursue a PhD. I appreciate you a lot and have a lot of respect for the critical analysis that you always manage to provide on close to 100% of the documents we sent you. Such reviews massively boost the scientific quality from your group and have played a big part in the academic growth I have experienced. Besides the academic part, I also thank you for the empathy and relaxed vibes that you create to lead the group. I clearly remember the chat we had after my disappointment regarding my master thesis result, and also the moment you passed by my office after a ZOOM call where we decided that you and Maarten would take the lead on writing the main text of the P1 paper. This was an endeavour that I actually wanted to take part in as well and even though it made full sense to me to divide the tasks as we did, you noticed it wasn't as I initially desired. And even though it was clear we had different lines of thought in the process of finalizing my draft thesis, I have appreciated the level of respect in the relatively intense discussions we had during that time to get to the point of handing in Form B. So all in all, I have learned a lot from you and am extremely happy to have spend my PhD under your supervision!

Thanks as well to **Ronald** for being my promotor and for many interesting and fun chats in the hallway! **Capsar**, **Jörg**, **Toeno**, **Gary** and **Yaroslav**, thanks for being part of my committee!

Maarten, Big shout-out to the P1s! Mate, my academic father. I am super happy I was allowed to spend my first year as a PhD student together with you. I have had a lot of fun with you and you have tought me many skills and insights. You're a honest person with a great heart! We have amazing times, such as spending days in a dark room lit up by 4 monitors and hours of staring at ADwin code we wrote ourselves that got use looping around from CASE 3 to EVENT 5 to CASE blablabla. I never forget that Peru sweater and the GREENBLASTER. Never I have seen two guys of nearly 30 (I think you were 30 already) being so thrilled when a double-frequency cosine fits data points. P1-P1 entanglement!

Guido, after Maarten left I needed a new sidekick. And I couldn't have wished for

a better one then you. Together we embarked on a completely different path than our group had routinely done. While both of us still danced with M1, we also abandoned the NV-center path in favor of silicon carbide. I've always very much liked to work together with you and have a lot of in-depth discussions about physics. I think your way of looking at physics is inspirational and allows to open up interesting research directions. I also appreciate your way of working, although it is rather different from mine. I liked to combination we had together. Besides a side-kick in research, I've always enjoyed our bullshit conversations and loved your support to convince one of our colleagues of my 'online side-business' during our post-March Meeting road trip (which was so much fun).

Laurens, The SiC team only consisted of Brabant-born-boys. We needed to diversify. That's when you came into the picture. And what an amazing picture that was. You are a perfect fit to the team. Relaxed, chilled, motivated, structured and very good with laser safety. After Guido and me spend so much time behind our screens to order the M3 components, we were thrilled to start building M3. But then you came in and built it all by yourself. Thanks for taking away our fun. No, big love to you and I am very happy you did such an amazing job on M3! It has been wonderful to work with you, especially when you set me to do some brain dead work for our amazing bachelor student **Théo** while I had a single spare day at the end of writing my thesis. I really appreciate your level of humor and the numerous discussions we had were we came to the conclusion that we agree to disagree on some very important things in life;).

Mohamed, grandfather of my academic life. Thanks to you I have some of the relaxing Egyptian waters in my work. You were always very chilled and a very nice person to chat to, as well as a person that could place our very hard work in perspective. Thanks a lot for being my master supervisor and helping to convince me to do a PhD. I'll always remember your physics derivations on napkins, though up to today I still wonder, why napkins Mo?

Gerben, working with you has been fabtastic! We've had great first interactions. As a supervisor of Quantum Hardware II, I needed to provide you feedback on your online presentation. Hard to properly do, as the light settings in your room only allowed me to stare at your silhouette for 30 minutes. And then, when you came for your MSc thesis to us, you had that lovely coffee story. Your cleanroom dedication, social skills and creativity is inspirational. I love your and **Laurens**' nanoart! You've been a super valuable humorous addition to the silicon carbide team. It has been dood en doodziek to have you in the team.

Anta, During my international times I've heard many pronunciations of my name. You topped all of them, 'swordy'! I honestly have never experienced somebody as humble and compassionate as you. A heart of gold, something that is super unique. I have deep respect for your journey. From Dinhata to Delft requires a tuktuk, a bus, an overnight train, a national flight and two international flights. And the amount of shit you experienced with customs, oh men. Though I have to give it to the Dutch handhaving, you shouldn't cycle on a pedestrian way. I loved being your paranymph together with **Jake**. Thanks for being a good friend.

Nikolas makala ree mou, Andras me alfa kefaleo. Pame na pioume Koumantaria. I still don't know how to write your real name. You've been an amazing office mate. I hope

my future will still allow me to enter the office in the morning and start the day with a greeting like we always gave each other. Bro, keep hitting that gym. Thanks for all the fun times. We've shared many things, but too little beers. Please make yourself more available, you and your Dutch schedule...

Kian, if there is anyone that has been like a rock in the storm for me to share my office life with, then it is without a doubt you. We started our PhD's on the same day and it was instantly clear that you are motivated to be a winner. My accusation of you joining team diamond without a cake backfired hard. What a cake you made, hilarious. Then I knew we would get along well. We've a shared offices nearly all our PhD and we had many very good, inspirational and in-depth discussions about everything. Besides, I'm happy to have been able to share a good chunk of nonsense with you.

Tijmen, mister alligator! Thanks for always sharing your one-year-in-advance holiday plans with your PhD supervisors. You initially just wanted to get your MSc diploma, but we were thrilled to see your developing into a photonic night owl! You set the stage for mister **Dani**, Spanish lord! I won't forget that train ride where you enlighted me and my salsa partner with your full-detail-capturing sickness struggles. Keep your shameless story-telling attitude, I love it!

Florian, thanks for all the nice interactions on conferences, via email and during your visit in Delft. I admire how helpful you have always been and how much effort you have put in getting a European silicon carbide quantum research line from the ground. I am happy we are in such good touch. All the best in fake Netherlands! Hopefully we can some time take a big pitcher over there.

I am extremely grateful to have had the pleasure to meet a lot of amazing support staff within QuTech. I want to thank all of them for their energy and I think their qualities and help are so much more valuable than what is typically expressed to them. You all are great. I'd like to specifically acknowledge some of the support staff that I have interacted with a lot.

Olaf, you are a men of tidiness, directness and punctuality. I wonder whether I have ever met somebody with such a dedicated schedule. You were there always in time, thanks for all those encounters in our meeting room! Still waiting to celebrate carnaval with you.

Jason, thanks to you there is never a moment of awkward silence at the lunch table. You're like one of my favourite funfair attractions. You toss one coin in it, and the apparatus keeps entertaining you indefinitely. Thanks as well for always making time to help, and giving me that crank to fix my bike pedal.

Siebe and **Vinod**, speaking about bike pedals. What a lovely day when both of you got my back in saving me from the broken pedal. Using metal bars of a meter long and tricky tools from Jason and the TU Delft, you managed to get the bike pedal unstuck. It was a tough challenge, certainly as I spend an hour trying to get my bike pedal loose the night before not realizing that I was turning the screw the wrong direction. Also apart from that experience, I like how extremely relaxed, helpful and interested both of you always are.

Mark, we had a lot of special conversations and I feel like we got to know each other very well in the little time that we were given to spend with each other. Thanks for shar-

ing the stories of your kids and how they enjoyed King Fridge, and thanks for showing that people without a smartphone still exist. I deeply value you as a person and a colleague. Hope you and **Remco** are doing well at Delft Circuits, you both deserve it!

Jelle, it was lovely to always share the passion for tennis together with you. Both speaking about all the players and their games, as well as hitting some balls on the court with you! Court number 4 under the tennis balloon in the winter, it was a very nice experience!

Hitham Master of safety! You have a very nice and intrinsic character, keep it that way. Thanks for always apologizing for not pronouncing my name correctly (it is no problem of course). Sadly, I only learned recently that I have always been pronouncing your name incorrectly. Promise me that next year you won't come up with an excuse not to celebrate carnaval with your kids! Stay safe.

Roy It was a lot of fun spending the QuTech uitjes with you. Racing through Delft on the bike for the scavenger hunt and enjoying some party-time in Arnhem. A big thanks to you and Siebe for being huge ambassadors of King Fridge, what came out of that is invaluable:)!

Raymond and **Raymond**, the two of you together with **Roy** are an incredible resource for QuTech. The openness you guys have to help us is amazing. Even if I came in with probably the most basic electronics questions, you were there to help me out. I think you guys are a massive part of the success of QuTech. Raymond V, I love how electronics is your hobby and how you count years in bits, a true nerd in the best of its sense!

Nico, I really like the chat we had. You come across as someone extremely honest and genuine. Thanks for that and your availability to fix everything you do there in the workshop! We are happy to have you in QuTech.

Regis, thanks for being an approachable person. We haven't worked together a lot as Laurens was mostly taking care of our laser safety. But the few chats in the corridors and the beach day were very nice. Good to have you around! **Cleanroom staff**, absolutely not to be forgotten. You guys are so helpful, also you are extremely important for QuTech. Special thanks to **Bas**, **Eugene**, **Pauline**, **Arnold** and **Anja**.

Shannon, you've been an amazing person to meet. Always interested and happy to chat. You confused me with your ability to switch between Dutch and English. Should I talk English or Dutch to you? I still don't know. Next time, don't film me, but dance with me!

Jenny haha, what a fun running into you in the corridors or wherever, even in Aachen that random time. I've had so much fun chatting with you during the QuTech uitjes. We got along so well, that I was starting to doubt whether you were serious when you proposed that I could start dating one of your daughters. Even though that has not happened, I'm more than happy to join your next Christmass meal irrespectively.

Marja, you are a blast! You work neatly and calm, but when you hit the dancefloor you turn into an absolute example! I wish everyone would dance like you do. I was honoured to stand alone with you in the middle of a circle, entertaining the rest of QuTech during the Christmass party while we hit the floor on the Black Eyed Peas' Pump It. You and Jenny are a marvellous party-organizing team! I'm gonna miss those.

Sara and **Esther**, thanks a lot for being super helpful in all the requests I've made for either finishing my PhD (Sara) or helping out on organizing the QINC beach day (Esther).

Also thanks to **Helena** and **Shannon** for the QINC beach day organisation! **Chantal**, you are not to be forgotten. Solid force, always ready to help. Hope America is treating you well!

Also thanks to the QuTech communications team, you guys are providing us with many cool opportunities. I have interacted mostly with **Erik** and **Aldo**. Thanks a lot, also for always being available for a chat on scientific outreach endeavors.

Conor, mister Bradley! Thanks for all the fun times and British humour that you allowed me to experience. You have always been very open to help and you have the quality to be short, concise and to the point. Lovely to have been colleagues! Hope to re-experience a night like the Belgium beer night together! **Joe** The British tandem is not complete without mister Randall. You always managed to make me laugh, especially when your sarcastic humor came up. This especially surfaced under the presence of 'een lekker biertje'. Great that you raised **Floris** to become a fully fledged master of science, his enthusiasm and desire to undertake social activities was great to have around in the group.

Hans Bartling, your intense commitment to go for a nice coffee and a nice cheese practically anywhere on the globe where you are make you an inspiration by yourself. I am sad there was not a chance to enjoy more of your football skills. Thanks for all, and especially for answering all my practical thesis questions. Looking forward to the next joint drunk photo-booth machine session.

Besides Hans and Guido, I have been extremely happy to spend the post-March Meeting road trip with an amazing, diverse and interesting group. While a priori this wouldn't be a group with which a holiday would be booked, the March Meeting allowed us to do so. And it really was an amazing trip. Thanks to Guido for allowing us to have a getting-the-car-unstuck experience, and thanks to Hans for his genius idea to read the manual for instructions. This holiday was one of the highlights of the year. Thanks to **Nina** for a lot of good and fun chats, **Alejandro** and **Jiwon** for insane imitations of typically native English accents. Stunning quality. **Yanik** for bringing along great snow boots for hiking and a waterproof bag, as well as fighting about the TV channels with Alejandro in the hotel room of Guido and me. I got some photo coverage;). **Benjamin P**, lovely sarcasm and humor and a great bottom-to-the-ground Grand Canyon slider! **Juulleke** like I texted you before, a pleasure for the emotional well being of every person. You bring loads of joy with your typical laughter and your amazing night-time preps for major-conference presentations. Thanks to all of you for supporting me in the pizza challenge.

Arian, I have always enjoyed your unsalted opinions, which I think are typically backed by many sensible arguments. The trip together with Hans to the Lunteren conference with the cancelled train through the rain was amazing. Also many thanks for always inviting me to the ADE trip one evening in advance! **Benjamin O**, python guru. I thought team diamond was doomed after the incredible **Matteo Pompili**, who was skilled in programming, art, physics, music and very helpful, left. But happily you step in his footsteps. Not sure about your arts and music qualities though;). You're a great guy to have around. Nice to see how you joined forces on M2 with Jiwon and Margriet. **Margriet**, I will miss your sarcastic humor. You always directly understand my nonsense. Another thing I will really miss is making you jump just by the sound of my

voice. Mind your surroundings;). **Kai**, amazing to have you joining our team. You are a great guy that always has a spark on his face. I love that face where I know you are having fun about something, but nobody knows what. We had a great time in Stockholm. Nice to have you joining on M1, with Christina's many body simulations project. You guys solved the C29 mistery. **Aletta**, thanks for kickstarting my first PhD year with all your preparatory work on the P1-project. Also thanks for the many good chats we had during our times as MSc students. **Christina**, you are a more than welcome addition to the team with a lot of compassion and a desire to make fun. I was genuinly impressed by the amount of social activities you joined when you came to QuTech. Insane. Please burry Qtlab with respect. **Damian**, you are not to be forgotten when it comes to lots of fun and M1 carbon spins.

    Sophie, I love you curiosity and drive to ask questions. I think it is an amazing skill! **Max**, for a brief time we shared offices. I admire your dedication, research skills and social ability. While writing my thesis, your thesis served as a big inspiration. I think it is one of the nicest ones that I have read. Hope to meet you again! **Julius**, thanks, also to Yanik, for joining forces in organizing the QINC beach day and the infamous 'diamond cup'. It was obvious team Taminiau had the strongest team and would outperform team Hanson in anything (obviously except basketball –> Dutch pillars: Arian + Kian + Hans Beukers). However, you took the rules fluidly and invited former bachelor students (e.g **Yuran**, sprinting) and people to become team diamond members (e.g. **Niv**, tennis), so that you had a significant chance to beat us. My sincere congratulations to winning the diamond cup. **Hans Beukers**, what an enthusiasm you have for anything you do, inspiring. Congrats with Hanna and I love your appreciation for the 'Loenen diaper under diaper' technique, credits to my sister **Lynn**. What I do not love, is your appreciation for our ordering system. It is a shit system, end of the discussion.

    Kamiel, we did many things together. Studying physics, playing football and celebrating carnaval in Tilburg. You even convinced me to join in the King Side of the one-but-best football club of the Netherlands. You're a great friend and it was lovely to share so many different aspects of my life with you. **Christian**, congrats on running the Rotterdam marathon, amazing job! You're a great guy, kind and humorous. I want revanche for the time you beat me in tennis. **Matteo Pasini**, your art skills are amazing. Maybe the coolest laymen's talk I have ever seen! I love the sarcasm and humor we shared. I don't love your effort to steal my tennis shoes. **Simon**, you're an amazing personality. Thanks for allowing me to buy your TV and always being very kind and open to answer questions or have discussions. Amazing how you, your wife and your kids are doing with the campervan! **Elvis**, thanks for the great discussions we had about the importance of breathing and the lives we shared in the cleanroom. Your drive to live healthy is truly inspirational! Very nice you went on a long desired trip to China! **Tim Turan**, you surprised me that time that I thought you were shaving your beard in the morning on the TU Delft restroom. Keep up surprising your colleagues. I don't understand how you can possibly be so comfortable with that lab chair you use in your office. **Mariagrazia**, I loved your moving-to-the-Netherlands story, specifically the part of the suitcases. You and **Christopher** came on the same day to join team diamond and turned out to become a great combination! **Marie-Christine**, **Matthew** and **Lorenzo**,

thanks for being open to chat and having such relaxed personalities. Thanks as well to **Colin** and **Tobi** and all the other master students that were fun to work with!

Vicky, thanks for a lot of fun and serious chats. It is good to have some Mediterranean influence. **Lukas**, thanks for meeting you. I didn't think someone with that level of passion, dedication and the desire to tell others about exactly that passion non-stop. Teaching quantum hardware with you and Vicky was a lot of fun. Nice that we did those beers in the city center. **Luc**, when Lukas is named, you cannot run behind. Actually, I think you usually run in front of Lukas. I love your passion for sport and it was amazing to spend a day with you on the skis in Austria. Amazing to have you as a colleague in QuTech.

A special thanks to the people that dragged me through this outside of my office. First of all the Spieringboys! **Stijn**, a.k.a. Ronnie. Thanks for teaching me that things become lighter when you scream they become lighter. It allowed me to apply this to my PhD. When you came to live with us, I knew we would bond well when I saw you watching Avatar, The Legend of Aang. You were a driving force behind our Corona night-time hour of watching two episodes of this amazing series every evening. Thanks for joining me in speaking out aloud the entire intro of each episode! Water, aarde, vuur lucht. Lang geleden leefde de vier naties in vrede samen, maar alles veranderde toen **Jorn**, studio JB, in het huis kwam. Sleeping in was impossible and likewise the times of a spacious toilet without sand and 100% of his kite gear were over. Beltmanus, mister creativity, every Friday, half past 5, the beats roared from your speakers to announce the Friday afternoon drinks. Urinals in India to love bubbles on the Dutch outskirts to selling tosti's on the Zwarte Cross. A blast to spend time with you and thanks for the master class in kiting. **Thomas**, mister DDRF, I was thrilled to have you at my side. Toghether we needed to withstand the architect vibe in our house and counterbalance this with our physics minds. It was obvious we had the cleanest rooms of the four of us. No place for dirt if there is no place for decoration. Your minimalist style of room decoration was well reflected in your squash qualities. I'm up for revenche, next time I'll play with my legs tied together, let's see whether you can make a point. Guys, our skiing trip was unforgettable. Schnaps Hansbar, backup, 24 hours on skying boots going through 5 different apres ski bars and making me forget that we had dinner. And that full day of skiing to get to the Goasstall, where we had a blast of fun with are grateful to Djoeke and the girls to serve us beers like kings.

Wim, you are not to be forgotten as a valuable addition to our time at the Spieringstraat. You are truly a unique man! Thanks to you I made my debut as a TV star. You were dedicated to get me on that show and eventually managed to convince me. Thanks for that, life's good as a superstar. Thanks also for always making me rush when we needed to get to our football trainings and immersing your flatmates with useless facts! **Thijs**, gruwelijk mooie vent! So nice to have lived with you, your storytelling skills are unheard of, I don't know how you can make every story a compelling story to listen to. You convinced me to take on the Annapurna trail challenge, your stories, photo coverage and ebook experience were definitely a big part for me to embark on that trail. Thanks for all those times you guided me with your guitar on our late night drunk times singing Brabant of Guus Meeuwis in our living room after our Corona flat parties.

I have also been happy to share that amazing student flat with **Constantijn** Molengraph. Sadly you left after a few months. But thanks to you I could move in. Incredible how calm you are when you are sober and how wantonly you get when you start drinking. Great to have joined you also in the defense line of Ariston, and thanks for sometimes passing the ball back to me so that I didn't complete the warm up to just watch you guys scoring 8 goals. **Sander**, your down-to-earthness together with Wim's personality were a great combination. **Casper** Maarten Mulder, 11-times employer of the month at staff you, incredible performance. I'm happy you are still dating Judith and that you found your place at CGI. **Sam**, padel, cycling, rowing, running, is there anything you would not coin yourself a skilled person in? Your cooking skills are amazing and I loved teaming up to always make Casper react to our statements in the way we wanted. **Niels**, thanks for all the great fun and laughter. I hope you keep appreciating the special calendars we had in our house. I have really enjoyed sharing the bathroom with you for two weeks, after which I left to Rotterdam.

Thanks a lot to Stroveertjes **Casper** and **Marc** for being incredible flatmates, dragging me through the last months of my PhD. Casper, since I live with you everything is so nice and chill. Your attitude is maybe the most positive one I have ever experienced, you are truly the best! Marc, philosopher of the universe, your lifestyle is amazing. You value your friends a lot and prioritize it to spend time with them. You cook amazingly and your 30th bday party was greatly organized. Thanks for letting me ironing your shirt and helping you to shine. Guys, I hope in the time to come we will manage to dine together a bit more frequently than twice every month.

A special thanks to **Vincent** and **Brian**, literally every time it was a great pleasure meeting up with you. The ability to switch between discussing die-hard physics and die-hard nonsense is something that I only find with the two of you. Thanks for being a listening and understanding ear for the PhD trouble we sometimes needed to go through. I loved our 'tour de parants' by bike and our trip to Deventer. We've learned a lot about holy water or something like that, as well as all the crazy inhabitants of that city. Both your defenses were stunningly great. And the parties that followed were one of the best parties to have experienced and to remember! Thanks for everything.

During my PhD, I have had the amazing pleasure to work together with three amazing friends. Together with **Koen**, **Niels** and **Dennis** we embarked on a hiking trip every summer from which the idea arose to develop a card game. One and a half year later, King Fridge arrived at the doorsteps of our first customers. Guys, the interactions and the experiences that we have had are of really great value to me. Also, working together with you and discussing hours long about what words and font size to use were unforgettable. Koen, thanks a lot for your creativity and amazingly complimentfull attitude, I think that is an amazing skill of you. Also big shout-out to you for the cover design, I knew I could trust on the master designer of King Fridge. Thanks mate! Dennis, thanks for always seeing opportunities and taking initiative to start up those opportunities. Niels, thanks for always teaming up against Koen and Dennis when they had another idea that we were not to much fan of. Thanks also for putting me through that half-marathon in the Alps. I thought it was a safe bet to say I would only do it if you would do it. Turned out not to be. But it was one of the best experiences!

Aled, you have always been a great friend, and likewise a person to share PhD-related stuff with. Thanks for the many great tennis experiences we have shared. **Laureen**, you inspired me to start taking salsa classes more seriously and I have enjoyed every single moment of it. It has always been nice to share good dinners and stories with you, being your grasshopper in the karate classes, dining skills or salsa experiences. It was also nice to be able to share PhD-related things with you. **Jessie**, thanks a lot for all the fun we have had during our salsa classes and beyond. It was a gift to meet you during the try-outs of the salsa school. Our personalities matched so well that thanks to you I am always looking forward to our salsa classes. Thanks as well for helping me to pimp my room with a good amount of plants! **Irma**, thanks for spending a lot of nice time together! Your humour is something that I really value, and how down-to-earth your reasoning about anything is, is very nice. Even without a background as a PhD, you always made me feel understood when I made you listen to my successes and struggles. You've played a great part the time of my PhD, thanks for that! Nice to have you as a great friend. Thanks to **Djoeke** for giving me the opportunity to disseminate my research to a laymen's audience while enjoying a good mean in an insanely nice location. Your passion for research is insanely inspiring, and actually very motivating as well! Thanks also for all the fun times afterwards. The beers and the chats, and a highlight the evening we kinda randomly met up at our skiing holiday. **Kaz**, I have always loved interacting with you and I think you are a great and respectful personality. I like how you approach and pursue your goals. Thanks for hosting me in Werkwerkwerk de podcast! **Nadia**, thanks a lot for listening to me during the last bits of my PhD and supporting my late-night work sessions to get my thesis finished. Thanks also for making me work these late-night hours. Without you, I wouldn't have realized that I needed to hurry up. I was way too relaxed. You made me realize it is important to start making appointments with the printing company in time and hence that I needed to soon finalize my thesis and thesis cover. Thanks to you I was able to still integrate updates of chapters that I wanted to get upgraded.

During my PhD I have been happy to make two amazing visits to great friends from Costa Rica. **Alonso**, ever since we met up in CERN, we connected very well and it was instantly clear that we shared so many interests. We had spend such a nice time together over there that definitely contributed to making that entire trip one of the best, if not the best, summer of my year. A year later, we spend a lovely time during our one-week roadtrip through your amazing country. You introduced me to many of your amazing friends. And also I was eager to meet **Sofia**. It was so nice to be invited to your wedding together with **Sjoerd's mom**. That entire month being there and spending so much time together with all your beloved ones, including your family (**Olga**, **José**, **Susy**, **Carmen**) is such a lovely experience I was allowed to witness. It is lovely to have you living in the Netherlands now.

Via these trips I was super happy to get to meet you **Adán** and **Alhyssa**! You might be my favourite couple. The way that you interact with each other is so nice to see, I really think you two are the best fit. And both of you are so super kind and willing to spend time with me and showing me around in Costa Rica, and specifically Rancho Redondo. My god Àdan, please stop trying to converse with me when I am giving it all to climb up

that damn mountain. Doña H is so touched by how the two of you interact and she loves you. It was such a nice gesture that you invited me for your wedding, that meant a lot to me. The act to write something personal for everyone on their lunch cards to me once again shows how amazingly attached you are to the people around you. Being at your wedding was a true pleasure!

My summer school in CERN also allowed me to build many other extremely valuable relationships. **Alfonso Amayuelaz Fernandez**, Pepito, brother, you are so buff it is incredible. I think I have seen and felt your biceps more than anything else from you. We have covered many places together. Switzerland, the Netherlands, Cuba (el flaco), Greece, Costa Rica and the United States. All those experience with you are amazing. I love bullshitting with you, and also value the spare moments we have a serious conversation. You are a really good friend! Thanks for being such an amazing host during my visit in Santa Barbara, where indeed the sun always shines....

Marina, kastana tha psinoume sto tzaki, something we actually should do together some time! My god, we have shared some experiences together. An outstanding one: singing para poli together with Alfonso and **Christos** Christaki, my uncle Chris. You taught us that song so well that Alfonso and me impressed many Greek people. Thanks for visiting me in December 2022. You are so smart, all that knowledge in your head! We nearly participated in the Bruggenloop, until Sourtis got sourta. Apart from that, we had such a nice week, it was one of the best weeks of that year for me. You are an amazing person and I am looking forward to spend much more time together.

Nachiappan Valliapan, likewise you have been an important person in my life. Sharing memories in CERN where you forced me to feed myself with my fingers, until the point that I started eating yoghurt with my fingers. Sharing many songs of Linkin Park together, holiday experiences in Amsterdam and in Sweden together with Alonso and joining forces on Alonso's wedding. You have a very nice personality and I am looking forward to meeting up with you. Thanks for being such an important contributor to Sjoerdish!

Cecilia, darling, thanks for being opposite neighbours during our CERN time and spending many great meals together and enjoying the firework festival at lake Geneva. Sadly we got separated for 4 years until we had a blast of a reunion in Paris. Those couple of days together were like we never separated, it was so nice to meet up again. That continued while you were being a magnificent host during my time in LA. Thanks to you those weeks staying over at your place were amazing. You had planned so many nice adventures together. From the touristic stuff, to the sunset beach, to immersing me in a much to high quality salsa event, to taking me on a nice hike. I loved spending these moments with you and look forward to spending more experiences together.

David thanks for all the good meals and we made together during CERN, the nice visits me and Alonso could make to you in Aachen and your extended and eloquent stories. I am looking forward to seeing you again!

Ilirjan, you were an incredibly nice flatmate. You have shown a level of dedication that I had never witnessed before. It was truly inspiring to see you working and especially to hear your life story. I have a lot of respect for you. I am very happy I had the pleasure to meet you and share a big part of my CERN summer with you!

Thanks to many others that have made the past four years incredibly nice! **Cansin**,

you still refuse to acknowledge that you were completely lost on the first day we met and I offered my help to a lost lady in the QuTech corridors. It was nice to get to know you better during the QuTech uitje. We became really close friends. Thanks for always being there to listen to me when I wanted to tell some nonsense, or when I really needed a good chat. Thanks for sharing intense moments together, it was and is lovely to have you as a great friend. **Michel**, your down-to-earthness is relativating. Thanks to you and **Gabriella** for all the support. **Casper** and **Peet**, you joined forces in making many new year's eve celbrations a stunning success. **Brian**, thanks for completing our padel competition team and for the good times we spent together. A pity that tent party we passed by after our season ending celebration was over, otherwise we would definitely have had a lot of fun there.

Speaking about fun, **Loïc** what a character are you. If you want to hear constant chatter, just give you a call. Even when you are on the other side of the tennis court I only hear you shouting and screaming. Most heard 'Lossie time'. This thing you shout when you finally manage to hit a forehand past me. No jokes aside, you've become a great friend and we have shared many stories and experiences. Let's continue our tennis endeavors. I also want to thank **Jorge**, **Vidharsana** and **Francisco** for all the tennis experiences. **Sebas**, what fun to always meet you. You always are so positive and bring laughter to your surroundings. You are an extremely nice person and it is nice to see you and **Milou** together. Thanks to you two, but especially **Anouk**, King Fridge has risen to unforeseen heights! **Jarn** Scholtens de Jong, I'm so happy you introduced me to many of the above mentioned people, but most of all that you introduced me to yourself. Apart from the noise you generated by putting nuts in a 1.5 liter coca-cola plastic bottle to subsequently get them out again, you have been the best to sit next to during my MSc thesis. Lovely to get a full-fledged lecture on quantum error correction on my first day in a quantum institute. You also introduced me to **Nima**, with whom I shared an amazing trip to Nepal. Hyped as we were to start hiking, you sadly needed to abandon on day two. That set the mark for me some days later. Irrespective of that, we had a lot of fun the first two days wondering around in Kathmandu. **Stanley**, thanks for your refreshing, sharp and funny comments in real life and in our Grand Slam chat!

Bouwe, thanks for all the sport sessions we have done together. Constantly looking to your but from the goal during football, or looking at that massive forehand while playing tennis or padel. The carnaval celbrations were amazing. **Martijn**, we need to keep doing the buikspierkwartiertjes! Also the others of the **Ariston** selection, you made it a nice distraction to go and play football, drink beers and go out together!

Rutger, **Lars**, **Danny**, gekke boys, thanks for al dat slap geouwehoer! It has always been nice to meet up together, although that actually never happens since Lars and me always end up reading that one of you two cancels. I'm sure we will manage to meet up the four of us in the future, and that Danny and me will witness many interesting discussions between Rutger and Lars.

Wout, **Max**, **Michael**, **Oscar**, **Jeroen**, great friends to have around and to know you since elementary school or high-school. Thanks for sharing many great experiences in Brno-no-no-no-no, Germany, France on festivals and on the tennis court.

Mike, the Geile Gieters were already special by itself, but you made it even more spe-

cial! We share a long history. I always remember playing zwervertje with you when we were really young kids while your parents were watching temptation island. Now, many years later, we live far apart, but I am happy we still take moments to share beers and interesting life stories. Grateful to have you as a friend, and looking forward to spend time together!

Jochem, it was always nice to discuss everything with you. I really enjoyed the beach day we recently had, it was amazing. **Simone** thanks for making me aware of my allergies and SiKoCi. It was nice to go to the UP reunion together. **Iris**, cool to have the 5 minutes of skiing and après-skiing together last year. It was a lot of fun. Together with **Dionne** and **Azra** you guys gave me a super cool, instructive and fun year in between practising physics. I learned a lot from you all, specific thanks for all those times you forced me to shop with you under your commands.

B-boy Boiszerboy, **Gerbinator**, **Takkie**, **Yoepos**, **Weertsio**, **Kwant**, **Yuri**, it was amazing to undertake everything that prepared me for my PhD together with all of you in Eindhoven. I loved the times Gerben banged his head into the staircase post to convince himself it was a good idea to come to the pub, the indoor softball matches with oranges, the fruitful discussions about carburators and bougies, the FIFA matches, my birthday parties, de woonboot and the Zwarte Cross experiences.

Hermy, mom, thanks for always making the effort to listen to what I was doing in my life. Whether it was a trip to one of the friend groups that I got to know during my University life, whether it was about my studies, or whether it was about my PhD. It was a very valuable experience to have you next to me during Alonso's wedding and also to have you meet Nachi and Alfonso, two of my other friends of which I told you many stories. In addition, it was very valuable to spend the roadtrip with you and **Rick**! **Jan**, dad, thanks a lot for all the fun chats we had and for your interested in what I was persuing in life. It has always been nice to pass by your house, eat together and have a good chat while enjoying a beer. Next to a dad, you are a great friend. **Hans**, I'm very happy to have you in my life for a long time. You have always been very supportive in everything I did. It is nice to have someone like you around that is always looking for ways in which you can be helpful to us.

Wout, **Lynn** and **Jens**, you are a great set of siblings and I still always love singing Pokémon or Big Time Rush songs with you. Wout, we have shared many experiences, and while sometimes in the moment I wasn't too happy going out together, in the end I am very happy we were allowed to spend time as great friends, brothers, and tennis and football companions. Lovely you met **Richelle**, she is an amazing addition to the family, and it is super nice to see how happy and lovely you both are with **Guus**. **Lynn**, even though our personalities collided when we were teenagers, we have many great experiences together. I still vividly remember us practising 'de schaar', a football trick, on the grass field in our backyard. Thanks for always cooking very nice dishes (preferably without a cashew boemboe). I'm happy I was there that time the spark flew over between you and **Teun** when you entered the living room hungover in your bath rope while Teun and me were organizing a team outing. It is amazing to see how much you both love and enjoy **Mees**. **Jens**, thanks for all the positivity and love that you bring into life. Thanks for visiting me in Delft! Your laugh is the most remarkable laugh I know and it is so contagious. You always make every encounter filled with loads of fun. And

the best thing is, you also have such a nice ability to gauge when people are not feeling very well emotionally. You are able to be a listening ear that anyone desires at such moment. I love it to see how involved you are in Groeningen and Vierlingsbeek. Insane to see how literally everyone knows you and everyone likes you. That most definitely includes me!

Rob, we have been friends since we were young and I really appreciate you as a step-brother. You are always very interested, filled with humor and a listening ear in anything someone is struggling with. I have a lot of respect for you and admire you as a person! I am super happy you met **Daphne** and that you are expecting your first child. What a moment to look forward to, I'm looking forward to seeing both of you shine. That Daphne is not to be confused with your sister **Daphne**. Daffy duck, I really love the interactions we always have, whether it is in person chatting about some nonsense, or whether it is sending GIFs of André Pronk or Avatar. It is very nice to have you as a step sister and spending for example the skiing holidays together. **Jeroen**, you are a great step-brother as well. Cool to have spent our skiing holiday together. Much respect for how you took up the challenge to build your own house and how you, Rob and Hans built the cafe we have in our backyard. It is super enjoyable. Lovely to see you and your daughter together!

In general I am very blessed with both the **Loenen** and **Voermans** families. They are both lovely and it is nice to have such a large pool of family. I am very happy to have amazing, diverse and very interested aunts and uncles on both sides of the family along with many great cousins of many different ages that all have their own amazing unique character that I really like to interact with. Importantly, while sadly non of them is able to witness my defense in person, I have a very loving set of grandparents that have set an example with how they have raised their families. Thanks to all four of you for that. Both families have had a very big positive influence on my life and I am very grateful for all the amazing experiences we have shared together. A special thanks to **Arjan**, with whom I could share many of the PhD stories. That was always interesting and insightful. Especially also the fun we made besides discussing those stories.

Indy, **Hindje**, **Hector**, **Faya** and **Nova**, sadly coming home nowadays means not meeting most of you. But you girls and guy have always made me want to come home so happily. I adored all of you and really loved spending time together. Whether it was at home in the grass, outdoor near a lake, or while you were on my lap. Especially you Indy, I don't know how you did it, but you always knew when I had a rough time and when I could find comfort in your company. Having you lying close to me, with your head on my lap, softened all my struggles. All of you were or are great friends that have a special place in my heart and life!

List of Publications

7. *Spectral diffusion dynamics of lifetime-limited optical transitions in commercially-available bulk silicon carbide.*
S.J.H. Loenen*, G.L. van de Stolpe*, L.J. Feije*, G.M. Timmer, A. Das, T.H. Taminiau,
In preparation - Ch. 5 of this thesis

6. *Quantum network nodes with real-time noise mitigation using spectator qubits.*
S.J.H. Loenen, Y. Wang, N. Demetriou, C.E. Bradley, M. Markham, D.J. Twitchen, B.M. Terhal, T.H. Taminiau,
In preparation - Ch. 4 of this thesis

5. *Control of individual electron-spin pairs in an electron-spin bath.*
H.P. Bartling*, N. Demetriou*, N.C.F. Zutt, D. Kwiatkowski, M.J. Degen, **S.J.H. Loenen**, C.E. Bradley, M. Markham, D. J. Twitchen, T. H. Taminiau,
arXiv:2311.10110

4. *Robust quantum-network memory based on spin qubits in isotopically engineered diamond.*
C.E. Bradley, S.W. de Bone, P.F.W. Moller, S. Baier, M.J. Degen, **S.J.H. Loenen**, H.P. Bartling, M. Markham, D.J. Twitchen, R. Hanson, D. Elkouss, T.H. Taminiau,
npj Quantum Information **8**, 122 (2022)

3. *Fault-tolerant operation of a logical qubit in a diamond quantum processor.*
M.H. Abobeih, Y. Wang, J. Randall, **S.J.H. Loenen**, C.E. Bradley, M. Markham, D.J. Twitchen, B.M. Terhal, T.H. Taminiau,
Nature **606**, 884-889 (2022)

2. *Entanglement of spin-pair qubits with intrinsic dephasing times exceeding a minute.*
H.P. Bartling, M.H. Abobeih, B. Pingault, M.J. Degen, **S.J.H. Loenen**, C.E. Bradley, J. Randall, M. Markham, D.J. Twitchen, T.H. Taminiau,
Physical Review X **12**, 011048 (2022)

1. *Entanglement of dark electron-nuclear spin defects in diamond.*
M.J. Degen*, **S.J.H. Loenen***, H.P. Bartling, C.E. Bradley, A.L. Meinsma, M. Markham, D.J. Twitchen, T.H. Taminiau,
Nat. Commun. **12**, 3470 (2021)

---

*Equally contributing authors

SJOERD
JOHANNES
HENDRIKUS
LOENEN

February 3th, 1994
Groeningen, Brabant
The Netherlands (NL)

2006 - 2012	High school Metameer Stevensbeek
2012 - 2015	BSc. Applied Physics Eindhoven University of Technology, NL Thesis: 'Fresnel diffraction on a semi-infinite opaque screen' Advisors: Prof. O.J. Luiten & Dr. E.D.J. Vredenbregt
2015	NAHSS: Netherlands Asia Honors Summer School 7 weeks Hong Kong + Shanghai, China
2015 - 2016	UniPartners Nederland - student consultancy enterprise IT manager & vice-president - full time
2016 - 2019	MSc. Applied Physics Eindhoven university of Technology, NL Thesis: 'Improving single-shot readout for diamond quantum processors' - QuTech TU Delft Advisor: Dr. T.H. Taminiau
2017	CERN summer school - 9 weeks Project: Top quark decay in forward proton collisions (TOTEM) Advisors: Dr. M. Mulders & Dr. L. Forthomme
2017	Research internship - Oxford University Thesis: 'Experimental photon state preparation for on-chip experiments' Advisors: Dr. J.J. Renema & A. Eckstein & Prof. A. Fiore
2019 - 2024	PhD in experimental physics, Delft University of Technology, NL Thesis: 'Spins in diamond and silicon carbide for quantum networks' Advisor: T.H. Taminiau
2020+	Cardgame designer - https://www.kingfridgegame.com